

A Thesis Submitted to the University of Kent for the Degree of  
Doctor of Philosophy in Electrical Engineering

**Applications of Origami Folding  
Techniques on Antenna Structures using  
Flexible Substrates**

**By  
Calvin Chun Hin Ng**

## Abstract

This thesis investigates the use of Origami folding techniques in antenna structures. This application would be suitable for space satellites and military secure communications.

The main research is divided into three segments. The first one presents a Vivaldi antenna using flexible substrates, Kapton and Mylar. They are simulated in Computer Simulation Technology (CST) Studio and tested with a Vector Network Analyser (VNA) in the anechoic chamber. The reason for using various flexible substrates is to determine which substrate would perform better when folded. Each substrate has unique electrical and mechanical properties.

Secondly, a more specific Origami folding pattern called Miura Ori is introduced. It is integrated into two antenna designs: Slot antenna and Substrate Integrated Waveguide (SIW) antenna. The Miura Ori folding technique is a repeated pattern with some interesting mechanical properties. It would be able to switch between different states: flat, partially folded or fully folded. This would be beneficial for applications where the cost, size and weight are limited. Both antenna designs are simulated and optimised to achieve a good performance, before incorporating the Miura Ori folding technique. There are special parameters that require the model to be functional, Inner angle and Folding angle. Each antenna is simulated by varying those two parameters, because of that the resonant frequency, reflection coefficient ( $S_{11}$ ), gain and the direction of the radiating angle is changed.

Lastly, a microwave switch with nanowires is investigated to provide a fast switching network at each individual antenna. The microwave switch is simulated on a flexible substrate.

Calvin Chun Hin Ng

April 2019

## **Acknowledgements**

I would like to express my sincere appreciation to my supervisor, Dr Paul Young, for the guidance throughout the course of this thesis. Without his support, this work would not have been possible.

I am also grateful to all the administration and technical staff at the University of Kent. Their contribution was very important and I am truly grateful for their support.

Lastly, I would like to express my gratitude to all my family and friends, for the love and support that they provided. They were always there for me and believe that I can finish this thesis.

# Contents

<b>Abstract</b>	<b>i</b>
<b>Acknowledgements</b>	<b>ii</b>
<b>1 Introduction</b>	<b>1</b>
1.1 Overview and Motivation . . . . .	1
1.2 Research Aim and Objectives . . . . .	1
1.2.1 Aims . . . . .	2
1.2.2 Objectives . . . . .	2
1.3 Thesis Outline . . . . .	2
1.4 Publications arising from this work . . . . .	4
<b>2 Origami and Engineering</b>	<b>6</b>
2.1 Introduction . . . . .	6
2.2 Origami Theory . . . . .	7
2.2.1 Mathematics in Origami Folding . . . . .	7
2.2.2 Folding Technique . . . . .	9

---

2.2.3	Miura Ori . . . . .	11
2.2.4	Origami Science . . . . .	15
2.3	Origami Antennas . . . . .	18
2.3.1	Helix Antenna . . . . .	18
2.3.2	Frequency Selective Surfaces . . . . .	23
2.3.3	Nojima Folding . . . . .	24
2.3.4	Others . . . . .	25
2.4	Summary . . . . .	29
<b>3</b>	<b>Vivaldi Antennas</b>	<b>30</b>
3.1	Introduction . . . . .	30
3.2	Antenna Theory . . . . .	31
3.2.1	Microstrip Line Transmission . . . . .	31
3.2.2	Matching Network . . . . .	33
3.2.3	Vivaldi Antenna . . . . .	34
3.3	Academic Research on Vivaldi Antennas . . . . .	35
3.4	Vivaldi Antenna using flexible substrate . . . . .	39
3.4.1	Flexible Vivaldi Antenna Design . . . . .	40
3.4.2	Single Vivaldi Antenna - Simulated Results . . . . .	40
3.4.3	Single Vivaldi Antenna - Measured Results . . . . .	48
3.5	Foldable Arrays of Vivaldi Antennas . . . . .	52
3.5.1	Schematic . . . . .	52

---

3.5.2	Arrays of Vivaldi Antennas - Design . . . . .	55
3.5.3	Arrays of Vivaldi Antennas - Simulated Results . . . . .	56
3.5.4	Arrays of Vivaldi Antennas - Measured Results . . . . .	59
3.6	Summary and Conclusion . . . . .	64
<b>4</b>	<b>Flexible and foldable Slot Antennas</b>	<b>67</b>
4.1	Introduction . . . . .	67
4.2	Babinet's Theory . . . . .	68
4.3	Academic Research on Slot Antennas . . . . .	68
4.4	Slot Antennas . . . . .	73
4.4.1	Single Slot Antenna - Design . . . . .	73
4.4.2	Single Slot Antenna - Simulated and Measured Results . . . . .	82
4.5	Arrays of Slot Antennas . . . . .	100
4.5.1	Arrays of Slot Antennas - Design . . . . .	101
4.5.2	Arrays of Slot Antennas - Simulated and Measured Results . . . . .	103
4.6	Summary and Conclusion . . . . .	121
<b>5</b>	<b>Substrate Integrated Waveguide Antennas</b>	<b>124</b>
5.1	Introduction . . . . .	124
5.2	Substrate Integrated Waveguides . . . . .	125
5.3	Academic Research on Substrate Integrated Waveguides . . . . .	127
5.4	Substrate Integrated Waveguide Antennas . . . . .	134

---

5.4.1	Single SIW Antenna - Design . . . . .	134
5.4.2	Single SIW Antenna - Simulated Results . . . . .	140
5.5	Arrays of SIW Antennas . . . . .	148
5.5.1	Arrays of SIW Antennas - Design . . . . .	148
5.5.2	Arrays of SIW Antennas - Simulated Results . . . . .	151
5.6	Summary and Conclusion . . . . .	159
<b>6</b>	<b>Microwave Switches using Coplanar Waveguide with Nanowires</b>	<b>161</b>
6.1	Introduction . . . . .	161
6.2	Coplanar Waveguide Theory . . . . .	162
6.2.1	Operations with Nanowires . . . . .	163
6.3	Academic Research on Microwave Switches . . . . .	164
6.3.1	Co-Planar Waveguides . . . . .	166
6.3.2	Nanowires . . . . .	168
6.4	Microwave Switch using Coplanar Waveguide Design . . . . .	170
6.4.1	Design Requirements and Constraints . . . . .	171
6.5	Simulated Results . . . . .	172
6.5.1	Initial Microwave Switch Design . . . . .	173
6.5.2	Improved Microwave Switch Design . . . . .	184
6.6	Applying Microwave Switch to Antennas . . . . .	194
6.6.1	Simulated Results . . . . .	195
6.7	Summary and Conclusions . . . . .	198

<b>7 Conclusion</b>	<b>200</b>
7.1 Summary of Thesis Achievements . . . . .	200
7.2 Applications . . . . .	204
7.3 Future Work . . . . .	204
<b>References</b>	<b>206</b>



# List of Tables

3.1	Table of Mechanical and Electrical Properties for Kapton and Mylar . . .	39
3.2	Vivaldi Antenna values for both Kapton and Mylar . . . . .	48
4.1	Table of Parameters used with Slot Antenna . . . . .	77
4.2	Single Slot Antenna - Simulated Resonant Frequency (GHz) . . . . .	86
4.3	Single Slot Antenna - Measured Resonant Frequency (GHz) . . . . .	86
4.4	Single Slot Antenna - Simulated reflection coefficient (dB) . . . . .	87
4.5	Single Slot Antenna - Measured reflection coefficient (dB) . . . . .	88
4.6	Single Slot Antenna - Simulated Gain (dBi) . . . . .	89
4.7	Matching Network Values . . . . .	102
4.8	Arrays of Slot Antennas - Simulated Resonant Frequency (GHz) . . . . .	106
4.9	Arrays of Slot Antennas - Measured Resonant Frequency (GHz) . . . . .	106
4.10	Arrays of Slot Antennas - Simulated reflection coefficient (dB) . . . . .	108
4.11	Arrays of Slot Antennas - Measured reflection coefficient (dB) . . . . .	108
4.12	Arrays of Slot Antennas - Simulated Gain (dBi) . . . . .	109
5.1	Single SIW Slot Antenna - Table of Parameters . . . . .	137

5.2	Single SIW Slot Antenna - Resonant Frequency (GHz) . . . . .	140
5.3	Single SIW Slot Antenna - Reflection coefficient (dB) . . . . .	141
5.4	Single SIW Slot Antenna - Gain (dBi) . . . . .	142
5.5	Arrays of SIW Antennas - Matching Network Values . . . . .	149
5.6	Arrays of SIW Antennas - Resonant Frequency (GHz) . . . . .	151
5.7	Arrays of SIW Antennas - Reflection coefficient (dB) . . . . .	152
5.8	Arrays of SIW Antennas - Gain (dBi) . . . . .	153
6.1	Design Requirement . . . . .	172
6.2	Design Material Properties . . . . .	172

# List of Figures

2.1	Huzita & Hatori Axioms . . . . .	8
2.2	Valley Fold . . . . .	9
2.3	Mountain Fold . . . . .	9
2.4	Carboard Fold . . . . .	10
2.5	Outside Reverse Fold . . . . .	10
2.6	Inside Reverse Fold . . . . .	10
2.7	Folding Pattern . . . . .	11
2.8	Miura Ori . . . . .	12
2.9	Single Unit Cell - Miura Ori . . . . .	13
2.10	Origami Solar Panel [14] . . . . .	13
2.11	Origami Architecture Building [15] . . . . .	14
2.12	Origami Solar Panel Prototype [14] . . . . .	15
2.13	Folded Paper Lithium-ion Battery [18] . . . . .	16
2.14	Cell Origami [19] . . . . .	16
2.15	Cosmic Origami [20] . . . . .	17

2.16 Self Folding Origami [21] . . . . .	18
2.17 Origami Quadrifilar Helix Antenna: (a) Loop Idea Helical Antenna Model; (b) Unfolded and Folded States; (c) $S_{11}$ and Radiation Pattern [23] . . . . .	20
2.18 Origami Segmented Helical Antenna with Switchable Sense of Polarisation: (a) Origami paper base; (b) Origami pattern for hyperbolic paraboloid with antenna traces; (c) Top and Side view; (d) Measured Far-field characteristic of Segmented Helical Antenna [24] . . . . .	22
2.19 Origami Tunable Frequency Selective Surfaces: (a) Chevron Pattern with conducting element; (b) Transmission coefficient for Simulated and Measured; (c) Fabricated tunable FSS [26] . . . . .	23
2.20 Morphing Origami Conical Spiral Antenna Based on Nojima Wrap: (a) Nojima Pattern with a 15 folded and a Nojima Origami square; (b) Nojima Square prototype unfolded and folded state; (c) Simulated and Measured Reflection Coefficient; (d) Simulated and Measured Realised Gain [27] . . . . .	25
2.21 Low-Cost Circularly Polarised Origami Antenna: (a) Geometry of Circular Polarised Origami Antenna; (b) Simulated and Measured Reflection Coefficients [28] . . . . .	26
2.22 Self-Folding Origami Microstrip Antenna: (a) Microstrip Patch (Prior) and Monopole (After); (b) Simulated and Measured for Microstrip Patch; (c) Simulated and Measured for Monopole [29] . . . . .	27
2.23 3D-Printed Origami Packaging With Inkjet-Printed Antennas: (a) InkJet printed Patch unfolded and folded state; (b) Measured Reflection Coefficient; (c) Origami Package with harvester electronic [30] . . . . .	28

2.24	Physical Reconfiguration of an Origami-Inspired Deployable Microstrip Patch Antenna Array: (a) Microstrip Patch Antenna Array; (b) Intermediate State at different angle; (c) Simulated Reflection Coefficient for each angle [31] . . . . .	29
3.1	(a) Microstrip and (b) Fringing Field . . . . .	32
3.2	Quarter Wave Matching Network . . . . .	33
3.3	Single Exponential Vivaldi Design . . . . .	34
3.4	Linear Tapered Slot Vivaldi Antenna with Corrugated Edges for UWB Applications: (a) Proposed Linear Vivaldi Antenna; (b) Reflection Coefficient of the proposed Linear Vivaldi Antenna [38] . . . . .	35
3.5	Switchable-feed Reconfigurable Ultra-Wide Band Planar Antenna: (a) Reconfigurable Vivaldi Antenna; (b) Antenna Electric Field Characteristic; (c) Simulated and Measured Reflection Coefficient [39] .	36
3.6	New Tapered Slot Vivaldi Antenna for UWB Applications: (a) Tapered Vivaldi Antenna with microstrip; (b) Reflection Coefficient of the Tapered Vivaldi Antenna [40] . . . . .	37
3.7	Flexible UHF/VHF Vivaldi Antenna for Broadband and Gas Balloon Applications: (a) Fabricated antenna with curve support; (b) Reflection Coefficient of the antenna under stress; (c) Antennas attached onto balloon [41] . . . . .	38
3.8	Single Vivaldi Design . . . . .	39
3.9	Single Vivaldi Dimension Chart . . . . .	40
3.10	Single Vivaldi Antenna with Kapton - W Sweep . . . . .	41
3.11	Single Vivaldi Antenna with Kapton - Wl Sweep . . . . .	42

---

3.12	Single Vivaldi Antenna with Kapton - Stub Sweep . . . . .	42
3.13	Single Vivaldi Antenna with Kapton - Cir Sweep . . . . .	43
3.14	Single Vivaldi Antenna with Kapton - Simulated Co and Cross Polar .	44
3.15	Single Vivaldi Antenna with Mylar - W Sweep . . . . .	45
3.16	Single Vivaldi Antenna with Mylar - Wl Sweep . . . . .	45
3.17	Single Vivaldi Antenna with Mylar - Stub Sweep . . . . .	46
3.18	Single Vivaldi Antenna with Mylar - Cir Sweep . . . . .	47
3.19	Single Vivaldi Antenna with Mylar - Simulated Co and Cross Polar . .	48
3.20	Single Vivaldi Antenna with Kapton - Measured Reflection Coefficient .	49
3.20	Single Vivaldi Antenna with Kapton - Measured Radiation Pattern . .	50
3.21	Single Vivaldi Antenna with Mylar - Measured Reflection Coefficient .	51
3.21	Single Vivaldi Antenna with Mylar - Measured Radiation Pattern . . .	51
3.22	Phase Matching . . . . .	53
3.23	Transmission Coefficient - Phase . . . . .	54
3.24	Matching Network of an array of Vivaldi Antennas . . . . .	55
3.25	Array of Vivaldi Antennas with Kapton in Flat and Folded State - Simulated Reflection Coefficient . . . . .	56
3.26	Array of Vivaldi Antennas with Kapton in Flat and Folded State - Simulated Radiation Pattern . . . . .	57
3.27	Array of Vivaldi Antennas with Mylar in Flat and Folded State - Simulated Reflection Coefficient . . . . .	58

3.28 Array of Vivaldi Antennas with Mylar in Flat and Folded State - Simulated Radiation Pattern . . . . .	59
3.29 Folding at $90^\circ$ - Crack and Discontinuity . . . . .	60
3.30 Folding at $90^\circ$ - with crease line . . . . .	60
3.31 Array of Vivaldi Antennas with Kapton in Flat and Folded State - Measured Reflection Coefficient . . . . .	61
3.32 Array of Vivaldi Antennas with Kapton in Flat and Folded State - Measured Radiation Pattern . . . . .	62
3.33 Array of Vivaldi Antennas with Mylar in Flat and Folded State - Measured Reflection Coefficient . . . . .	63
3.34 Array of Vivaldi Antennas with Mylar in Flat and Folded State - Measured Radiation Pattern . . . . .	63
4.1 A 5.8 GHz Flexible Microstrip Fed Slot Antenna: (a) The antenna configuration and a PEDOT realisation; (b) Simulated and measured reflection coefficients [45] . . . . .	69
4.2 A Flexible Circular Polarized Wide Band Slot Antenna for Indoor IoT Applications: (a) Flexible Antenna on a 2D Layout; (b) Simulated reflection coefficient for different state [46] . . . . .	70
4.3 UWB Circularly polarised Planar antenna on flexible Substrate: (a) Layout of the circularly polarised antenna; (b) Reflection Coefficient of the antenna while under stress; (c) Cross section of antenna under stress [47] . . . . .	71

4.4	Wearable Flexible Reconfigurable Antenna Integrated With Artificial Magnetic Conductor: (a) Dimensions of Folded Slot Antenna; (b) Measured reflection coefficients of antenna configurations; (c) Fabricated antenna on curve structure and on human body [48] . . . . .	72
4.5	Single Slot Antenna Design . . . . .	73
4.6	Single Slot Design- Dimensions Chart . . . . .	74
4.7	Single Slot Antenna Design - Dimensions with $\beta$ . . . . .	74
4.8	Single Slot Antenna Design - Sweep on the length of the slot on both x and y . . . . .	76
4.9	Single Slot Antenna Design - Ml Sweep . . . . .	77
4.10	Slot Antenna Parameter List . . . . .	79
4.11	Drawing 3-D Polygon . . . . .	79
4.12	Slot Antenna Design in 3-D Geometry . . . . .	79
4.13	Translate and Loft Curve . . . . .	80
4.14	Change in $\alpha$ and $\beta$ . . . . .	81
4.15	Fabricated Single Slot Antenna . . . . .	84
4.16	Single Slot Antenna - Simulated Reflection Coefficient . . . . .	91
4.17	Single Slot Antenna - Simulated Radiation Pattern . . . . .	94
4.18	Single Slot Antenna - Measured Reflection Coefficient . . . . .	96
4.19	Single Slot Antenna - Measured Radiation Pattern . . . . .	99
4.20	Total Pattern of four isotropic elements . . . . .	100
4.20	Slot Array Pattern Multiplication - Radiation Pattern . . . . .	101



4.21	Matching Network . . . . .	102
4.22	Change in Alpha and Beta . . . . .	103
4.23	Fabricated Arrays of Slot Antennas . . . . .	105
4.24	Arrays of Slot Antennas - Simulated Reflection Coefficient . . . . .	112
4.25	Arrays of Slot Antennas - Simulated Radiation Pattern . . . . .	115
4.26	Arrays of Slot Antennas - Measured Reflection Coefficient . . . . .	117
4.27	Arrays of Slot Antennas - Measured Radiation Pattern . . . . .	120
5.1	High-gain narrow-band slotted antenna based on ENZ SIW structure: (a) Substrate Integrated Waveguide ENZ Antenna; (b) Reflection Coefficient with various height; (c) Simulated and Measured reflection coefficient; (d) Fabricated Antenna Structure [54] . . . . .	128
5.2	Flexible dual-frequency substrate integrated waveguide antenna based on metamaterial: (a) Individual cELC unit and the equivalent circuit; (b) Reflection Coefficient with four cELC units; (c) Radiation Pattern at 35.63 GHz [55] . . . . .	129
5.3	Plastic-based Substrate Integrated Waveguide (SIW) Components and Antennas: (a) Substrate Integrated Waveguide filter on PET substrate; (b) Simulated and Measured response; (c) Slotted SIW Waveguide Antenna; (d) Simulated and Measured of proposed antenna [56] . . . . .	130
5.4	Air-Filled Substrate Integrated Waveguide A Flexible and Low Loss Technological Platform: (a) Air Filled SIW; (b) Proposed Tapered Transition; (c) Simulated Reflection Coefficient in Ka-Band [57] . . . . .	131

5.5	Substrate Integrated Waveguide Horn Antenna on Thin Substrate With Back-Lobe Suppression and Its Application to Arrays: (a) Top and Side view of SIW horn Antenna; (b) SIW Horn Antenna Array 1 by 4; (c) Simulated reflection coefficient with the effect on slots and vias [58] . . .	132
5.6	Planar Slot Antenna Backed by Substrate Integrated Waveguide Cavity: (a) Proposed SIW Cavity planar slot antenna; (b) Simulated and measured reflection coefficient and gain [59] . . . . .	133
5.7	Single SIW Slot Antenna Design . . . . .	134
5.8	Single SIW Slot Antenna - Offset Sweep . . . . .	135
5.9	Single SIW Slot Antenna - (a) Slot Width Sweep; (b) MOffset Sweep . .	137
5.10	Single SIW Slot Antenna - Dimension Chart . . . . .	138
5.11	Change in $\alpha$ and $\beta$ . . . . .	139
5.12	Single SIW Slot Antenna - Simulated Reflection Coefficient . . . . .	144
5.13	Single SIW Slot Antenna - Simulated Radiation Pattern . . . . .	147
5.14	SIW Array Pattern Multiplication - Radiation Pattern . . . . .	148
5.15	Matching Network . . . . .	149
5.16	Change in $\alpha$ and $\beta$ . . . . .	150
5.17	Arrays of SIW Antennas - Simulated Reflection Coefficient . . . . .	155
5.18	Arrays of SIW Antennas - Simulated Radiation Pattern . . . . .	158
6.1	Conformal Switched Beam Antenna: (a) Side view of the aperture coupled antenna; (b) Birds eye view on a single curved antenna; (c) Fabricated antenna with a switching network using the UWB port switch; (d) Simulated and Measured Reflection Coefficient . . . . .	165

6.2	RF MEMS Switches and Switch Circuits: (a) Broadside MEMS Switches; (b) Fabricated MEMS Switch and measured isolation and insertion loss [63] . . . . .	166
6.3	A 25 to 75-MHz RF MEMS Tunable Filter: (a) RF MEMS Switch with Bondwires; (b) Simulated Reflection Coefficient [64] . . . . .	167
6.4	Conformal Ink-Jet Printed C Band Phased-Array Antenna Incorporating Carbon Nanotube Field-Effect Transistor Based Reconfigurable True-Time Delay Lines: (a) Layout of CNT based FET; (b) Fabricated FET with delay lines [65] . . . . .	168
6.5	A Stretchable RF Antenna With Silver Nanowires: (a) Fabricated Transmission line model with results; (b) Fabricated RF Antenna with reflection coefficient [66] . . . . .	169
6.6	Optically Transparent Patch Antennas Based on Silver Nanowires for mm-Wave Applications: (a) Coplanar Waveguide transmission line with Silver nanowires; (b) Simulated and Measured results of the CPW transmission line; (c) Simulated results of Patch antenna operating at 61 GHz [67] . . . . .	170
6.7	Initial Microwave Switch Design . . . . .	171
6.8	CPW Transmission Line . . . . .	173
6.9	Electric Field on Waveguide Port . . . . .	174
6.10	Initial Simulation Results without Microwave Switches . . . . .	174
6.11	Initial Microwave Switch - $Lg$ Sweep . . . . .	175
6.12	Initial Microwave Switch - $Lg = 0.1$ , D Sweep . . . . .	176
6.13	Initial Microwave Switch - $Lg = 0.5$ , D Sweep . . . . .	177
6.14	Initial Microwave Switch - $Lg$ Sweep - 0.1 mm to 0.01 mm . . . . .	177

6.15	Initial Microwave Switch - $Lg = 0.01$ , ON and OFF State . . . . .	178
6.16	Initial Microwave Switch - $Lg = 0.1$ , ON and OFF State . . . . .	179
6.17	Initial Microwave Switch - Gate Offset $D$ Sweep . . . . .	181
6.18	Initial Microwave Switch - Dielectric Height $h_1$ Sweep . . . . .	182
6.19	Initial Microwave Switch - Resistance Sweep - $Lg = 1$ mm . . . . .	183
6.20	Initial and Improved Schematic Diagram . . . . .	184
6.21	Improved Version of the CPW Microwave Switch Design . . . . .	185
6.22	Improved Microwave Switch - $Lg$ Sweep - 0.1 mm to 0.01 mm . . . . .	185
6.23	Improved Microwave Switch - $Lg = 0.1$ mm, ON and OFF State . . . . .	186
6.24	Improved Microwave Switch - $Lg = 0.01$ mm, ON and OFF State . . . . .	187
6.25	Improved Microwave Switch - Gate Offset $D$ Sweep . . . . .	188
6.26	Improved Microwave Switch - Dielectric Height ( $h_1$ ) Sweep . . . . .	190
6.27	Improved Microwave Switch - Resistance Sweep - $Wg = 0.1$ mm . . . . .	191
6.28	Solution processed InAs nanowire transistors as RF/microwave switches: (a) New design concept and an Optical image of the CPW switch; (b) Reflection Coefficient $S_{22}$ AND Transmission Coefficient $S_{21}$ at various voltage levels [69] . . . . .	193
6.29	Vivaldi Antennas with proposed Microwave Switch: (a) Design of the proposed Microwave Switch; (b) Simulated results when Port 2 is at an OFF state . . . . .	194
6.30	Four way Vivaldi Antenna Design with individual Microwave Switches . . . . .	195
6.31	Vivaldi Antenna with Microwave Switch - Reflection Coefficient $S_{11}$ . . . . .	196

6.32	Vivaldi Antenna with Microwave Switch - Radiation pattern at 22 GHz	197
6.33	Vivaldi Antenna with Microwave Switch - Radiation pattern at 24 GHz	197
6.34	Vivaldi Antenna with Microwave Switch - Radiation pattern at 25 GHz	198

# Chapter 1

## Introduction

### 1.1 Overview and Motivation

The idea of using a flat piece of paper to transform into an intriguing 3-Dimensional (3-D) object has been fascinating researchers for centuries. Origami was originally known as Ori-Kata, meaning folded shapes but it was later changed to Ori-gami, meaning folding paper. In modern times, people became attracted by the idea of creating various shapes using folding techniques, such as: animals, flowers and structures.

As the amount of interest in Origami emerged, researchers have looked into its applications in packaging products, creative mathematical designs and engineering [1]. There is a lot of interest in combining Origami in mathematical and science applications. This allows scientists to discover new innovative ideas and designs [2–5].

### 1.2 Research Aim and Objectives

The main purpose of this research is to investigate various antenna structures using an Origami technique called Miura Ori. To be able to do that, a suitable flexible substrate will need to be investigated. Once a suitable flexible substrate is identified, the Miura

Ori folding technique can be incorporated into various antenna designs.

### 1.2.1 Aims

The aims of this thesis are:

1. To have an in depth understanding of the Origami folding techniques and its applications.
2. To investigate the use of Origami folding techniques on various antenna designs.
3. To design a microwave switch with nanowires using flexible substrates.

### 1.2.2 Objectives

The objectives of this thesis are:

1. To be able to obtain an in depth knowledge of various flexible substrates.
2. To perform Origami folding techniques using flexible substrates.
3. To investigate the Miura Ori folding technique on various antenna types.
4. To create and simulate a realistic 3-D Miura-Ori model within Computer Simulation Technology Microwave Studio (CST Studio).
5. To design a microwave switch with nanowires, which could be applied to antenna designs.

## 1.3 Thesis Outline

Chapter 2 provides a literature review on Origami. The history of Origami and its science applications. It also provides information on existing researches on Origami

antennas. This chapter will include the use of the Miura Ori folding technique and the equations needed to apply the structure into a modelling software, with the requirements needed to achieve that.

Chapter 3 gives a detailed comparison of two different types of flexible substrates. The two flexible substrates are Kapton and Mylar. Both materials will be analysed in the simulation software, Computer Simulated Technology Studio (CST Studio). The fabricated antennas will undergo measurements using the Vector Network Analyser (VNA) from Rohde and Schwarz and then will be tested in the anechoic chamber for radiation pattern measurements.

Chapter 4 demonstrates the antenna design that has incorporate the Miura Ori folding technique. Firstly, the antenna will be optimised on a 2-D planar view, then by applying Miura Ori equations onto each rectangle, it will be optimised in a 3-D model. The Miura Ori design will then be simulated and measured by changing two factors: Inner angle (Alpha) and Folding angle (Beta). Afterwards, an array of slot antennas with matching network will be applied into the design. The 2 by 2 array of slot antennas will be simulated and measured with the VNA and anechoic chamber for the return loss (S11) and radiation pattern measurements.

Chapter 5 presents the second antenna design that is combined with the Miura Ori folding technique. The antenna is using a Substrate Integrated Waveguide (SIW). To being the investigation, the SIW antenna is optimised in a 2-Dimensional (2-D) planar view, then the Miura Ori equation is applied onto the design to achieve a 3-D model. The optimised design will be simulated on CST Studio with the change of two angle factor: Inner angle ( $\alpha$ ) and Folding angle ( $\beta$ ). A matching network will be added onto the design to create a 2 by 1 array of SIW antennas. The arrays of SIW antennas will be simulated to obtain the return loss value and radiation pattern results.

Chapter 6 provides an investigation on microwave switches with nanowires using a flexible substrates. The microwave switch with nanowires is simulated on a Co-Planar Waveguide (CPW), utilising the gap between the copper tracks as a Field



Effect Transistor (FET). A thorough investigation will be performed in the chapter using different parameters. Firstly, the initial design will be tested with all the parameters to determine if the microwave switch with nanowires is operational on the two different states: ON and OFF. The design will be changed into an improved design with a better transmission across all parameters. Later, the microwave switch with nanowires will be applied to an array of Vivaldi antennas to determine the functionality of the microwave switches.

Chapter 7 concludes the work presented in this thesis. It summarises the work carried out on each chapter. It also includes any relevant future work that could improve the research.

## 1.4 Publications arising from this work

- [1] C. C. H. Ng and P. R. Young, "Origami folding technique using flexible substrate with arrays of vivaldi antennas," 12th European Conference on Antennas and Propagation (EuCAP 2018), London, 2018, pp. 1-4.
- [2] A. J. Cole, C. C. H. Ng, F. A. Almalki and P. R. Young, "Chipless RF liquid sensor," 2015 IEEE MTT-S International Microwave and RF Conference (IMaRC), Hyderabad, 2015, pp. 243-245.
- [3] D. M. George, A. Chandroth, C. C. H. Ng and P. R. Young, "High-gain narrow-band slotted antenna based on ENZ SIW structure," Journal of Physics D: Applied Physics, March 2018, pp. 123102
- [4] S. Swaisaenyakorn, A. J. Cole, C. C. H. Ng and P. R. Young, "Conformal switched beam antenna," 2016 Loughborough Antennas & Propagation Conference (LAPC), Loughborough, 2016, pp. 1-4.
- [5] B. Mirkhaydarov, H. Votsi, A. Sahu, P. Caro, P. R. Young, V. Stolojan, S. G. King, C. C. H. Ng, V. Devabhaktuni, H. H. Tan, C. Jagadish, P. H. Aaen, and M.

Shkunov, "Solution-processed InAs nanowire transistors as microwave switches,"  
Advanced Electronic Materials, vol. 5, no. 1, p.1800323, 2019.

# Chapter 2

## Origami and Engineering

### 2.1 Introduction

Akira Yoshizawa was known to be the grand-master of Origami. She was not the first artist to discover Origami, however she had the idea of creating original Origami designs. Many modern Origami artists have been influenced by Akira Yoshizawa's designs. Besides all the designs Yoshizawa has created, her other impact on Origami, were detailed instructions on making folded shapes, which included arrows, dotted and dashed lines. By utilising those steps, each Origami artist would be able to see the movements from the beginning to the end of each shape [6].

This chapter explains the origin of Origami and the mathematics behind it, as well as, the folding techniques that are essential in any Origami pattern. It will also explain the Origami folding technique called Miura Ori, which is used throughout the course of this thesis. The main focus of this chapter is Origami science application [7], ranging from deployable solar arrays for space missions to DNA nano-robots in Bioscience. It will follow onto a specific topic, which is antenna application. The use of Origami folding techniques has inspired many scientists to create antenna designs, that were not available before. What makes the structures interesting is their ability to change size by folding and collapsing. It can also lower the manufacturing cost.

## 2.2 Origami Theory

### 2.2.1 Mathematics in Origami Folding

2000 years ago, a Greek mathematician named Euclid of Alexandria wrote a book called “The Elements”. In the book, he specified five basic rules of geometry using a straight edge and a compass [8].

These five axioms include:

- A straight line may be drawn between any two points
- A piece of straight line may be extended indefinitely
- A circle may be drawn with any given radius and an arbitrary centre
- All right angles are equal
- If a straight line, crossing two other straight lines, makes the interior angle on the same side less than two right angles, then the two straight lines intersect.

Humiaki Huzita and Koshiro Hatori, a modern age scientist, using those axioms, constructed a similar set of rules for Origami geometries. These are assumed to be completed on a flat piece of paper where all folds are linear. Humiaki Huzita presented a series of papers, in which she identified 6 different ways to fold or crease a planar sheet, by aligning combinations of different points and lines. These 6 operations were called Huzita Axioms. By applying these rules, it was possible to solve quadratic equations and divide an arbitrary angle. Huzitas axioms were the basis of Origami geometry in terms of construction until 2002, when Koshiro Hatori found one more element that was not included initially. In total, there are 7 Axioms in geometry construction, and they are called Huzita & Hatori Axioms, [9, Fig. 2.1].

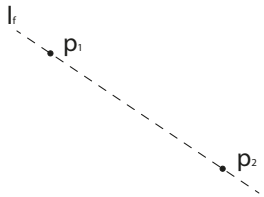
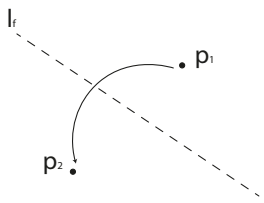
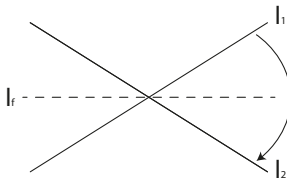
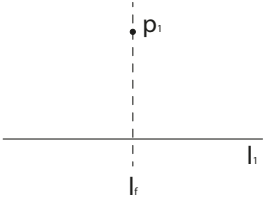
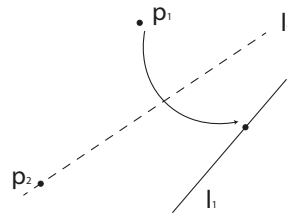
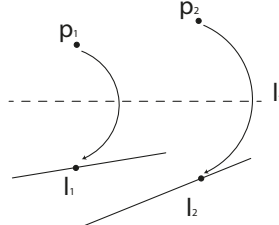
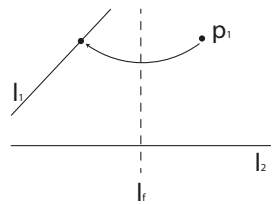
	<p>Given two points <math>p_1</math> and <math>p_2</math>, we can fold a line connecting them</p>
	<p>Given two points <math>p_1</math> and <math>p_2</math>, we can fold <math>p_1</math> onto <math>p_2</math></p>
	<p>Given two lines <math>l_1</math> and <math>l_2</math>, we can fold line <math>l_1</math> only <math>l_2</math></p>
	<p>Given as point <math>p_1</math> and a line <math>l_1</math>, we can make a fold perpendicular to <math>l_1</math> passing through the point <math>p_1</math></p>
	<p>Given two points <math>p_1</math> and <math>p_2</math> and a line <math>l_1</math>, we can make a fold that places <math>p_1</math> onto <math>l_1</math> and passes through the point <math>p_2</math></p>
	<p>Given two points <math>p_1</math> and <math>p_2</math> and two lines <math>l_1</math> and <math>l_2</math>, we can make a fold that places <math>p_1</math> onto line <math>l_1</math> and places <math>p_2</math> onto line <math>l_2</math></p>
	<p>Given a points <math>p_1</math> and two lines <math>l_1</math> and <math>l_2</math>, we can make a fold perpendicular to <math>l_2</math> that places <math>p_1</math> onto line <math>l_1</math></p>

Figure 2.1: Huzita & Hatori Axioms

### 2.2.2 Folding Technique

The traditional Origami was done using paper. It can be observed that after folding paper too many times, it loses its folding ability. Most Origami relies on the fibres located within the paper and their ability to bend and stretch slightly during the fold. There are plenty of folding techniques to form the desired shapes from a piece of paper [10]. The most important two folding techniques are the Valley Fold, see Fig. 2.2, and the Mountain Fold, see Fig. 2.3. Because most of the shapes are made from those two folding techniques, they became a fundamental part of Origami.

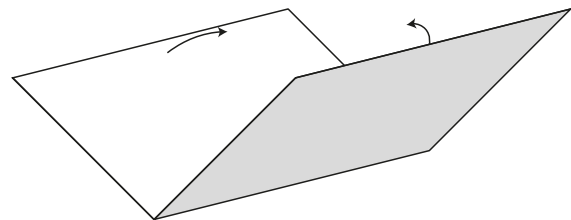
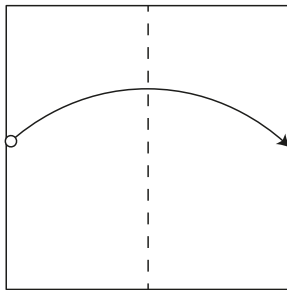


Figure 2.2: Valley Fold

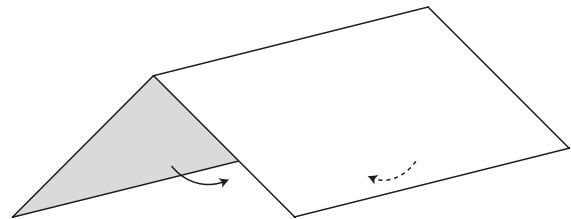
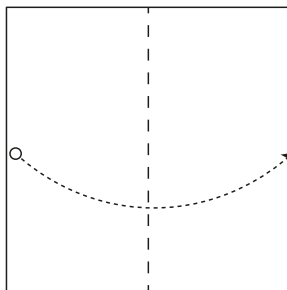


Figure 2.3: Mountain Fold

Apart from the two folding techniques, there are others, that are crucial in creating Origami objects. These are the Cupboard Fold, see Fig. 2.4, Outside Reverse Fold, see Fig. 2.5 and Inside Reverse Fold, see Fig. 2.6. These techniques are frequently used for a variety of Origami constructions.

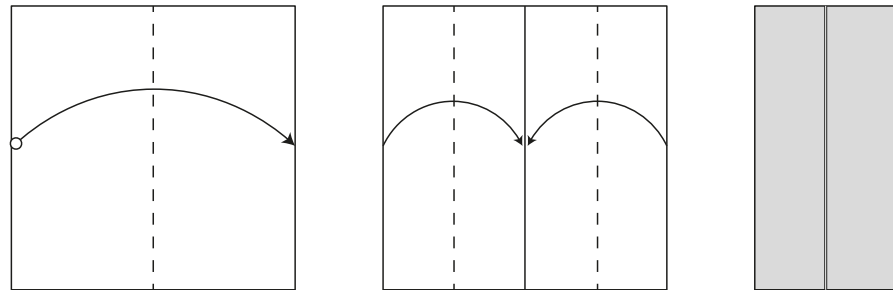


Figure 2.4: Carboard Fold

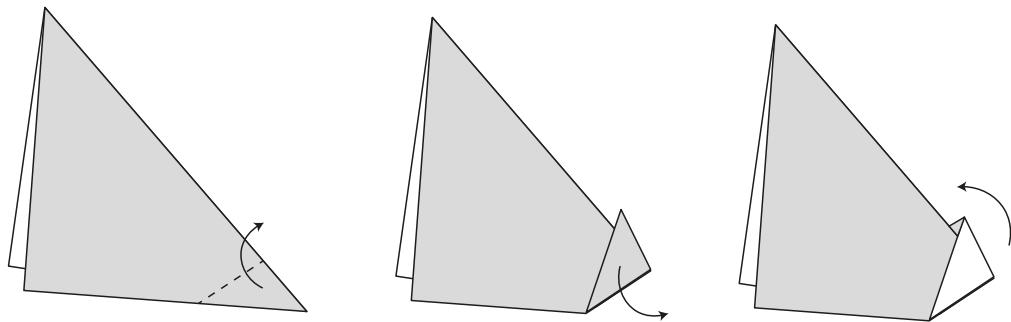


Figure 2.5: Outside Reverse Fold

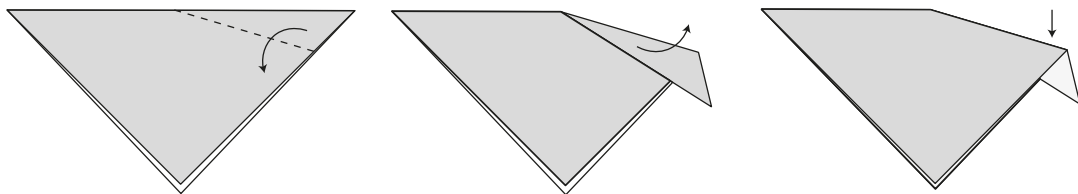


Figure 2.6: Inside Reverse Fold

From the given techniques, mathematicians decided to challenge themselves further by looking into tessellations. Tessellations are made from repeated patterns. They were first inspired by tessellations on a flat tile surface or a plane surface. They are made up of one or more geometry shapes such as triangles, squares or hexagons. By tiling them together with no overlaps or gaps, they have a potential to create an extraordinary surface.

Shuzo Fujimoto [11] was the first mathematician to adopt the idea of using tessellations in developing complicated designs that could be folded with the given folding technique. Robert J. Lang [8] used Computer Aid Design (CAD) to create Origami tessellations, before making a real life folded structure. By using CAD, Origami tessellations designs can be seen on a computer screen, before being folded with paper into any shape or form.

### 2.2.3 Miura Ori

In 1982, a Japanese astrophysicist Koryo Miura introduced a new form of Origami tessellation called Miura Ori. This Origami style, was able to fold a piece of paper into a minimal structure, while giving it some interesting mechanical properties [12]. The Miura Ori fold is considered to be one of the main folding patterns, due to its simplicity and mechanical properties, such as stiffness, rigidity, as well as, the ability to collapse, see Fig. 2.7 and 2.8.

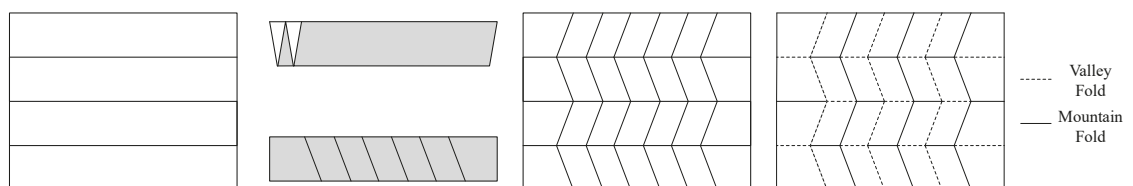


Figure 2.7: Folding Pattern



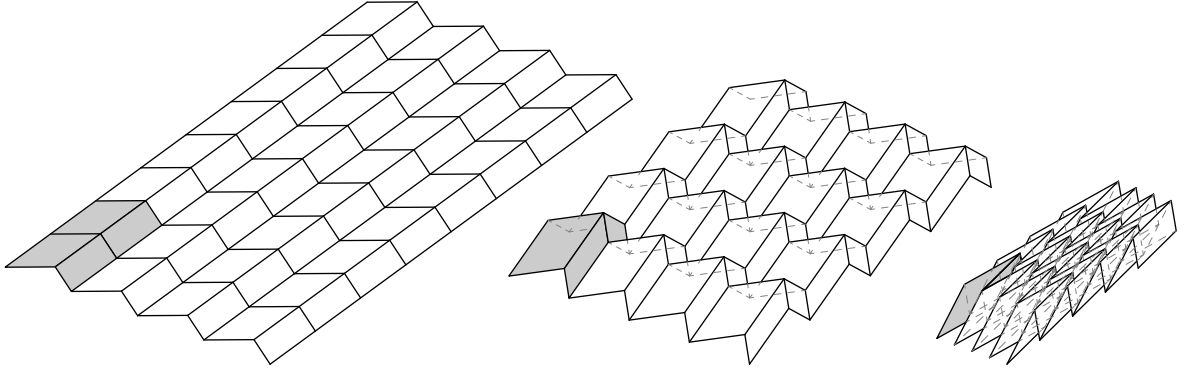


Figure 2.8: Miura Ori

The first fundamental of Mirua Ori Fold consists of a single unit cell. It is then repeated throughout the whole design [13]. A single Miura Ori cell is formed of 4 parallelograms. The size and angle of the fold can be parametrised. Each parallelogram consist of side  $(a)$ ,  $(b)$  with an acute angle of  $(\alpha)$  and the dihedral folding angle of  $(\beta)$ . The dimensions of the output are, defined shown in Fig. 2.9 and (2.1) - (2.4).

$$H = a.\sin\beta\sin\alpha \quad (2.1)$$

$$S = b.\frac{\cos\beta.\tan\alpha}{\sqrt{1 + \cos^2\beta.\tan^2\alpha}} \quad (2.2)$$

$$L = a.\sqrt{1 - \sin^2\beta.\sin^2\alpha} \quad (2.3)$$

$$V = b.\frac{1}{\sqrt{1 + \cos^2\beta.\tan^2\alpha}} \quad (2.4)$$

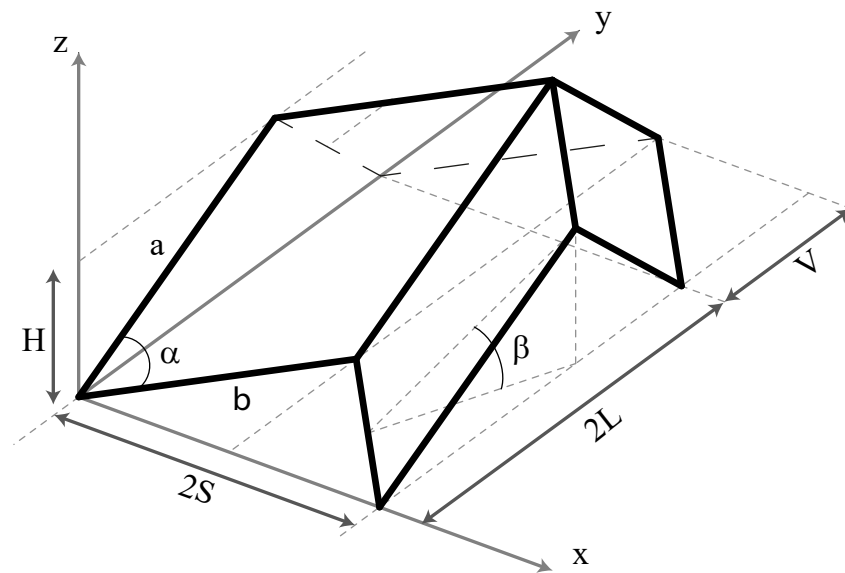


Figure 2.9: Single Unit Cell - Miura Ori

The Miura Ori Fold has helped the science and engineering industry. Researchers have been inspired by its design and developed prototypes for its various applications [7]. These inventions include sandwich panel cores, Origami stents, self-folding membranes, solar panels (see [14, Fig. 2.10]), high density batteries, as well as, building facades (see [15, Fig. 2.11]).

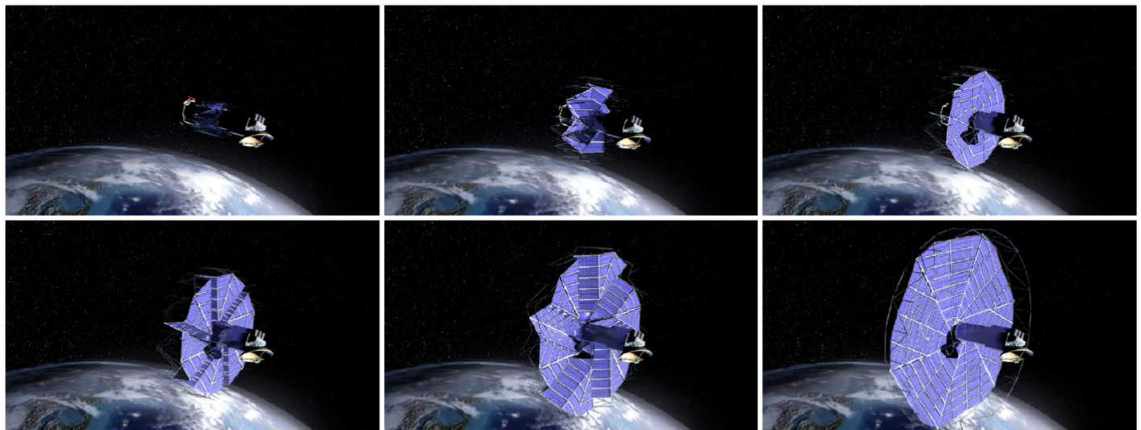


Figure 2.10: Origami Solar Panel [14]



Figure 2.11: Origami Architecture Building [15]

### 2.2.4 Origami Science

Origami techniques are being used for science applications around the world. In engineering [16], the mathematics behind Origami has inspired scientists to create innovative and intriguing designs. The list below shows some of those Origami inspired applications [17].

An Origami expert Robert Lang [8] investigated an Origami design with NASA's Jet Propulsion Laboratory. Together they have designed a compact way to transport large objects, such as solar panels, inside a narrow rocket, to save dimensional space [14]. The design, as seen in [14, Fig. 2.12], can be folded neatly and can be later deployed to outer space. When the solar panel is deployed, it can reach up to 25 metres, however when it is folded, the diameter of the design is only 2.7 metres.



Figure 2.12: Origami Solar Panel Prototype [14]

Q. Cheng [18] created a paper based Lithium-ion battery using the Miura-Ori Origami technique, see [18, Fig. 2.13]. The geometry started from a flat sheet, then it was folded into a compact structure. The size of the lithium-ion battery was reduced 25 times, while the energy density within the folded structure was only 14 times smaller.

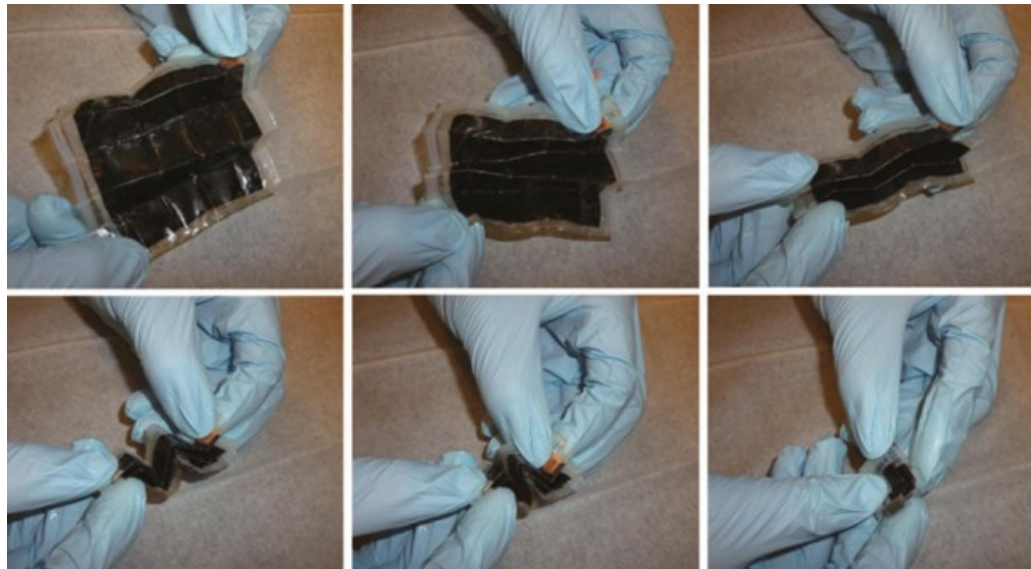


Figure 2.13: Folded Paper Lithium-ion Battery [18]

In December 2012, K. Kuribayashi-Shigetomi placed a living cell onto a microscopic plate [19]. When the adjacent cells were in contact with each other, a contraction, called Cell Traction Force (CTF) occurred. The microscopic plates joint together to form a cube and encapsulated cells in the surrounding. Plates with different geometry could fold into other 3D shapes such as dodecahedron and spirals. This biological technique has been beneficial in fabricating artificial tissues with a hollow shape especially important in medical research, see [19, Fig. 2.14].

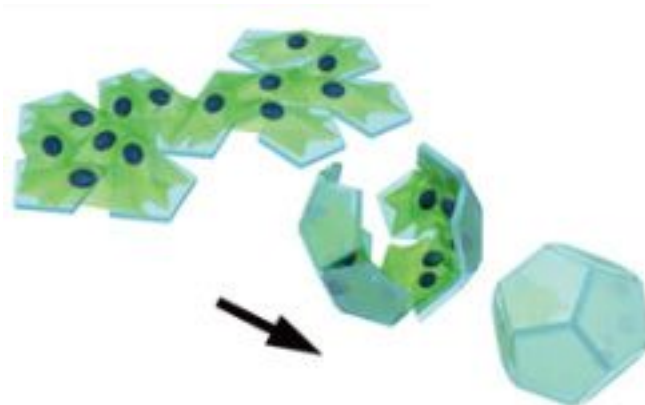


Figure 2.14: Cell Origami [19]

Origami structures have led researchers [20] to create Origami tessellations. The Researchers: M. Neyrinck and M. Aragon-Calvo were awarded a new frontiers price

for working on “Origami Universe”. The tessellation was made from a specific folding crease, called a tiled hexagon, see [20, Fig. 2.15].

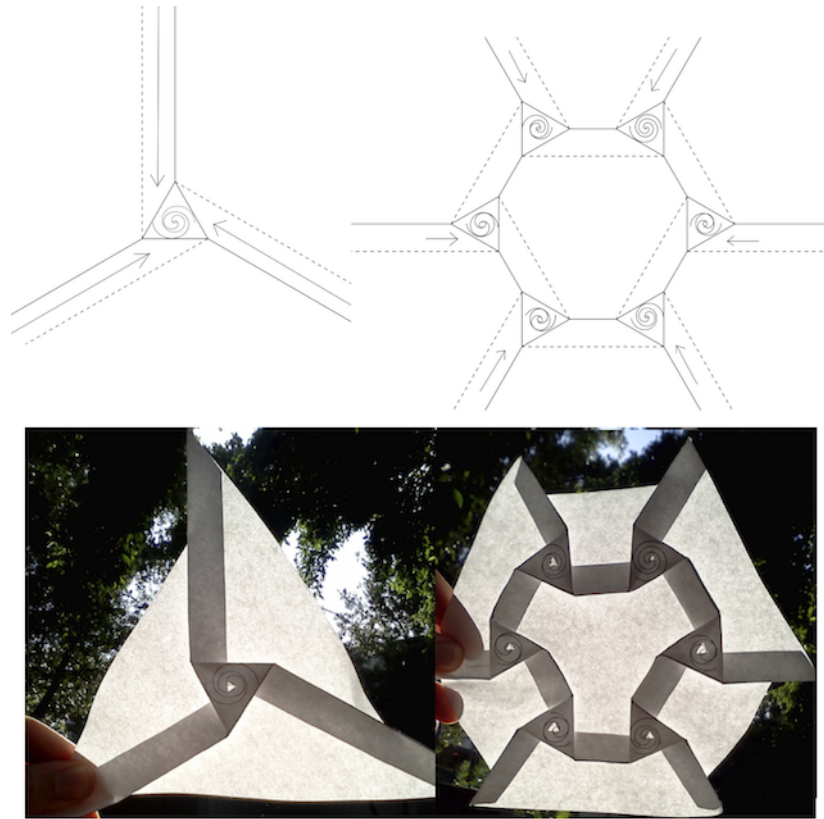


Figure 2.15: Cosmic Origami [20]

In November 2011, M. Dickey [21] developed a technique where plain polymer sheets were folded automatically when exposed to light. The polymer was made of polystyrene. The idea of using this product for picture designs has been around since 1973 [22]. A plain sheet of polymer can be shrunk about one third of its original size, while the thickness can be nine times thicker. M. Dickey [21] was able to adapt this concept, while applying the Origami theory. He was able to laser print black crease lines onto the polymer structure. When the sheet is exposed to light, it will then automatically fold along the line, due to the black colour absorbing more energy than any other colour, so when high intensive light is exposed onto the line, it will then heat up, shrink and lead to folding along the crease line automatically, see [21, Fig. 2.16].

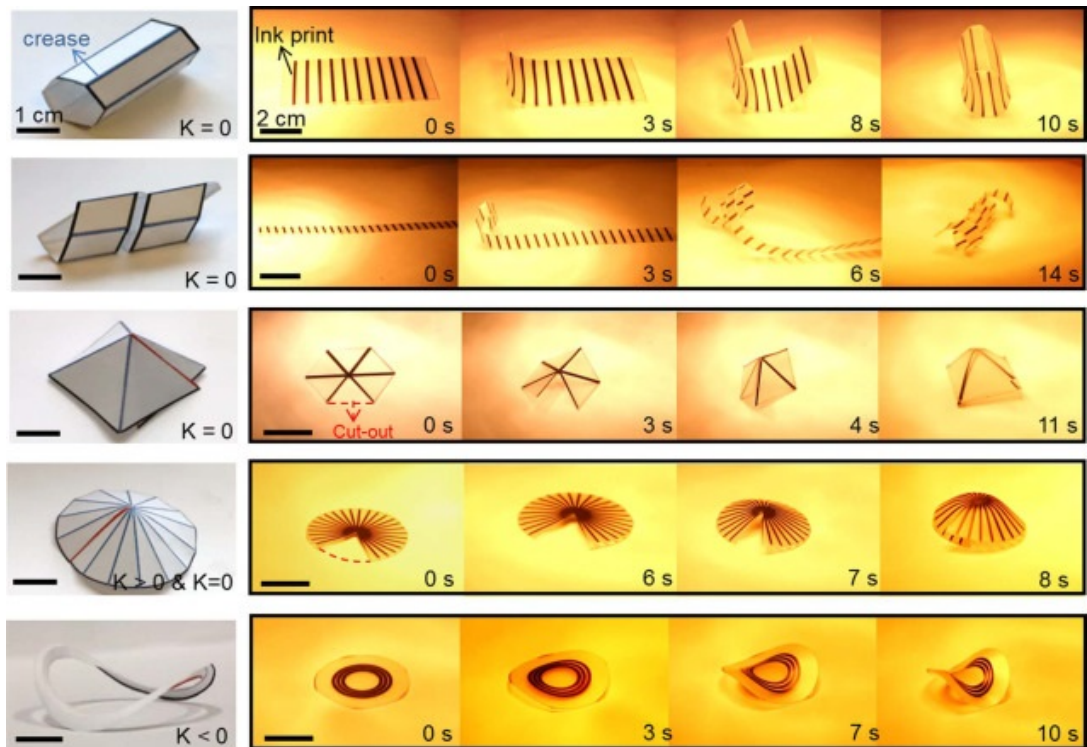


Figure 2.16: Self Folding Origami [21]

## 2.3 Origami Antennas

Various Origami techniques have been applied in fields ranging from nano-technology to space [17]. In the past, antennas were big physical objects that were inconvenient and heavy. Nowadays, researchers are aiming to find a suitable, low cost and lightweight antenna design. Origami, with its ability to collapse and unfold is inspiring. When applied, it helps to overcome limitations, such as the size. Which is still a major issue for modern antennas.

In the section below, unique Origami antenna designs, such as: Folded Helix antenna, Frequency Selective Surface, Nojima Folding technique will be investigated.

### 2.3.1 Helix Antenna

The different types of Helix Antenna include the Quadrifilar Helix Antenna (see [23, Fig. 2.17]) and Segmented Helical Antenna (see [24, Fig. 2.18]). Many Helix Antennas [25] have been used in space and satellite communication systems due to their high

gain and directivity of the antenna, as well as, the fact that they are circular polarised. They are highly used in satellite communications.

X. Liu has proposed a deployable Helix Antenna, which can be collapsed and is therefore easy to transport. The proposed design demonstrates the Helix Antenna ability to extend and collapse within the height of the structure. The height of the Origami Helix Antenna can be determined by the amount of sides, as well as, layers. In the paper [23], X. Liu used 6 sides to make a hexagonal cylindrical structure. By rotating the centre angle ( $\beta$ ), the height increases or decreases, therefore the structure can fold and unfold.

The proposed design was simulated in two states, folded and unfolded, shown in [23, Fig. 2.17b]. The antenna operated at 1.92 GHz with a 7 dBi gain when it is unfolded, see [23, Fig. 2.17c]. The folded state is 74% smaller than the unfolded state. Due to the pitch between the feeding points, the frequency shifted. When it is in the folded state, the frequency operated at 2.95 GHz with a 7.1 dBi gain.



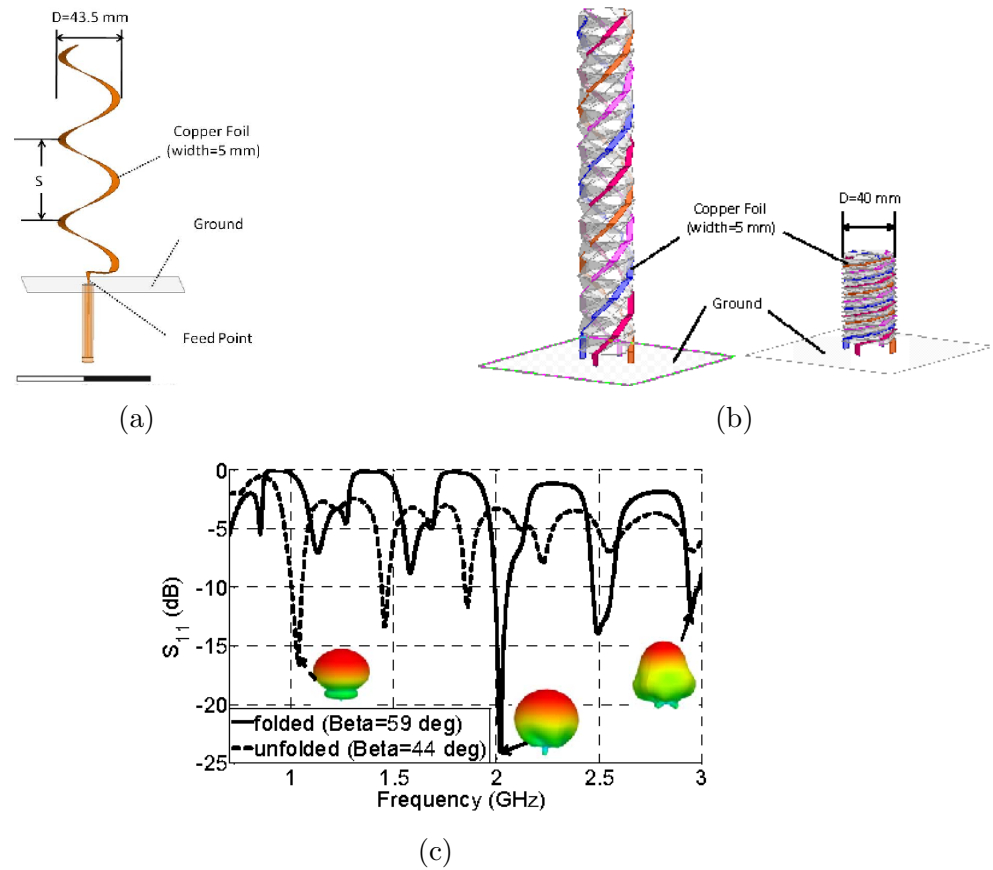


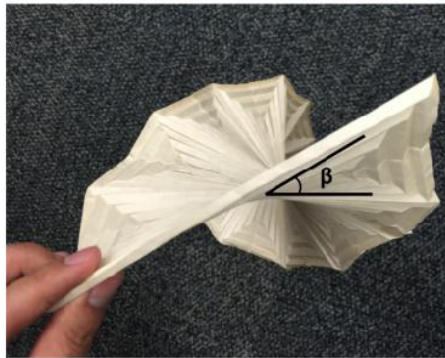
Figure 2.17: Origami Quadrifilar Helix Antenna: (a) Loop Idea Helical Antenna Model; (b) Unfolded and Folded States; (c)  $S_{11}$  and Radiation Pattern [23]

S. Yao [24] has proposed a Segmented Helical Antenna which had similar performance compared to a standard Helical Antenna. The idea of using segmented wires was implemented due to easier support, as well as, minimising cost of manufacture. The size of a standard Helical Antenna at lower frequency would require a stronger support.

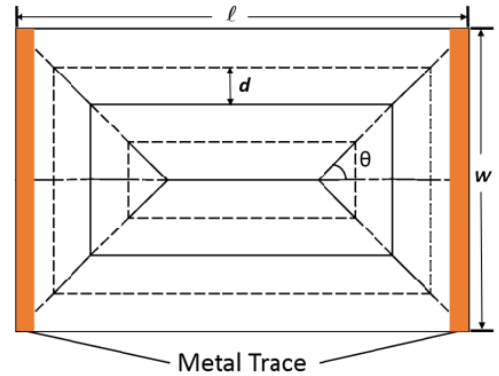
Proposed in [24, Fig. 2.18a] was an Origami folding technique called Hyperbolic Paraboloid Origami. A square piece of paper is folded into a pattern to support the weight and the shape of the antenna. The hyperbolic paraboloid has a unique rotating mechanism where it rotates around its centre axis. This led to the proposed design (see [24, Fig. 2.18c]), where copper tracks were added onto the edge of the structure, which then created a segmented Helical Antenna.

In most circular Polarised Helical Antennas, either left handed or right handed circular polarisation occurs. That is due to the orientation of the antenna and the way it spirals. In this proposed Origami antenna design, two states can be distinguished: a left handed and a right handed state. This Origami design is combined with a metal tape on the side. The structure is rotated between the two states by  $180^\circ$  and changes the polarisation of the antenna.

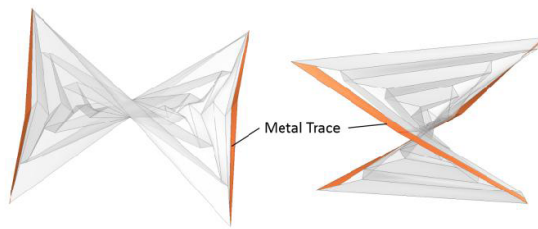
In the proposed design, the segmented Helical Antenna design operated between 0.7 GHz to 1.4 GHz. It had a narrow bandwidth, however it achieved four resonant frequencies. The far-field characteristic of each resonant frequency displayed the axial ratio, co-polarisation realised gain and cross-polarisation realised gain which can be seen in [24, Fig. 2.18d].



(a)



(b)



(c)

Antenna Characteristics	Skeleton Hexagon SHA	Skeleton Square SHA	Origami SHA	Conventional HA
Pitch Angle	14.4°	15.2°	13.4°	14.2°
Operating Frequency	1.08 GHz	1.16 GHz	0.98 GHz	1.03 GHz
Reflection Coefficient	-18 dB	-17 dB	-13 dB	-18 dB
Axial Ratio	0.74 dB	1.12 dB	0.94 dB	0.72 dB
Co-polarization Realized Gain	8.1 dBi	7.73 dBi	6.82 dBi	8.22 dBi
Cross-polarization Realized Gain	-11.32 dBi	-13.96 dBi	-9.28 dBi	-9.76 dBi
E-plane HPBW	55°	58°	62°	57°
H-plane HPBW	56°	57°	69°	56°

(d)

Figure 2.18: Origami Segmented Helical Antenna with Switchable Sense of Polarisation: (a) Origami paper base; (b) Origami pattern for hyperbolic paraboloid with antenna traces; (c) Top and Side view; (d) Measured Far-field characteristic of Segmented Helical Antenna [24]

### 2.3.2 Frequency Selective Surfaces

The main focus of the paper written by K. Fuchi on “Origami Tunable Frequency Selective Surfaces” [26], was to investigate the change in resonant frequency of Frequency Selective Surfaces (FSS). In recent years, alternative techniques were published where the resonant frequency can be tuned by adding lumped elements, such as varactors, into the design. The dielectric property of the substrate can also be changed by adding liquid crystal, or the resonant frequency can be shifted mechanically.

The proposed design in [26, Fig. 2.19a] used an Origami folding technique to change the resonant frequency. By transforming the surface geometry, extending and collapsing the structure the resonant frequency on FSS was tuned. The Origami technique used was Miura-Ori fold, of which details have been explained in Chapter 2.2.3. By using this folding technique, K. Fuchi combined each parallelogram with cross-shaped printed copper applied onto each face. When the Origami was folded at a certain angle, there was a percentage shift in the resonant frequency.

The three curves in [26, Fig. 2.19b] represented the 3 different angles. When the folding angle ( $\beta$ ) increased, there was a shift in resonant frequency. However, there was a decrease in polarisation due to the distance between each element gradually getting smaller. The proposed design used the Origami structure to provide a feasible way of tuning, by a simple mechanical configuration. By changing the folding angle ( $\beta$ ), the resonant frequency was able to shift by 19% from  $0^\circ$  to  $60^\circ$ .

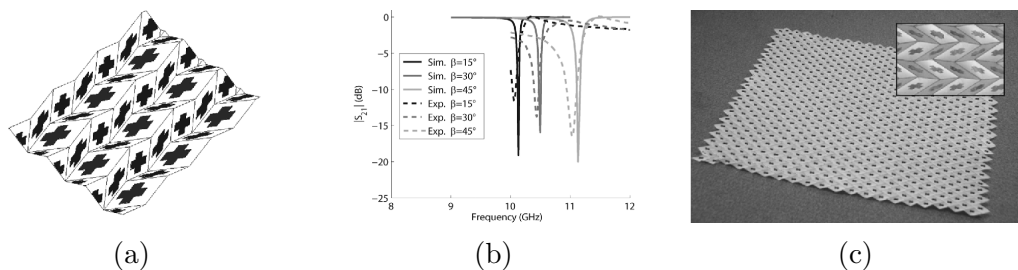


Figure 2.19: Origami Tunable Frequency Selective Surfaces: (a) Chevron Pattern with conducting element; (b) Transmission coefficient for Simulated and Measured; (c) Fabricated tunable FSS [26]

### 2.3.3 Nojima Folding

One of the most used frequency dependent antennas is the Conical Spiral Antenna. It is used in satellite communications. A standard Conical Spiral Antenna consists of two arms which spiral down from the centre point. S. Yao [27] determined that in space and satellite missions, a low cost and lightweight design is needed. This paper [27] presented a Origami folding technique called Nojima Origami.

The proposed in [27, Fig. 2.20] design used the Nojima Origami folding technique. This antenna design can be folded from a 2-D net into a 3-D shape without cutting or adhesive applied onto the surface. This led S. Yao [27] to propose a concept of applying Conical Spiral Antenna to the Nojima Origami.

The design used two Conical Spiral Antennas by wrapping the copper tape around the face of Nojima Origami, as seen in [27, Fig. 2.20b]. S. Yao added copper tape on the edge of the folding pattern. More gain can be achieved by increasing the width of the copper tape. The design had two states: unfolded and folded. When the design was unfolded, it operated as a dipole. In this paper, the operating frequency of a half wave dipole was 0.5 GHz. When the proposed design was in the folded state, the operating frequency bandwidth was ranging from 2.1 GHz to 3.5 GHz for both simulated and measured designs with a wide band. The realised peak gain for the folded design was above 4 dBi at the operating frequency, see [27, Fig. 2.20c] and [27, Fig. 2.20d].

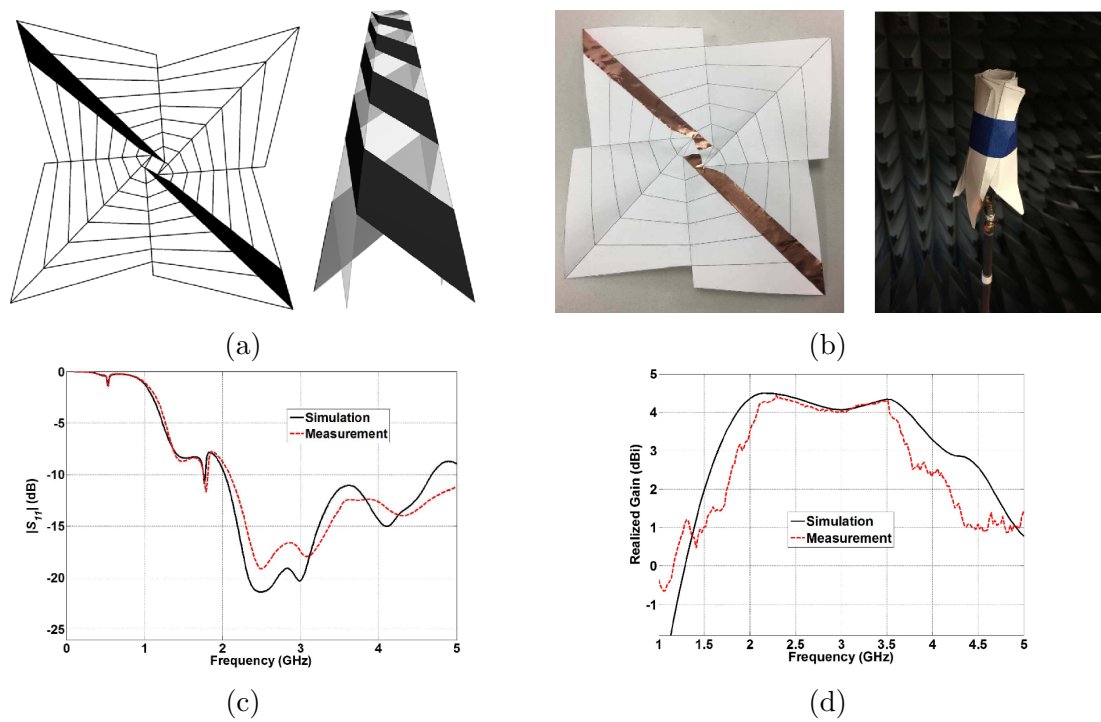


Figure 2.20: Morphing Origami Conical Spiral Antenna Based on Nojima Wrap: (a) Nojima Pattern with a 15 folded and a Nojima Origami square; (b) Nojima Square prototype unfolded and folded state; (c) Simulated and Measured Reflection Coefficient; (d) Simulated and Measured Realised Gain [27]

### 2.3.4 Others

Aside from the antenna designs listed above, there are other researches worth mentioning, such as High Gain Yagi-Uda Origami Antenna [28], Self-folding Origami Microstrip Antennas [29], 3-D printed Origami Packaging with Inkjet-printed antennas for RF harvesting Sensors [30] and Physical Reconfiguration of an Origami-Inspired Deployable Microstrip Patch Antenna Array [31].

In [28], S. Shah designed a High gain Yagi-Uda Origami Antenna with a paper substrate folded into an Origami tetrahedron shape. The Yagi-Uda Antenna consisted of a triangular shaped monopole with a reflector and 2 directors to guide the transmitting wave. S. Shah achieved a -10 dB impedance bandwidth from 2 GHz to 4 GHz with a slight difference between the measured and simulated versions due to fabrication errors. The peak gain was 9.6 dBi at a frequency of 2.6 GHz, see [28, Fig. 2.21b].

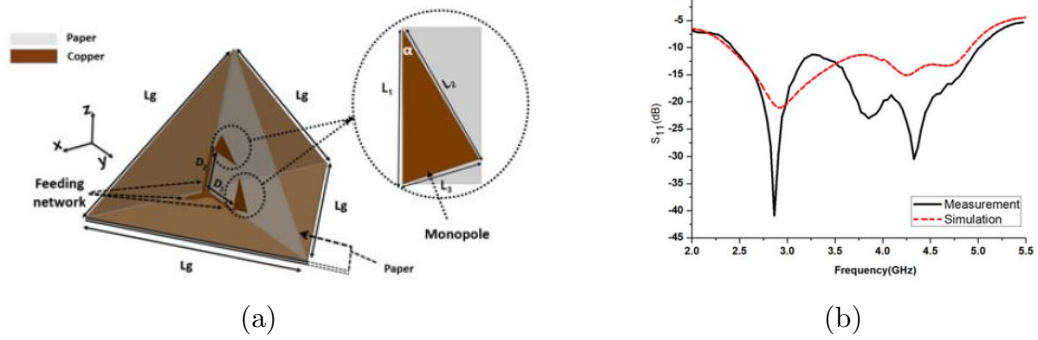


Figure 2.21: Low-Cost Circularly Polarised Origami Antenna: (a) Geometry of Circular Polarised Origami Antenna; (b) Simulated and Measured Reflection Coefficients [28]

G. Hayes [29] looked into using pre-stressed polymer sheets, as a new application in antenna designs. As explained in Section 2.2.4, the self-folding polymers sheets will have black ink line printed on its surface. When there is an increase of light source onto the polymer sheets, it shrinks quicker, due to black colour absorbing heat faster. Therefore, the polymer folds, which allows the proposed design to go from a patch into a monopole.

The proposed design [29] used the polymer material as a microstrip transmission line. One side is copper coated and the other has a black ink line. This study showed that the polymer will be able to shrink at the black region and disconnect from port 2 of the transmission line. This allows the polymer to create a hinge at the desired location, hence making the two ports electrically isolated. G. Hayes implemented the design into a microstrip patch, which can be changed from a patch into a standing monopole with a light source exposed to the polymer sheet. In [29, Fig. 2.22a], the antenna design operates as a microstrip patch, before light activation, however, the design transforms into a monopole after light activation. The proposed design before a light activation has an operating frequency of the microstrip patch of 2.4 GHz, see [29, Fig. 2.22b]. After light activation, the monopole operated at 2.2 GHz, see [29, Fig. 2.22c].

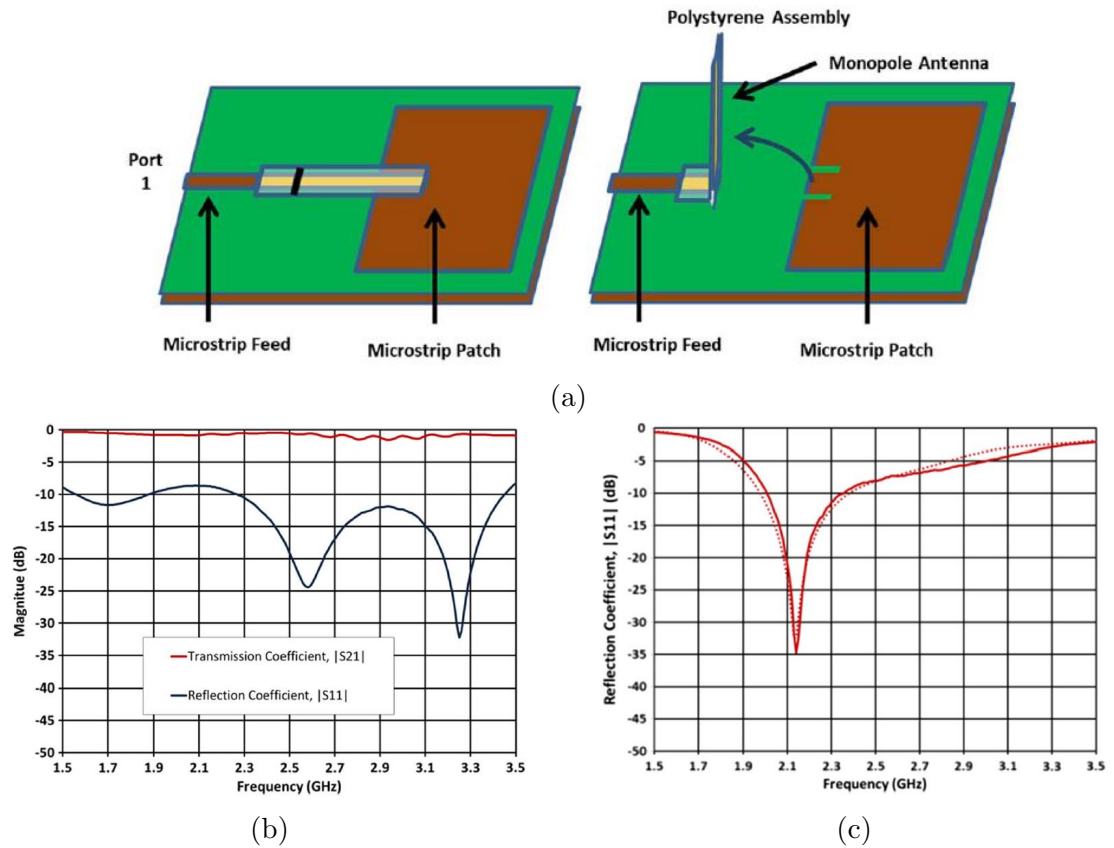


Figure 2.22: Self-Folding Origami Microstrip Antenna: (a) Microstrip Patch (Prior) and Monopole (After); (b) Simulated and Measured for Microstrip Patch; (c) Simulated and Measured for Monopole [29]

In this paper [30], J. Kinionis demonstrated a complex 3-D printed Origami structure with a Radio Frequency (RF) signal reception for either harvesting or communication at different orientations. The 3-D printed design was made from a cube net. The hinges were made with a smart shaped-memory material that allowed the hinges to fold after applying heat. This application reduced the fabrication time and eliminated the need for supporting the 3-D design, see [30, Fig. 2.23b].

The proposed design [30], as seen on [30, Fig. 2.23c], was made from squares, 57 mm by 57 mm by 3 mm, which were folded into a cube shape. On two sides of the cube, there are patch antennas, designed to have the centre frequency of 2.3 GHz. The patch antennas were fabricated with a 3-D Ink Jet Printer with two different type of ink, Silver nanoparticle ink and Diamminesilver acetate ink. Each patch from [30, Fig. 2.23a] operated at 2.3 GHz with a 10 dB bandwidth of 100 MHz.



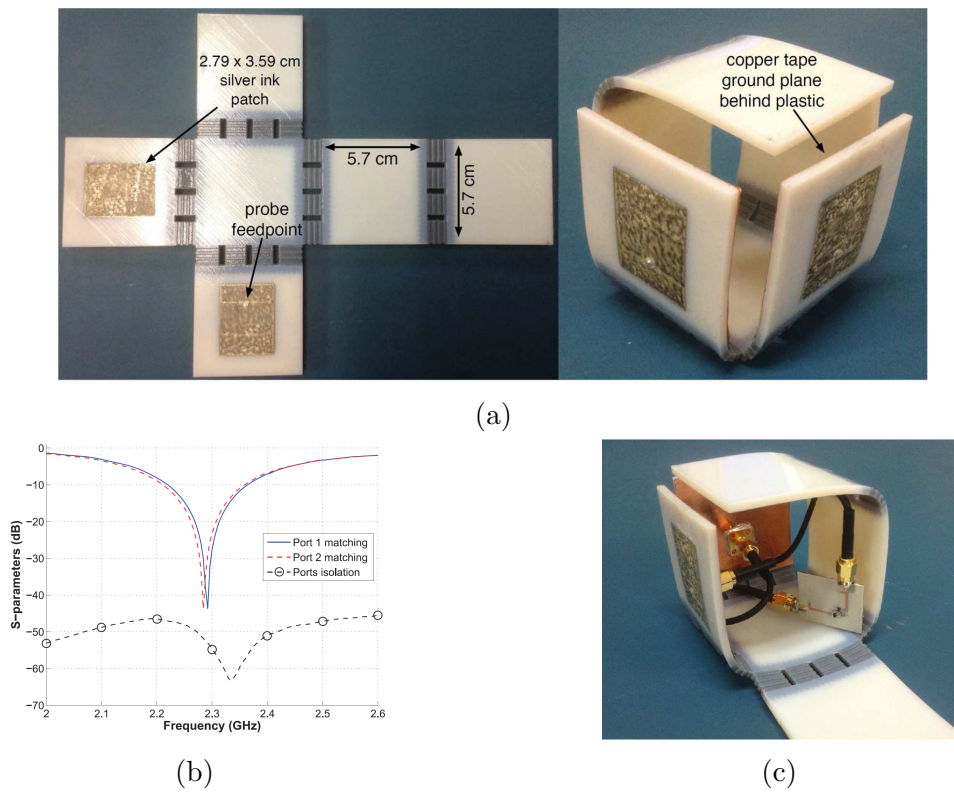


Figure 2.23: 3D-Printed Origami Packaging With Inkjet-Printed Antennas: (a) InkJet printed Patch unfolded and folded state; (b) Measured Reflection Coefficient; (c) Origami Package with harvester electronic [30]

S. Seiler [31] designed a 2 by 2 microstrip fed patch antenna array. This proposed design incorporated the Origami folding technique, Miura Ori, see [31, Fig. 2.24a]. The antenna design can be deployed from a compact folded state into a flat state. This allowed the design to change the performance, as well as, the physical state of the antenna. [31, Fig. 2.24b] displays the change in the folding angle ( $\beta$ ). When varying the folding angle ( $\beta$ ), the operating frequency shifts, as shown in [31, Fig. 2.24c].

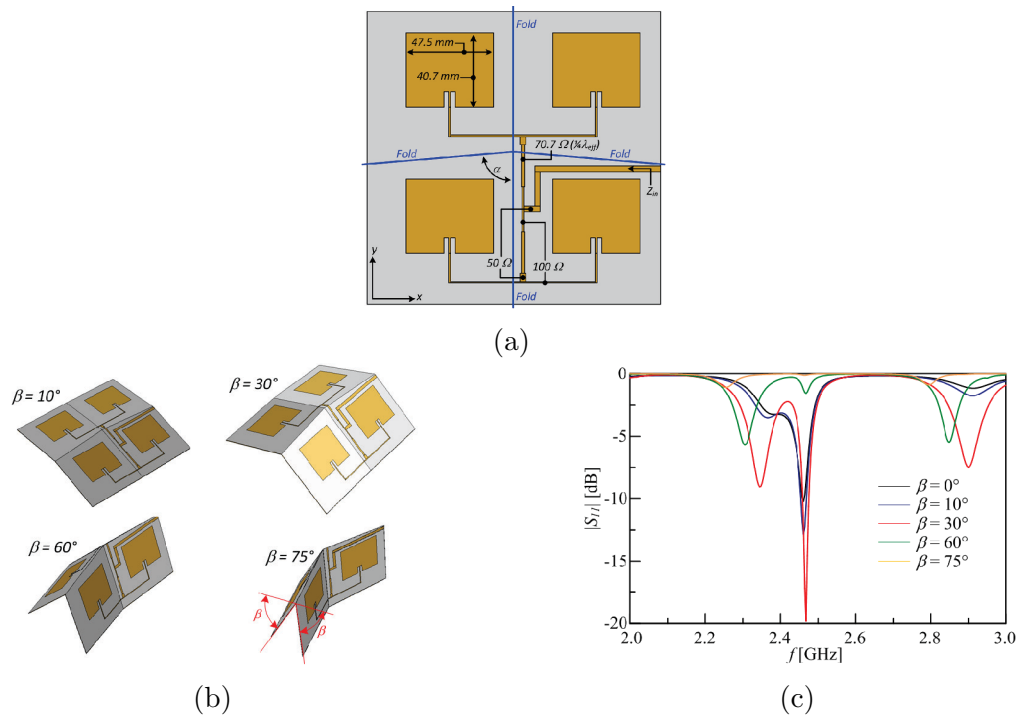


Figure 2.24: Physical Reconfiguration of an Origami-Inspired Deployable Microstrip Patch Antenna Array: (a) Microstrip Patch Antenna Array; (b) Intermediate State at different angle; (c) Simulated Reflection Coefficient for each angle [31]

## 2.4 Summary

Origami designs can be complicated and difficult to design, due to the mathematical calculation behind it. However, there are researchers creating software and programs to tackle this problem such as Origami Editor 3D [32]. This tool creates complicated Origami models. It gives a basic understanding on Origami and enables the user to design the pattern of the desired shape and see its folded shape on a computer screen. Using similar tools inspires others to investigate the art of Origami and its folding techniques, leading them to creating innovative and fascinating antenna designs.

Origami has also been beneficial to mathematicians and scientists, especially in the form of antennas. There were few antenna designs using Origami folding techniques. The researchers mentioned above studied the folding mechanism and engineered new designs based on old antennas. Although the performance of the new design was not comparable to an older antenna., it had other properties, such as low cost of materials, better portability and ability to collapse.

# Chapter 3

## Vivaldi Antennas

### 3.1 Introduction

Space communications satellite relies on Radio Frequency (RF) component to be able to communicate between the satellite and the ground station on Earth, as this is the only means of controlling the satellite in space [33]. Recent developments such as the Tracking and Data Relay Satellite Systems (TDRSS) and European Data Relay Systems (EDRS) proposed that satellites should communicate between satellites with less latency time between signals since they would not have to pass through ground stations to then be transmitted back to space. An reconfigurable antenna is required to scan and communicate between each satellite in a short distance, to then relay information signals to further away objects such as ground stations or Low Earth Orbit (LEO) satellites.

In this chapter, two flexible substrates: Kapton and Mylar, were investigated to determine which flexible substrates would perform better under folding mechanical stress. The antenna that was used in this chapter was the Vivaldi antenna. Each substrate underwent a series of simulations and measurements to determine the performance of the antenna, both electrically and physically. The array of Vivaldi antennas consists of four Vivaldi antennas radiating at four directions, as it folds, it

concentrates the beams into one single direction allowing a higher directivity.

## 3.2 Antenna Theory

A Vivaldi antenna is known as a tapered slot antenna [34]. It can be fabricated from a metal block, a Printed Circuit Board (PCB) or a flexible material with metallisation on both sides. Vivaldi antennas are part of a group of end-fire tapered slot antennas such as Linear Tapered Slot Antennas (LTSA), Constant Width Slot Antennas (CWSA) and exponentially tapered antennas (ESTA) [35].

A traditional Vivaldi antenna is an Ultra-Wide Band (UWB) antenna that tapers from a narrow slot section to a wider slot section [34]. Most Vivaldi antennas use the exponentially tapered design but for simplicity a Linear Tapered Slot design will be used in this chapter.

There are some advantages and disadvantages of using Vivaldi antennas, one advantage would be the wide bandwidth. To utilise the broad frequency range, the higher frequency is limited by the slot width at the base and the lower frequency is determined by the widest dimension of the mouth opening. As for the disadvantages, Vivaldi antennas cannot go above 10 dBi directivity. To overcome this, multiple Vivaldi antennas in an array would be required.

### 3.2.1 Microstrip Line Transmission

Microstrip line is one of the most popular transmission lines because it can be resized to any microwave design. The geometry can be defined as per Fig. 3.1a, while the characteristic of the fringing field from a microstrip transmission line is shown in Fig. 3.1b. The microstrip line will have a given thickness of the substrate ( $h$ ) with a permittivity of the substrate ( $\epsilon_r$ ), a width of a microstrip line on the top ( $w$ ) and a ground plane on the bottom.

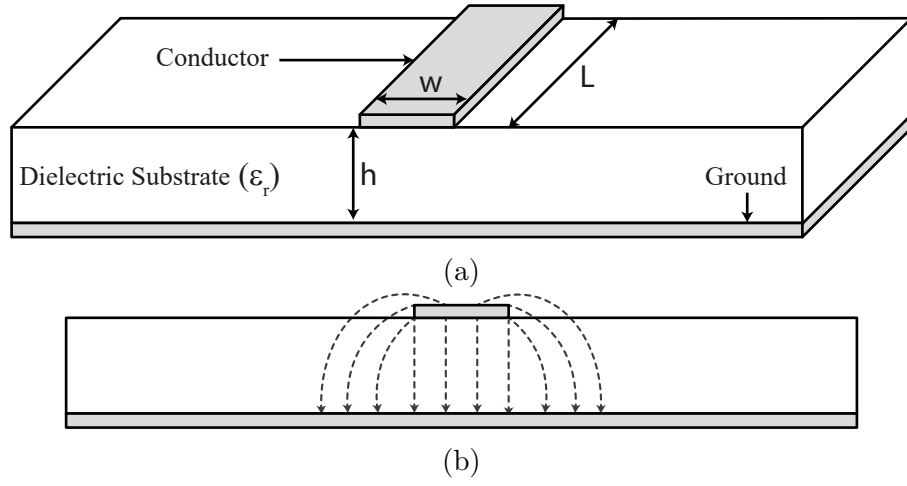


Figure 3.1: (a) Microstrip and (b) Fringing Field

(3.1) below from [36] obtains the width of the microstrip line with a given characteristic impedance ( $Z_0$ ) or the characteristic impedance with a given width of the microstrip line ( $w$ ). To use (3.1) - (3.3), the effective dielectric constant ( $\epsilon_{eff}$ ) has to be calculated by using the dielectric constant with the dimensions of the thickness of the substrate ( $h$ ) and the width of the microstrip line ( $w$ ).

$$\epsilon_{eff} = \frac{\epsilon_r + 1}{2} + \frac{\epsilon_r - 1}{2} \frac{1}{\sqrt{1 + 12h/w}} \quad (3.1)$$

$$Z_0 = \begin{cases} \frac{60}{\sqrt{\epsilon_{eff}}} \ln \left( \frac{4h}{w} + \frac{w}{4h} \right), & \text{for } \frac{w}{h} \leq 1 \\ \frac{120\pi}{\sqrt{\epsilon_{eff}} \left[ \frac{w}{h} + 1.393 + 0.667 \ln \left( \frac{w}{h} + 1.444 \right) \right]}, & \text{for } \frac{w}{h} \geq 1 \end{cases} \quad (3.2)$$

$$\frac{w}{h} = \begin{cases} \frac{8e^A}{e^{2A} - 2}, & \text{for } \frac{w}{h} < 2 \\ \frac{2}{\pi} \left[ B - 1 - \ln(2B - 1) + \frac{\epsilon_r - 1}{2\epsilon_r} \left\{ \ln(B - 1) + 0.39 - \frac{0.61}{\epsilon_r} \right\} \right], & \text{for } \frac{w}{h} > 2 \end{cases} \quad (3.3)$$

where

$$A = \frac{Z_0}{60} \sqrt{\frac{\epsilon_r + 1}{2}} + \frac{\epsilon_r - 1}{\epsilon_r + 1} \left( 0.23 + \frac{0.11}{\epsilon_r} \right)$$

$$B = \frac{337\pi}{2Z_0\sqrt{\epsilon_r}}$$

### 3.2.2 Matching Network

When designing antenna arrays, it is crucial to create a sufficient impedance matching network, to minimise the energy reflected back through the transmission line to the load [36]. One of the most commonly used matching network is a quarter wave transformer. It uses transmission lines with various characteristic impedance and has a length  $1/4$  of the guided wavelength of the desired frequency. A circuit schematic of a quarter wave transformer has been shown in Fig. 3.2 below.

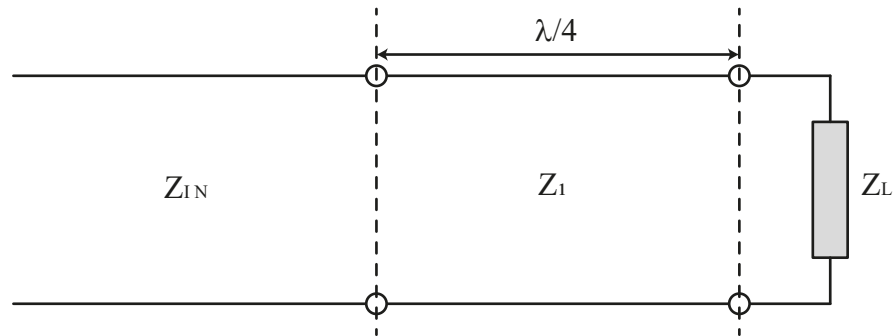


Figure 3.2: Quarter Wave Matching Network

The quarter wave transformer input impedance is calculated with (3.4). When looking at the input towards  $Z_1$ , and when the guided wavelength become  $l = \frac{\lambda}{4}$ , that will give  $\beta l = \frac{\pi}{2}$ , the equation can be reduced to (3.5) and the equations can be rearrange to find  $Z_1$  shown in (3.6).

$$Z_{in} = Z_1 \frac{Z_L + jZ_1 \tan \beta l}{Z_1 + jZ_L \tan \beta l} \quad (3.4)$$

$$Z_{in} = \frac{Z_1^2}{Z_L} \quad (3.5)$$

$$Z_1 = \sqrt{Z_{in}Z_L} \quad (3.6)$$

### 3.2.3 Vivaldi Antenna

A Linear Tapered Vivaldi Antenna has a microstrip line on one side with a linear tapered slot on the other shown in Fig. 3.3. The microstrip line will have a feed point, which will pass through the slot line and have  $\lambda/4$  stub away. When it resonates at the slot, the wave travels back to a closed slot with a circular shape.

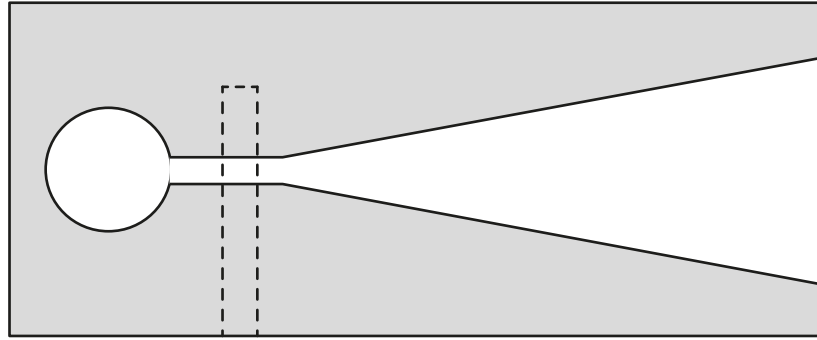


Figure 3.3: Single Exponential Vivaldi Design

As explained by G. Kalbhor [37], the length of the Vivaldi antenna had to be greater than  $3\lambda_c$  with the width of mouth opening ( $w$ ) greater than  $\lambda_c$ , where  $\lambda_c$  was the wavelength of the centre frequency. For a LTSA [35], it behaved like an optimal end-fire travelling wave antenna. (3.7) evaluates the widest mouth opening necessary to make the Vivaldi antenna ( $w$ ) efficient, while the width has to be smaller than  $\lambda_o/2$ , where  $\lambda_o/2$  was the half of the wavelength in free space.

$$w < \frac{\lambda_o}{2} \quad (3.7)$$

### 3.3 Academic Research on Vivaldi Antennas

In this paper [38, Fig. 3.4], R. Singha presented a design using a thin substrate Roger TMM3 with a thickness of 0.3807 mm and a permittivity ( $\epsilon_r$ ) of 3.27. The antenna design used a Linear Tapered Slot design, as it had a good relation with beam width and side lobe level. There were 3 linear tapered lines. One linear tapered region was used for high frequency whilst the other linear regions were for lower frequencies. [38, Fig. 3.4a] displayed at the edge for the antenna design to suppress the surface current. In [38, Fig. 3.4a], the operating frequency oscillated between 3.1 GHz to 20 GHz and a radiation pattern gain of 10 dB at 12 GHz.

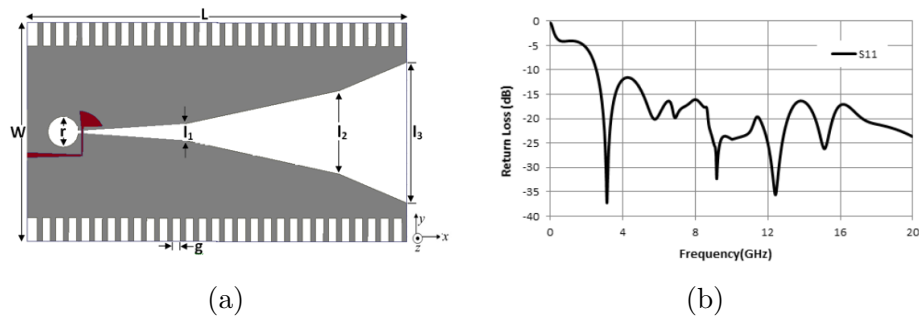


Figure 3.4: Linear Tapered Slot Vivaldi Antenna with Corrugated Edges for UWB Applications: (a) Proposed Linear Vivaldi Antenna; (b) Reflection Coefficient of the proposed Linear Vivaldi Antenna [38]

S. Sheel had presented a paper [39] where an array of Vivaldi antennas could be reconfigured by using switching PIN diodes. The diodes acted as a voltage controlled switches, allowing the current to travel to a specific line. The proposed design consisted of 8 identical Vivaldi antennas. Using the PIN diode, it was switching between each Vivaldi antenna. The operating frequency ranged from 2 GHz to 6 GHz, with a radiation pattern gain of 5 dB, see [39, Fig. 3.5].



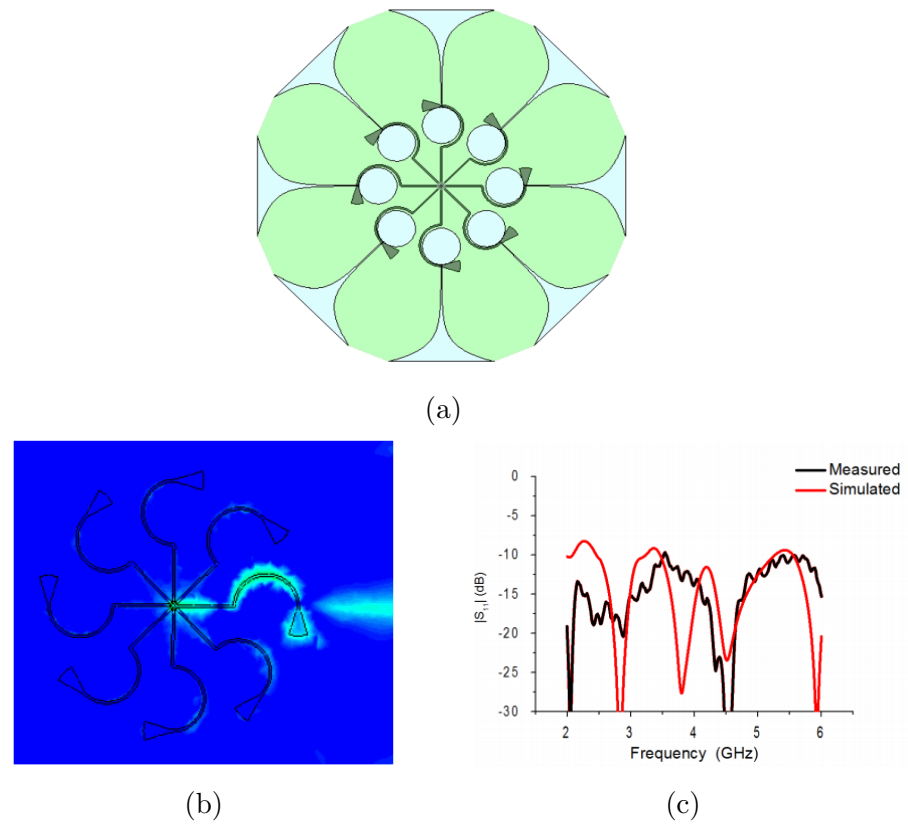


Figure 3.5: Switchable-feed Reconfigurable Ultra-Wide Band Planar Antenna: (a) Reconfigurable Vivaldi Antenna; (b) Antenna Electric Field Characteristic; (c) Simulated and Measured Reflection Coefficient [39]

In 2012, D. Kerarti have proposed a tapered slot Vivaldi antennas for UWB applications. [40] The substrate was TACONIC TLX-8 with a thickness of 0.76 mm and the permittivity ( $\epsilon_r$ ) of 2.55. The 10 dB reflection coefficient bandwidth was between from 2.14 GHz and 11.33 GHz. Across the frequency band, the Voltage Standing Wave Ratio (VSWR) was below 2. In [40, Fig. 3.6], the gain of the proposed antenna varied from 2 dB to 9 dB over the entire operating range.

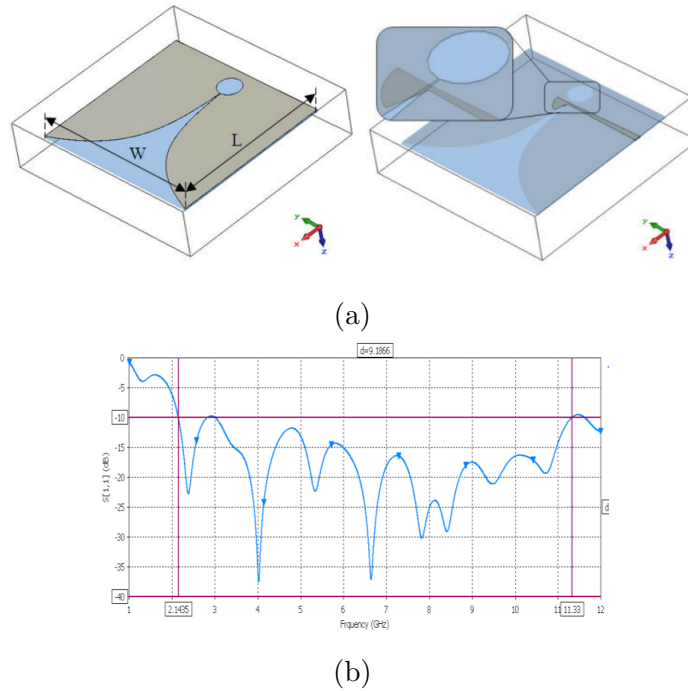
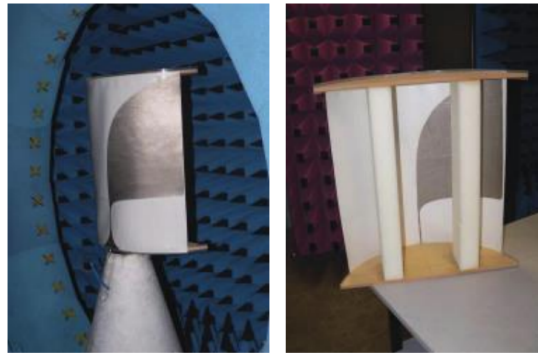
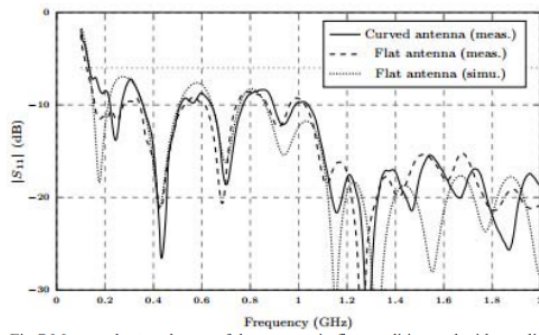


Figure 3.6: New Tapered Slot Vivaldi Antenna for UWB Applications: (a) Tapered Vivaldi Antenna with microstrip; (b) Reflection Coefficient of the Tapered Vivaldi Antenna [40]

A. Presse [41] has proposed a curved antipodal Vivaldi antenna on a silicone substrate. It was able to bend around a cylindrical object. The silicon substrate was 1.5 mm thick with a permittivity ( $\epsilon_r$ ) of 2.97 and a loss tangent ( $\tan\delta$ ) of 0.035. The 10 dB reflection coefficient bandwidth started at 150 MHz and was going to 2000 MHz. A. Presse attached six identical antipodal Vivaldi antennas on a large flexible surface, to a helium gas balloon, without any matching network, as shown in [41, Fig. 3.7]. During testing, he was able to detect Frequency Modulation (FM) radio wave over several km away.



(a)



(b)



(c)

Figure 3.7: Flexible UHF/VHF Vivaldi Antenna for Broadband and Gas Balloon Applications: (a) Fabricated antenna with curve support; (b) Reflection Coefficient of the antenna under stress; (c) Antennas attached onto balloon [41]

### 3.4 Vivaldi Antenna using flexible substrate

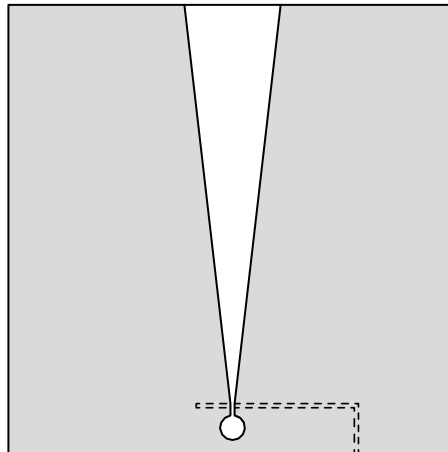


Figure 3.8: Single Vivaldi Design

For this section, a single linear tapered slot Vivaldi antenna was simulated using CST studio, as well as, measured in the anechoic chamber with Vector Network Analyser (VNA). The idea of using a linear tapered slot design, instead of a exponential slot design was due to its simplicity, see Fig. 3.8. The Vivaldi antenna is simulated with two different flexible substrates; Kapton and Mylar. Both substrates are developed by DuPont. Kapton is made from a polyimide film and Mylar is made from a stretched Polyethylene Terephthalate (PET). Both substrates have a large number of applications ranging from science, general electronics and acoustics. Although both substrates have similar electrical properties, they have a different mechanical properties, as shown in Table 3.1 below. The section would focus on the two substrates and would investigate any changes in resonant frequency, as well as, radiation pattern gain.

Table 3.1: Table of Mechanical and Electrical Properties for Kapton and Mylar

	Kapton	Mylar
Mechanical Properties		
Thickness, mm	0.125	0.125
Tensile Strength, MPa	231	180
Elongation, %	72	150
Shrinkage at 150°C, %	0.013	0.03
Electrical Properties		
Permittivity, $\epsilon_r$	3.54	3.4
Loss Tangent, $\tan\delta$	0.0026	0.003

### 3.4.1 Flexible Vivaldi Antenna Design

The dimensions of the LTSA are shown in Fig. 3.9. The width and length of the antenna (*length*) remained equal, as it would be used with an array of Vivaldi antennas folded into a three-dimensional (3-D) structure. The width of the microstrip (*ms*) is equal to the smallest tapered section, the widest tapered mouth opening (*w*), the length of the tapering (*Wl*), the length of the slot before the tapered section (*Bw*), the radius of the circular slot (*Cir*) and the length of the open ended stub from the microstrip perpendicular to the slot (*stub*).

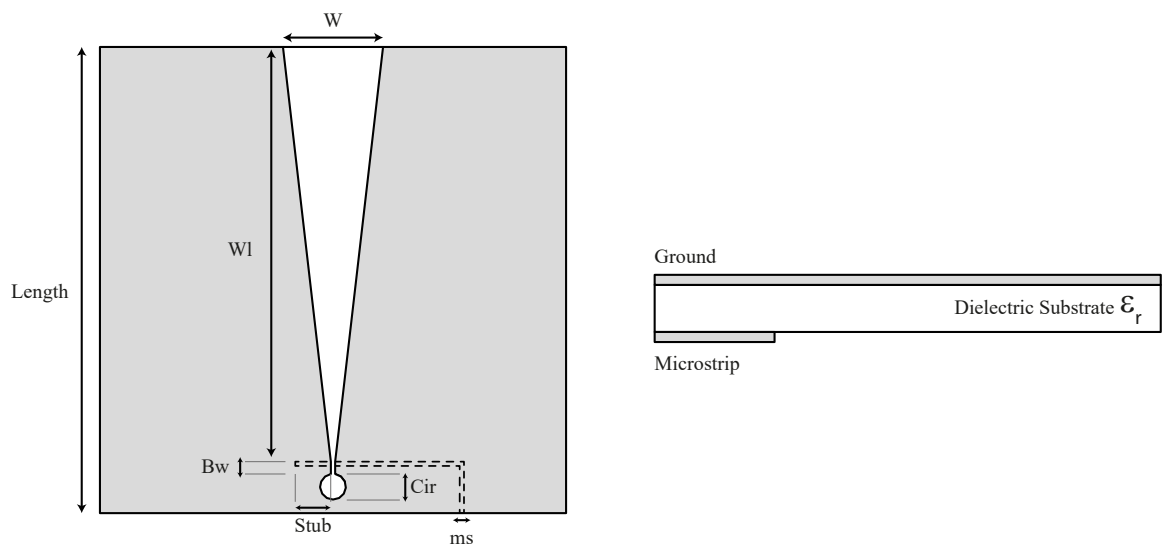


Figure 3.9: Single Vivaldi Dimension Chart

### 3.4.2 Single Vivaldi Antenna - Simulated Results

A series of simulations were performed on both Kapton and Mylar substrate. This was done to see the difference and to compare the 2 substrates. The electrical properties of the two substrates would be used in the simulations. The variables that would be simulated and optimised were the widest mouth opening (*w*), the length of the tapered section (*Wl*), the extended microstrip over the slot line (*stub*) and the radius of the circular slot (*Cir*).

Firstly, Kapton would be simulated on these variables. In Fig. 3.10 below, the results

were simulated when varying the values of the widest mouth opening ( $w$ ). When  $w = 6$  mm, the operating frequency is at 7.8 GHz and the reflection coefficient ( $S_{11}$ ) of -35 dB with a 10 dB bandwidth between 6 GHz to 9 GHz. As the mouth opening ( $w$ ) increased, the electrical length of the slot increased, therefore a frequency shift occurred. When  $w = 8$  mm, the operating frequency is at 7.4 GHz,  $S_{11}$  has increased to -46 dB, the bandwidth has decreased from 3 GHz to 2.4 GHz.

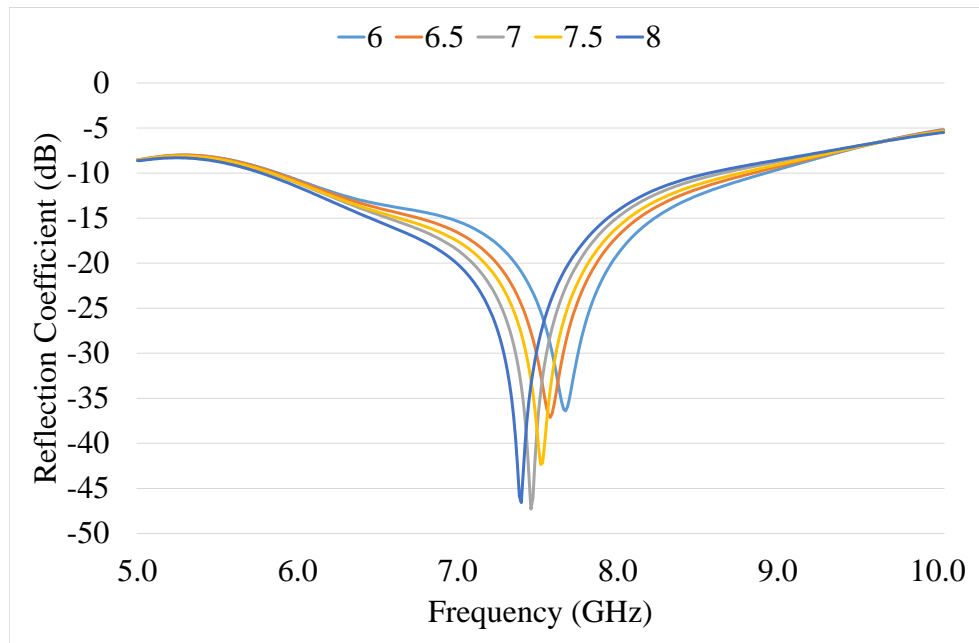


Figure 3.10: Single Vivaldi Antenna with Kapton - W Sweep

The length of the tapered section ( $Wl$ ) varied from 27 mm to 29 mm with an increment of 0.5 mm, shown in Fig. 3.11. When  $Wl = 27$  mm, it had the biggest bandwidth from 5 GHz to 8.5 GHz. The resonant frequency was at 8 GHz and  $S_{11} = -20$  dB. When  $Wl = 29$  mm, the resonant frequency was at 7.5 GHz,  $S_{11} = -42$  dB and a bandwidth of 3 GHz. As the length ( $Wl$ ) increased, the greater the performance on individual resonant frequency. However, the bandwidth decreased from 3.5 GHz to 3 GHz.

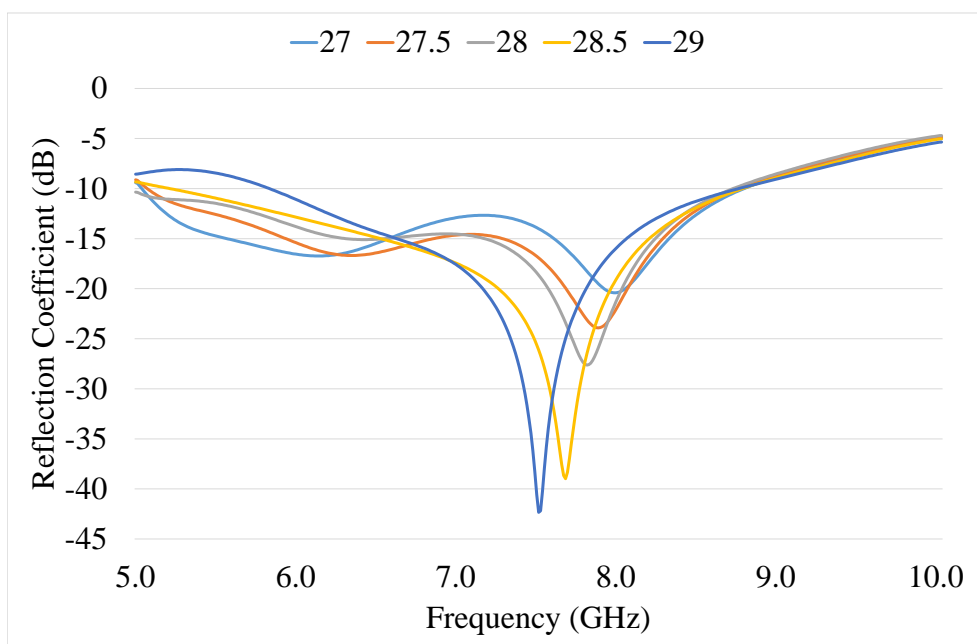


Figure 3.11: Single Vivaldi Antenna with Kapton - Wl Sweep

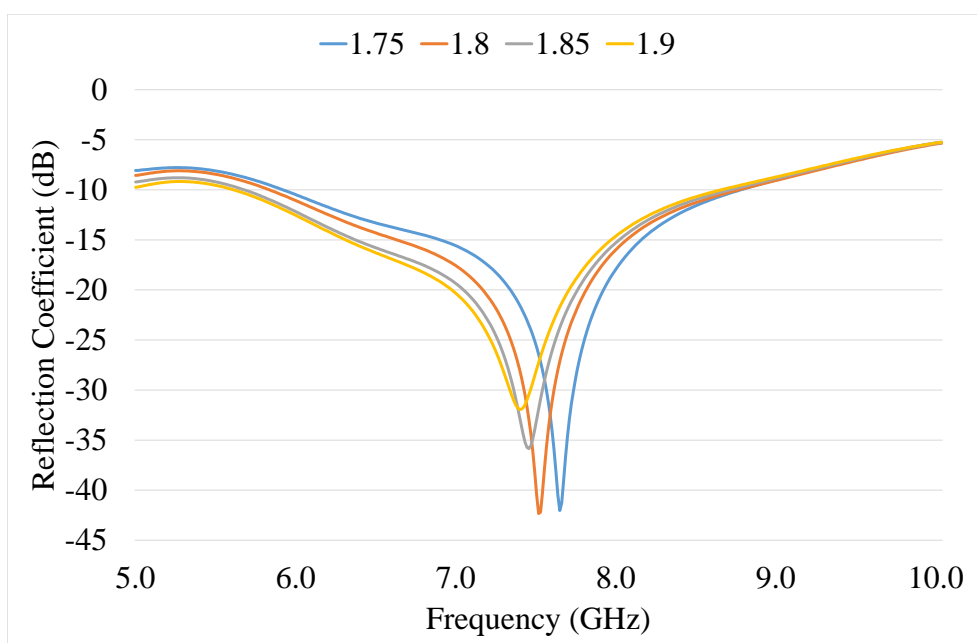


Figure 3.12: Single Vivaldi Antenna with Kapton - Stub Sweep

From Fig. 3.12, the microstrip stub (*stub*) was varied between 1.75 mm and 1.9 mm. When *stub* = 1.75 mm, the resonant frequency was at 7.7 GHz,  $S_{11} = -42$  dB with a bandwidth of 3 GHz. As the microstrip stub (*stub*) increased, the resonant frequency lowered and  $S_{11}$  performance drops. When *stub* = 1.9 mm, the resonant frequency was at 7.35 GHz and  $S_{11} = -32$  dB with a bandwidth of 3.5 GHz

The radius of the circular slot (*Cir*) was changed to values between 0.7 mm to 0.9 mm as shown in Fig. 3.13 below. When *Cir* = 0.7 mm, the resonant frequency was at 8.2 GHz with a 10 dB reflection coefficient bandwidth between 6 GHz to 9.5 GHz. The operating range had a performance below -15 dB, therefore, when *Cir* = 0.7 mm, the operating range was much smaller. When *Cir* = 0.9 mm, the resonant frequency was at 7.5 GHz and  $S_{11}$  at -42 dB with a bandwidth of 3 GHz. The electrical length increased as the circumference of the circular slot increased (*Cir*).

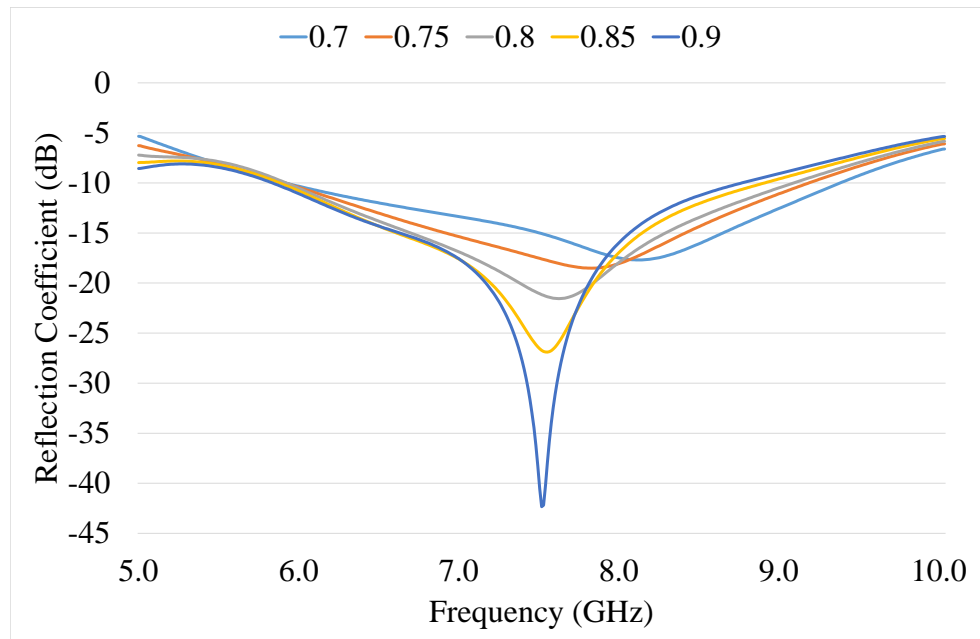


Figure 3.13: Single Vivaldi Antenna with Kapton - Cir Sweep

The best performance seen in Fig. 3.10 - 3.13, occurred at 7.5 GHz with -42 dB. The values of each variable includes: the widest of the mouth opening ( $w$ ) = 7 mm, the tapered length ( $Wl$ ) = 29 mm, the microstrip stub length (*stub*) = 1.8 mm and the



radius of the circular slot ( $Cir$ ) = 0.9 mm. A far-field plot of the antenna with a Kapton substrate at 7.5 GHz was shown in Fig. 3.14. The maximum gain in the co-polar plot was at 4.5 dBi, the co-polar plot also showed the Half Power Beam Width (HPBW) that had a total of  $70^\circ$ . The cross-polar plot has a null region at -45 dB.

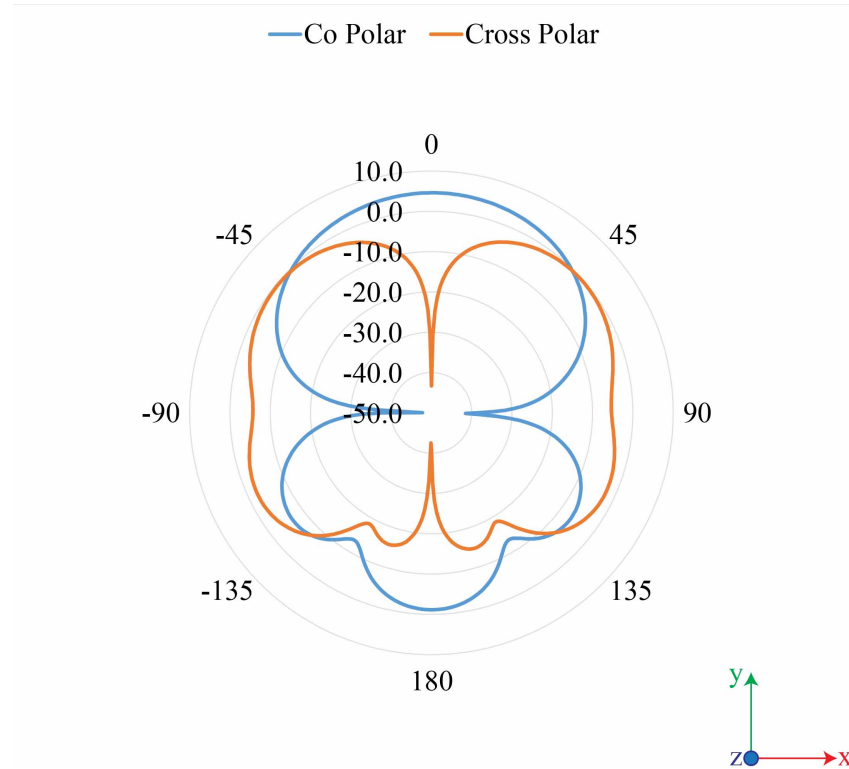


Figure 3.14: Single Vivaldi Antenna with Kapton - Simulated Co and Cross Polar

The substrate was changed to Mylar, so a comparison could be analysed between the two materials. The value used in Fig. 3.10 - 3.13 would be compared with the Mylar substrate. In Fig. 3.15, the widest mouth opening ( $w$ ) was simulated between 6 mm and 7.5 mm. When  $w = 6$  mm, the resonant frequency was at 7.9 GHz with  $S_{11}$  at -37 dB. When  $w = 7.5$  mm, the resonant frequency was at 7.5 GHz with  $S_{11} = -40$  dB. All results had 10 dB reflection coefficient bandwidth of 3 GHz.

In Fig. 3.16, the length of the tapering ( $Wl$ ) was varied from 27 mm to 29 mm. When  $Wl = 27$  mm, the resonant frequency was at 8 GHz with the bandwidth 4 GHz wide. As the length ( $Wl$ ) increased, the resonant frequency shifted and the performance increased down to -47 dB, however the bandwidth dropped from 4 GHz to 3 GHz, when  $Wl = 29$  mm.

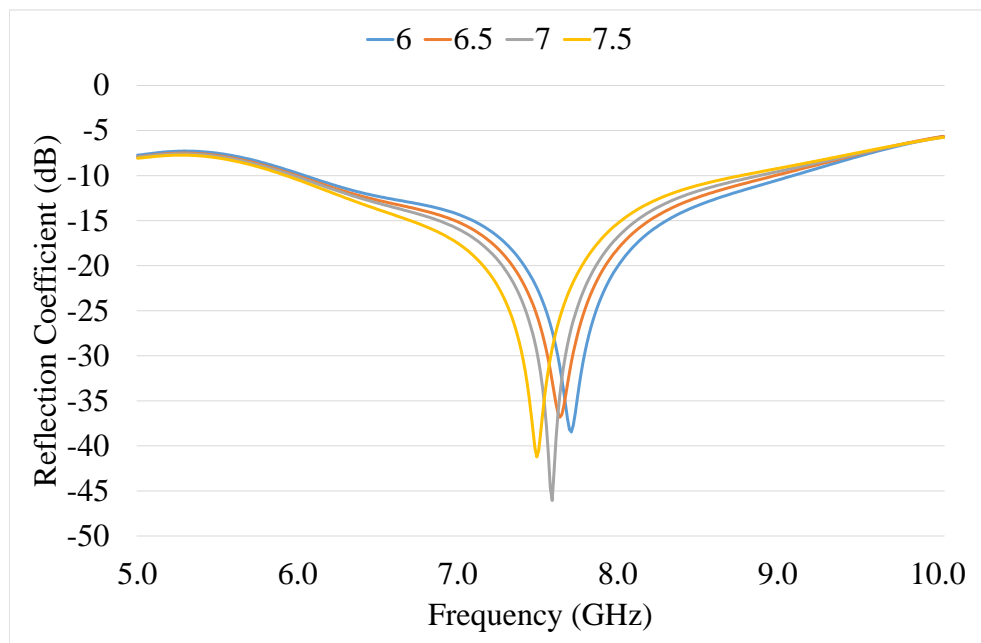


Figure 3.15: Single Vivaldi Antenna with Mylar - W Sweep

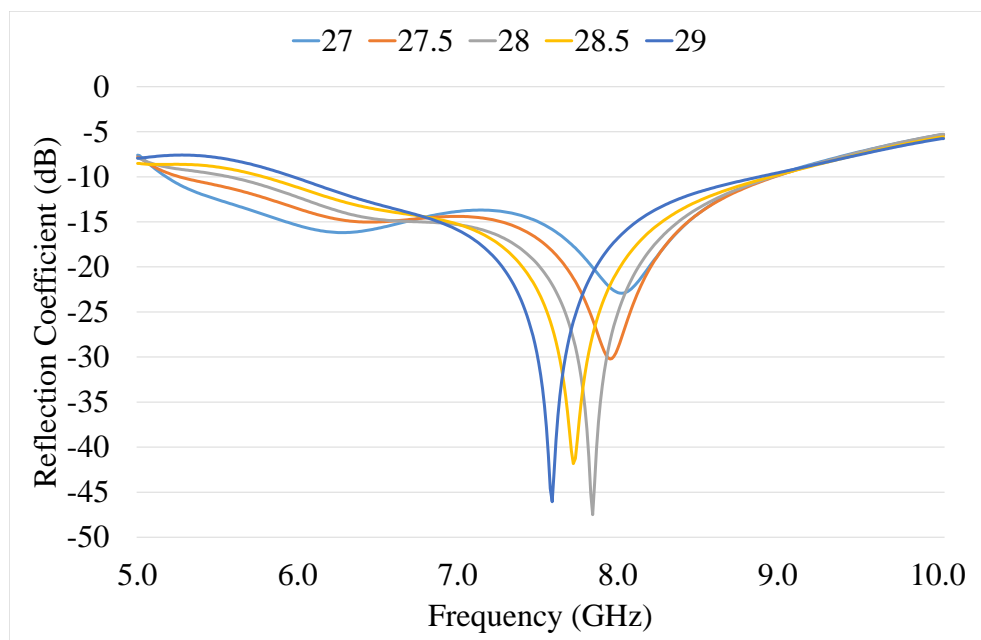


Figure 3.16: Single Vivaldi Antenna with Mylar - W1 Sweep

The microstrip stub (*stub*) was changed to be between 1.7 mm and 1.9 mm, as shown in Fig. 3.17. When  $stub = 1.7$  mm and 1.75 mm, both resonant frequencies were at 7.9 GHz with a bandwidth of 2.5 GHz. The wavelength in the microstrip line increased as *stub* increased from 1.7 mm to 1.9 mm. The performance had decrease slightly when the length increased from -47 dB down to -40 dB.

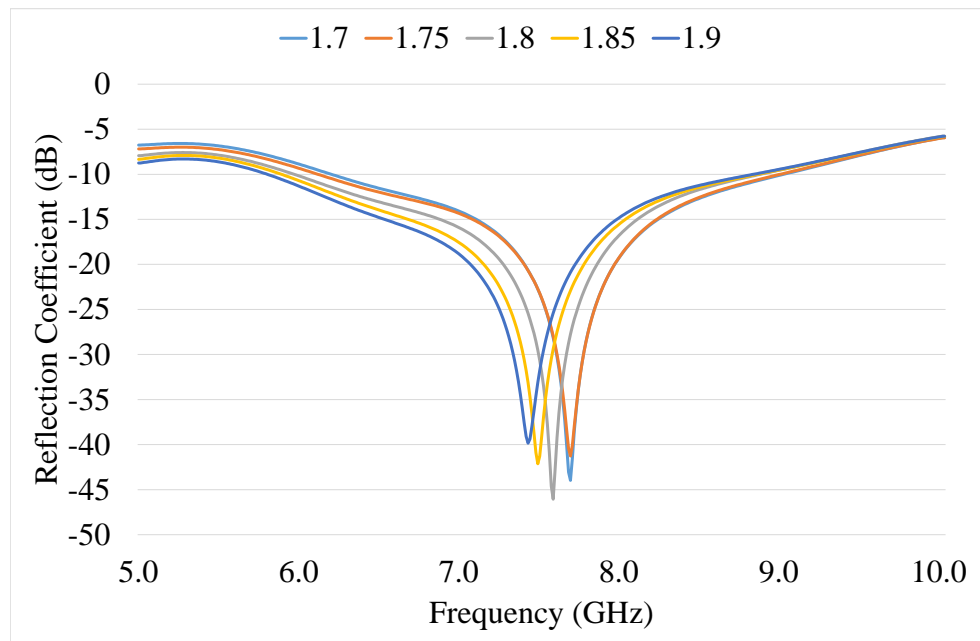


Figure 3.17: Single Vivaldi Antenna with Mylar - Stub Sweep

In Fig. 3.18, the radius of the circular slot (*Cir*) was varied between 0.7 mm to 0.9 mm. As  $Cir = 0.7$  mm, the resonant frequency was at 8.2 GHz,  $S_{11} = -18$  dB and a 10 dB reflection coefficient bandwidth from 6.2 GHz to 9.5 GHz. As *Cir* increased, the resonant frequency was shifted, due to the circumference of the circular slot increasing, therefore increases the wavelength. The performance level increased from -15 dB to -47 dB, unfortunately the 10 dB reflection coefficient bandwidth decreased from 3.3 GHz to 3 GHz.

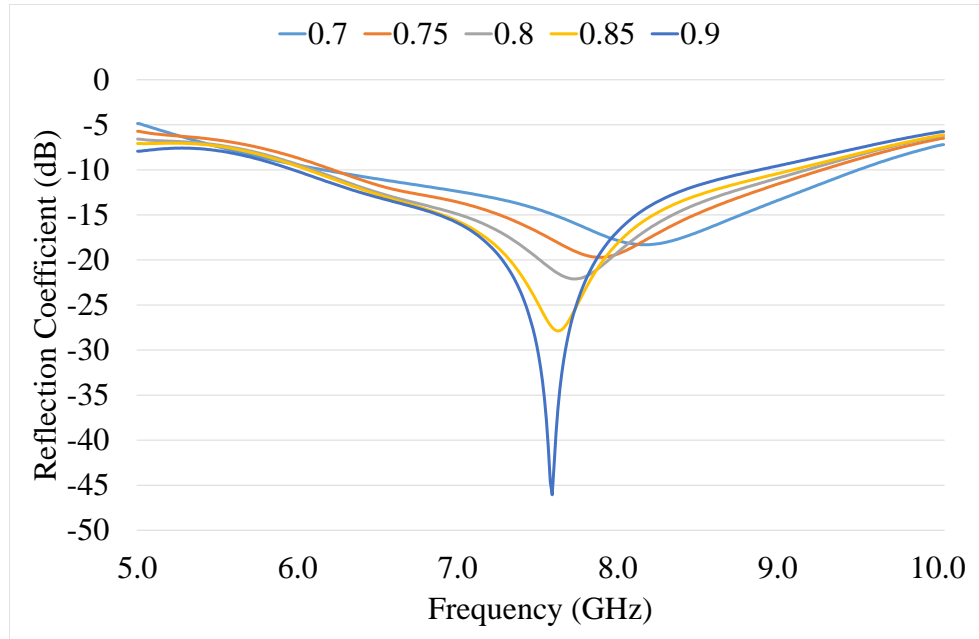


Figure 3.18: Single Vivaldi Antenna with Mylar - Cir Sweep

The far-field plot shown in Fig. 3.19, were taken, when the antenna was operating at 7.8 GHz. The maximum gain of the antenna with a Mylar substrate was 4.5 dB with a HPBW of 70°. The cross-polar plot displayed a null region at -44 dB.

Comparing the simulated results of Kapton and Mylar, with all of the variables kept the same was done. The resonant frequency increased from 7.5 GHz with Kapton to 7.8 GHz with Mylar. Both  $S_{11}$  and 10 dB reflection coefficient bandwidths remained constant at -47 dB and with 3 GHz bandwidth. The resonant frequency changed due to the change in permittivity ( $\epsilon_r$ ) of both substrates. The loss tangent ( $\tan\delta$ ) was similar, therefore the  $S_{11}$  performance remained the same. The far-field results displayed same simulated gain and beam width.

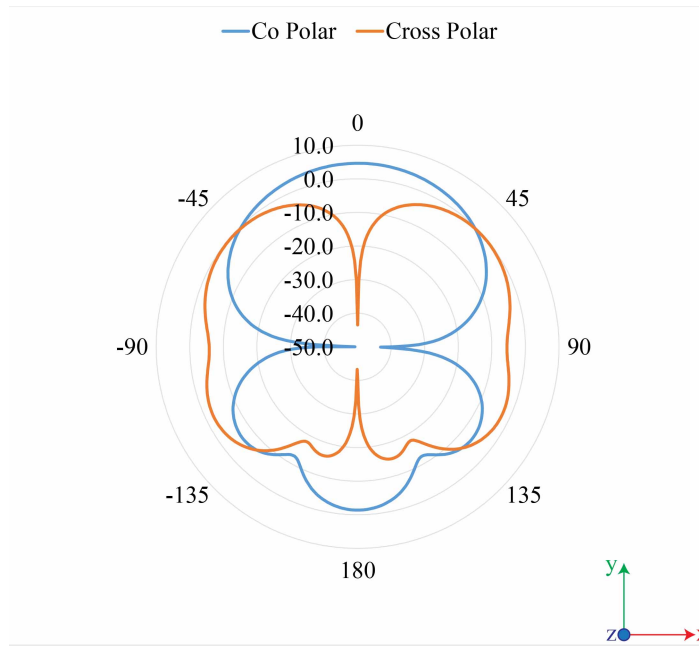


Figure 3.19: Single Vivaldi Antenna with Mylar - Simulated Co and Cross Polar

The values of each parameter were shown in Table 3.2. Using those values, the Vivaldi Antenna design can be fabricated and measured using a Vector Network Analyser (VNA).

Table 3.2: Vivaldi Antenna values for both Kapton and Mylar

Parameters		Value ( <i>mm</i> )
Length	( <i>Length</i> )	34
Width of Microstrip	( <i>ms</i> )	0.3
Widest tapered mouth opening	( <i>W</i> )	7
Length of tapering	( <i>Wl</i> )	29
Length before tapering	( <i>Bw</i> )	1
Radius of the circular slot	( <i>Cir</i> )	0.9
Stub	( <i>Stub</i> )	1.8

### 3.4.3 Single Vivaldi Antenna - Measured Results

Each Vivaldi antenna went through a standard etching process. The photo-resist layer was placed onto both side of the substrate. The antenna design was exposed with an UV light box. The developer stripped away the photo-resist layer exposing the unwanted copper. The machine etched away all the unwanted exposed copper leaving the desired antenna design.

The fabricated antennas were connected to a single port VNA from Rohde and Schwarz with a 0.2 mm pin SubMiniature version A (SMA) connector. The VNA could detect frequency range from 9 KHz up to 13.6 GHz. The VNA was calibrated prior to any measurements. The anechoic chamber could only perform radiation pattern measurements as the standard horn for gain measurements was out in repair. In all far-field polar plots below, the values were normalised to 0 dB as the maximum value.

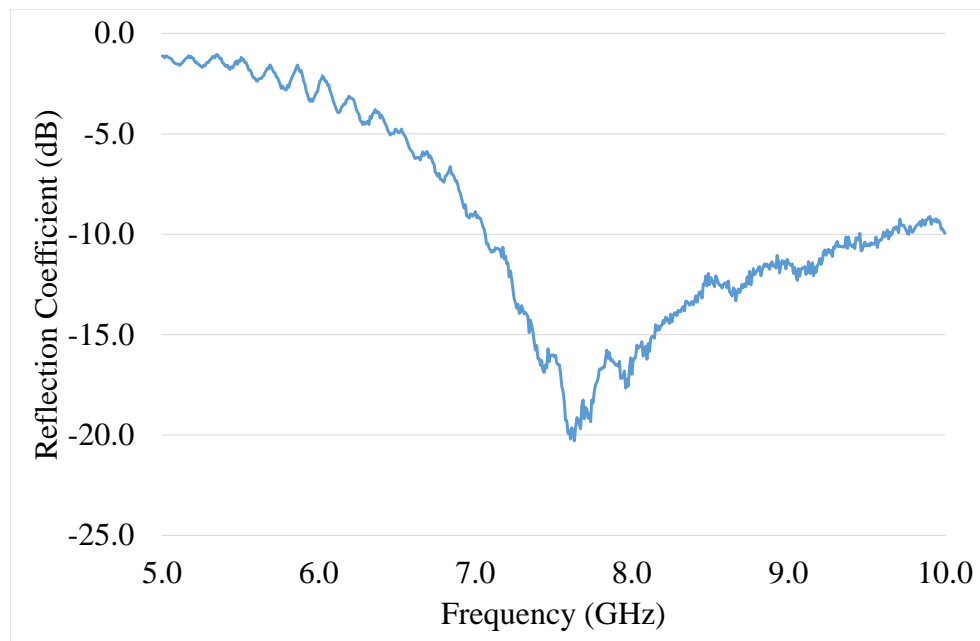


Figure 3.20: Single Vivaldi Antenna with Kapton - Measured Reflection Coefficient

Fig. 3.20 displays the reflection coefficient of the fabricated Vivaldi antenna with Kapton as a substrate. The resonant frequency was at 7.6 GHz and  $S_{11}$  at -20 dB with a 10 dB reflection coefficient bandwidth from 7 GHz to 9 GHz. Comparing to the simulated results with the measured, the resonant frequency had shifted by 100 MHz. The  $S_{11}$  performance had decreased from -42 dB to -20 dB with the bandwidth decreased from 3 GHz to 2 GHz. The measured results were normalised with 0 dB as the maximum value. In Fig. 3.20, the co-polar plot had a HPBW of 60°, to the simulated results, the HPBW had decreased by 10°. The null region in the

cross polar plot was at -40 dB compared to the simulated the results, it decreased by -5 dB.

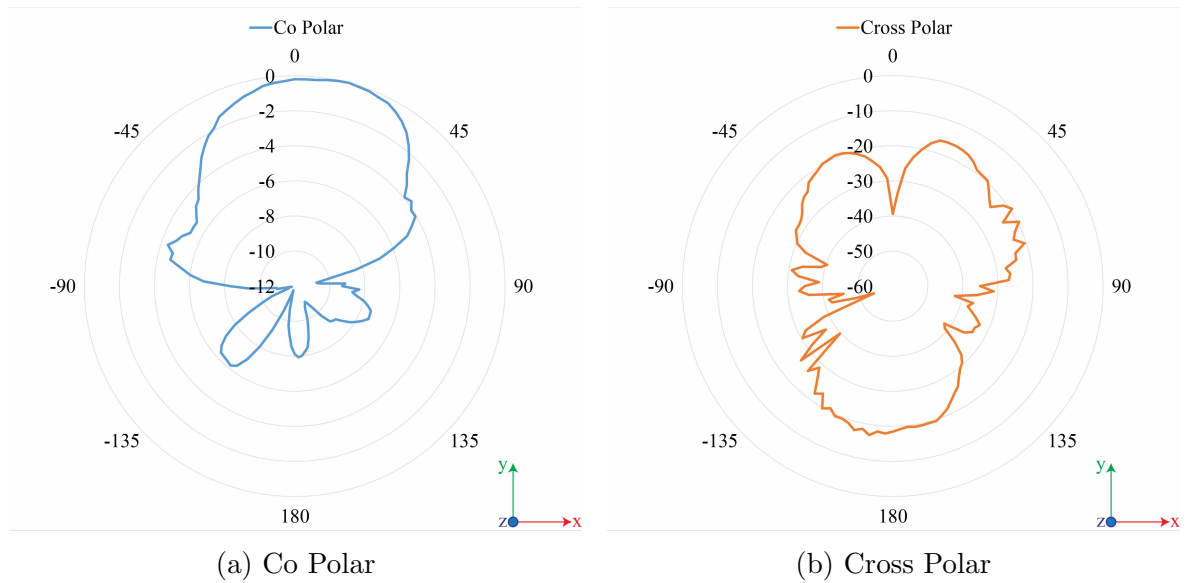


Figure 3.20: Single Vivaldi Antenna with Kapton - Measured Radiation Pattern

The result of the fabricated Vivaldi antenna with Mylar were seen in Fig. 3.21. The resonant frequency was at 7.8 GHz as expected from the simulated results but the  $S_{11}$  level decreased from -45 dB to -21 dB. The 10 dB reflection coefficient bandwidth was between 7.5 GHz and 8.4 GHz, it decreased dramatically from 2.5 GHz to 0.9 GHz. In Fig. 3.21, the co-polar plot had a HPBW of  $60^\circ$  which was a small  $10^\circ$  decrease, comparing to the simulated results.

When comparing the two substrates, Kapton and Mylar, on their electrical properties. Both simulated and measured results displayed similarity, as they had a similar permittivity ( $\epsilon_r$ ) and loss tangent ( $\tan\delta$ ). As the permittivity increased, the resonant frequency decreased. The loss tangent value given in the simulations was lower than fabricated design, therefore the  $S_{11}$  performance decreased.

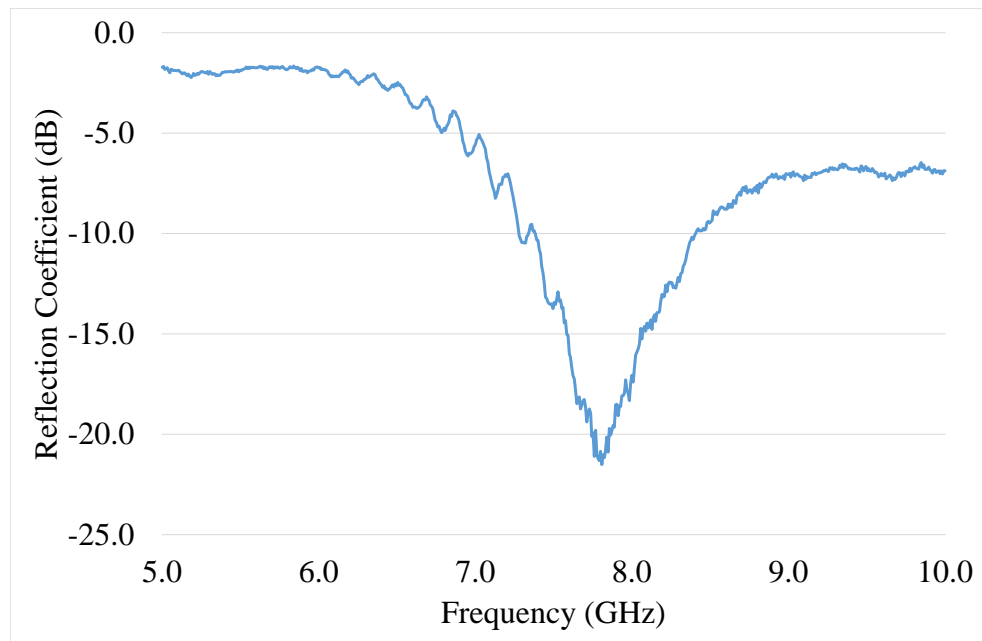


Figure 3.21: Single Vivaldi Antenna with Mylar - Measured Reflection Coefficient

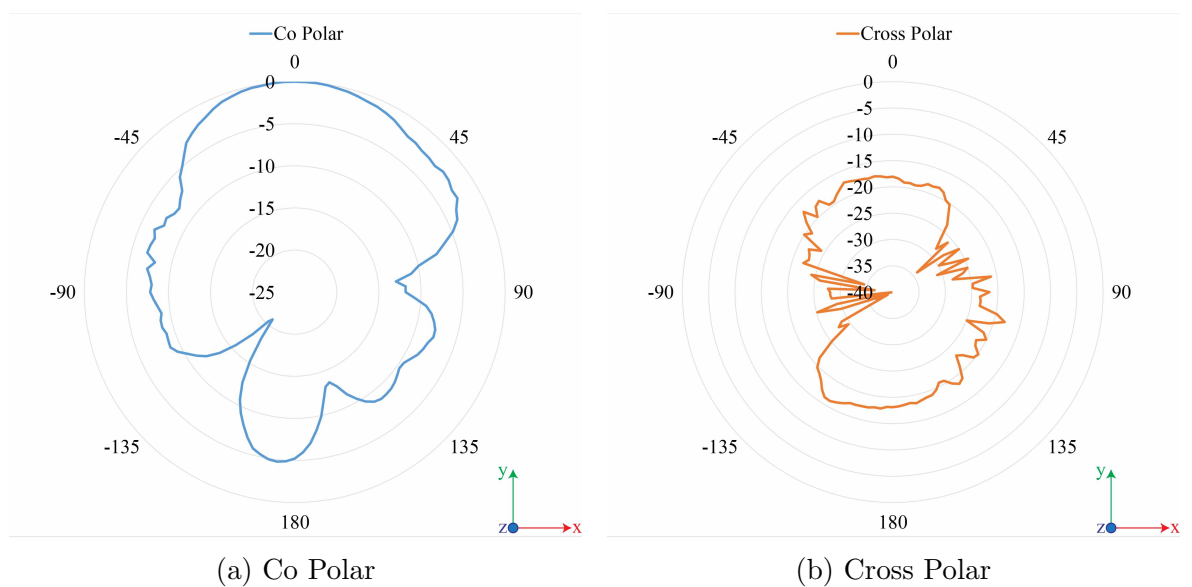


Figure 3.21: Single Vivaldi Antenna with Mylar - Measured Radiation Pattern



## 3.5 Foldable Arrays of Vivaldi Antennas

From the Chapter 3.4 above, the Vivaldi antennas with both different substrates, Kapton and Mylar, were simulated on CST studio and measured with VNA and the anechoic chamber. To create an array of Vivaldi Antennas, it required a matching network. An idea was proposed to have each individual antenna radiating at different phase, which allowed the design to radiate at all directions, when it was in the Flat state but when it was in the Folded state, it was able to radiate all the energy at a single point direction.

### 3.5.1 Schematic

There were a few methods to create a matching network in CST Studio. It could be created by using solid block with a given dimensions in the 3-D model view. However, it would take too long to optimise the design, if minor changes were needed. On CST Studio, there is a function that uses schematics. It includes various types of microstrip line function such as T-junction and  $45^\circ$  bend. This allowed a matching network to be created. Firstly, the reference box had to be added. This contained the substrate height ( $H$ ), the thickness of the microstrip ( $T$ ), the permittivity of the substrate ( $\epsilon_r$ ) and the loss tangent ( $\tan\delta$ ).

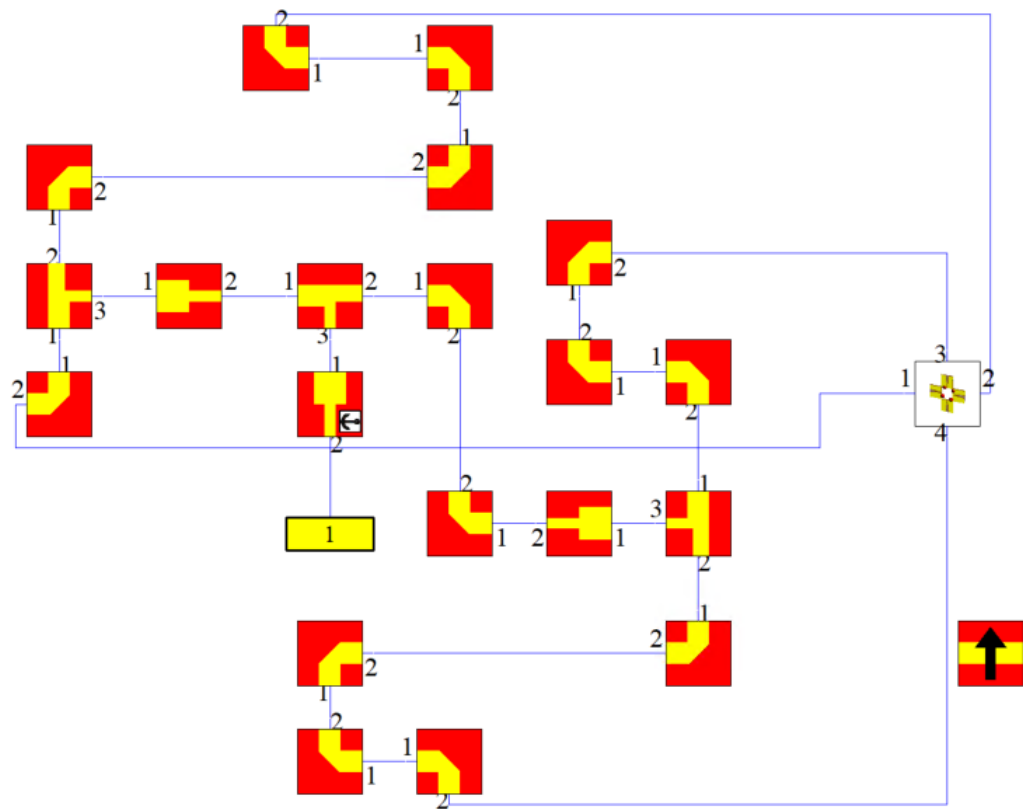


Figure 3.22: Phase Matching

Fig. 3.22 displays the matching network in the schematic windows, where port 1 was the beginning of the microstrip line. The energy was transferred through a quarter wave matching network. This allowed the characteristic impedance to drop evenly from  $50 \Omega$  to  $25 \Omega$ . The microstrip line splits with a T-junction, where the characteristic impedance was back at  $50 \Omega$ . At ports 4 and 5, there was an additional length  $\lambda/2$  added to ports 4 and 5 to create the phase difference at  $180^\circ$  to ports 2 and 3.

In ports 2 and 3, the microstrip line travelled to another quarter wave matching network to create a characteristic impedance of  $25 \Omega$ . Ports 4 and 5 travelled to another quarter wave matching network. Ports 3 and 5 had an added length  $\lambda/4$ , which changed the phase by  $90^\circ$ . In Fig. 3.23, the graph displays the phase of each transmission coefficient. The frequency was designed to be operating at 7.5 GHz. For each port:  $S_{21}$ ,  $S_{31}$ ,  $S_{41}$  and  $S_{51}$ , the phases were  $-30.5^\circ$ ,  $-121.8^\circ$ ,  $151.0^\circ$  and  $61^\circ$  respectively.

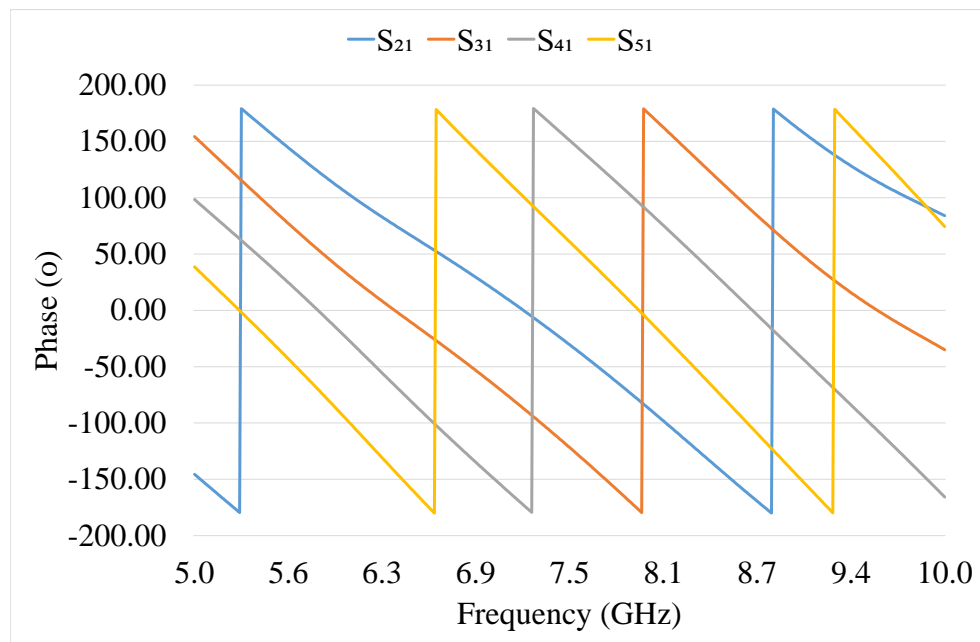


Figure 3.23: Transmission Coefficient - Phase

### 3.5.2 Arrays of Vivaldi Antennas - Design

The matching network was transferred to a separate project that included the antenna design. The matching network had adjusted to connect the ports with the new antenna design, as shown in Fig. 3.24. A discrete port of  $50 \Omega$  was connected in the centre of the design. In the fabricated antenna, a hole was drilled through the substrate to allow a SMA connector to be connected to the microstrip line.

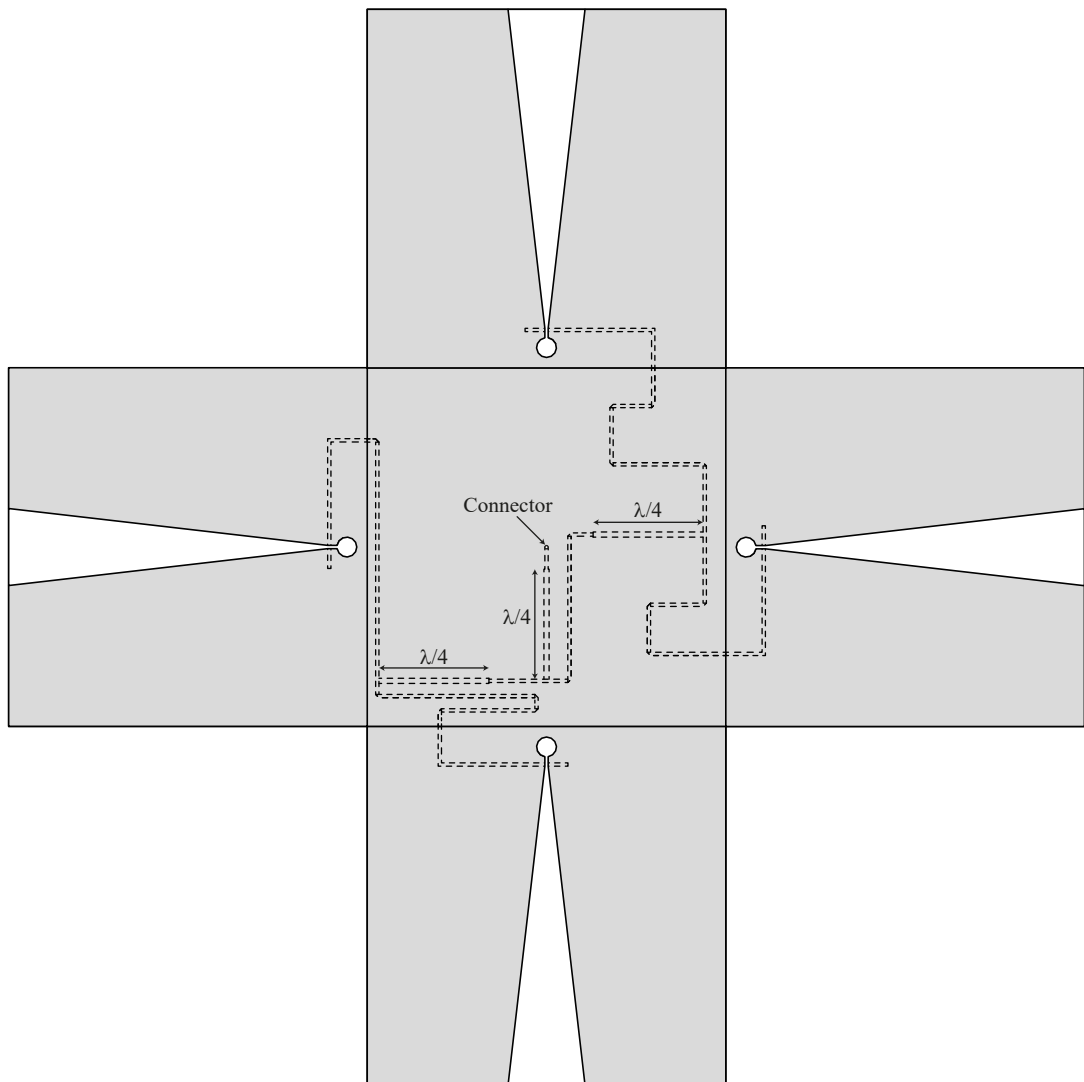


Figure 3.24: Matching Network of an array of Vivaldi Antennas

### 3.5.3 Arrays of Vivaldi Antennas - Simulated Results

In this section, the array of Vivaldi antennas was simulated in two different states, Flat and Folded. When the antenna design is in the Flat state, the antennas were designed on the XY-plane, as it transformed into a Folded state, the plane rotated to the XZ-plane. The results were obtained and exported into Microsoft Excel, where in the Flat state, the results were obtained when  $\Theta = 0^\circ$  and in the Folded state, the results were obtained when  $\Phi = 0^\circ$ .

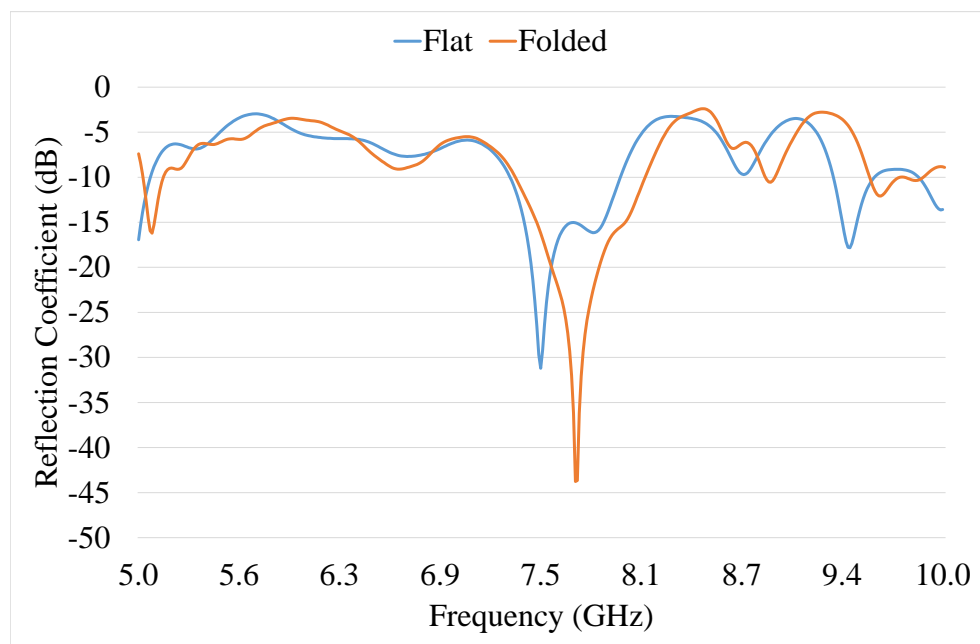


Figure 3.25: Array of Vivaldi Antennas with Kapton in Flat and Folded State - Simulated Reflection Coefficient

The array of Vivaldi antennas was simulated with a Kapton substrate, shown in Fig. 3.25. It displayed the  $S_{11}$  of both Flat and Folded states. When the antenna was at a Flat state, the resonant frequency was at 7.5 GHz with  $S_{11}$  at -30 dB, the 10 dB reflection coefficient bandwidth was between 7.2 GHz to 8 GHz. As the antenna transitioned to a Folded state, the resonant frequency shifted to 7.8 GHz with  $S_{11}$  at -44 dB, the 10 dB reflection coefficient bandwidth was between 7.2 GHz to 8.1 GHz. In Fig. 3.26a, when the antenna was in a Flat state, the absolute maximum gain was

2.5 dBi. When looking at the co-polar and cross-polar plots, they were perpendicular to each other as they were  $180^\circ$  out of phase.

As the antenna translated into a Folded state, all energy were radiated in a single direction. The radiation pattern was circular polarised, as shown in Fig. 3.26b, because each radiating element was  $90^\circ$  out of phase. As the folded state was circular polarised, the plots were shown as Right Hand Circular Polarisation (RHCP) and Left Hand Circular Polarisation (LHCP). The absolute maximum gain was 9 dBi with a HPBW of  $36^\circ$ . The antenna was designed to operate in RHCP, therefore in LHCP, there was a null at the radiating angle. The null region was at -15 dB.

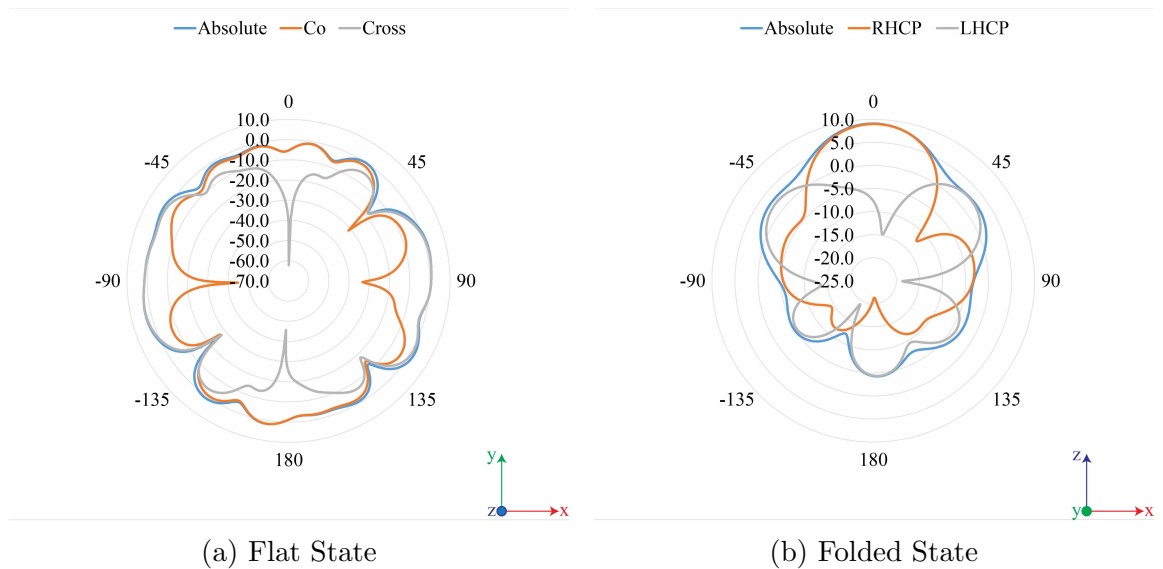


Figure 3.26: Array of Vivaldi Antennas with Kapton in Flat and Folded State - Simulated Radiation Pattern

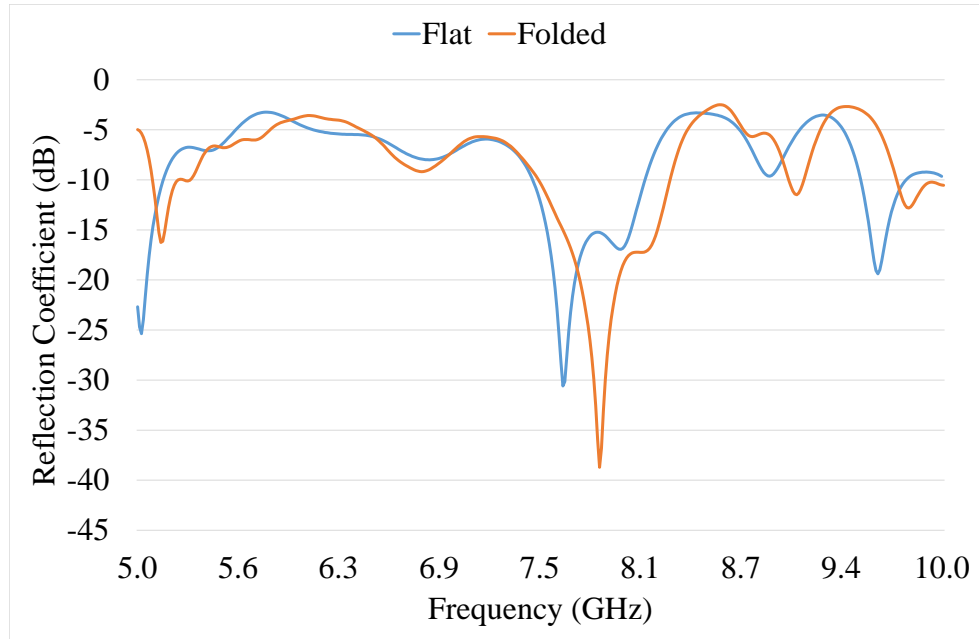


Figure 3.27: Array of Vivaldi Antennas with Mylar in Flat and Folded State - Simulated Reflection Coefficient

Similarly, in Fig. 3.27, the substrate was changed from Kapton to Mylar. When the array of Vivaldi antennas was in a Flat state, the resonant frequency was at 7.8 GHz with  $S_{11}$  at -30 dB and a 10 dB reflection coefficient bandwidth of 500 MHz. As the array of Vivaldi antennas went into the Folded state, the frequency shifted to 8 GHz with  $S_{11} = -39$  dB and a bandwidth of 800 MHz. In Fig. 3.28, the far-field plots showed the radiation pattern for both Flat and Folded states. As for the Flat state, the absolute maximum gain was at 2.3 dBi, the co-polar and cross-polar plots displayed similar results. When the antenna was in the Folded state, the maximum gain was at 8.8 dBi with a HPBW of  $34^\circ$ , the design had a RHCP, therefore at LHCP, the null region was -20 dB at the radiating angle.

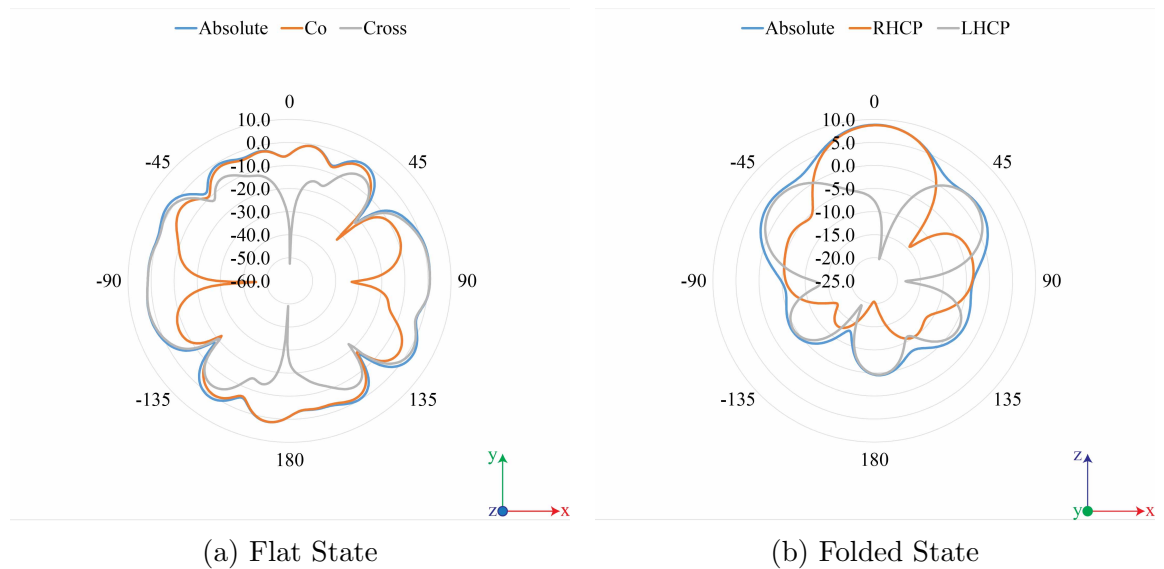


Figure 3.28: Array of Vivaldi Antennas with Mylar in Flat and Folded State - Simulated Radiation Pattern

### 3.5.4 Arrays of Vivaldi Antennas - Measured Results

The fabricating process was explained in Chapter 3.4.3 earlier. The fabricated array of Vivaldi antennas was connected with a 0.2 mm pin SMA connector in the centre of the design. The fabricated antennas were connected to the VNA at both Flat and Folded states. The fabricated antennas were transferred to the anechoic chamber for radiation pattern measurements. In the Flat state, the array of Vivaldi antennas were placed on an XY-plane, it rotated on the Z-axis to achieve the Flat state radiation pattern. In the Folded state, the array of Vivaldi antennas were pointing at the transmit antenna at an XZ-plane, it rotated in a Z-axis to achieve the Folded state radiation pattern. When the antennas were measured in the anechoic chamber, the transmit antenna was a low gain dual polarised antenna, therefore it was not able to perform circular polarised measurements for the Folded design.

When the structure was folded, a problem occurred, when the folding angle increased over  $90^\circ$ . Due to the mechanical stress on the substrate caused by the folding, the copper tracks started to break and caused discontinuity across the microstrip line, see Fig. 3.29. One solution to alleviate the issue was to use a non-sharp object to score out the folding pattern before any folding mechanism was applied. This allowed the



substrate to fold more, see Fig. 3.30. Another issue occur when folding the antenna, the fabricated antenna cannot return to the Flat state as there was a crease line along the folded corners. One solution was to use adhesive tape to flatten the fabricated antenna design.

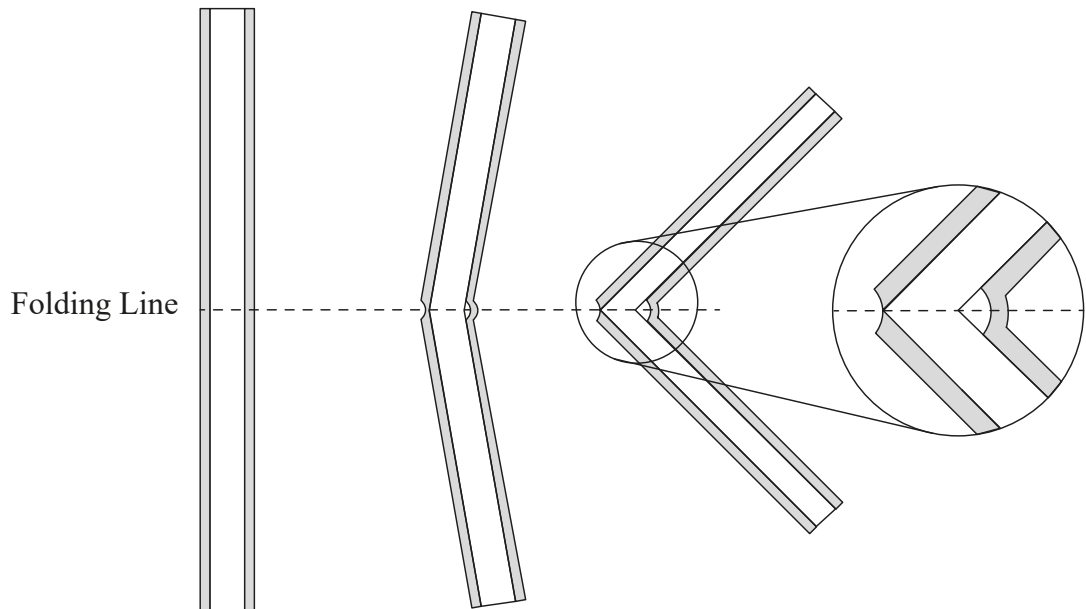


Figure 3.29: Folding at  $90^\circ$  - Crack and Discontinuity

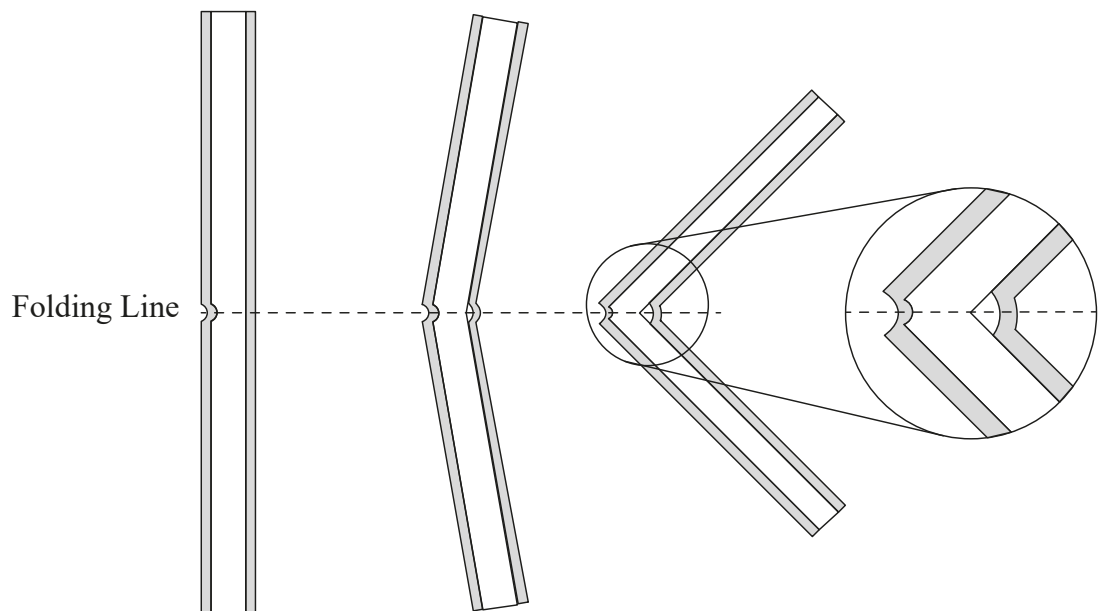


Figure 3.30: Folding at  $90^\circ$  - with crease line

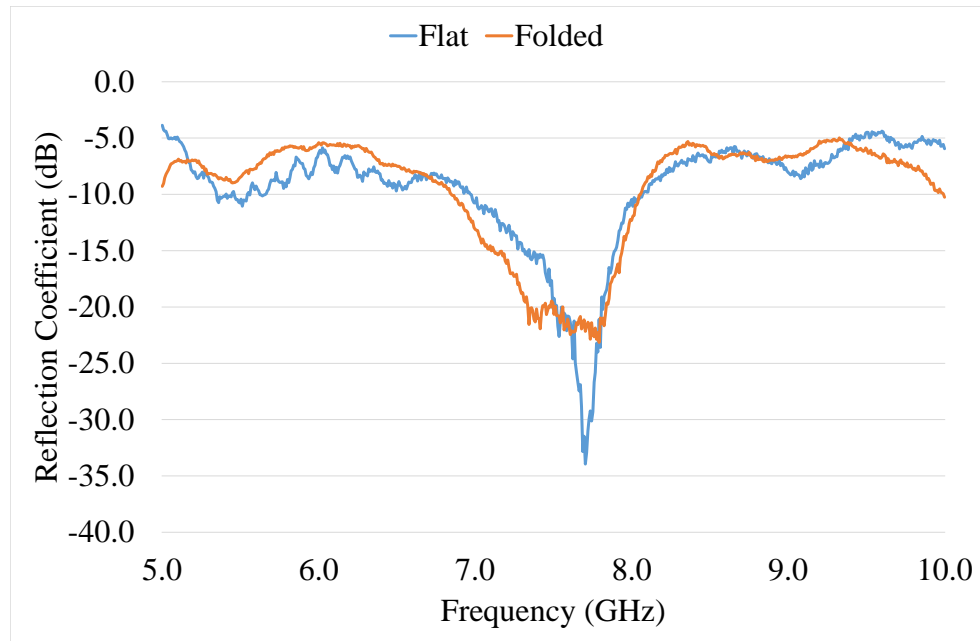


Figure 3.31: Array of Vivaldi Antennas with Kapton in Flat and Folded State - Measured Reflection Coefficient

Fig. 3.31 displays the reflection coefficient of the fabricated antenna with a Kapton substrate. When the fabricated antenna was in the Flat state, the resonant frequency was at 7.7 GHz,  $S_{11}$  at -34 dB with a 10 dB reflection coefficient bandwidth of 1 GHz. When the fabricated antenna was in the Folded state, the frequency was at 7.8 GHz,  $S_{11}$  at -23 dB with a bandwidth of 1.2 GHz.

Comparing to the simulated results, when the fabricated antenna was in either state, the resonant frequency shifted by a small amount. When the fabricated antenna was in the Flat state,  $S_{11}$  increased from -30 dB up to -34 dB. When the antenna was in the Folded state,  $S_{11}$  decreased down from -44 dB to -23 dB. Although gain was not measured, the anechoic chamber did manage to measure radiation pattern. In Fig. 3.32, the radiation pattern in the Flat state is similar to the simulated results, where the beams are radiating at all four directions. As the antenna went into the Folded state, it could be seen that the co-polar had a radiation angle at  $0^\circ$  and a HPBW of  $40^\circ$ . Although the transmit antenna was a dual linear polarised, the fabricated antenna

was circular polarised as the co-polar and cross-polar has the same radiating angle. In practice, the fabricated antenna was dual linear polarised as it was only tested with a dual linear polarised antenna.

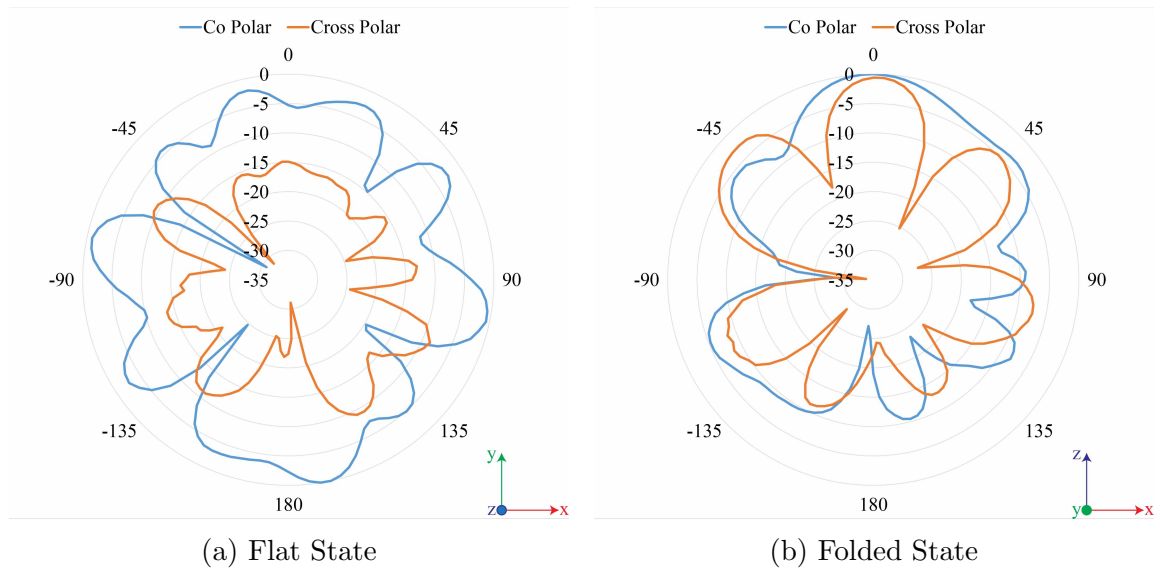


Figure 3.32: Array of Vivaldi Antennas with Kapton in Flat and Folded State - Measured Radiation Pattern

When the substrate was changed into Mylar, its reflection coefficient is shown in Fig. 3.33. When the fabricated antenna was in the Flat state, the resonant frequency was at 8 GHz and  $S_{11}$  was below -40 dB with a 10 dB reflection coefficient value between 7.5 GHz to 8.4 GHz. Comparing the measured results to the simulated results, the resonant frequency shifted by 200 MHz. The reflection coefficient value increased by -10 dB and the bandwidth remained the same as the simulated results. Fig. 3.34, it displays the co-polar and cross-polar for both Flat and Folded states. When the antenna was in a Flat state, the radiating angle was similar to the simulated result as it radiates at all four directions. As the antenna transitioned to the Folded state, the co-polar plot had a radiating angle at  $0^\circ$  with a HPBW of  $42^\circ$ . Similarly, the fabricated antenna was circular polarised but due to measurements with a dual linear polarised antenna, it was only able to test on linear polarisation.

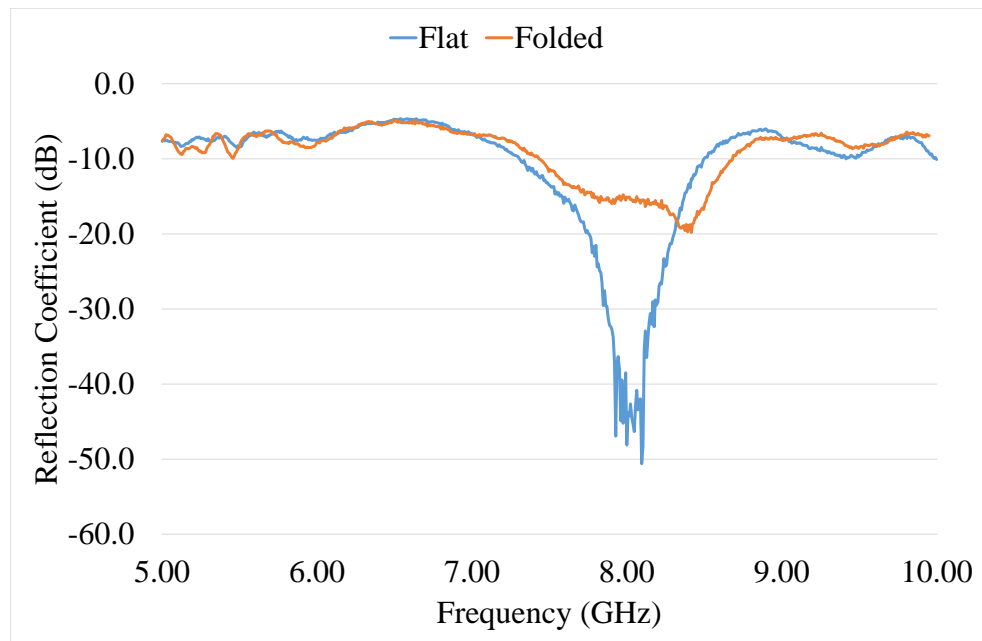


Figure 3.33: Array of Vivaldi Antennas with Mylar in Flat and Folded State - Measured Reflection Coefficient

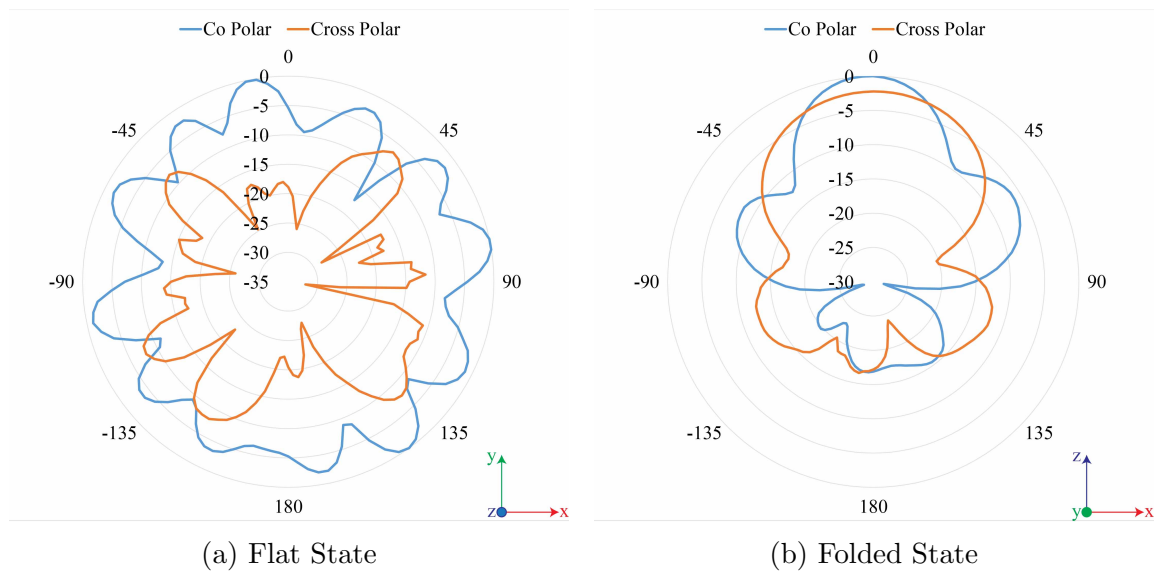


Figure 3.34: Array of Vivaldi Antennas with Mylar in Flat and Folded State - Measured Radiation Pattern

## 3.6 Summary and Conclusion

In this chapter, a study of using various flexible substrates were presented. There were two different substrates, Kapton and Mylar. Both substrates were investigated with a single Vivaldi design. When simulated on both substrates, the resonant frequencies were at 7.5 GHz and 7.8 GHz respectively, the far-field plots of both were very similar in terms of radiating angle and the HPBW. In the physical testing on each Vivaldi antenna, the results were very similar to the simulated results, they have similar resonant frequency but the  $S_{11}$  performance dropped by a small amount. This was due to the physical loss tangent value, which was different to the simulated, hence a drop in  $S_{11}$  performance occurred.

As the single Vivaldi antenna transform into an array of Vivaldi antennas, a matching network was required. The network could be created within CST Studio under the schematic window. This contained microstrip parameters such as T-Junction and  $45^\circ$  bend. The quarter wave matching network was also required within the matching network as it could change the characteristic impedance without losing power along the transmission line. The matching network had four outputs, each port contained a phase difference of  $90^\circ$ .

The matching network was created in a new project with four Vivaldi antennas. The design was rearranged with the matching network in the middle, with each Vivaldi antenna radiating at each directions in a Flat state. In the Folded state, it was able to focus all the energy at a single point direction achieving a higher gain. Again, both flexible substrates were simulated in CST Studio and measured with a VNA in the anechoic chamber. The antennas were simulated on an XY-plane, when it was in the Flat state, as it transform into the folded state, the antenna design was simulated on XZ-plane.

For both simulated results, there was a clear trend that as the array of Vivaldi antennas changed from a Flat state into a Folded state, the resonant frequencies shifted by

300 MHz. In both measured results, there was a shift in resonant frequency by 300 MHz on each substrate, with a relatively good  $S_{11}$  performance in the Flat state. However, as the antenna design went into the Folded state, the resonant frequencies remained similar but  $S_{11}$  performance dropped by a significant amount.

The far-field plots displayed an interesting results, in the simulated Flat state, the maximum gain were at 2.5 dBi using Kapton and 2.3 dBi using Mylar. The measured results were similar in terms of radiation patterns, it could be seen that they were radiating at all four directions. In the simulated Folded state, the maximum gain increased to 9 dBi using Kapton and 8.8 dBi using Mylar, it was radiating at a single direction with a circular polarisation. Although gain measurements were not available, the radiation pattern was measured with a dual linear polarised antenna. Both fabricated antennas could be seen radiating similarly at co-polar and cross-polar, suggesting that they were dual linear polarised.

Although the electrical properties for each substrates were very similar, the main focus of this chapter was the mechanical properties of each substrate. During physical measurements, a lot of antenna feeding networks broke due to the folding process. This was caused by the substrate folding at  $90^\circ$ . As the substrate was folded, the copper on the outside was stretching, as it reached the folding angle of  $90^\circ$ , the copper tracks were broken causing discontinuity. One solution to the folding mechanism was to use a non-sharp object to score the folding pattern onto the antenna design prior to folding. This would allow the substrate to bend more efficiently without the copper tracks breaking.

In conclusion, a series of simulations and measurements were performed on Vivaldi antennas using flexible substrates, Kapton and Mylar. This chapter presented a reconfigurable way of changing between: Flat and Folded state. While the antenna was Flat, it was able to radiate at all four directions, whereas in the Folded state, it was able to focus the single direction with a much higher gain.

This could be very useful in terms of applications for satellite data relaying systems.

---

When satellites are close to each other and require communication between the satellites, a standard communication path would be formed from the first satellite to the ground station then be re-transmitted to the second satellite. Whereas using a four way Vivaldi antenna, it would be able to scan and communicate in a shorter distance. When the array of Vivaldi antennas goes into the Folded state, where the energy is focused at a single direction, it would be able to relay the information to a further object such as an LEO satellite.

# Chapter 4

## Flexible and foldable Slot Antennas

### 4.1 Introduction

Origami folding technique can be incorporated in many ways. One application would be in military secure communications [42]. One of the major problems are the radios that the soldiers carry during the time of deployment, they are very robust but due to that, the radios are very heavy. Military personal might require to carry the radio for approximately 48 hour per mission [43]. An improvement could include a lightweight secure communication device. One that could be lighter and more portable, compact device that could take up less weight and space for longer missions. The frequency bands for Radio Navigation and Radio Location is between 2.5 GHz to 2.8 GHz. The requirement for the alternative antenna design would be between the wanted frequency range, it must be portable and lightweight, so soldiers could potentially carry it in their backpacks.

In this chapter, a U-shaped slot antenna was investigated with the use of the Miura Ori folding technique. One of the objectives was to model a 3-D antenna structure with the Miura Ori folding technique. This folding technique is very fascinating as it has multiple functionality. It can be used when it is completely flat or partially folded. In the fully folded state, the antenna becomes portable. Investigations were performed



to determine the performance of a single slot antenna and an array of slot antennas when the 3-Dimensional (3-D) structure is being folded. This was explained in the form of tables and graphs, which display any change in the reflection coefficient ( $S_{11}$ ) performance and the far-field plots at the resonant frequency.

## 4.2 Babinet's Theory

According to Babinet's principle [44], "When the field behind a screen with an opening is added to the field of a complementary structure, the sum is equal to the field, when there is no screen." This is used by antenna engineers to find the complementary impedance, shown in (4.1), where  $Z_s$  and  $Z_c$  are the terminal impedance and  $\eta$  is the intrinsic impedance.

$$Z_s Z_c = \frac{\eta^2}{4} \quad (4.1)$$

A large ground plane with a slot can act as the screen with an opening while a dipole can act as a complementary structure. In practice, a slot can be created in a large piece of metal waveguide or structure. The slot length is  $\lambda/2$  at the frequency desired. The most common way to excite a slot is using a microstrip line. The length towards the slot is not critical, however the stub end of the microstrip line is an important factor. Slot antennas can be optimised with the slot sizes, shapes and the stub length at the end of a microstrip line. These antennas have a linear polarisation.

## 4.3 Academic Research on Slot Antennas

S. Chen have proposed a flexible polymer with 5.8GHz microstrip fed slot antenna [45]. The flexible material was called Poly (3,4-ethylenedioxythiophene) (PEDOT), it had a permittivity ( $\epsilon_r$ ) of 1.06, with a thickness of 1.6 mm. A slot was placed on one

side of the substrate and a microstrip on the other side. The resonant frequency was determined by the slot length with half of the operational wavelength. The proposed design was able to bend at a radius of  $R$  without changing the operating frequency. The radiation pattern of the PEDOT antenna can be shown in [45, Fig. 4.1]

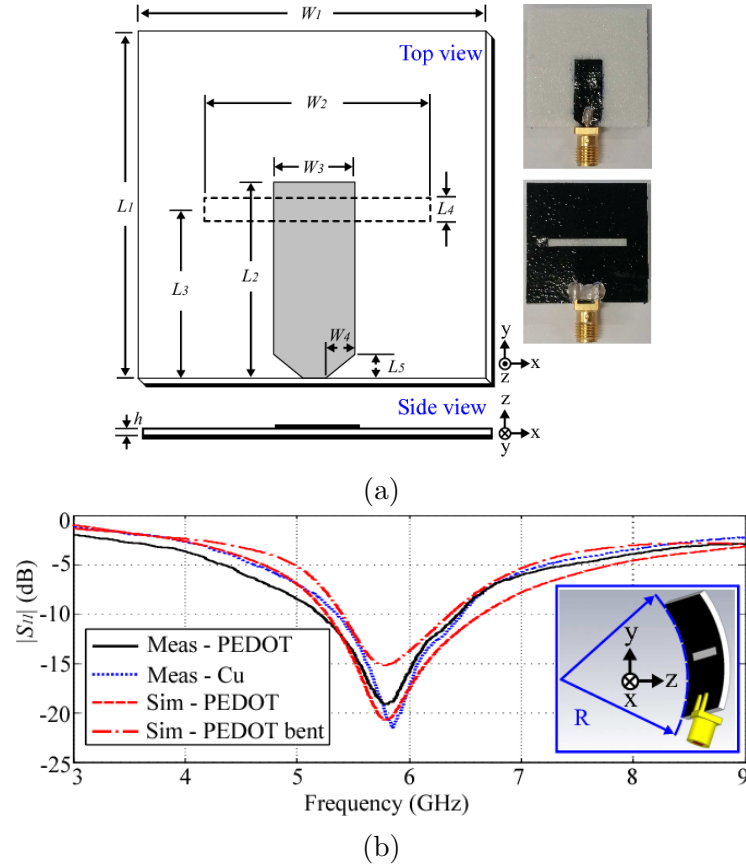


Figure 4.1: A 5.8 GHz Flexible Microstrip Fed Slot Antenna: (a) The antenna configuration and a PEDOT realisation; (b) Simulated and measured reflection coefficients [45]

S. Zahran [46] had introduced a flexible wide band CPW fed slot antenna. The proposed antenna was designed with Rogers ULTRALAM 3850 with a thickness of 0.1 mm with copper on both sides. The permittivity ( $\epsilon_r$ ) of the substrate was 3.14 with a loss tangent ( $\tan\delta$ ) of 0.0025. The proposed design was a circular monopole radiator with extra slots around the antenna, see [46, Fig. 4.2a]. With further optimisation, it was able to turn into the proposed design with a wide bandwidth. It was first simulated on a flat surface then transferred onto a curved surface. In [46, Fig. 4.2b], the 10 dB reflection coefficient bandwidth was from 4 GHz to 11 GHz, the far fields were represented below with the highest of 5 dB total.

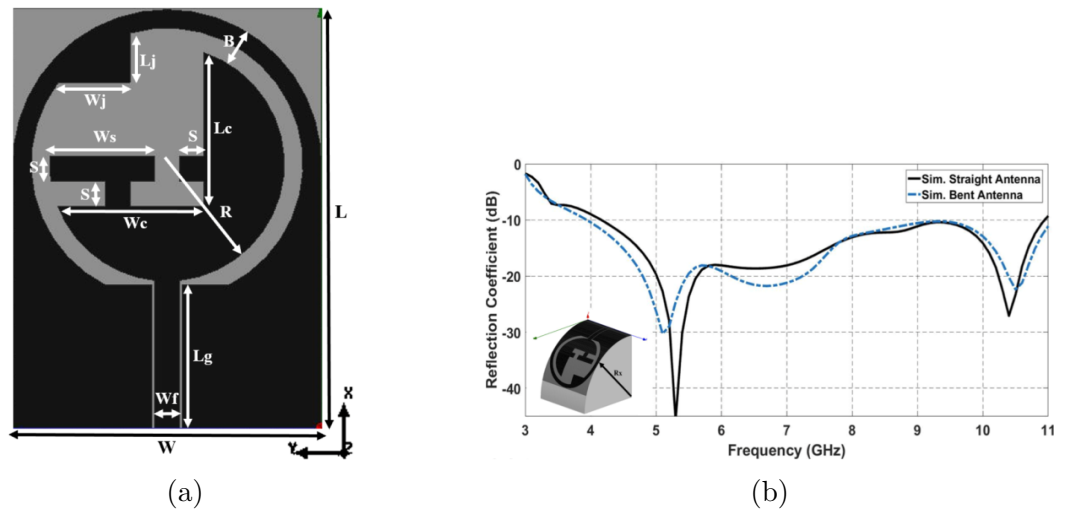


Figure 4.2: A Flexible Circular Polarized Wide Band Slot Antenna for Indoor IoT Applications: (a) Flexible Antenna on a 2D Layout; (b) Simulated reflection coefficient for different state [46]

An Ultra-Wide Band (UWB) circularly polarised antenna on a flexible substrate was presented by K. Fujita [47]. There were two slots on the antenna to create a circularly polarised wave, to optimise the bandwidth, which varied the length and width of the antenna slots. The slot antenna has a substrate thickness of 0.254 mm with a permittivity ( $\epsilon_r$ ) of 3.5. In [47, Fig. 4.3b], when the proposed antenna was flat, the operating frequency was between 7.11 GHz to 12.71 GHz. In [47, Fig. 4.3c], the slotted antenna is bend with an angle of  $A$ .

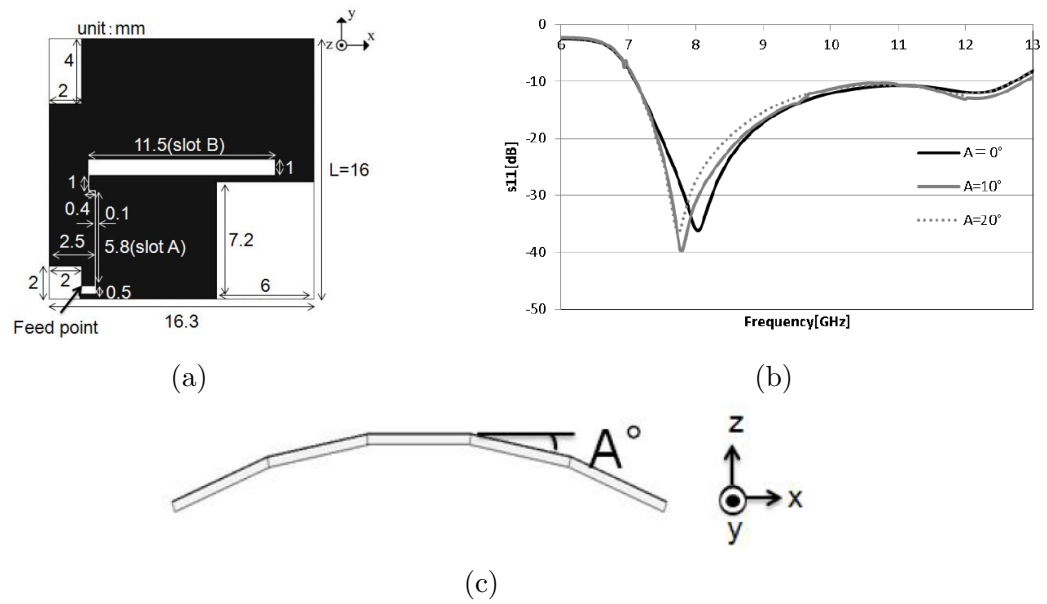
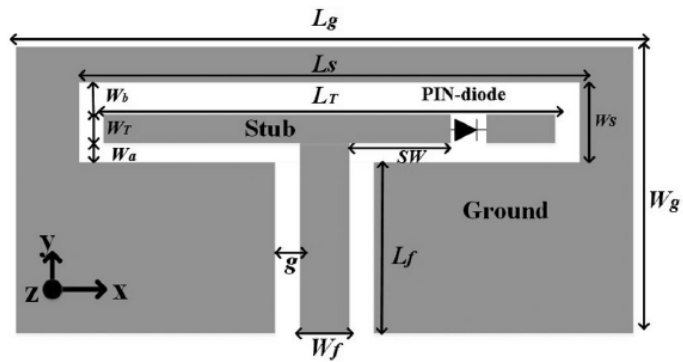
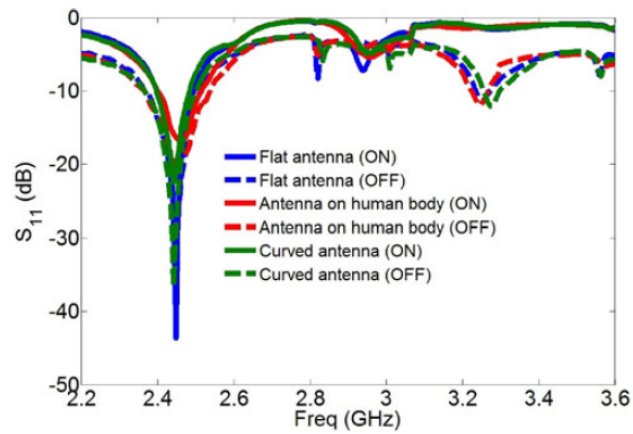


Figure 4.3: UWB Circularly polarised Planar antenna on flexible Substrate: (a) Layout of the circularly polarised antenna; (b) Reflection Coefficient of the antenna while under stress; (c) Cross section of antenna under stress [47]

In this letter [48], S. Saeed presented a wearable and flexible folded slot antenna. The proposed design consisted of a folded slot antenna. Where it was connected with a diode, there is a stub. This allowed the diode to switch on and off, as well as, altering the radiation characteristics. In [48, Fig. 4.4b], three configuration were simulated, Flat state, Curved state and on a human body. The proposed antenna was operating at 2.4 GHz, as shown in [48, Fig. 4.4b]. The gain at the resonant frequency for both states are 2.7 dBi and 2.6 dBi respectively.



(a)



(b)



(c)

Figure 4.4: Wearable Flexible Reconfigurable Antenna Integrated With Artificial Magnetic Conductor: (a) Dimensions of Folded Slot Antenna; (b) Measured reflection coefficients of antenna configurations; (c) Fabricated antenna on curve structure and on human body [48]

## 4.4 Slot Antennas

A U-shaped slot antenna was used for this chapter, the design of the slot antenna can be seen in Fig. 4.5. The slot antenna was simulated through Computer Simulation Technology (CST) studi, it was tested through a Vector Network Analyser (VNA) and in the anechoic chamber, Chapter 4.4.2.

The slot antenna was using a flexible substrate, Kapton HN, it had a thickness of 0.125 mm. Due to the thickness of the substrate having been so thin, it was able to fold in any desired 3-D form. The substrate has copper coating on both sides. The fabricating process is explained in Chapter 3.4.3. Due to the shortage of testing equipment in the anechoic chamber. All the far-field results below could only obtain the radiation pattern for co-polarisation and cross-polarisation. As for the gain measurements, the University of Kent does not have the standard high gain horn to obtain gain measurements.

### 4.4.1 Single Slot Antenna - Design

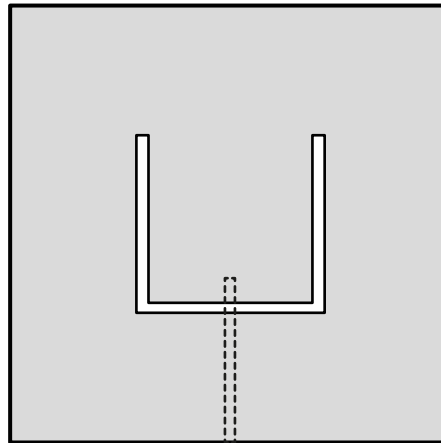


Figure 4.5: Single Slot Antenna Design

This slot antenna design had a U-shaped slot coupled with a microstrip line, see Fig. 4.5. It was fed from the middle of the slot creating an inverted dipole. The slot is designed to operate at 2.4 GHz when the electrical length was  $\lambda/2$ . The frequency was chosen

to operate at 2.4 GHz due to the size of the structure. This had been beneficial, when applying it to the Miura Ori folding mechanism.

The dimensions of the geometry with a single slot antenna is seen in Table 4.1 and Fig. 4.7: the width ( $a$ ) and length ( $b$ ) of individual parallelogram, the height of the substrate ( $T$ ), slot length in the x direction ( $x$ ), slot length in the y direction ( $y$ ), microstrip width ( $ms$ ), microstrip length ( $ml$ ), the inner angle of the Miura Ori ( $\alpha$ ) and the folding angle ( $\beta$ ).

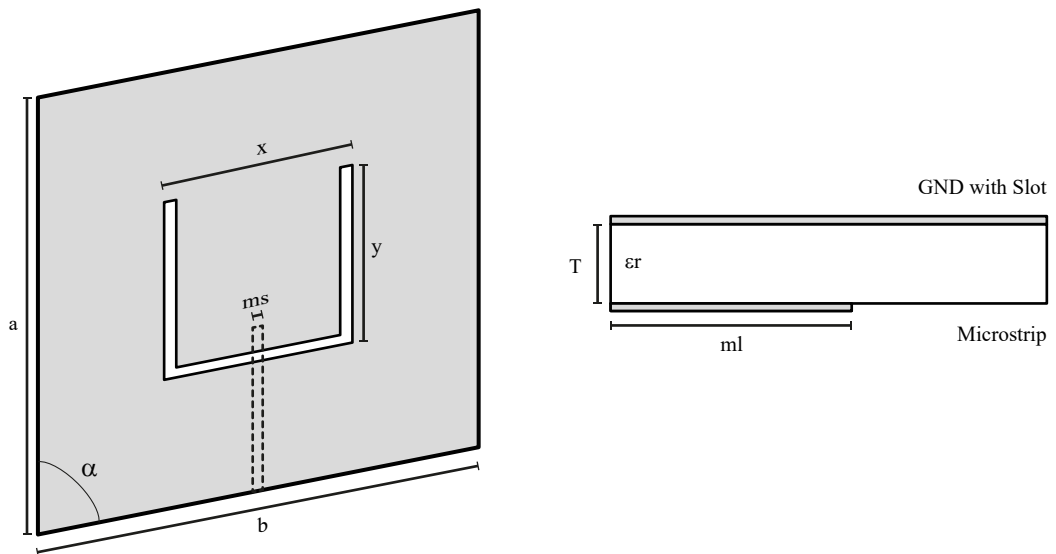


Figure 4.6: Single Slot Design- Dimensions Chart

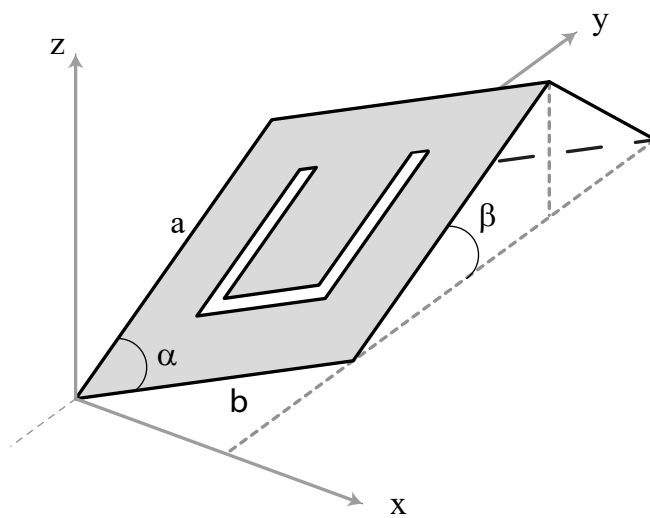


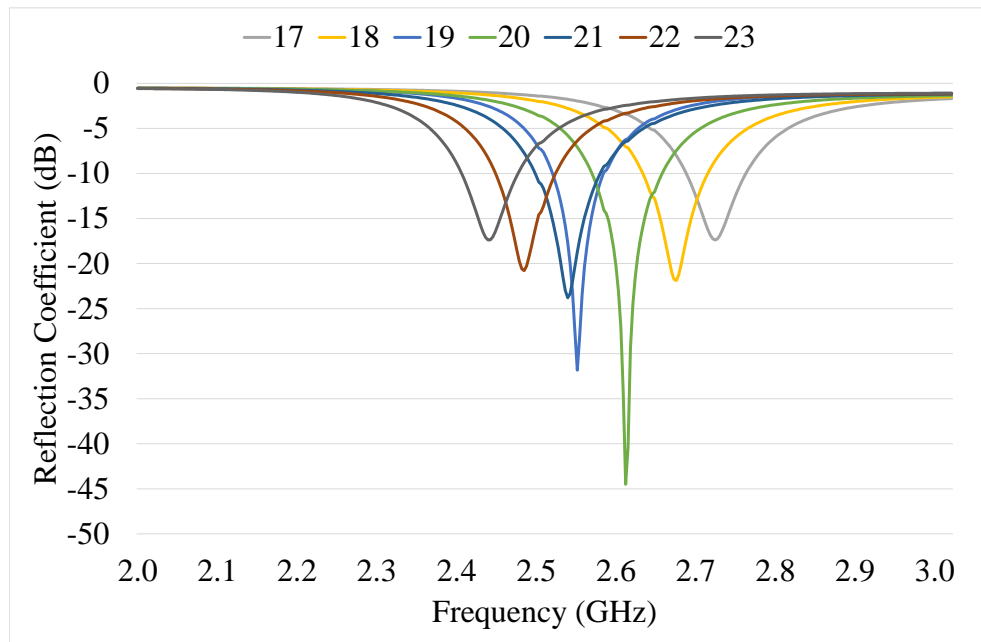
Figure 4.7: Single Slot Antenna Design - Dimensions with  $\beta$

Prior to modelling the slot antenna design with the Miura Ori folding technique, it was important to investigate the parameters that were required for the slot antenna to operate. These are the requirements for optimisation: length of the slot in X-axis ( $x$ ), length of the slot in Y-axis ( $y$ ) and the total length of the microstrip including the stub length ( $ml$ ). A U-bend slot was modelled on a 2-D planar view. The antenna design was created in CST studio. A discrete port at  $50 \Omega$  was added into the beginning of the microstrip line, as it was connected to a  $50 \Omega$  connector during physical measurements.

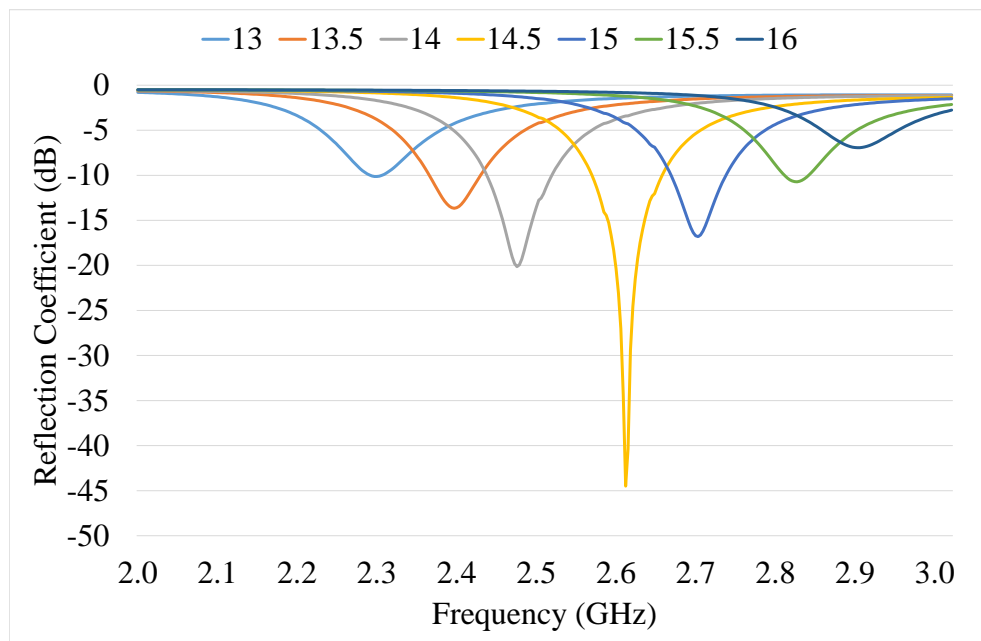
A series of simulations were performed on the length of the slot in both axis, seen in Fig. 4.8. The length of the slot ( $x$ ) varied between 17 mm to 23 mm, in Fig. 4.8a. The reflection coefficient of all lengths are below -15 dB with a bandwidth of 80 MHz. With the most significant  $S_{11}$  at -44 dB, when  $x = 20$  mm. As the length ( $y$ ) varied between 13 mm to 16 mm, similar trend occurred. However, only when  $y = 14$  mm to 15 mm,  $S_{11}$  is below -15 dB, with the best performance when  $y = 14.5$  mm, see Fig. 4.8b. As explained earlier, the slot length was equal to  $\lambda/2$  where  $\lambda$  is the wavelength. Therefore, as the length increased, the resonant frequency decreased.

The length of the microstrip ( $ml$ ) was set between 15.1 mm and 15.5 mm, as shown in Fig. 4.9. As the length ( $ml$ ) increased, there was a clear trend, where  $S_{11}$  improved greatly starting from -16 dB when  $ml = 15.1$  mm to -44 dB when  $ml = 15.2$  mm, however  $S_{11}$  dropped when  $ml \geq 15.3$  mm. As the length ( $ml$ ) increases, the resonant frequency increased.





(a) x sweep



(b) y sweep

Figure 4.8: Single Slot Antenna Design - Sweep on the length of the slot on both x and y

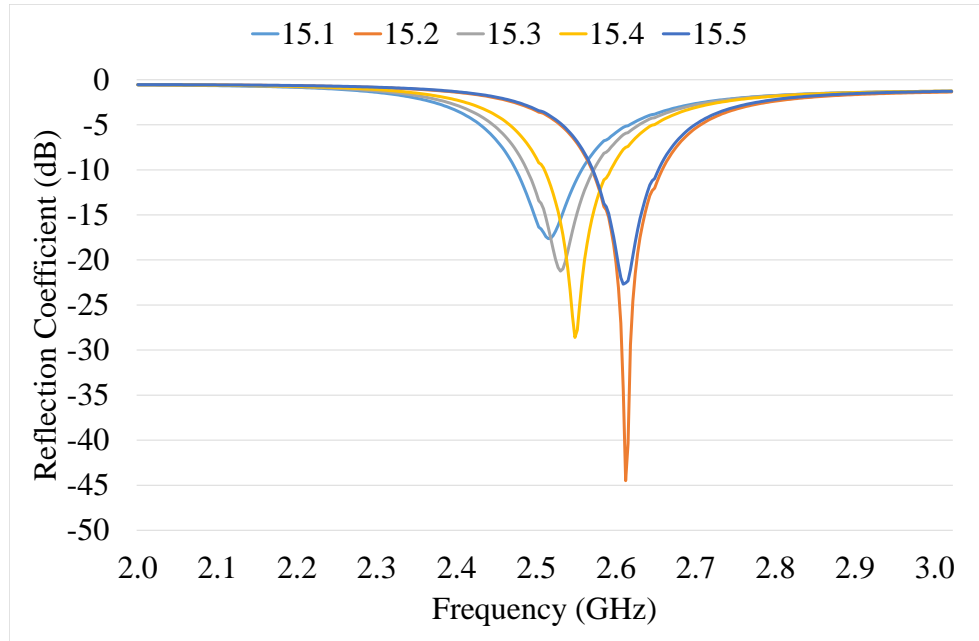


Figure 4.9: Single Slot Antenna Design - MI Sweep

A list of parameters were simulated above. The values of each parameters were shown in Table 4.1 below. Using these values, the antenna design could be modelled using the Miura Ori folding technique, shown in Section 2.2.3.

Table 4.1: Table of Parameters used with Slot Antenna

Parameters		Values ( <i>mm</i> )
Length	( <i>a</i> )	40
Width	( <i>b</i> )	40
Substrate Height	( <i>T</i> )	0.125
Slot Length in x direction	( <i>x</i> )	20
Slot Length in y direction	( <i>y</i> )	14.5
Microstrip Width	( <i>ms</i> )	0.3
Microstrip Length	( <i>ml</i> )	15.2
Inner Angle	( $\alpha$ )	Parameterise
Folding Angle	( $\beta$ )	Parameterise

(2.1) - (2.4) in Section 2.2.3 provided the method to model in CST Studio. The equations required four inputs: length of the rectangle (*a*), width of the rectangle (*b*), the inner angle ( $\alpha$ ) and the folding angle ( $\beta$ ). Each of these inputs were calculated in CST Studio to provide a set of outputs: height of the rectangle (*H*), length of the

rectangle ( $L$ ), width of the rectangle ( $S$ ) and extended length ( $V$ ). These were the necessary values to create a 3-D rectangle geometry in CST Studio. In Fig. 4.13a, (2.1) - (2.4) in Section 2.2.3 were added in the parameter list including all the input variables from Table 4.1. By utilising the 3-D polygon tool under the Curves section, the four output variables were placed in the 3-D polygon to create coordinate points, where they were connected to create a specific rectangle, shown in Fig. 4.13c.

All the 3-D polygons were created as curves. It was required to create a structure with a thickness that allows each solid to have their material properties. These curves were translated in the Z-direction and lofted between the two separate curves to create a solid object. The solid objects were assigned to a specific material, seen in Fig. 4.13e. The solid object was a substrate, therefore Kapton HN is assigned to the design.

The same technique, could be applied to all the curves including the microstrip and ground tracks. The material of the microstrip and ground tracks was Copper from the library given in CST Studio. When all solid objects were created, a discrete port of  $50 \Omega$ , at the start of the microstrip line, was defined from the Simulation tab.

a	=40	40	Length	Hs	= y * Height	4.88394928808524
b	=40	40	Width	Ss	= x * Side	19.6569334960043
beta	=20	20	folding angle	Ls	= y * Length	13.6527301061514
alpha	=10	10	Inner angle of paral...	Vs	= x * Ext	3.6884909561584
ang_theta	=beta * (pi / 180)	0.349065850398866	Radian of Theta	xs	= 1	1
ang_gamma	=(90 - alpha) * (pi / 180)	1.39626340159546	Radian of Gamma	ys	= y - xs	13.5
H	= a * Height	13.472963553386	Miura Height	zs	= x - 2 * xs	18
S	= b * Side	39.3138669920087	Miura Width	Ss1	= xs * Side	0.982846674800217
L	= a * Length	37.6627037411072	Miura Length	Ss2	= zs * Side	17.6912401464039
V	= b * Ext	7.3769819123168	Miura Extend	Ls1	= ys * Length	12.7111625126237
m	= 1	1	X Multiples	Vs1	= xs * Ext	0.18442454780792
n	= 1	1	Y Multiples	Hs1	= ys * Height	4.54712519925178
T	= 0.125	0.125	Thiickness Substrate	ms	= 0.3	0.3
Height	=sin(ang_theta) * sin...	0.336824088833465	(DO NOT TOUCH) ...	ml	= 15.2	15.2
Side	=sqr( (cos(ang_theta...	0.982846674800217	(DO NOT TOUCH) ...	Hm	= ml * Height	5.11972615026867
Length	=(sqr( 1 - ((sin(ang_th...	0.94156759352768	(DO NOT TOUCH) ...	Sm	= ms * Side	0.294854002440065
Ext	= ( 1 / (sqr( 1 + ((cos...	0.18442454780792	(DO NOT TOUCH) ...	Lm	= ml * Length	14.3118274216207
x	=20	20	Slot Width	Vm	= ms * Ext	0.055327364342376
y	=14.5	14.5	Slot Length	Tm	= 0.009	0.009

Figure 4.10: Slot Antenna Parameter List

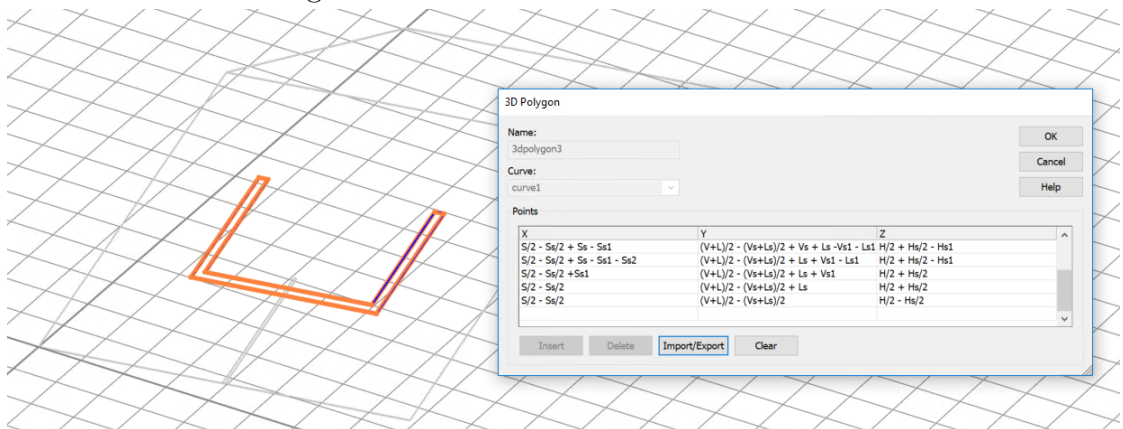


Figure 4.11: Drawing 3-D Polygon

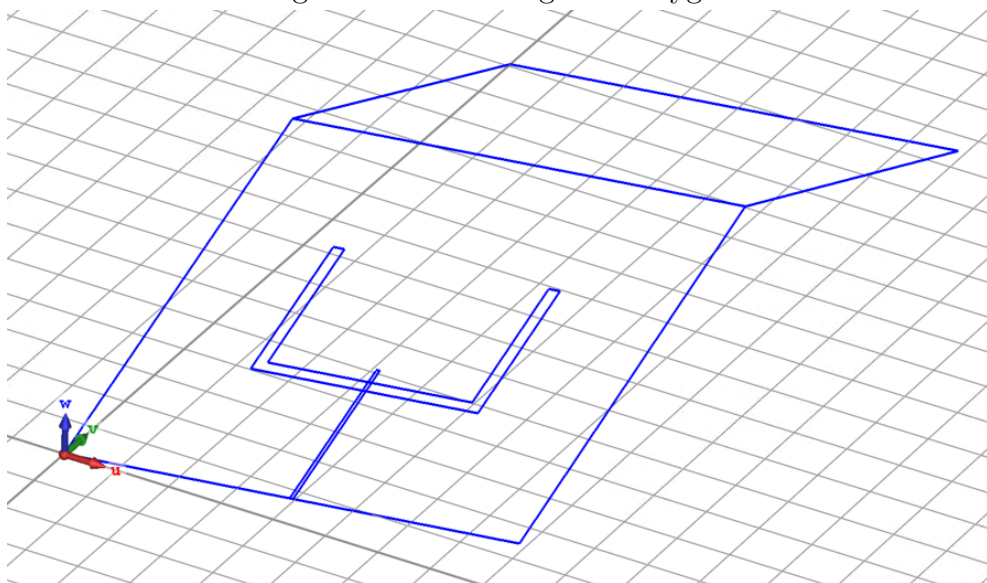


Figure 4.12: Slot Antenna Design in 3-D Geometry

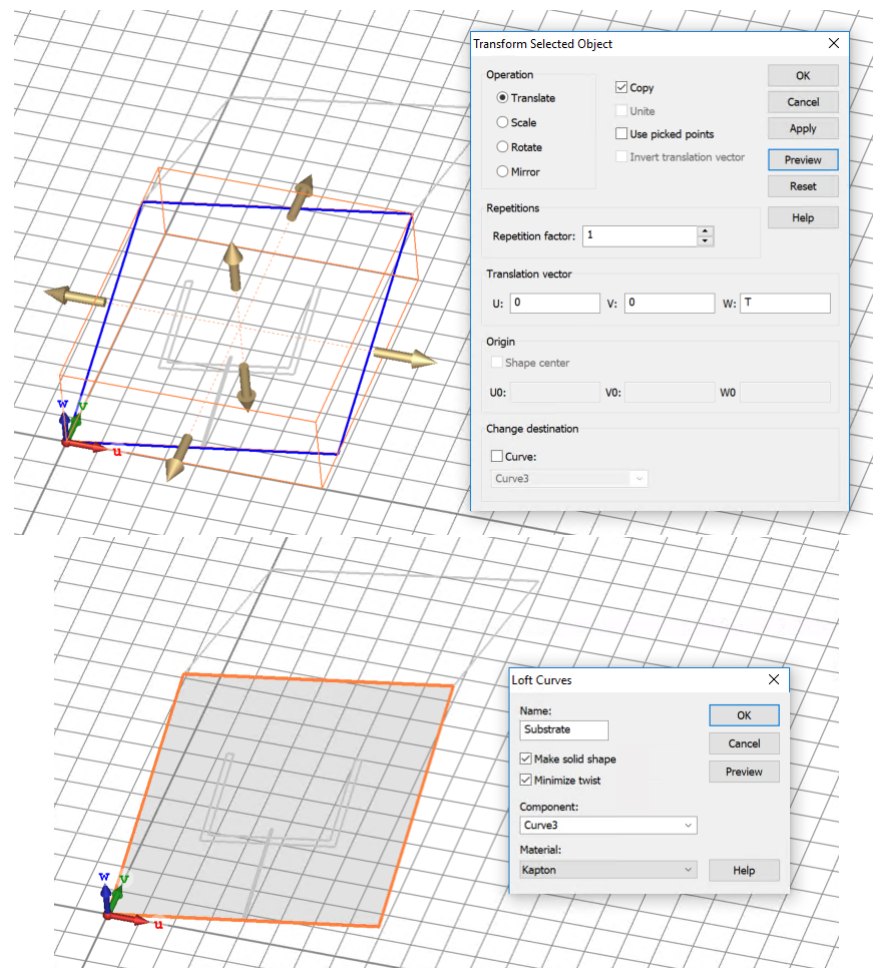
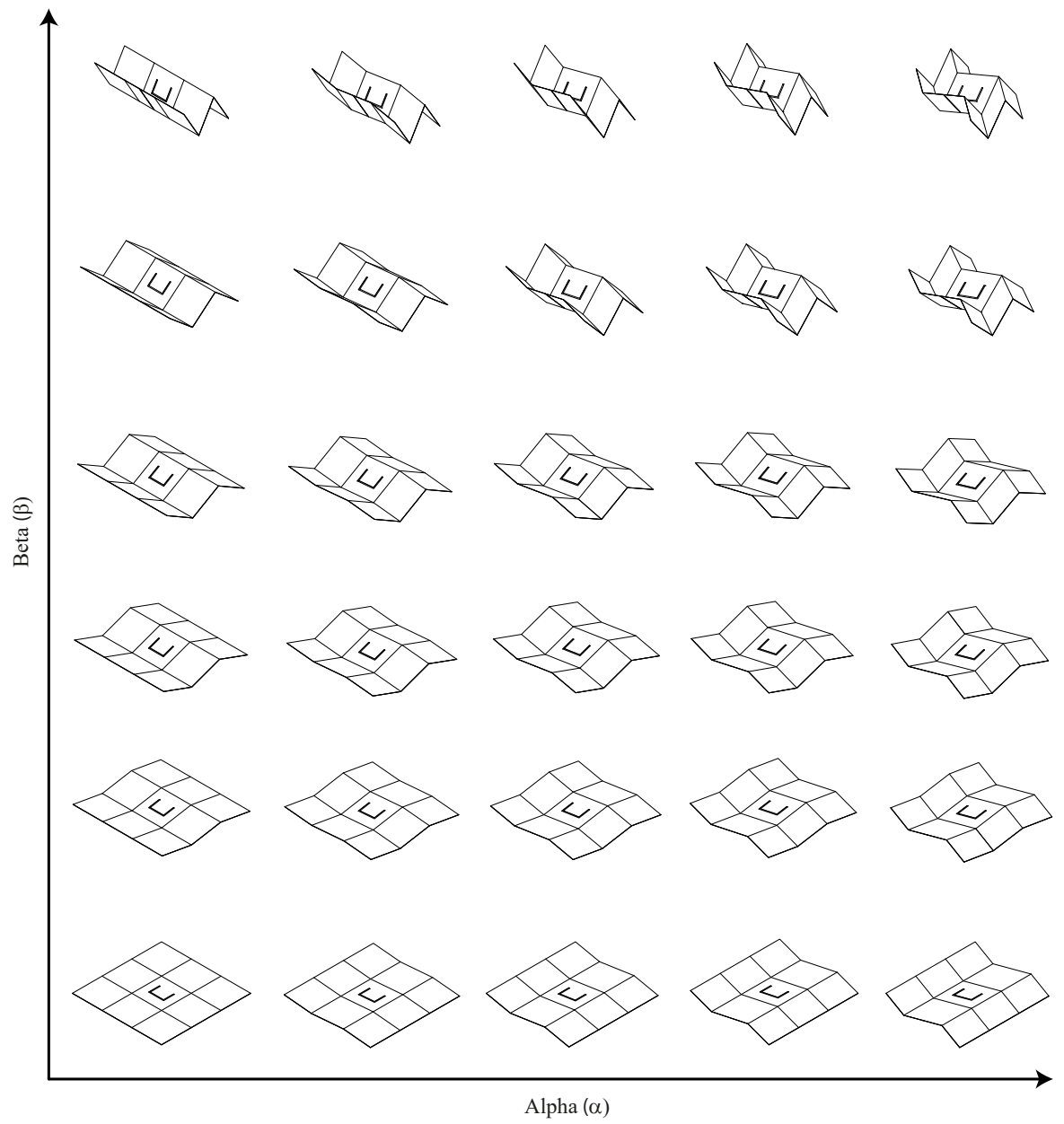


Figure 4.13: Translate and Loft Curve

The inner angle ( $\alpha$ ) and the folding angle ( $\beta$ ) were the main focus on this section so the values were investigated thoroughly. The inner angle ranged from  $0^\circ$ ,  $5^\circ$ ,  $10^\circ$ ,  $15^\circ$  and  $20^\circ$  while the folding angle ranged from  $0^\circ$ ,  $10^\circ$ ,  $20^\circ$ ,  $30^\circ$ ,  $40^\circ$  and  $50^\circ$ . Varying those two angles, allowed the antenna to determine, whether there would be a change in  $S_{11}$ , as well as, the change in radiation pattern, while it was being folded. Fig. 4.14 displayed a list of possible configurations of the antenna with the change in the inner angle ( $\alpha$ ) on the X-axis and the folding angle ( $\beta$ ) on the Y-axis. Each parameter was simulated and measured with a VNA in an anechoic chamber.

Figure 4.14: Change in  $\alpha$  and  $\beta$

### 4.4.2 Single Slot Antenna - Simulated and Measured Results

In this section, all simulations were performed with CST Studio and the measured results were tested with the VNA from Rohde and Schwarz in the anechoic chamber. Both results were collected in Comma-Separated Values (CSV) format, this enabled to export all results to Microsoft Excel. The simulated and measured results included the  $S_{11}$  values and the far-field plots at the resonant frequency. The list of possible configurations were given in Fig. 4.14.

In the simulated results, the antenna was designed on a XY-plane, therefore, the far-field plots were saved in the XZ-axis, displaying the co-polar and cross-polar plots. The co-polar plot was when  $\text{Phi} = 0^\circ$ , where the antenna was intended to radiate. Whereas, the cross-polar plot was when  $\text{Phi} = 90^\circ$ , where it determined the power transmitted in dB perpendicular to the desired direction.

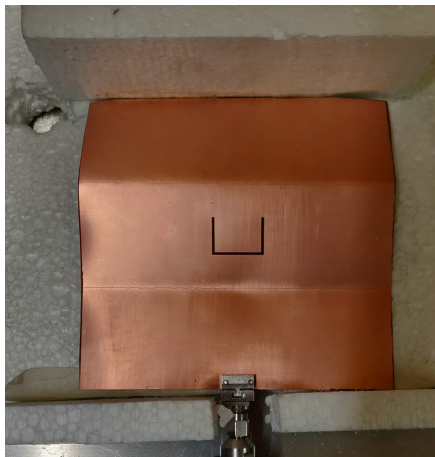
As for the measured results, the fabricated antennas required a suitable adapter from the antenna to the VNA. The connector used was the Low Profile SubMiniature version A (SMA) female End Launch Connectors from Southwest Microwave. The diameter of the pin was 0.254 mm, this allowed the connector to fit onto the microstrip line. If the pin was wider than the microstrip width, then there would be loss in the transmission line.

All fabricated antennas were folded using the Miura Ori folding technique before measurement. The pattern was creased onto the fabricated antenna using a non-sharp object, explained in Section 3.5.4. This would allow it to bend according to the mountain and valley fold, and create the Miura Ori folding design. The fabricated antenna would have to maintain the folding angle during measurements. Hence they were placed onto a polystyrene foam board with marked lines. The marked line indicated the width and length of the antenna structures when it was folded at a certain angle.

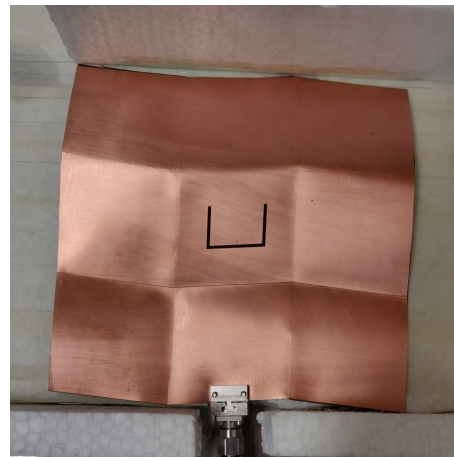
Fig. 4.16 displays the simulated  $S_{11}$  plots and Fig. 4.17 represents the simulated co-polar

and cross-polar plots. In Fig. 4.15, the fabricated antennas with 5 different inner angles are shown. The measured  $S_{11}$  plots were shown in Fig. 4.18. The anechoic chamber could only perform radiation pattern measurements. A slot antenna could radiate at  $0^\circ$  and  $180^\circ$ , however in the anechoic chamber, only one side,  $0^\circ$ , was able to perform measurements where the fabricated antennas were facing towards the transmitter. The antennas were on a XZ-plane pointing towards Y-axis. The radiation patterns were measured on the XY-axis as the fabricated antennas were rotated on the Z-axis. In Fig. 4.19, the co-polar and cross-polar plots were normalised to 0 dBi.

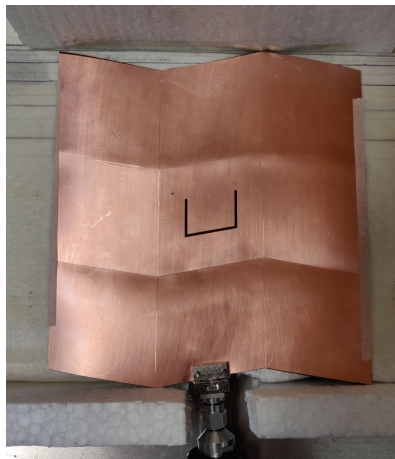




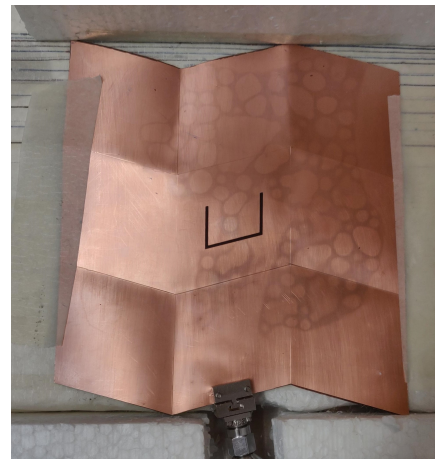
(a) Alpha - 0



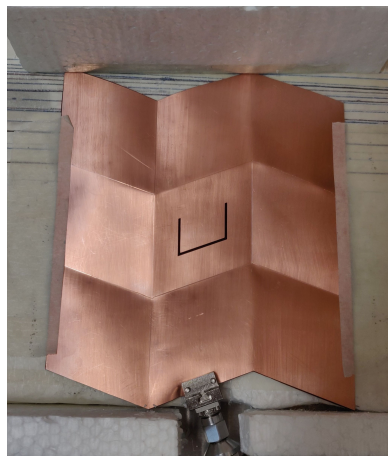
(b) Alpha - 5



(c) Alpha - 10



(d) Alpha - 15



(e) Alpha - 20

Figure 4.15: Fabricated Single Slot Antenna

Table 4.2 highlights the resonant frequency at all configurations with the use of inner angles ( $\alpha$ ) and folding angles ( $\beta$ ). The slot antenna was designed to operate at 2.5 GHz. When  $\alpha = 0^\circ$ , it could be seen that the resonant frequency had decreased from 2.60 GHz when  $\beta = 0^\circ$ , to 2.47 GHz when  $\beta = 50^\circ$ . However, while the resonant frequency decreased as the folding angle increased. The resonant frequencies raised slightly as the inner angle increased. The resonant frequency varied with the inner angles from 2.60 GHz when  $\alpha = 0^\circ$ , to 2.61 GHz when  $\alpha = 20^\circ$ .

The measured resonant frequency was displayed on Table 4.3. On average, the resonant frequency across all configurations was 2.65 GHz. When  $\alpha = 0^\circ$ , it could be seen that the resonant frequency had increased slightly from 2.63 GHz when  $\beta = 0^\circ$ , to 2.65 GHz when  $\beta = 50^\circ$ . Likewise, when varying the inner angles, the resonant frequency steadily increased from 2.63 GHz when  $\alpha = 0^\circ$ , to 2.66 GHz when  $\alpha = 20^\circ$ .

The resonant frequency had increased by 100 MHz when comparing measured to the simulated results. The span from the lowest frequency to the highest frequency was similar. This was due to the permittivity given in the simulations, which was different to the measured results. Overall, there was a clear trend in the simulated results where the resonant frequency decreased on average by 100 MHz when varying the folding angle ( $\beta$ ). However, there was a 20 MHz increment to the resonant frequency for the measured results.

Table 4.2: Single Slot Antenna - Simulated Resonant Frequency (GHz)

		Inner Angle ( $\alpha$ )				
		$0^\circ$	$5^\circ$	$10^\circ$	$15^\circ$	$20^\circ$
Folding Angle ( $\beta$ )	$0^\circ$	2.60	2.60	2.59	2.57	2.61
	$10^\circ$	2.57	2.57	2.60	2.60	2.60
	$20^\circ$	2.57	2.63	2.61	2.58	2.59
	$30^\circ$	2.57	2.54	2.54	2.56	2.60
	$40^\circ$	2.55	2.55	2.55	2.58	2.57
	$50^\circ$	2.47	2.50	2.49	2.59	2.51

Table 4.3: Single Slot Antenna - Measured Resonant Frequency (GHz)

		Inner Angle ( $\alpha$ )				
		$0^\circ$	$5^\circ$	$10^\circ$	$15^\circ$	$20^\circ$
Folding Angle ( $\beta$ )	$0^\circ$	2.63	2.63	2.67	2.64	2.66
	$10^\circ$	2.63	2.63	2.67	2.64	2.66
	$20^\circ$	2.63	2.63	2.67	2.64	2.67
	$30^\circ$	2.64	2.63	2.68	2.64	2.67
	$40^\circ$	2.64	2.64	2.68	2.65	2.67
	$50^\circ$	2.65	2.65	2.68	2.64	2.68

Table 4.4 compares  $S_{11}$  in dB at the resonant frequency across the inner angle ( $\alpha$ ) and the folding angle ( $\beta$ ). It could be seen that  $S_{11}$  dropped significantly, as the folding angle ( $\beta$ ) increased. When  $\alpha = 0^\circ$ ,  $S_{11}$  dropped from -44.53 dB when  $\beta = 0^\circ$ , to -11.09 dB when  $\beta = 50^\circ$ .  $S_{11}$  also decreased steadily when varying the inner angle ( $\alpha$ ). When  $\beta = 0^\circ$ ,  $S_{11}$  decreased from -44.53 dB when  $\alpha = 0^\circ$ , to -38.11 dB when  $\alpha = 20^\circ$ . Fig. 4.16 displays the 10 dB reflection coefficient bandwidth. On average, the 10 dB reflection coefficient bandwidth was 70 MHz wide.

In Table 4.5,  $S_{11}$  was compared at the resonant frequency.  $S_{11}$  dropped by a small amount as the folding angle ( $\beta$ ) increased. When  $\alpha = 5^\circ$ ,  $S_{11}$  dropped from -45.21 dB when  $\beta = 0^\circ$ , to -29.58 dB when  $\beta = 50^\circ$ .  $S_{11}$  fluctuated when varying the inner angle ( $\alpha$ ). When  $\beta = 30^\circ$ , on average,  $S_{11}$  was around -36.09 dB. Fig. 4.18, displays the 10 dB reflection coefficient bandwidth. In general, the reflection coefficient bandwidth was at 100 MHz across all configurations.

The measured  $S_{11}$  was significantly better than the simulated. When  $\beta = 50^\circ$ ,  $S_{11}$  went up, on average from -11.19 dB in the simulated, to -35.06 dB in the measured results. The 10 dB reflection coefficient bandwidth increased by a margin of 30 MHz. The ideal reflection coefficient value was below 15 dB or 20 dB, as 97% or 99% of the power would transfer to the antenna with a minimal loss reflected back to the input. A low  $S_{11}$  value was occurred to the mismatch in creating the solid objects using the loft function. The solid objects were not consistent compared with the fabricated antennas. Therefore as the structure was folded, it added a small stub length to the end of the microstrip line. a decrease in performance occurred, which caused the antenna not to be optimised. Overall, both simulated and measured  $S_{11}$  had decreased as the folding angle increased. However, the simulated  $S_{11}$  decreased as the inner angle increased, whereas the measured  $S_{11}$  remained similar across all values.

Table 4.4: Single Slot Antenna - Simulated reflection coefficient (dB)

		Inner Angle ( $\alpha$ )				
		$0^\circ$	$5^\circ$	$10^\circ$	$15^\circ$	$20^\circ$
Folding Angle ( $\beta$ )	$0^\circ$	-44.53	-40.72	-36.17	-36.61	-38.11
	$10^\circ$	-31.02	-29.81	-33.70	-33.12	-33.12
	$20^\circ$	-29.72	-38.00	-32.18	-28.98	-26.24
	$30^\circ$	-21.85	-20.57	-20.62	-20.00	-21.08
	$40^\circ$	-15.43	-15.22	-15.26	-18.48	-15.65
	$50^\circ$	-11.09	-10.60	-10.62	-11.79	-11.83

Table 4.5: Single Slot Antenna - Measured reflection coefficient (dB)

		Inner Angle ( $\alpha$ )				
		$0^\circ$	$5^\circ$	$10^\circ$	$15^\circ$	$20^\circ$
Folding Angle ( $\beta$ )	$0^\circ$	-39.28	-45.21	-30.05	-35.85	-23.02
	$10^\circ$	-38.24	-36.99	-50.86	-33.54	-25.69
	$20^\circ$	-34.14	-34.25	-50.93	-28.56	-30.15
	$30^\circ$	-35.66	-37.72	-37.48	-40.98	-28.62
	$40^\circ$	-34.30	-26.76	-34.90	-21.97	-25.90
	$50^\circ$	-35.25	-29.58	-33.35	-18.22	-23.82

The maximum gain value was obtained in Fig. 4.17. The far-field plots were collected at the resonant frequency at each configuration with the inner angle ( $\alpha$ ) and folding angle ( $\beta$ ), it was then placed into Table 4.6. The maximum gain value across all configurations was when  $\beta = 20^\circ$  at 4.81 dBi. It was consistently the maximum value across all inner angles from  $0^\circ$  to  $20^\circ$ . When the folding angle increased, the maximum gain value fluctuated until  $\beta = 50^\circ$ , the gain value dropped dramatically below 3 dBi. Furthermore, as the inner angle increased, the maximum gain value also decreased gradually.

Fig. 4.17, displays the radiating angle and Half Power Beam Width (HPBW) on co-polar plots and the null region on cross-polar plots. When changing the inner angle ( $\alpha$ ), it displayed a slight shift in the radiating angle from  $0^\circ$  to  $5^\circ$ . HPBW was 3 dBi below the maximum gain value, on average, the HPBW was at  $80^\circ$  at most configurations. On the cross-polar plots, as the folding angle ( $\beta$ ) increased, the null region increased from -25 dBi when  $\alpha = 0^\circ$ , to -47 dBi when  $\alpha = 20^\circ$ . When the folding angle increased, the null region on each inner angles gradually shifted in terms of radiating angle. It could be seen that when  $\alpha = 5^\circ$ , the null region shifted from  $0^\circ$  to  $-10^\circ$ .

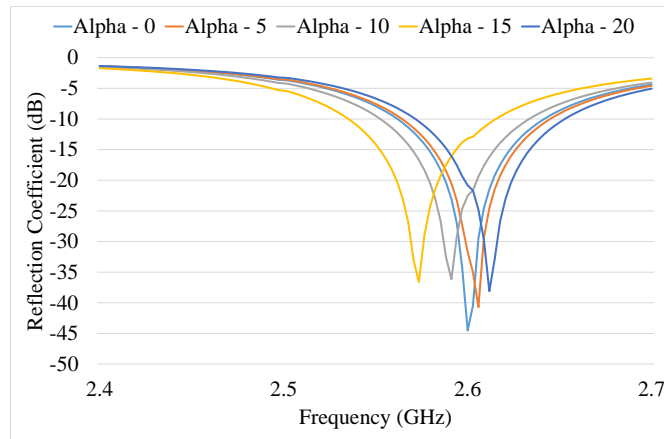
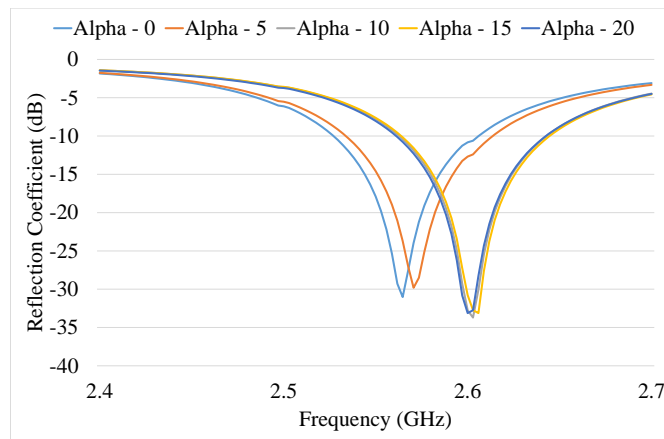
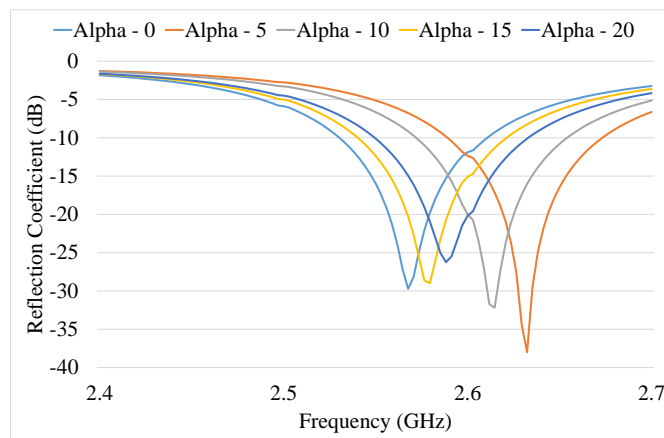
Table 4.6: Single Slot Antenna - Simulated Gain (dBi)

		Inner Angle ( $\alpha$ )				
		$0^\circ$	$5^\circ$	$10^\circ$	$15^\circ$	$20^\circ$
Folding Angle ( $\beta$ )	$0^\circ$	4.64	4.52	4.43	4.17	3.86
	$10^\circ$	4.69	4.63	4.57	4.34	3.98
	$20^\circ$	4.79	4.81	4.73	4.45	4.08
	$30^\circ$	4.68	4.52	4.40	4.15	3.88
	$40^\circ$	4.10	4.03	3.91	3.70	3.44
	$50^\circ$	2.87	2.90	2.88	3.01	2.65

Although the measured results does not contain contain gain measurement values. The fabricated antennas were able to measure radiation pattern, see Fig. 4.19. As shown in the co-polar plots, there was a small incremental shift in the radiating angle. When  $\beta = 10^\circ$ , the radiating angle increased from  $0^\circ$  when  $\alpha = 0^\circ$ , to  $12^\circ$  when  $\alpha = 20^\circ$ . The HPBW was 3 dBi below the maximum gain value. The maximum value on these plots was 0 dB, therefore the HPBW was measured at -3 dBi. On average, the HPBW of all fabricated antenna configurations was  $40^\circ$ .

Fig. 4.19 displays the null region on the cross-polar plots. As the inner angle increased, the radiating angle on the null region increased from  $0^\circ$  to  $18^\circ$  when  $\beta = 0^\circ$ . The cross-polar plots remained similar when varying the inner angle and the folding angle.

Overall, the simulated results showed that there was a downward trend as the inner angle ( $\alpha$ ) and folding angle ( $\beta$ ) increased. The folding angle had a more dramatic drop in the maximum gain. Also, when the inner angle was varied, there was an upward trend to the radiating angle from  $0^\circ$  to  $10^\circ$ . Comparing the simulated results to the measured results, the measured HPBW on average decreased from  $80^\circ$  to  $40^\circ$ .

(a)  $\alpha$  Sweep ;  $\beta = 0$ (b)  $\alpha$  Sweep ;  $\beta = 10$ (c)  $\alpha$  Sweep ;  $\beta = 20$

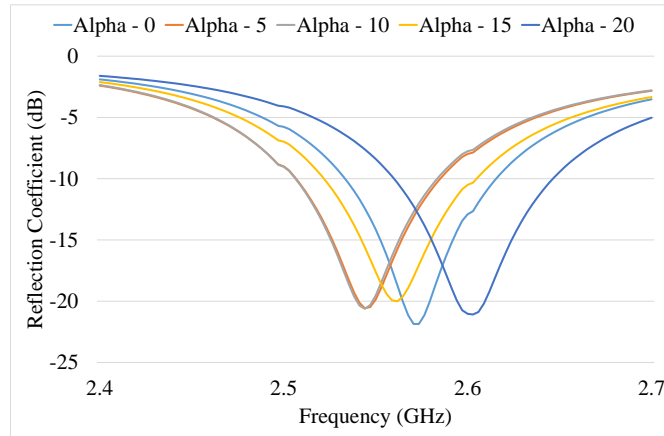
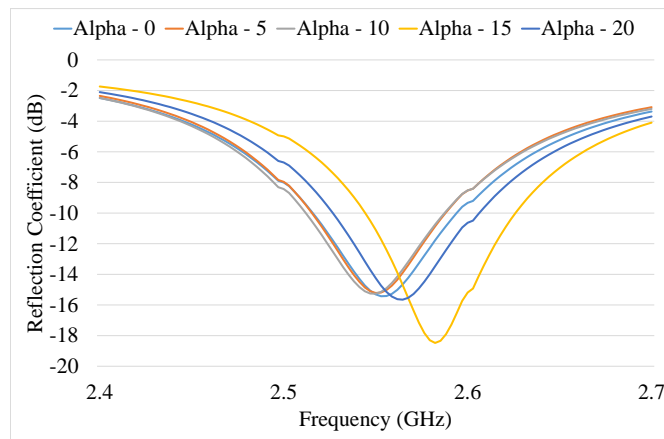
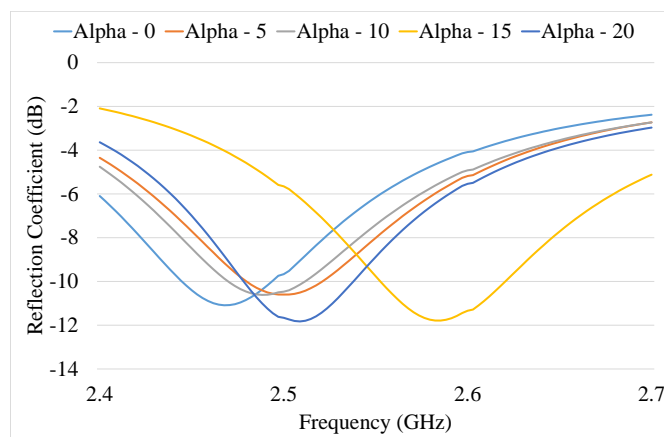
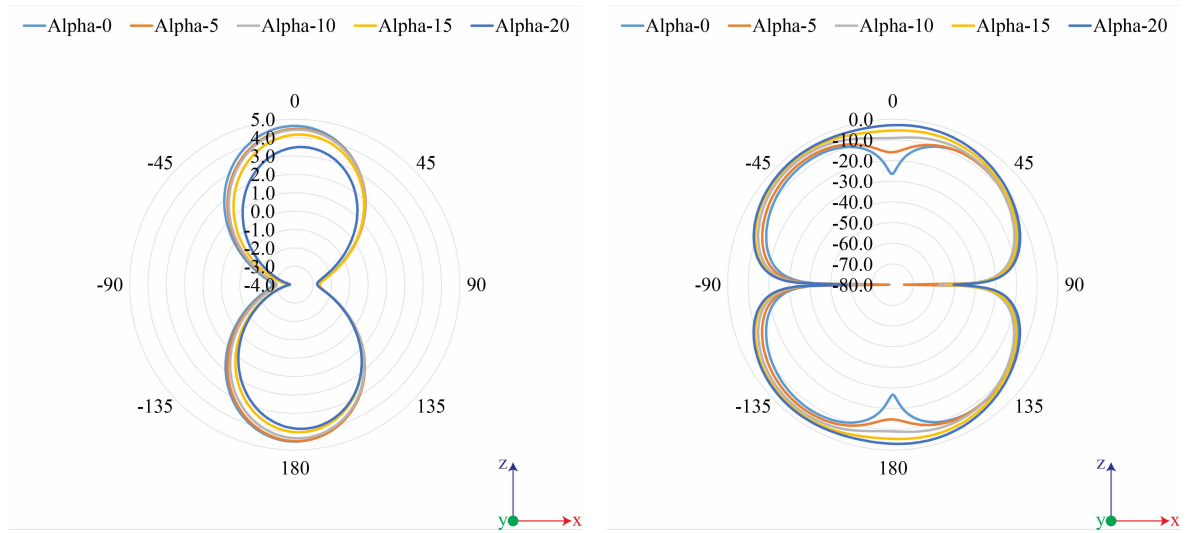
(d)  $\alpha$  Sweep ;  $\beta = 30$ (e)  $\alpha$  Sweep ;  $\beta = 40$ (f)  $\alpha$  Sweep ;  $\beta = 50$ 

Figure 4.16: Single Slot Antenna - Simulated Reflection Coefficient

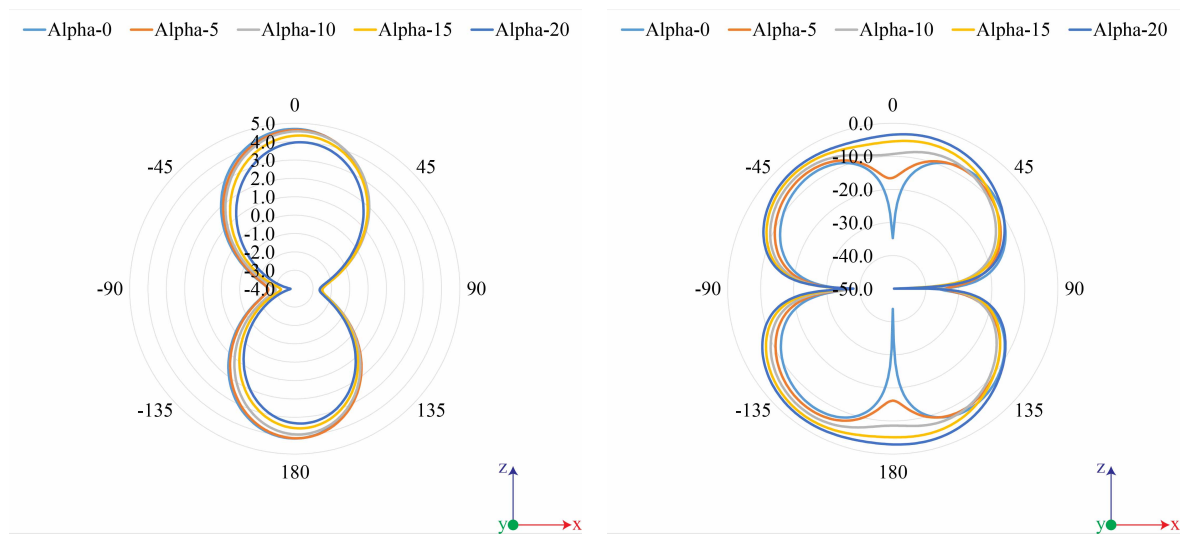




(a) Co Polar

(b) Cross Polar

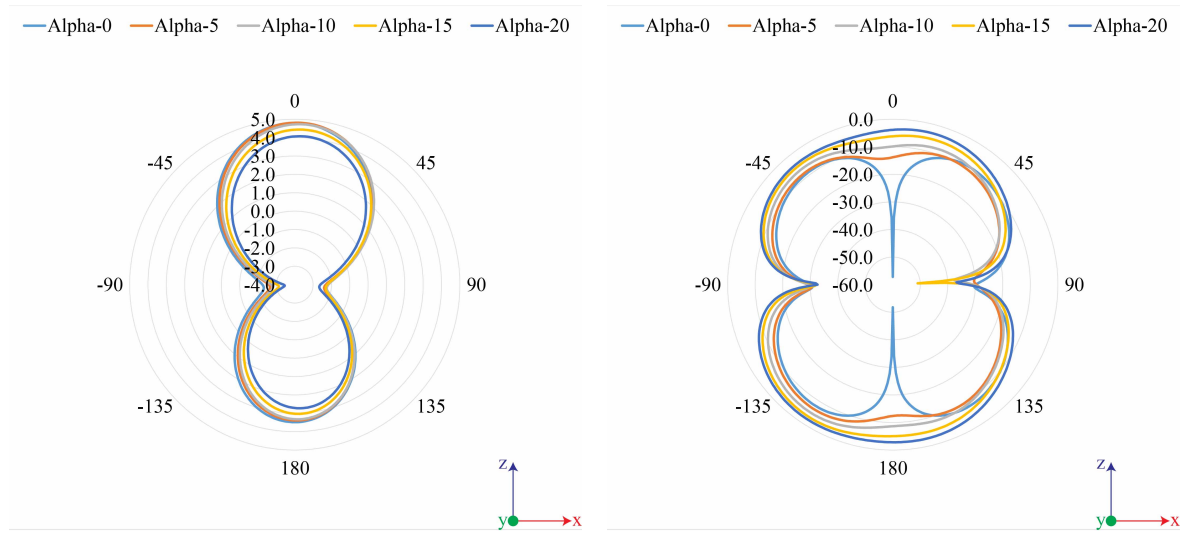
$\alpha$  Sweep ;  $\beta = 0$



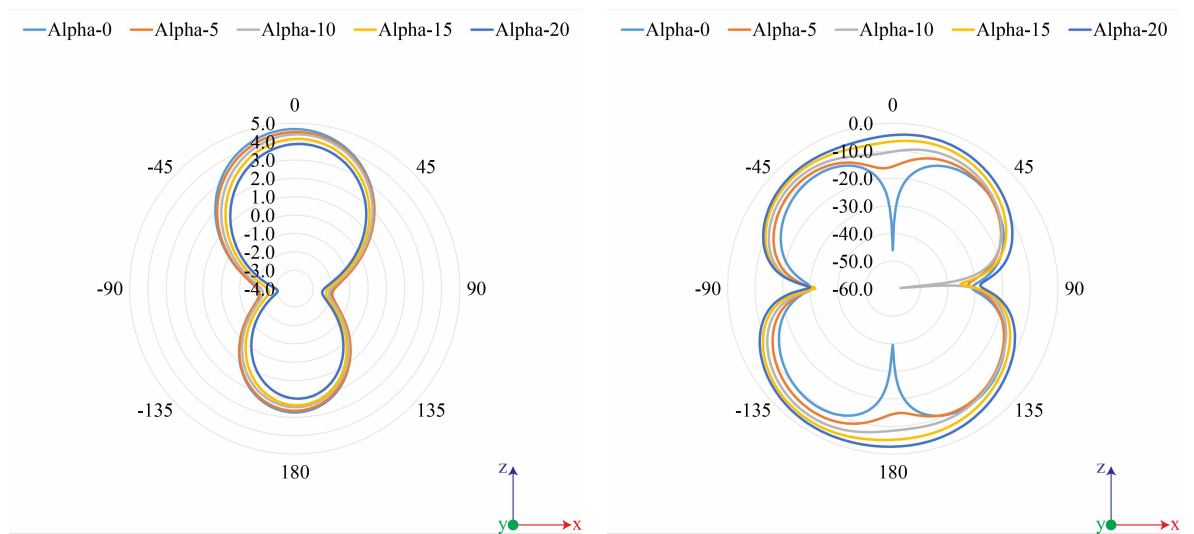
(a) Co Polar

(b) Cross Polar

$\alpha$  Sweep ;  $\beta = 10$



$\alpha$  Sweep ;  $\beta = 20$



$\alpha$  Sweep ;  $\beta = 30$

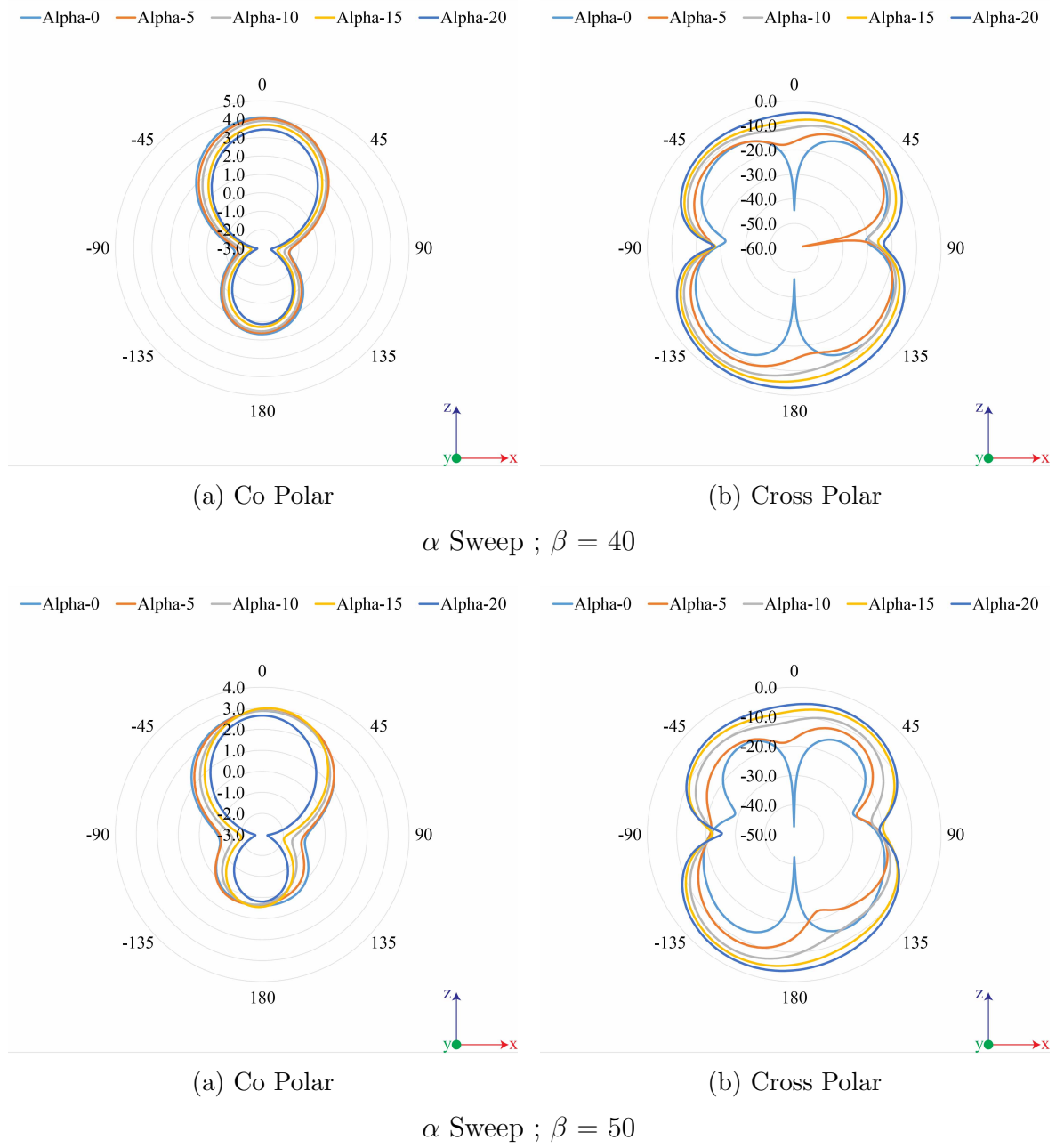
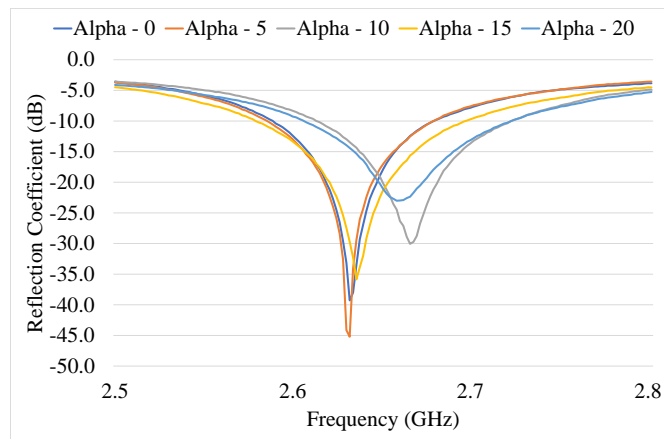
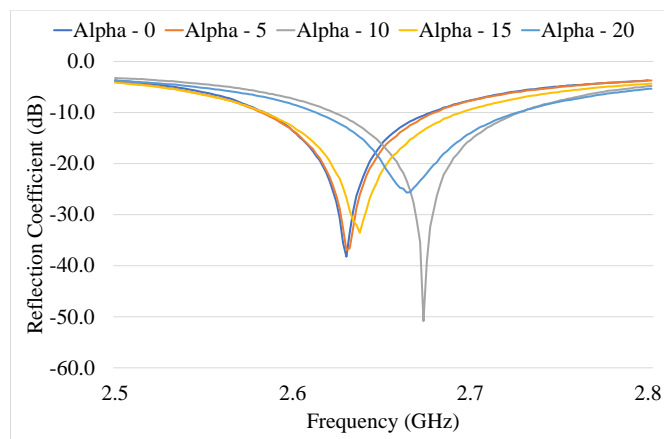
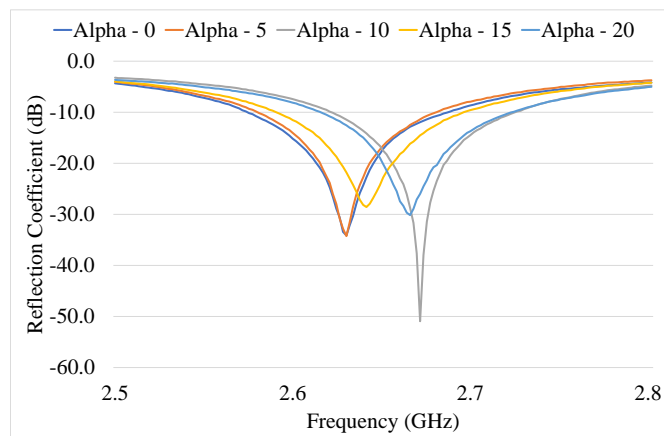


Figure 4.17: Single Slot Antenna - Simulated Radiation Pattern

(a)  $\alpha$  Sweep ;  $\beta = 0$ (b)  $\alpha$  Sweep ;  $\beta = 10$ (c)  $\alpha$  Sweep ;  $\beta = 20$

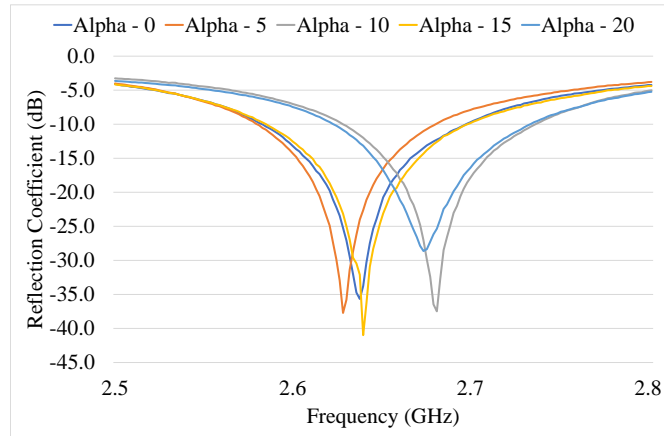
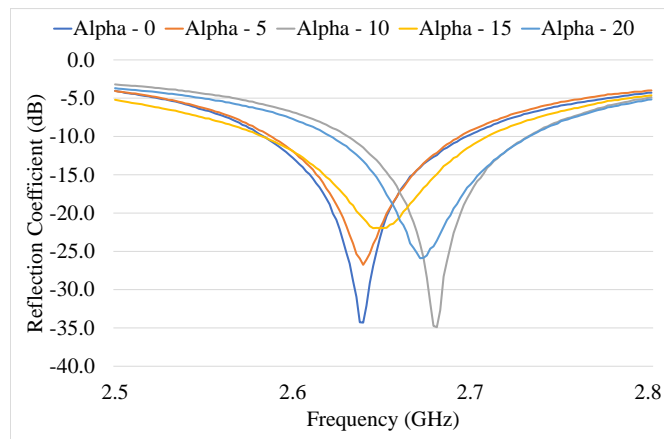
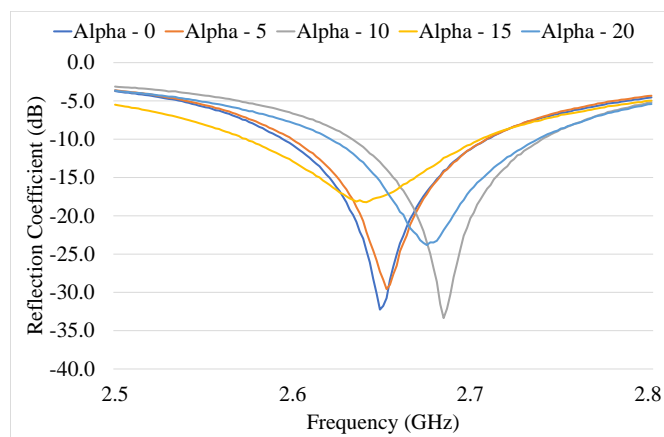
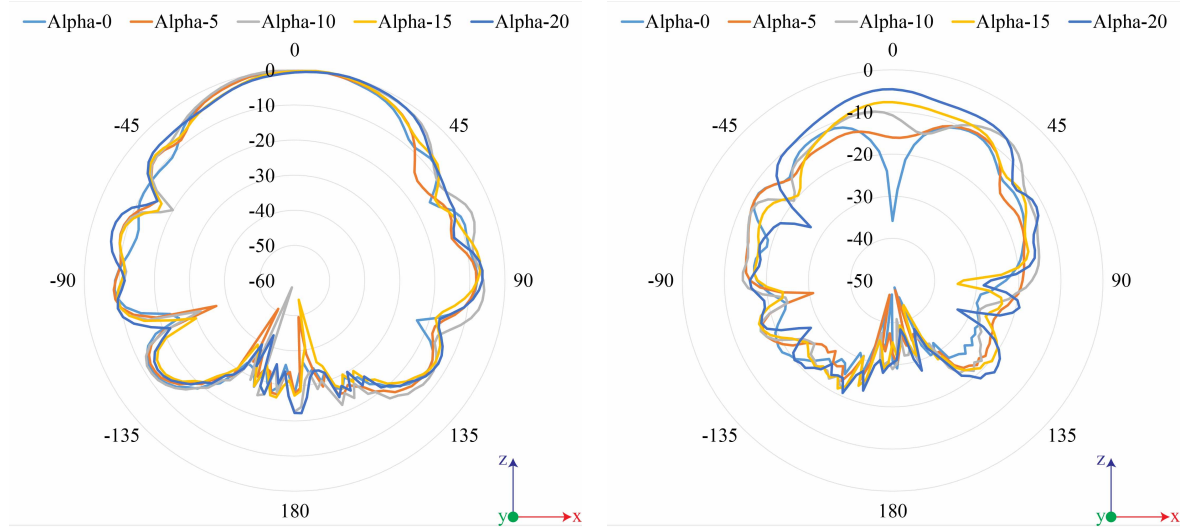
(d)  $\alpha$  Sweep ;  $\beta = 30$ (e)  $\alpha$  Sweep ;  $\beta = 40$ (f)  $\alpha$  Sweep ;  $\beta = 50$ 

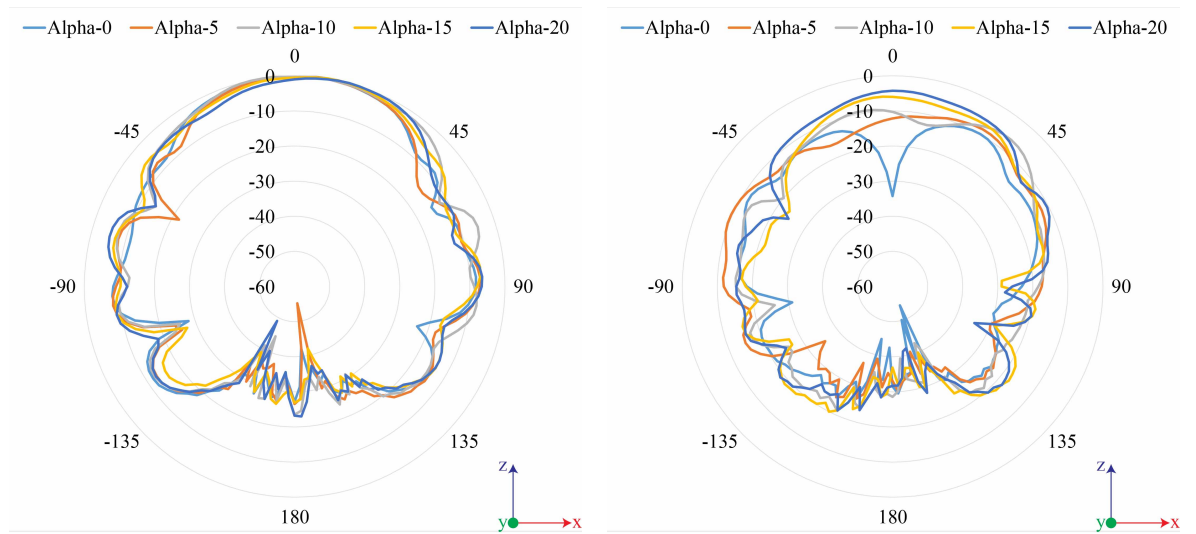
Figure 4.18: Single Slot Antenna - Measured Reflection Coefficient



(a) Co Polar

(b) Cross Polar

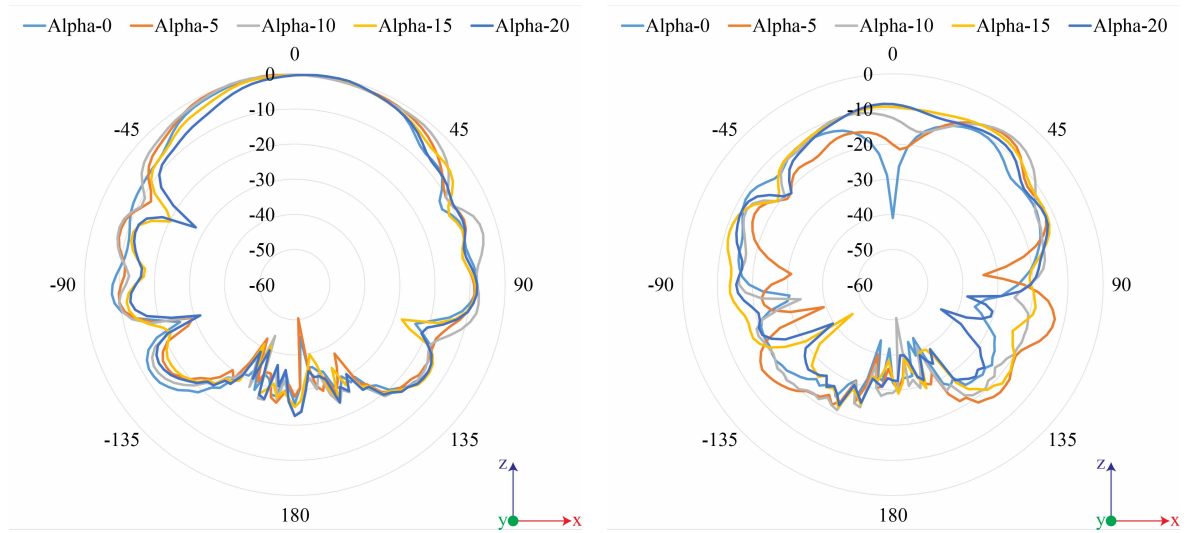
$\alpha$  Sweep ;  $\beta = 0$



(a) Co Polar

(b) Cross Polar

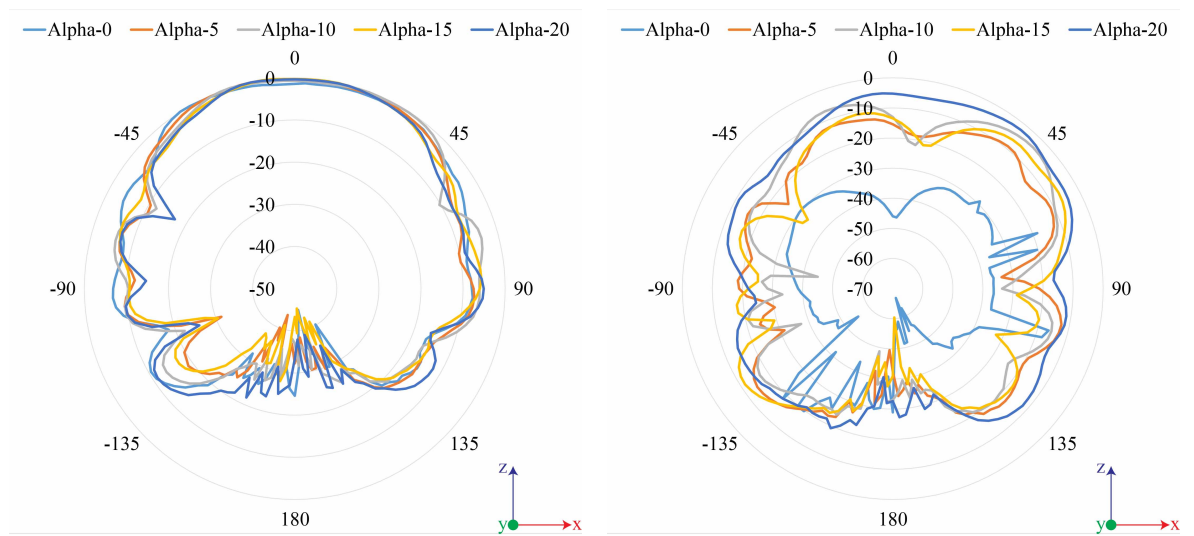
$\alpha$  Sweep ;  $\beta = 10$



(a) Co Polar

(b) Cross Polar

$\alpha$  Sweep ;  $\beta = 20$



(a) Co Polar

(b) Cross Polar

$\alpha$  Sweep ;  $\beta = 30$

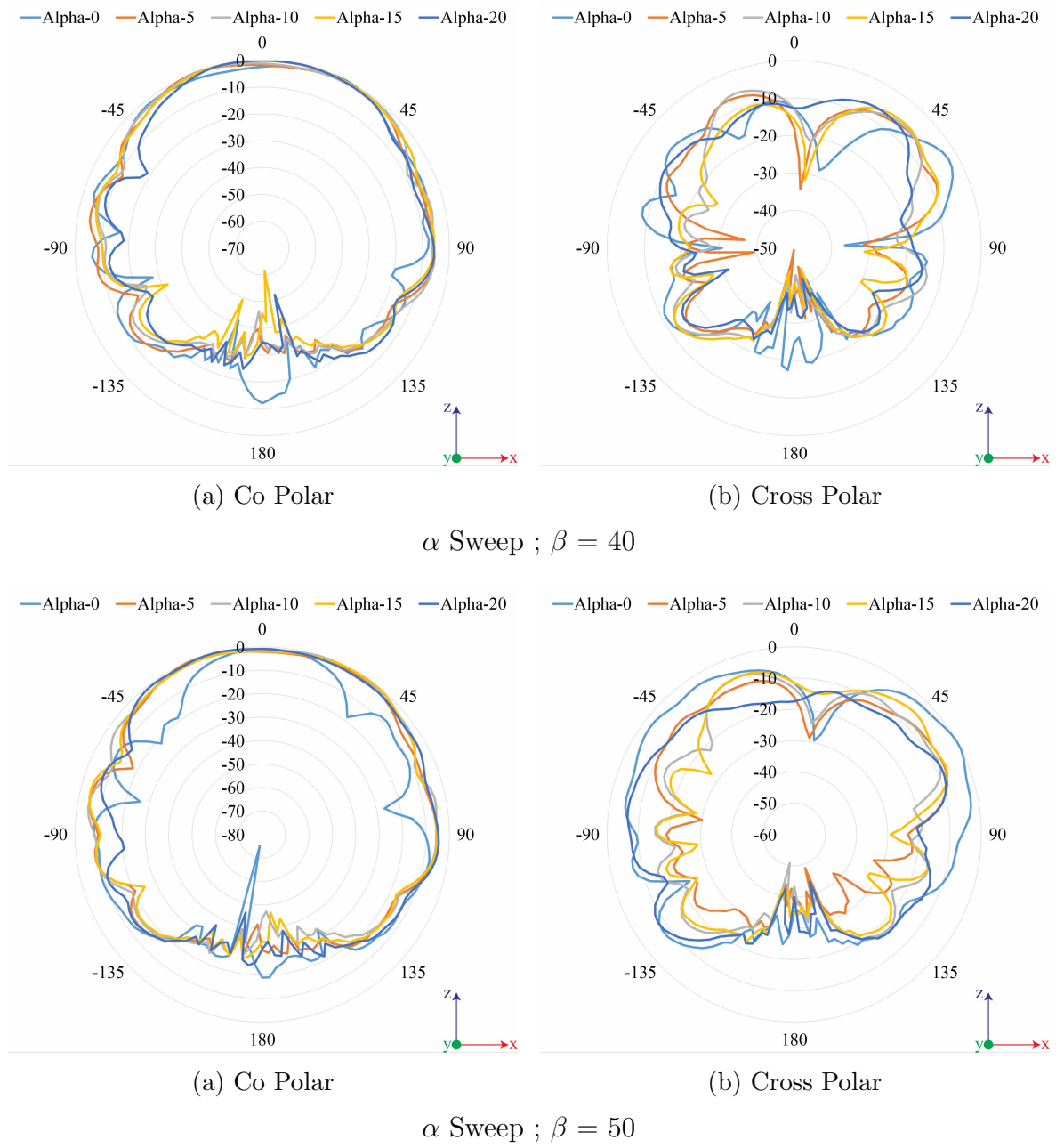


Figure 4.19: Single Slot Antenna - Measured Radiation Pattern



## 4.5 Arrays of Slot Antennas

To calculate and simulate an array of antennas, the pattern multiplication principle is introduced. The principle [44] states that “For a given number of identical antennas is a product between the pattern of one antenna with an array pattern.” The total radiated field can be found in (4.2) for each antenna, where the separation of each antenna ( $d$ ) and the phase ( $\beta$ ) is used.

$$E_{total} = E_{Single\ Element} AF \quad (4.2)$$

where the array factor AF is

$$AF = \sum_{n=1}^N e^{k(n-1)(kd \cos\theta + \beta)} \quad (4.3)$$

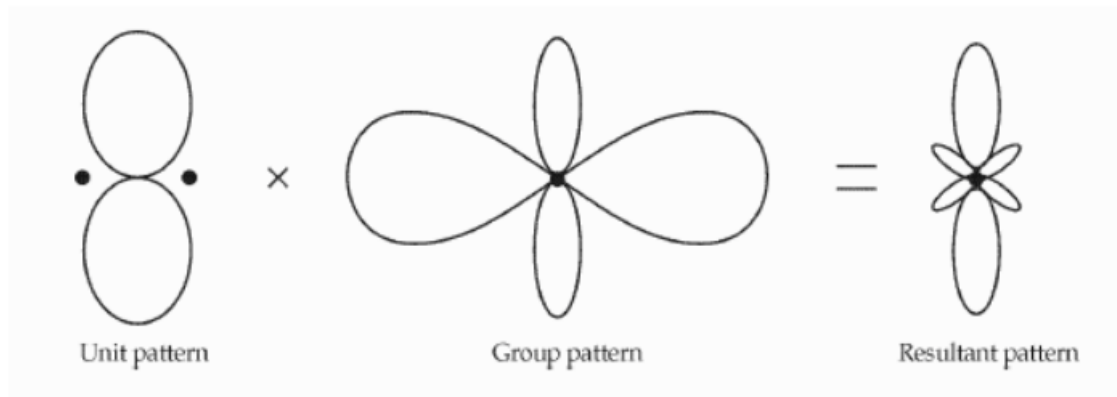


Figure 4.20: Total Pattern of four isotropic elements

In CST Studio, there was a function to calculate far-field array where the user defined individual element antenna into multiple arrays by a given X and Y direction. By inputting distance, it would be able to calculate the radiation pattern and the gain, when there was an array of the same individual antenna. As shown in Fig. 4.20, by placing the element 2 times the length ( $a$ ) and the width ( $b$ ) of the parallelogram, at 80 mm away, a 2 by 2 array of slot antennas using the far-field array function was created. Looking at the co-polar, the main beam had a gain of 10.8 dB with a side

beam of -1.35 dB radiating at  $90^\circ$  on each side and the HPBW being  $38^\circ$ . As for the cross polar plots, at the radiating angle, the null region was present with the level of -20 dB.

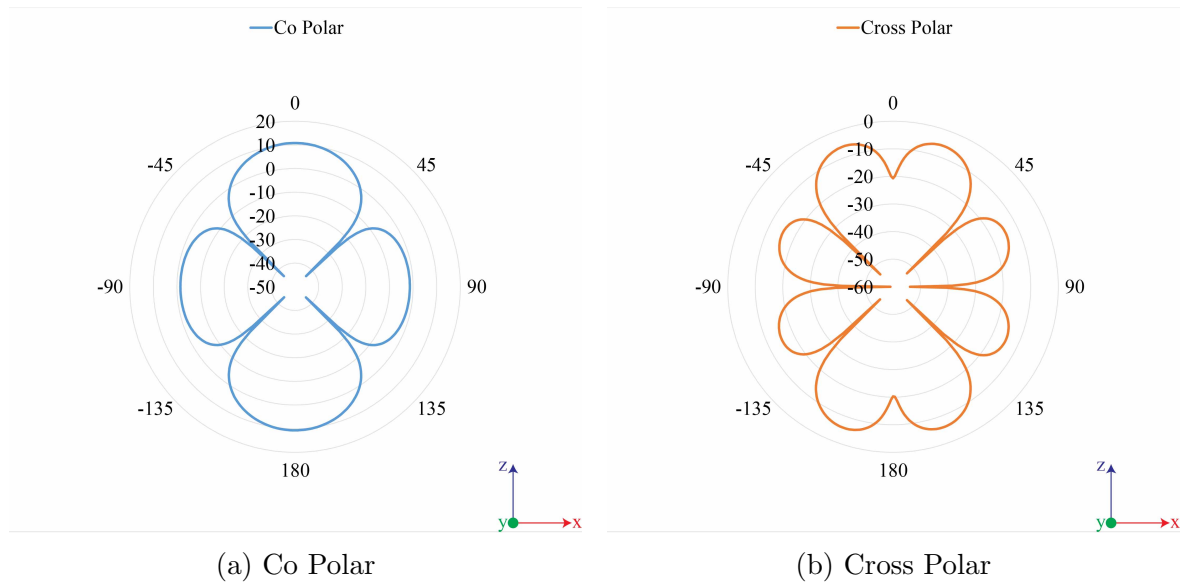


Figure 4.20: Slot Array Pattern Multiplication - Radiation Pattern

### 4.5.1 Arrays of Slot Antennas - Design

While a single slot antenna design could be simulated and measured without major difficulties, one of the main challenges of this chapter was to create an array of slot antennas. A matching network was required. The microstrip line used a quarter wave matching network to maximise the power transferred to each slot antenna, using eq. 3.2.2. The impedance was calculated and therefore the width of the microstrip line at the given impedance could be found. In this instance, the load ( $Z_{load}$ ) was  $25 \Omega$ , by using the quarter wave matching network, the impedance ( $Z_1$ ) was then  $35.4 \Omega$ , hence the width of the microstrip line was 0.475 mm. With the simulated operating frequency of the single slot antenna design at 2.5 GHz,  $\lambda/4$  was 30 mm. The full matching network is shown in Fig. 4.21 with the Table 4.7 showing the parameters used to create the matching network.

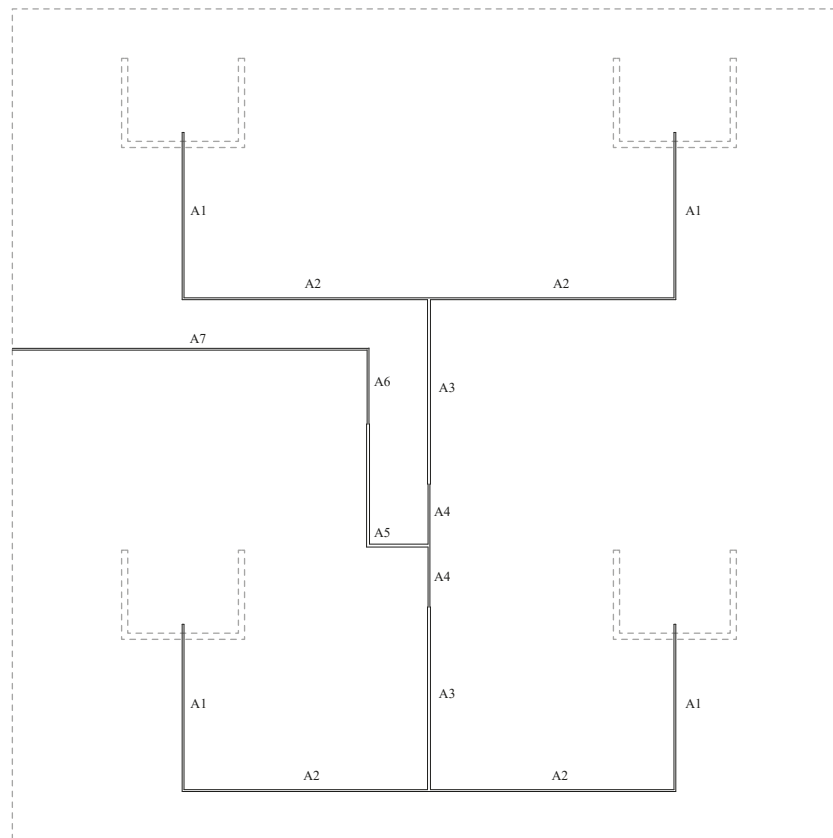


Figure 4.21: Matching Network

Table 4.7: Matching Network Values

Parameters	Values ( <i>mm</i> )
A1	27
A2	40
A3	30
A4	10
A5	30
A6	12.3875
A7	90.2375

To keep the table values above consistent while the structure was folded in the simulations, the Miura Ori (2.1) - (2.4) in Section 2.2.3. Since each microstrip line was on a different surface of the parallelogram. It was important that the length and the width of the microstrip was calculated according to (3.1). When the structure was folded, the total length of the quarter wave and the microstrip feed line remained the same when ranging from inner angle  $0^\circ$  to  $20^\circ$ . The process of creating 3-D polygon curves and assigning material was shown in Section 4.4.1. The computerised model of

an array of slot antennas is shown in Fig. 4.22, which displayed all 30 configurations.

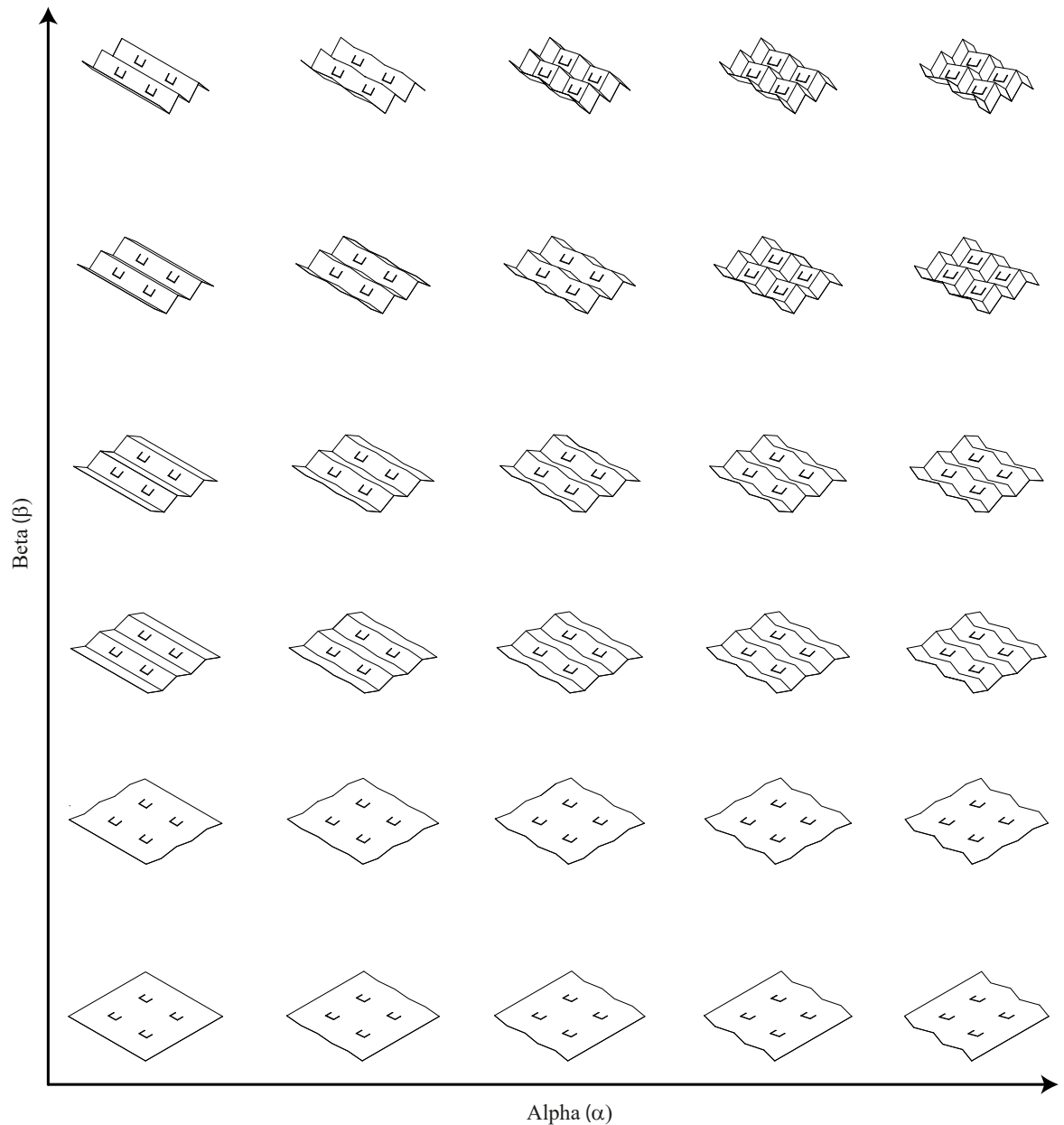


Figure 4.22: Change in Alpha and Beta

### 4.5.2 Arrays of Slot Antennas - Simulated and Measured Results

Similar to Section 4.4.2, the antenna design was modelled and simulated through CST Studio and the measured results were tested with a Vector Network Analyser (VNA) in the anechoic chamber. Using the matching network values from Table 4.7, the array

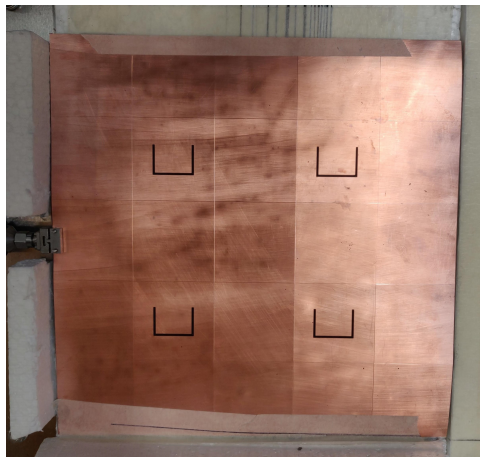
of slot design could be modelled. Both results were exported into Microsoft Excel and consisted of  $S_{11}$  values and far-field plots at the resonant frequency. The list of possible configurations as given in Fig. 4.22.

The simulated antennas were connected with a discrete port at  $50 \Omega$  and the fabricated antenna was connected with the Low Profile SMA End Launch connector. Fig. 4.24 highlights the simulated  $S_{11}$  plots and Fig. 4.25 displays the simulated co-polar and cross-polar plots. The fabricated array of slot antennas is shown in Fig. 4.23. The measured  $S_{11}$  plots are presented in Fig. 4.26. The co-polar and cross-polar plots were normalised to 0 dB shown in Fig. 4.27.

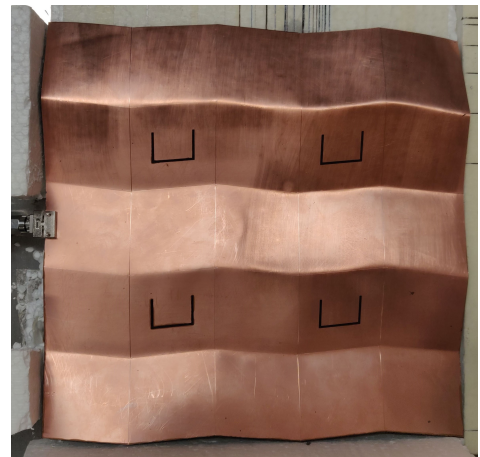
Table 4.8 highlights the resonant frequency at all configurations with inner angles ( $\alpha$ ) and folding angles ( $\beta$ ). The array of slot antennas was operating at 2.5 GHz. When  $\alpha = 0^\circ$ , it could be observed that the resonant frequency decreased by a small margin from 2.49 GHz when  $\beta = 0^\circ$ , to 2.45 GHz when  $\beta = 50^\circ$ . As the inner angle increased, the resonant frequency remained similar with a minor shift by an average of 30 MHz.

The measured resonant frequency at all possible configurations is shown in Table 4.9. On average, the resonant frequency at all configurations was 2.58 GHz. When  $\alpha = 0^\circ$ , it could be seen that the resonant frequency increased from 2.60 GHz when  $\beta = 0^\circ$ , to 2.64 GHz when  $\beta = 50^\circ$ . When varying the inner angles, the resonant frequency remained relatively consistent.

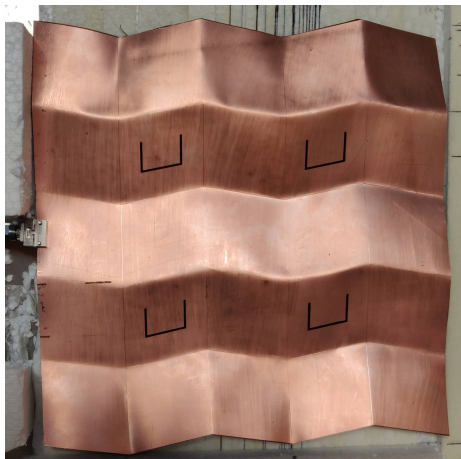
The resonant frequency shifted on average by 80 MHz when comparing the measured and simulated results. This was due to the permittivity stated in CST Studio. The value of the permittivity was not the same comparing to the fabricated antennas. There was a downward pattern when varying the folding angle ( $\beta$ ) in the simulated results. However, for the measured results, the resonant frequency remained similar across all configurations. When comparing the single slot antenna to an array of slot antennas, the results were also very similar.



(a) Alpha - 0



(b) Alpha - 5



(c) Alpha - 10



(d) Alpha - 15



(e) Alpha - 20

Figure 4.23: Fabricated Arrays of Slot Antennas

Table 4.8: Arrays of Slot Antennas - Simulated Resonant Frequency (GHz)

		Inner Angle ( $\alpha$ )				
		$0^\circ$	$5^\circ$	$10^\circ$	$15^\circ$	$20^\circ$
Folding Angle ( $\beta$ )	$0^\circ$	2.49	2.50	2.50	2.50	2.53
	$10^\circ$	2.51	2.49	2.50	2.51	2.52
	$20^\circ$	2.50	2.49	2.50	2.52	2.50
	$30^\circ$	2.50	2.48	2.48	2.50	2.51
	$40^\circ$	2.45	2.47	2.48	2.48	2.48
	$50^\circ$	2.45	2.43	2.45	2.46	2.41

Table 4.9: Arrays of Slot Antennas - Measured Resonant Frequency (GHz)

		Inner Angle ( $\alpha$ )				
		$0^\circ$	$5^\circ$	$10^\circ$	$15^\circ$	$20^\circ$
Folding Angle ( $\beta$ )	$0^\circ$	2.60	2.57	2.57	2.56	2.59
	$10^\circ$	2.60	2.56	2.58	2.57	2.59
	$20^\circ$	2.60	2.57	2.58	2.57	2.59
	$30^\circ$	2.60	2.58	2.59	2.58	2.59
	$40^\circ$	2.61	2.58	2.59	2.57	2.59
	$50^\circ$	2.64	2.59	2.59	2.59	2.59

In Table 4.10, the simulated results are compared with  $S_{11}$  in dB at all resonant frequencies across all inner and folding angles.  $S_{11}$  dropped sharply as the folding angle ( $\beta$ ) increased. When  $\alpha = 0^\circ$ ,  $S_{11}$  dropped from -23.34 dB when  $\beta = 0^\circ$ , to -5.86 dB when  $\beta = 50^\circ$ . When varying the inner angle ( $\alpha$ ),  $S_{11}$  decreased by a small amount. When  $\beta = 0^\circ$ ,  $S_{11}$  decreased from -23.34 dB when  $\alpha = 0^\circ$ , to -16.36 dB when  $\alpha = 20^\circ$ . In Fig. 4.24, there was another curve at a higher frequency at 2.7 GHz. This could be seen as another Transverse ElectroMagnetic Mode (TEM) appearing in the array of slot antennas. Fig. 4.24 displays the 10 dB reflection coefficient bandwidth.

On average, the 10 dB reflection coefficient bandwidth was 50 MHz.

Table 4.11,  $S_{11}$  is compared with all inner and folding angles. When  $\beta = 10^\circ$ ,  $S_{11}$  had fluctuated from -15.36 dB when  $\alpha = 5^\circ$ , to -23.18 dB when  $\alpha = 20^\circ$ . When varying the folding angle,  $S_{11}$  also fluctuated by a small amount. Again, there was a curve at the higher frequency at 2.75 GHz. This was due to the TEM mode appearing in the measured results.

Measured  $S_{11}$  was better in terms of consistency at all configurations. When  $\beta = 50^\circ$ , the simulated results had a reflection coefficient of -5.86 dB while the measured results improved to -18.14 dB. This showed that more than 97% of power was being transferred to the antenna rather than reflecting back to the input. When comparing both single slot antenna to an array of slot antennas, both simulated  $S_{11}$  dropped significantly, comparing to the measured results over all inner angles, especially when  $\beta = 50^\circ$ . As explained earlier in Section 4.4.2, the reason for the drop in  $S_{11}$  performance was due to the loft function within CST Studio. It extended the stub length by a small amount hence it caused mismatch between the microstrip line and the slot.

Overall,  $S_{11}$  had varied by a small amount when comparing the simulated to measured results. The measured results performed better comparing to the simulated results. However, a problem occurred when measuring the fabricated antennas while varying the folding angles. When the fabricated antenna started to fold, the copper on the substrate started to stretch at the folding corner. This caused the copper tracks to crack at an angle over  $90^\circ$  and led to discontinuity across the feeding network. This was explained in Section 3.5.4, the crease lines were used to reduce the microstrip line breaking across all feeding network.



Table 4.10: Arrays of Slot Antennas - Simulated reflection coefficient (dB)

		Inner Angle ( $\alpha$ )				
		$0^\circ$	$5^\circ$	$10^\circ$	$15^\circ$	$20^\circ$
Folding Angle ( $\beta$ )	$0^\circ$	-23.34	-19.03	-18.86	-19.63	-16.46
	$10^\circ$	-18.25	22.99	-21.61	-19.80	-19.35
	$20^\circ$	-23.66	-22.95	-24.62	-21.99	-26.25
	$30^\circ$	-35.10	-33.44	-44.65	-39.05	-36.33
	$40^\circ$	-14.41	-20.87	-22.57	-12.35	-19.52
	$50^\circ$	-5.86	-9.96	-6.35	-12.21	-8.69

Table 4.11: Arrays of Slot Antennas - Measured reflection coefficient (dB)

		Inner Angle ( $\alpha$ )				
		$0^\circ$	$5^\circ$	$10^\circ$	$15^\circ$	$20^\circ$
Folding Angle ( $\beta$ )	$0^\circ$	-18.84	-15.86	-19.96	-17.53	-22.73
	$10^\circ$	-19.16	-15.36	-19.76	-18.04	-23.18
	$20^\circ$	-19.39	-16.92	-22.47	-18.20	-22.56
	$30^\circ$	-18.22	-17.15	-21.97	-19.71	-22.61
	$40^\circ$	-18.24	-17.92	-21.84	-19.36	-22.41
	$50^\circ$	-18.14	-18.35	-20.93	-18.62	-21.93

Table 4.12 uses the maximum gain value in dBi at the resonant frequency of each possible configuration. The maximum value was obtained from Fig. 4.25. The maximum gain value across all configurations was 14.98 dBi, when  $\beta = 20^\circ$ . As the folding angle increased, the maximum gain value fluctuated between 14.53 dBi when  $\alpha = 0^\circ$ , and 11.11 dBi when  $\alpha = 50^\circ$ . The gain value dropped by 3 dBi when  $\beta = 50^\circ$ . As explained earlier, the extended of the stub length was causing a decrease in performance in the simulations. As the inner angle increased, the maximum gain value also gradually decreased. Comparing to the far-field array tool on CST Studio,

the simulated maximum gain was 10.8 dB. The simulated array of slots had a 3 dB higher gain, than the far-field array tool.

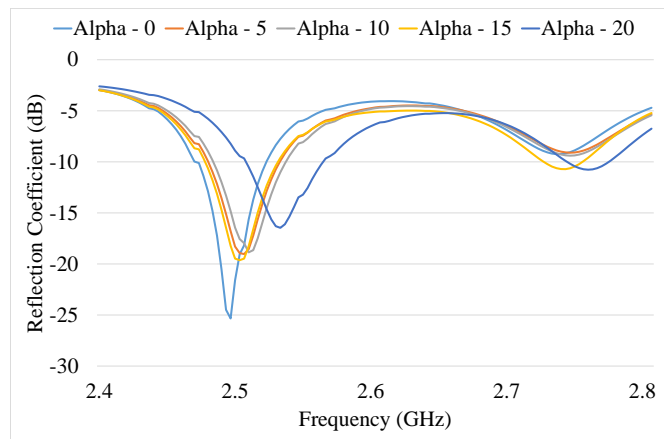
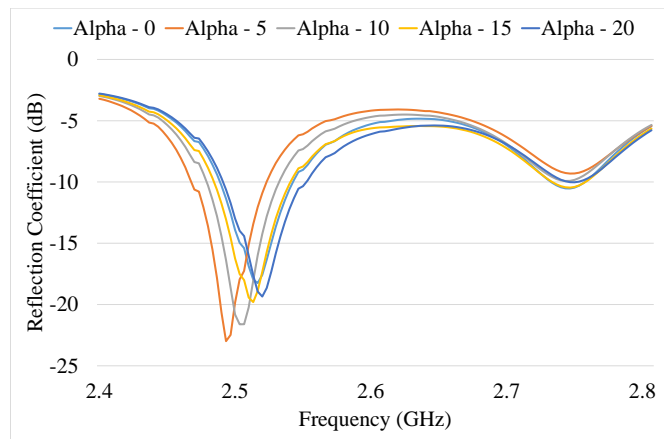
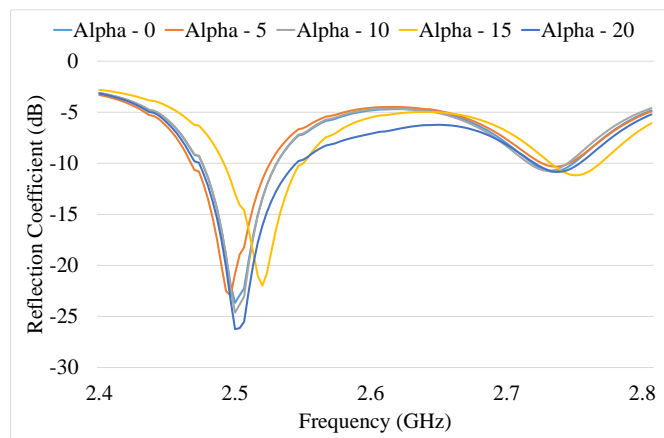
Fig. 4.25 displays the radiating angle, HPBW and the side lobes on the co-polar plots. As the inner angle ( $\alpha$ ) changed, there was not a noticeable shift in radiating angle. The HPBW across all configurations had an average of  $24^\circ$ . The side lobes, however, had an average peak value of 1 dBi with a radiating angles at  $-32^\circ$  and  $32^\circ$ . For the cross-polar plots, the null region could clearly be seen on all plots when  $\alpha = 0$ . The null value dropped as the folding angle increased from -40 dBi when  $\alpha = 0^\circ$ , to -28 dBi when  $\alpha = 20^\circ$ . As the inner angle changed, there was a clear shift in the radiating angle.

Table 4.12: Arrays of Slot Antennas - Simulated Gain (dBi)

		Inner Angle ( $\alpha$ )				
		$0^\circ$	$5^\circ$	$10^\circ$	$15^\circ$	$20^\circ$
Folding Angle ( $\beta$ )	$0^\circ$	14.53	14.34	13.94	13.57	13.27
	$10^\circ$	14.15	14.79	14.33	13.66	13.13
	$20^\circ$	14.86	14.98	14.79	13.89	12.83
	$30^\circ$	14.88	15.15	14.39	14.20	13.24
	$40^\circ$	13.78	13.90	13.69	11.32	13.23
	$50^\circ$	11.11	12.66	11.75	13.16	11.22

The fabricated antennas were measured for radiation patterns, see Fig. 4.27. As mentioned earlier, the maximum value for each polar plots were normalised to 0 dB. As shown in the co-polar plots, the radiating angle had a small shift when  $\beta = 0$ . The fabricated antenna was radiating at  $0^\circ$  when  $\alpha = 0^\circ$ , compared to  $8^\circ$  when  $\alpha = 20^\circ$ . The HPBW was -3 dB as the maximum gain value was at 0 dB. Therefore, on average, the HPBW was  $24^\circ$ . Both HPBW on simulated and measured results were very similar. However, there was a small decrease when comparing to the in-build far-field array tool on CST. The HPBW had dropped by  $10^\circ$ .

Fig. 4.27 shows the null region on the cross-polar plots. As the inner angle increased, the radiating angle on the null region shifted by a small amount. Although the gain measurement cannot be achieved, looking at the Fig. 4.27, for both co-polar and cross-polar plots, it can be seen clearly, that there was almost a 10 dBi difference at  $0^\circ$  from the co-polar plots compare with the cross-polar plots. Similarly, the co-polar and cross-polar plots in the simulation, see Fig. 4.25, displayed the same trend. Therefore it was clear to assume that the maximum gain value from the fabricated array of slot antennas were almost or close to achieving a 10 dBi in gain.

(a)  $\alpha$  Sweep ;  $\beta = 0$ (b)  $\alpha$  Sweep ;  $\beta = 10$ (c)  $\alpha$  Sweep ;  $\beta = 20$

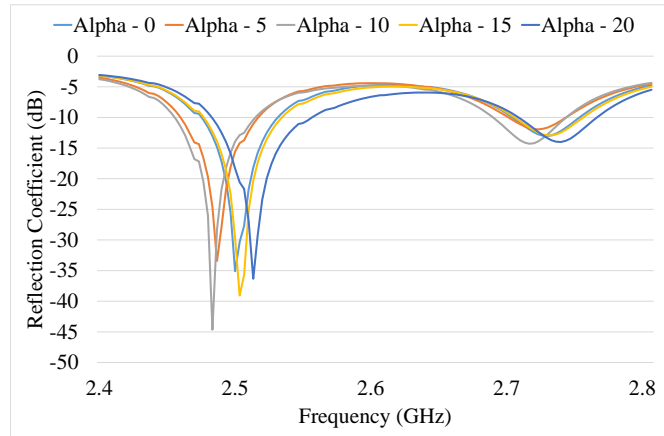
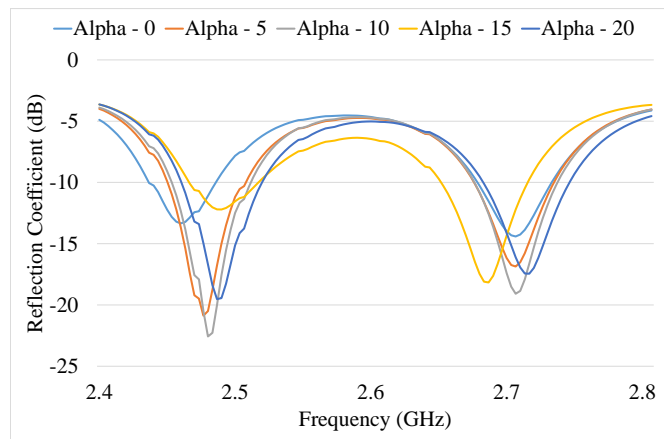
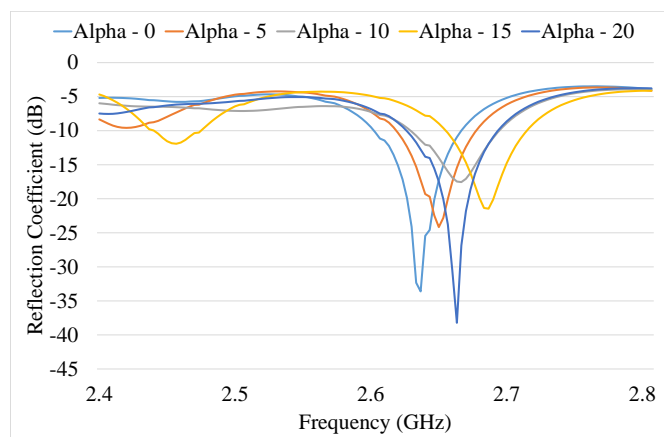
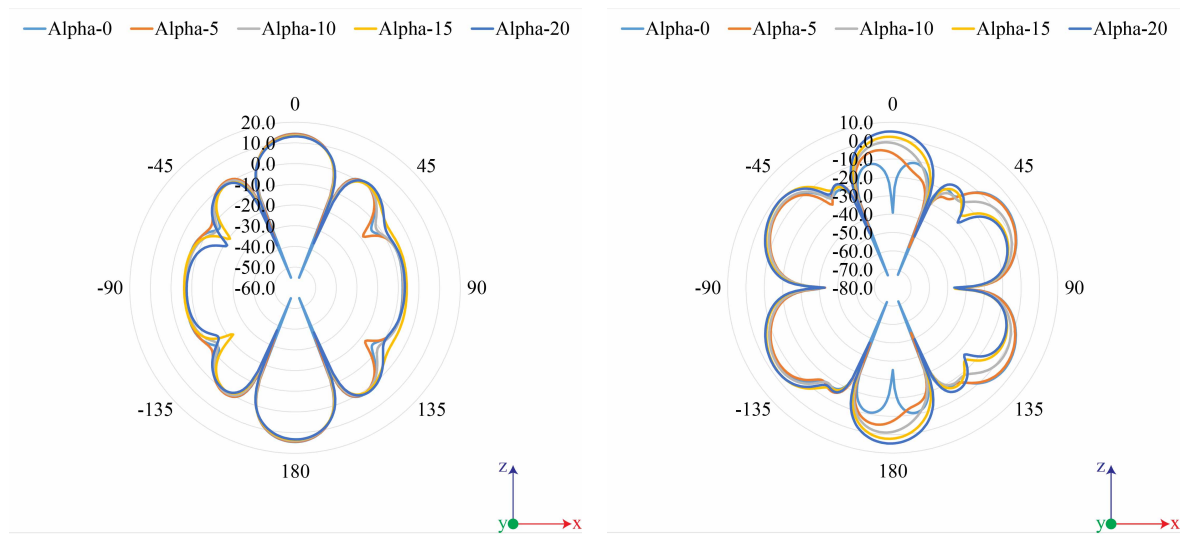
(d)  $\alpha$  Sweep ;  $\beta = 30$ (e)  $\alpha$  Sweep ;  $\beta = 40$ (f)  $\alpha$  Sweep ;  $\beta = 50$ 

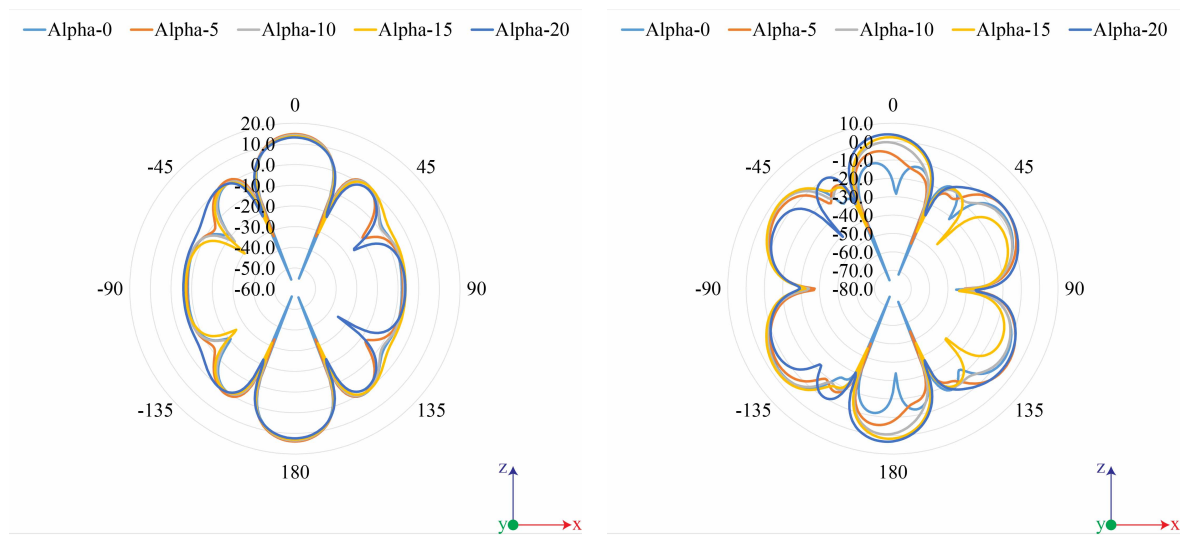
Figure 4.24: Arrays of Slot Antennas - Simulated Reflection Coefficient



(a) Co Polar

(b) Cross Polar

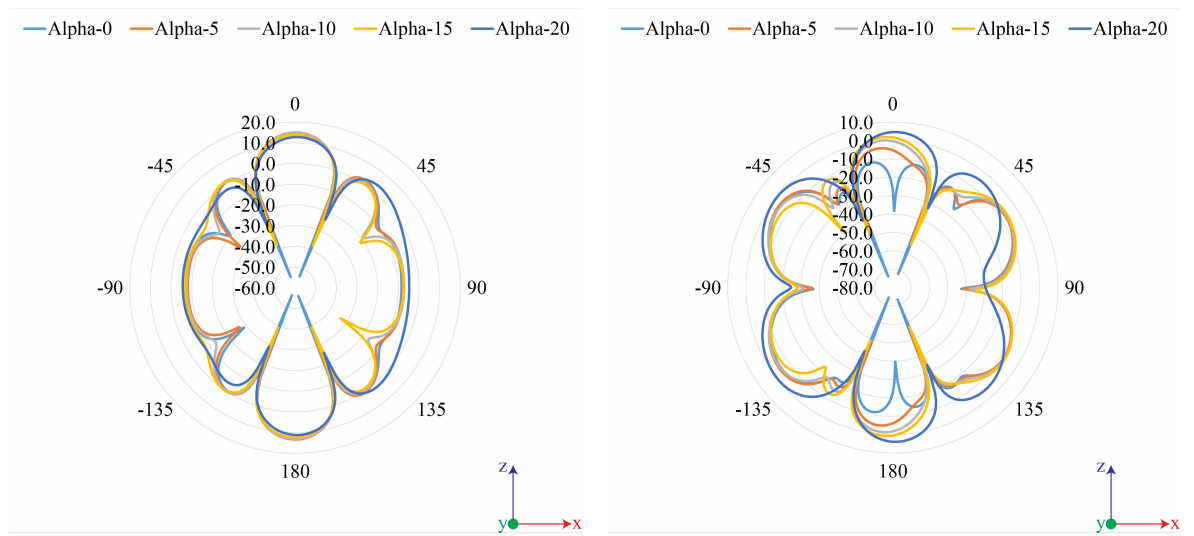
$\alpha$  Sweep ;  $\beta = 0$



(a) Co Polar

(b) Cross Polar

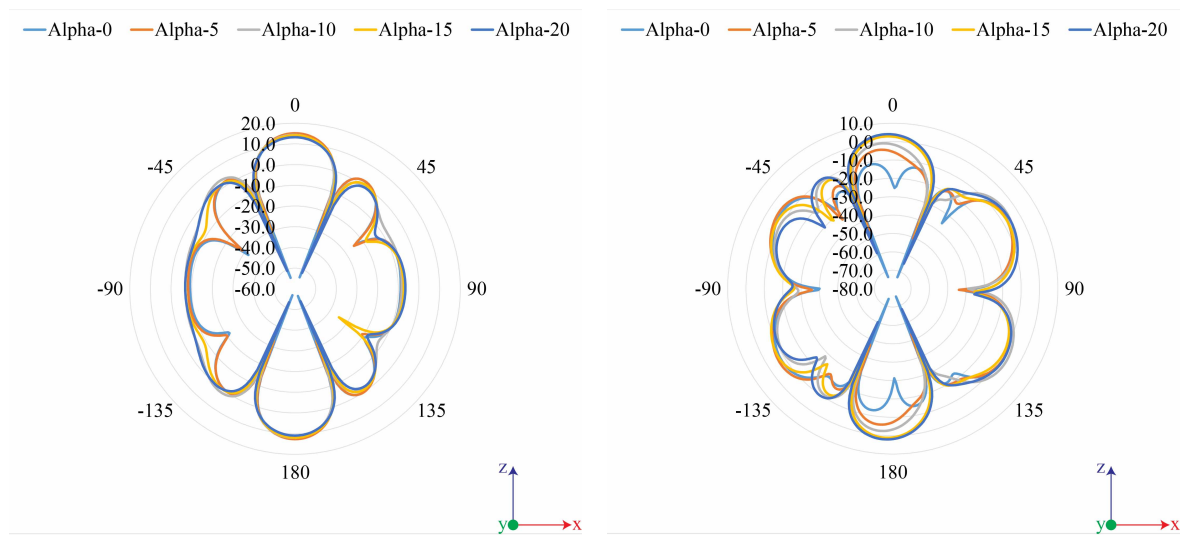
$\alpha$  Sweep ;  $\beta = 10$



(a) Co Polar

(b) Cross Polar

$\alpha$  Sweep ;  $\beta = 20$



(a) Co Polar

(b) Cross Polar

$\alpha$  Sweep ;  $\beta = 30$

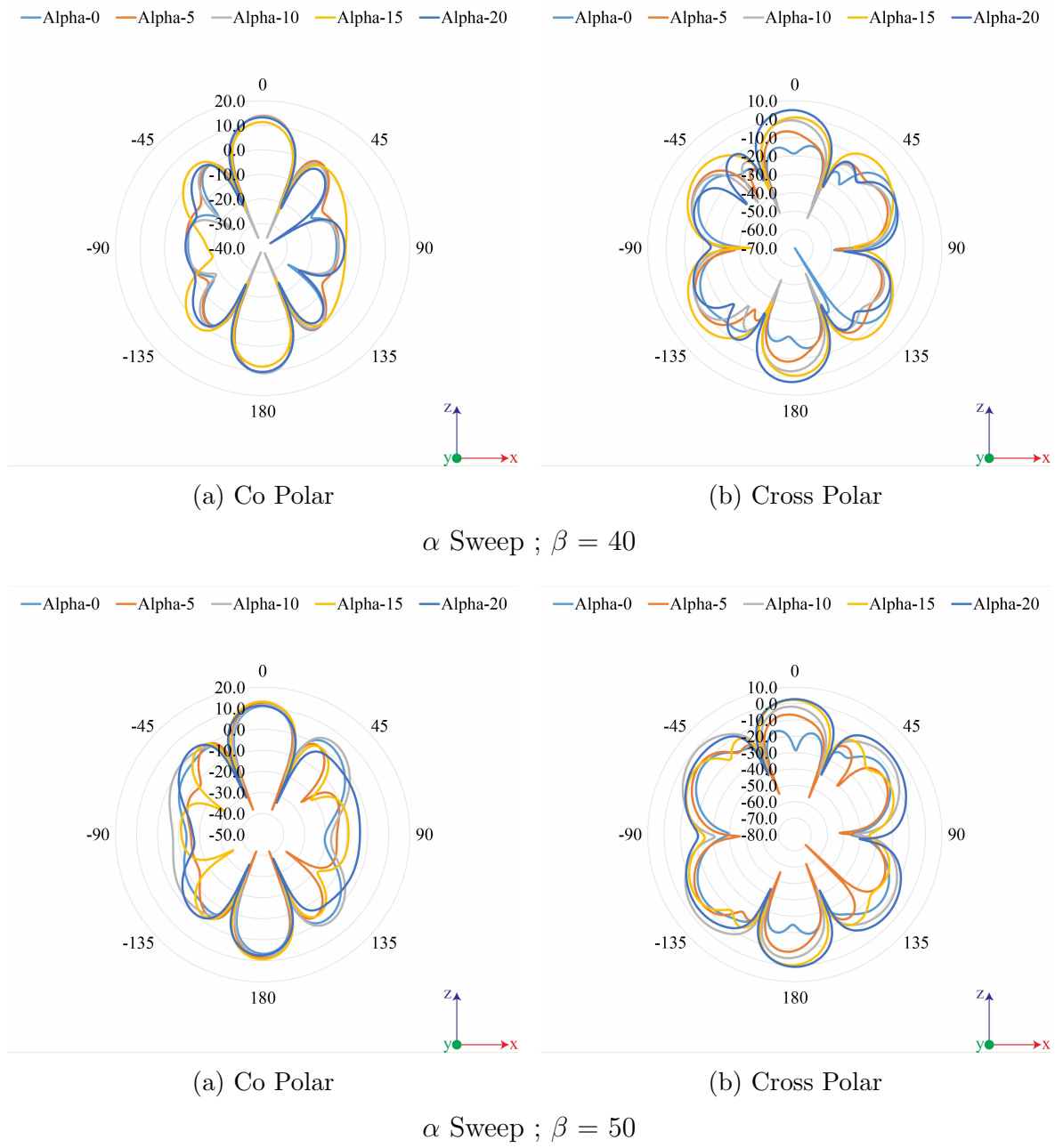
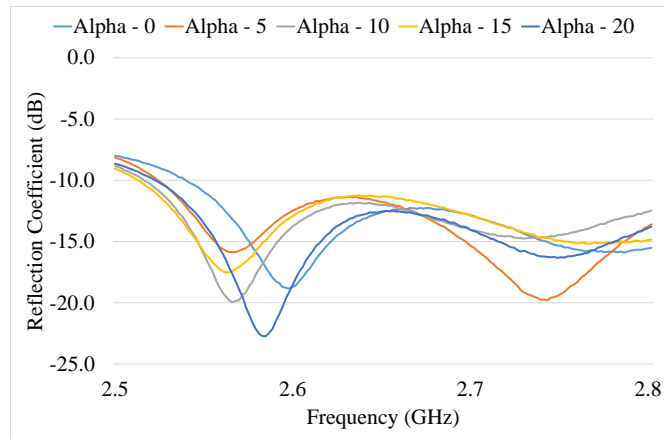
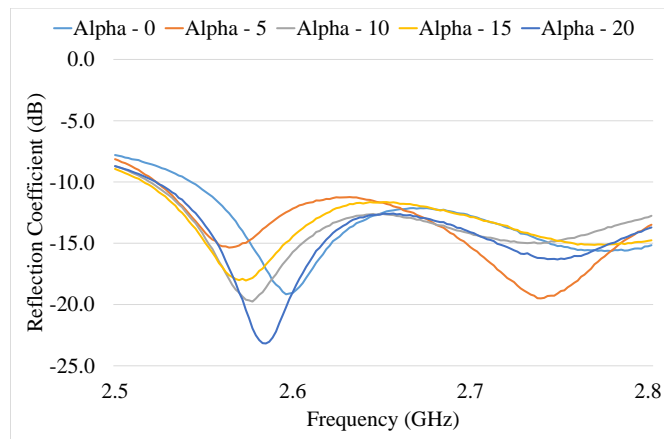
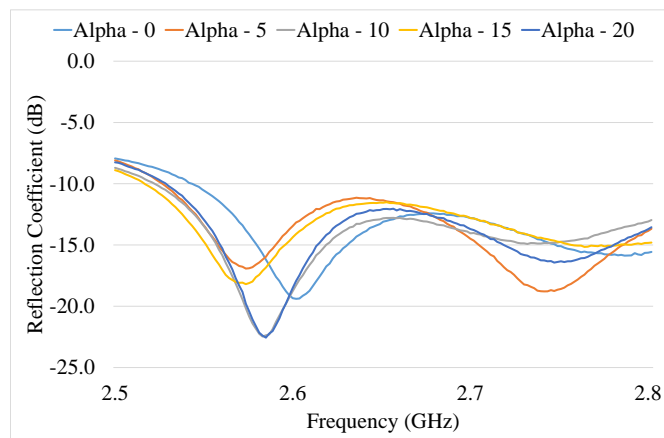


Figure 4.25: Arrays of Slot Antennas - Simulated Radiation Pattern



(a)  $\alpha$  Sweep ;  $\beta = 0$ (b)  $\alpha$  Sweep ;  $\beta = 10$ (c)  $\alpha$  Sweep ;  $\beta = 20$

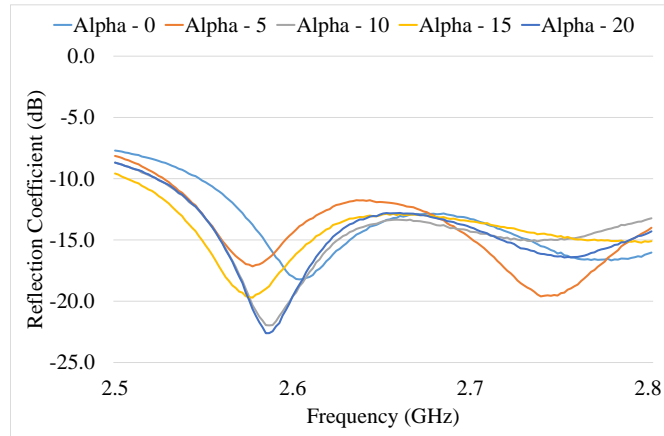
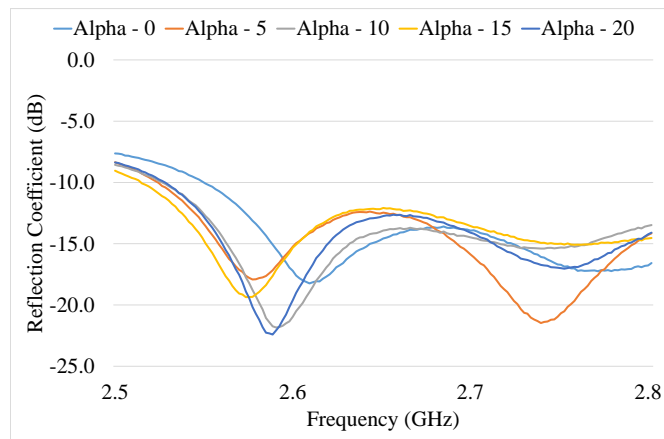
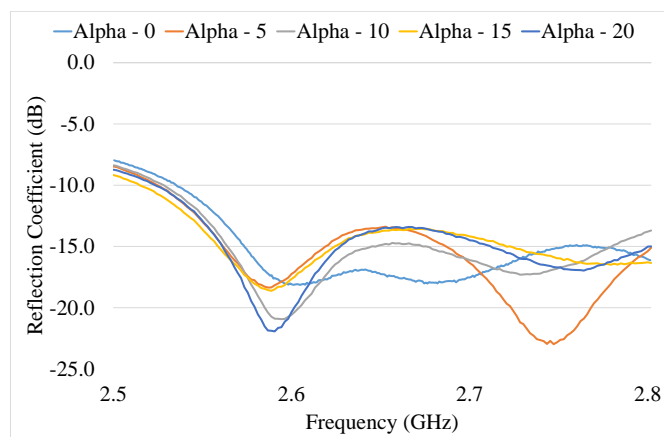
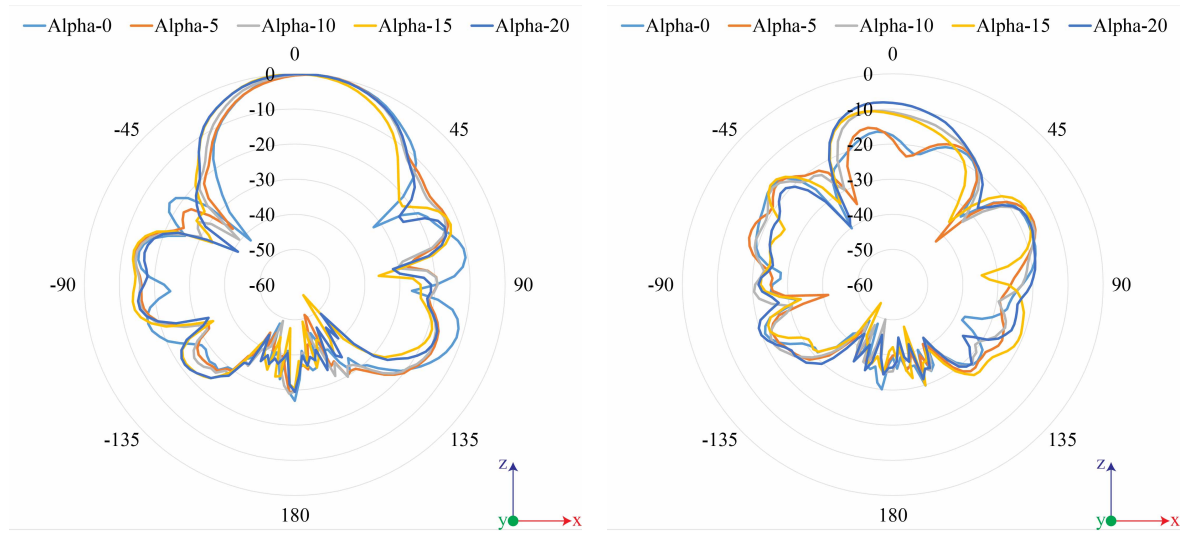
(d)  $\alpha$  Sweep ;  $\beta = 30$ (e)  $\alpha$  Sweep ;  $\beta = 40$ (f)  $\alpha$  Sweep ;  $\beta = 50$ 

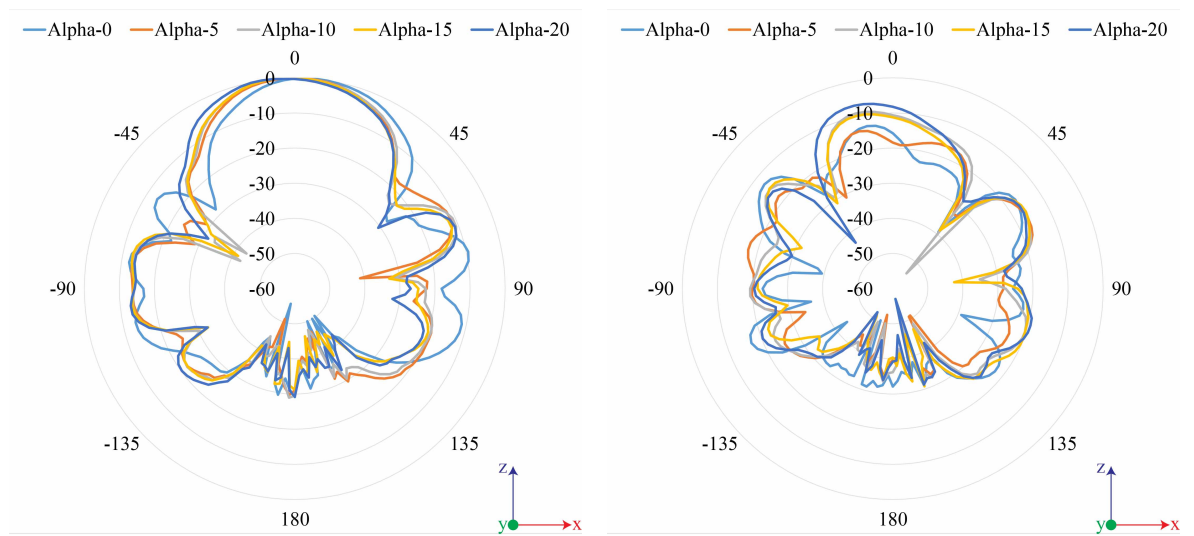
Figure 4.26: Arrays of Slot Antennas - Measured Reflection Coefficient



(a) Co Polar

(b) Cross Polar

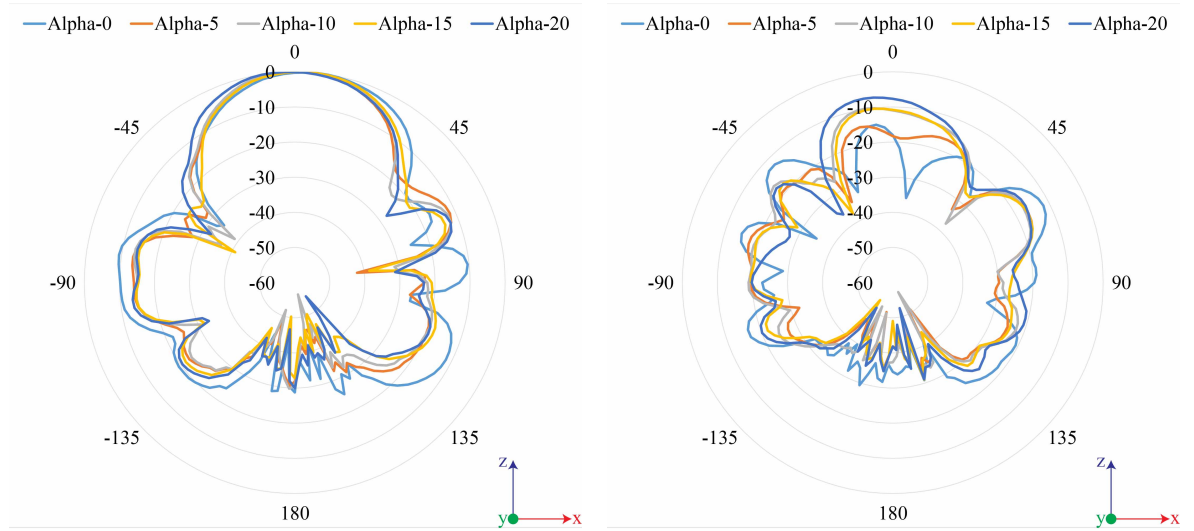
$\alpha$  Sweep ;  $\beta = 0$



(a) Co Polar

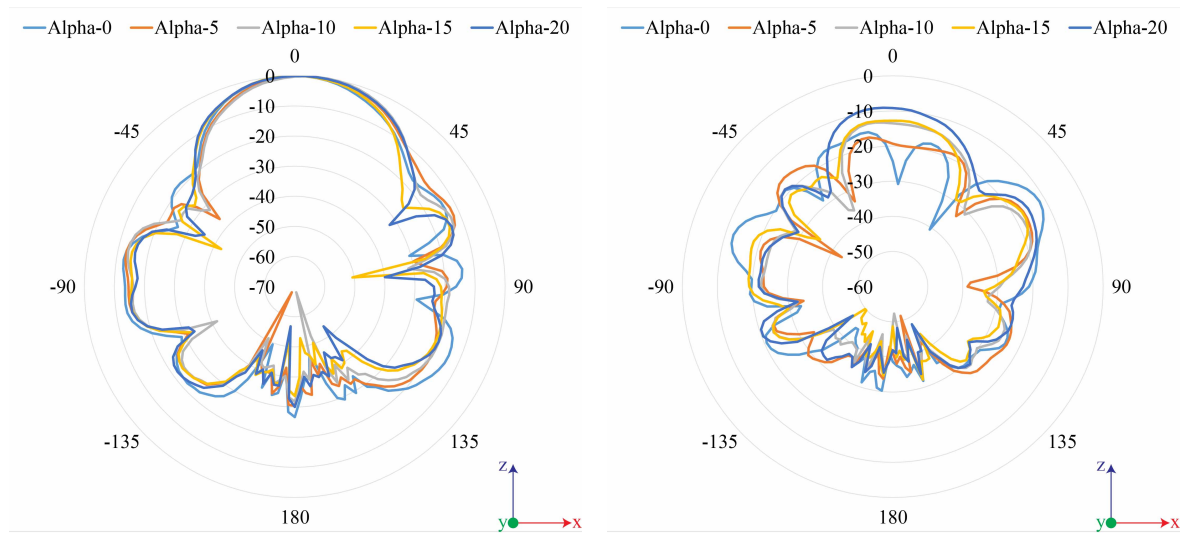
(b) Cross Polar

$\alpha$  Sweep ;  $\beta = 10$



(a) Co Polar

(b) Cross Polar

 $\alpha$  Sweep ;  $\beta = 20$ 

(a) Co Polar

(b) Cross Polar

 $\alpha$  Sweep ;  $\beta = 30$

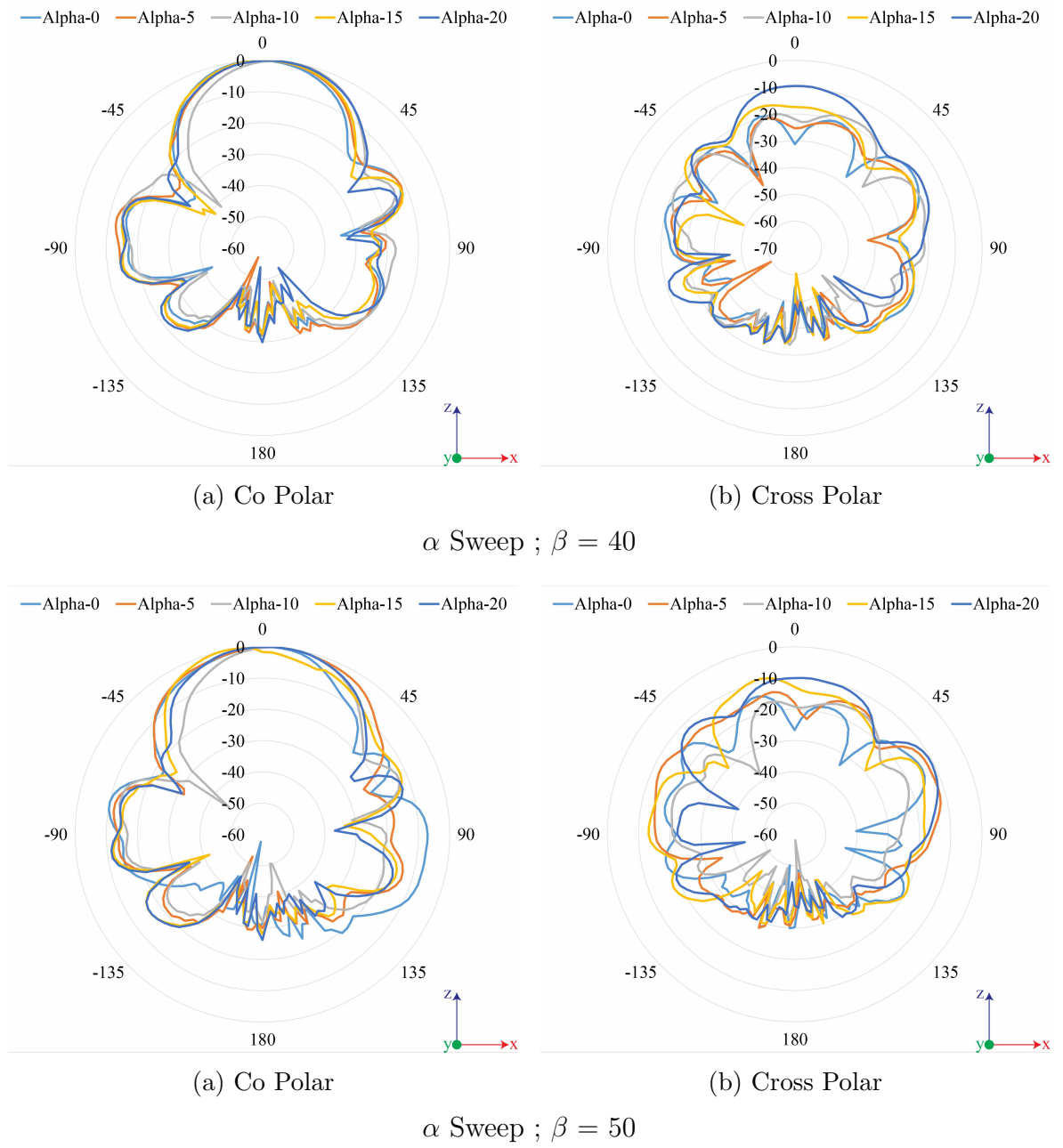


Figure 4.27: Arrays of Slot Antennas - Measured Radiation Pattern

## 4.6 Summary and Conclusion

In this chapter, the use of the Miura Ori folding technique had been thoroughly investigated with a single U-shaped slot antenna and an array of slot antennas. The investigation consisted of transforming a 2-Dimensional (2-D) planar antenna design into a 3-D foldable structure using flexible substrate. The equations for converting the 2-D planar antenna design into a 3-D structure were shown in Section 2.2.3. It used four main variables: the width of the parallelogram ( $a$ ), the length of the parallelogram ( $b$ ), the inner angle ( $\alpha$ ) and the folding angle ( $\beta$ ). The outputs from the equations were placed, as coordinate points in a curve and transformed into a solid object. To be able to fold the antenna design physically by hand, an A4 size model was preferred. The frequency was dependent to the wavelength, as the wavelength increased, the lower the frequency. Hence 2.5 GHz was chosen to be the operating frequency for a single slot antenna.

The antenna was simulated and optimised on a 2-D planar view with each variable: slot length in the X-axis ( $x$ ), and slot length in the Y-axis ( $y$ ), the microstrip length ( $ml$ ). When the antenna design was fully optimised, the antenna design was transferred into the Miura Ori model, where each individual rectangle was parameterised using (2.1) - (2.4) from Section 4.4.1. The 3-D modelled antenna design operated with two variables, inner angle ( $\alpha$ ) and folding angle ( $\beta$ ).

An investigation was performed using a single slot antenna with the Miura Ori folding technique. Both simulated and measured results were consistent. The range between the minimum and the maximum resonant frequency remained similar, the only difference was the 100 MHz shift, on an average at 2.60 GHz. The measured results remained operational as  $S_{11}$  were below -15 dB across all configurations. There was a problem that occurred during the simulated results.  $S_{11}$  decreased significantly as the folding angle ( $\beta$ ) increased. The method of creating the materials using loft curves was the main cause of the issue. The main objective was to create a consistent electrical length, as the structure was folded.

However, when the curves were translated in the Z-axis for lofting, the solid objects were not consistent compared with the fabricated. This caused mismatch and decrease in performance of the slot antenna. Nevertheless, it was decided that lofting curves would be the most suitable as the electrical length remained the same. Contrary to the measured results, where the same problem did not occur. However, as explained in Section 3.5.4, there were cracks formed on some fabricated antenna designs, as they were being folded. This caused discontinuity on some fabricated antennas and made them unable to perform further measurements.

A matching network was required to transform a single slot antenna into an array of slot antennas. The quarter wave matching network was performed and evenly distributed the power across all four slot antennas. The microstrip lines were designed with the Miura Ori equations from Section 2.2.3. A 2 by 2 array of slot antennas was created in CST Studio. An investigation were performed with varying the inner angle ( $\alpha$ ) and folding angle ( $\beta$ ) with an array of slot antennas. Both simulated and measured results displayed some upward and downward trends. The resonant frequency for both simulated and measured results were consistent, similar to a single slot antenna design, the resonant frequency was shifted by 100 MHz. In addition,  $S_{11}$  had improved on the measured results comparing to the simulated results. A related problem occurred when  $\beta = 50^\circ$ , the simulated results changed to -5 dB. This problem occurred, due to the method of modelling the 3-D structure in CST Studio, as explained earlier. As for the far-field plots, a consistent trend was presented when both co-polar and cross-polar plots only varied slightly with all configurations, except, when  $\beta = 50^\circ$ .

In conclusion, a series of simulations and measurements was investigated utilising the Miura Ori folding technique with a slot antenna. This chapter displayed interesting results. In the single slot antenna results the radiating angle shifted, as the inner angle changed. In an array of slot antennas, high gain was achieved with a reasonable HPBW. Although the 10 dB bandwidth of both single slot antenna and array of slot antennas were very narrow.

---

When applying the Miura Ori folding technique into military radio antennas, a single slot antenna and an array of slot antennas can be used. The folded state can be helpful when the user is moving across terrains, since the antenna is lightweight, it would be much easier to carry. As they move towards a remote area, military personal could deploy the Miura Ori Slot antenna for a narrow band secure communication between the base of operation and the operators.



# Chapter 5

## Substrate Integrated Waveguide Antennas

### 5.1 Introduction

Most waveguides are hollow or have air as the substrate, but researchers were able to switch to various material as a substitute given the permittivity ( $\epsilon_r$ ) and loss tangent ( $\tan\delta$ ). This led to a new waveguide design named Substrate Integrated Waveguide (SIW). It is formed of a Dielectric-filled Waveguide (DFW) with metal vias connecting the top and bottom layer by creating side walls. It is an inexpensive way of fabricating because it uses etching on both sides of metal to create the antenna design.

Many satellites use waveguides within their payload system. This is a concerning fact as satellites are becoming more complicated to shape for specific missions or telecommunications. This leads to intricate waveguide designs, however the available space within the payload system is limited. Using SIW could potentially change the waveguide designs, as it reduces weight, which is one of the major issues within payload system. Additionally, antenna could be used within SIW at the top level.

In this chapter, a SIW antenna will be studied similarly to Chapter 4. It would involve

the use of the Miura Ori folding technique. By investigating inner and folding angle, it will be able to determine the performance of a single and a 2 by 1 array of SIW antennas. This chapter consists of simulations only. There would be no fabrication or testing involved due to a shortage of technicians, that were able to fabricate the design. The antenna design required a set of uniform holes for vias, the current technician did not have enough experience to fabricate such a complicated antenna and the University had yet to find the replacement staff to fabricate antenna designs.

## 5.2 Substrate Integrated Waveguides

Rectangular waveguide is a hollow metal cavity filled with air. Normally rectangular waveguide is made with a single conductor [49]. There is an infinite amount of applications for using waveguide, as it carries electromagnetic waves across the cavity. Waveguide has many different modes, the rectangular waveguides, can be designed in such a way that the frequency will only operate at one mode. The size of the waveguide ( $W$ ) and its frequency can be determined. The greater the size of the waveguide ( $W$ ), the longer the wavelength ( $\lambda = 2W$ ). Frequency is defined as  $f = \frac{c}{\lambda}; = \frac{c}{2W}$ .

Calculating the cut off frequency of any mode of a rectangular waveguide can be achieved using (5.1), where:  $c$  is the Speed of Light;  $m, n$  are mode numbers;  $a$  and  $b$  are dimensions of the waveguide. For the  $TE_{10}$  mode, the formula is simplified, (5.2). When there is an dielectric substrate within the waveguide, calculations for ( $a_d$ ) are performed with (5.3). When calculating the width ( $a_s$ ) of the substrate integrated waveguide created by the vias, (5.4) can be used, where:  $d$  is the diameter of the via and  $p$  is the distance between the vias. For the designs, there are conditions that are required to create a SIW which are shown in (5.5) where the guided wavelength is given by (5.6).

$$f_c = \frac{c}{2\pi} \sqrt{\left(\frac{m\pi}{a}\right)^2 + \left(\frac{n\pi}{b}\right)^2} \quad (5.1)$$

$$f_c = \frac{c}{2a} \quad (5.2)$$

$$a_d = \frac{a}{\sqrt{\epsilon_r}} \quad (5.3)$$

$$a_s = a_d + \frac{d^2}{0.95p} \quad (5.4)$$

$$\begin{aligned} d &< \frac{\lambda_g}{5} \\ p &< 2d \end{aligned} \quad (5.5)$$

$$\lambda_g = \frac{2\pi}{\sqrt{\frac{\epsilon_r(2\pi f)^2}{c^2} - \left(\frac{\pi}{a}\right)^2}} \quad (5.6)$$

There are some advantages and disadvantages of using SIW.

Advantage include:

- Power handling is higher than Printed Circuit Board (PCB) or Microstrip;
- Radiation loss are lower;
- Cost of fabrication is significantly lower;
- With the use of metal on top and bottom, the conductor loss is lower.

Disadvantage include:

- Leakage loss is bigger depending on the pitch of each vias;
- With the use of dielectric in a waveguide, it adds dielectric loss as the SIW comparing with air substrate in a rectangular waveguide.

### 5.3 Academic Research on Substrate Integrated Waveguides

The use of Substrate integrated waveguide (SIW) has been increasingly popular due the low profile, light weight and consistent integration with planar circuits. SIW could be fabricated and manufactured at a very low cost. There are many researches [50–53] that have implemented antenna designs with the use of SIW.

D. George [54] presented in the journal of Physics, a slotted antenna, based on using Epsilon Near Zero (ENZ) material and used vias to create a radiating slotted SIW antenna. D. George used Duroid 5880 with a permittivity ( $\epsilon_r$ ) of 2.2 and a loss tangent ( $\tan\delta$ ) of 0.0009. She performed a number of studies on thickness, slot width, waveguide width and waveguide length. In the D. George final design, she has chosen the thickness of 0.254 mm. In [54, Fig. 5.1], the operating frequency was at 5.97 GHz with a bandwidth of 82.7 MHz and the gain of the proposed antenna was 5.29 dBi.

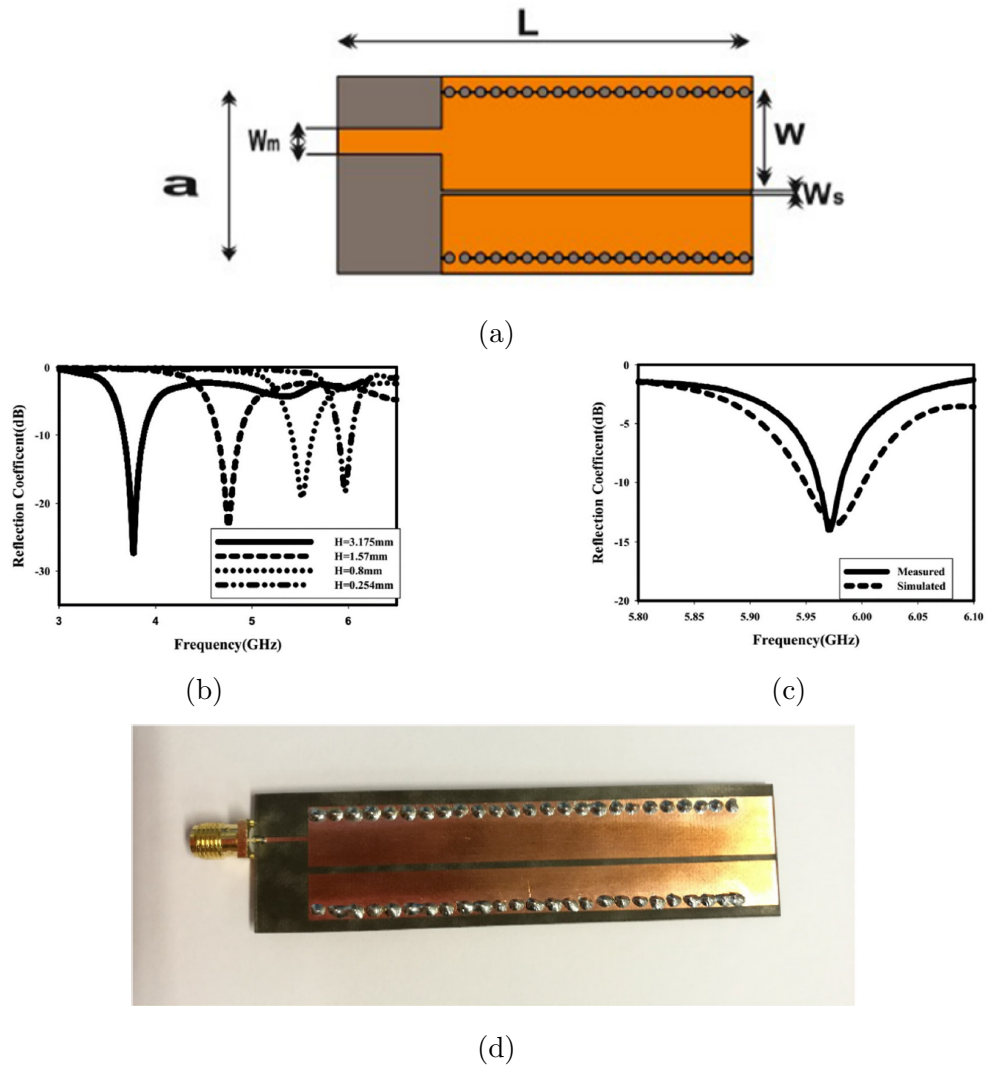


Figure 5.1: High-gain narrow-band slotted antenna based on ENZ SIW structure: (a) Substrate Integrated Waveguide ENZ Antenna; (b) Reflection Coefficient with various height; (c) Simulated and Measured reflection coefficient; (d) Fabricated Antenna Structure [54]

J. Bai had implemented an SIW antenna design based on flexible metamaterial [55]. J. Bai used Rogers RT5880 that had a permittivity ( $\epsilon_r$ ) of 2.2 and thickness ( $\tan\delta$ ) of 0.508 mm. The substrate was etched with a metamaterial unit like a magnetic resonator. It was called complementary Electric-LC (cELC) metamaterial units, as shown in [55, Fig. 5.2a]. The resonant frequency could be varied. To achieve dual frequency antenna, J. Bai created four cELC units with different width ( $g$ ). In [55, Fig. 5.2b]. The proposed antenna achieved the resonant frequencies at 31.58 GHz and 35.64 GHz. The directivity of each resonant frequencies were 5.73 dBi and 6.53 dBi respectively, see [55, Fig. 5.2c].

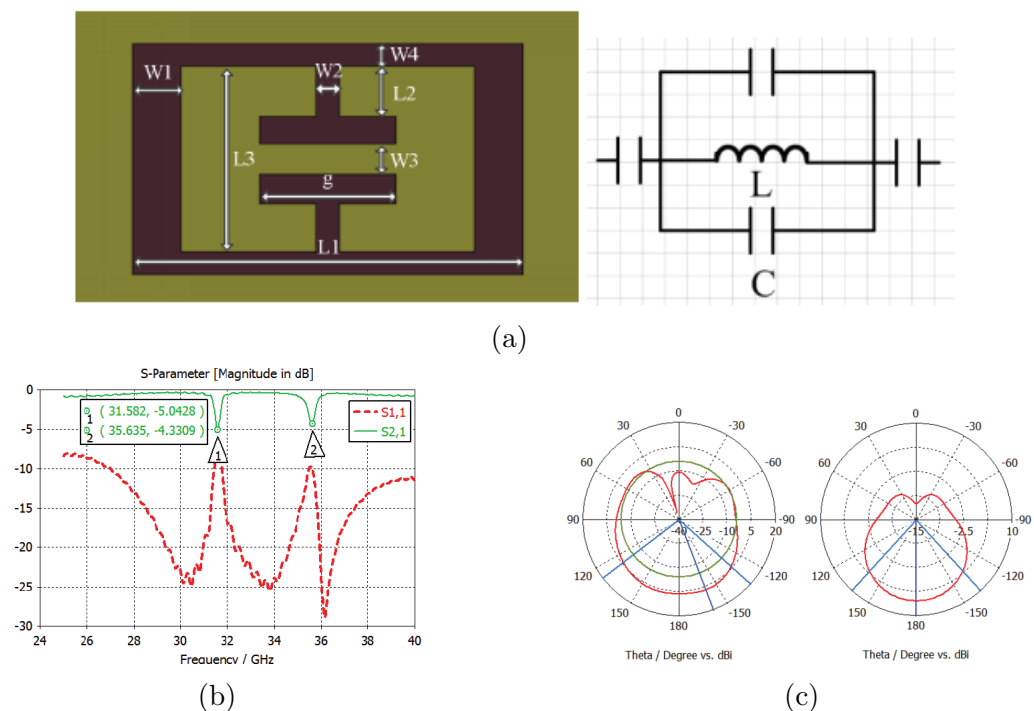


Figure 5.2: Flexible dual-frequency substrate integrated waveguide antenna based on metamaterial: (a) Individual cELC unit and the equivalent circuit; (b) Reflection Coefficient with four cELC units; (c) Radiation Pattern at 35.63 GHz [55]

Polyethylene Terephthalate (PET) is a cheap and flexible material. Riccardo Moro and Maurizio Bozzi [56] utilised the material and designed transmission lines, filters and antennas with the use of SIW. The first SIW design made by R. Moro and M. Bozzi was a SIW filter, as shown in [56, Fig. 5.3a]. It created a band-pass filter at 5 GHz with a measured insertion loss of 7 dB shown in [56, Fig. 5.3b]. The second SIW design, R. Moro and M. Bozzi proposed a slotted SIW antenna, see [56, Fig. 5.3c],

it consisted of four radiating elements. The linear slots were placed on the top of the SIW. In [56, Fig. 5.3d], the resonant frequency was at 5 GHz with a bandwidth of 400 MHz.

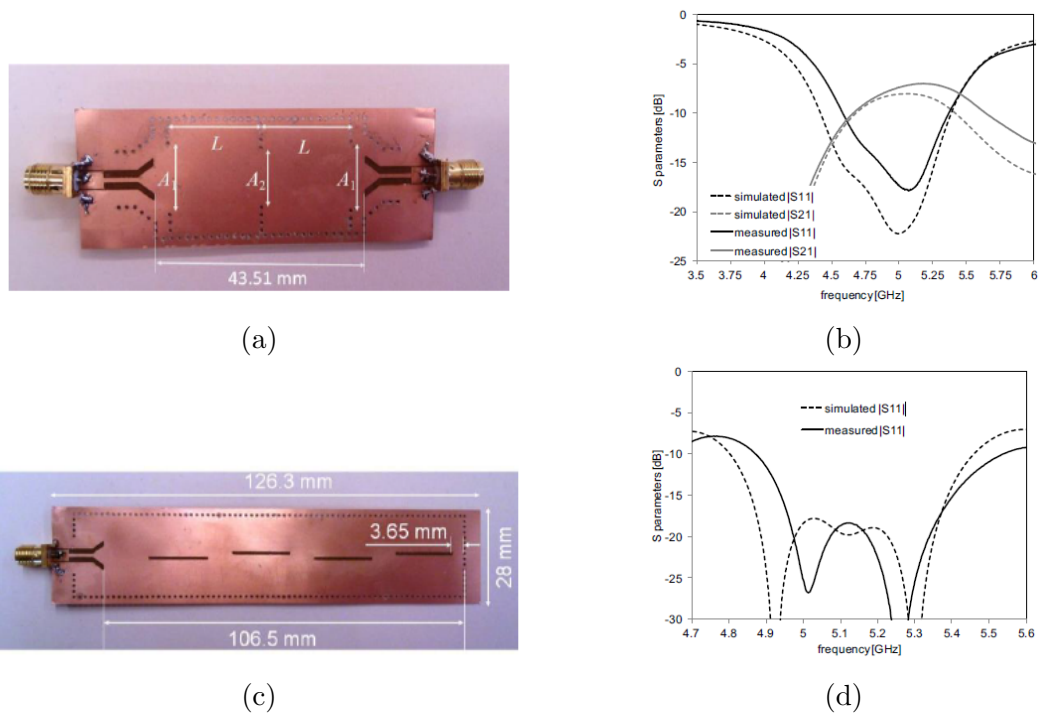


Figure 5.3: Plastic-based Substrate Integrated Waveguide (SIW) Components and Antennas: (a) Substrate Integrated Waveguide filter on PET substrate; (b) Simulated and Measured response; (c) Slotted SIW Waveguide Antenna; (d) Simulated and Measured of proposed antenna [56]

In 2014, A. Ghiotto had used multi-layered Printed Circuit Board (PCB) to create an air-filled SIW [57]. An air filled SIW was used due to low cost of manufacturing, high integration density, low weight and low insertion loss. The design introduced a standard SIW design into a linear tapered design, which was transitioned into an air filled SIW, shown in [57, Fig. 5.4].

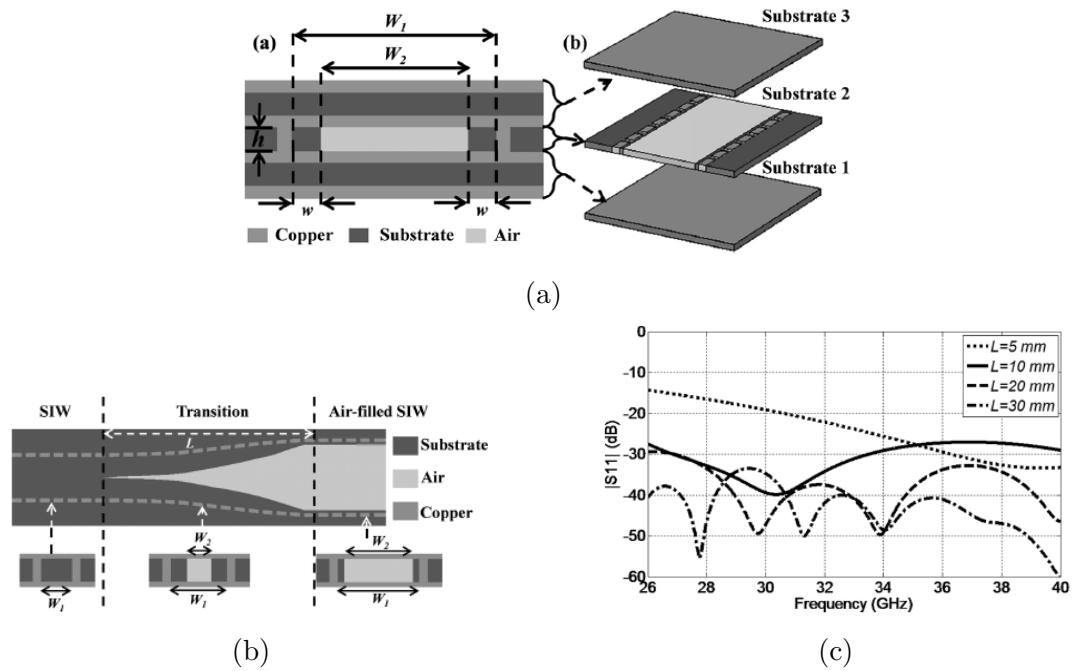


Figure 5.4: Air-Filled Substrate Integrated Waveguide A Flexible and Low Loss Technological Platform: (a) Air Filled SIW; (b) Proposed Tapered Transition; (c) Simulated Reflection Coefficient in Ka-Band [57]

Y. Luo [58] had demonstrated a SIW made with a thin substrate using a horn antenna, as shown in [58, Fig. 5.5a]. It achieved a 1 by 4 planar array design with an operating frequency of 12.4 GHz, in [58, Fig. 5.5b]. The proposed design used a thin substrate Rogers 6006 with a thickness of 2.5 mm. Y. Luo used SIW to create a side wall leaving an aperture in the centre, similarly to a standard horn antenna. Y. Luo included additional slots that radiated power together, along with the aperture of the horn antenna. In [58, Fig. 5.5c], the measured gain of the array antenna was 19.4 dBi at the operating frequency of 12.4 GHz.



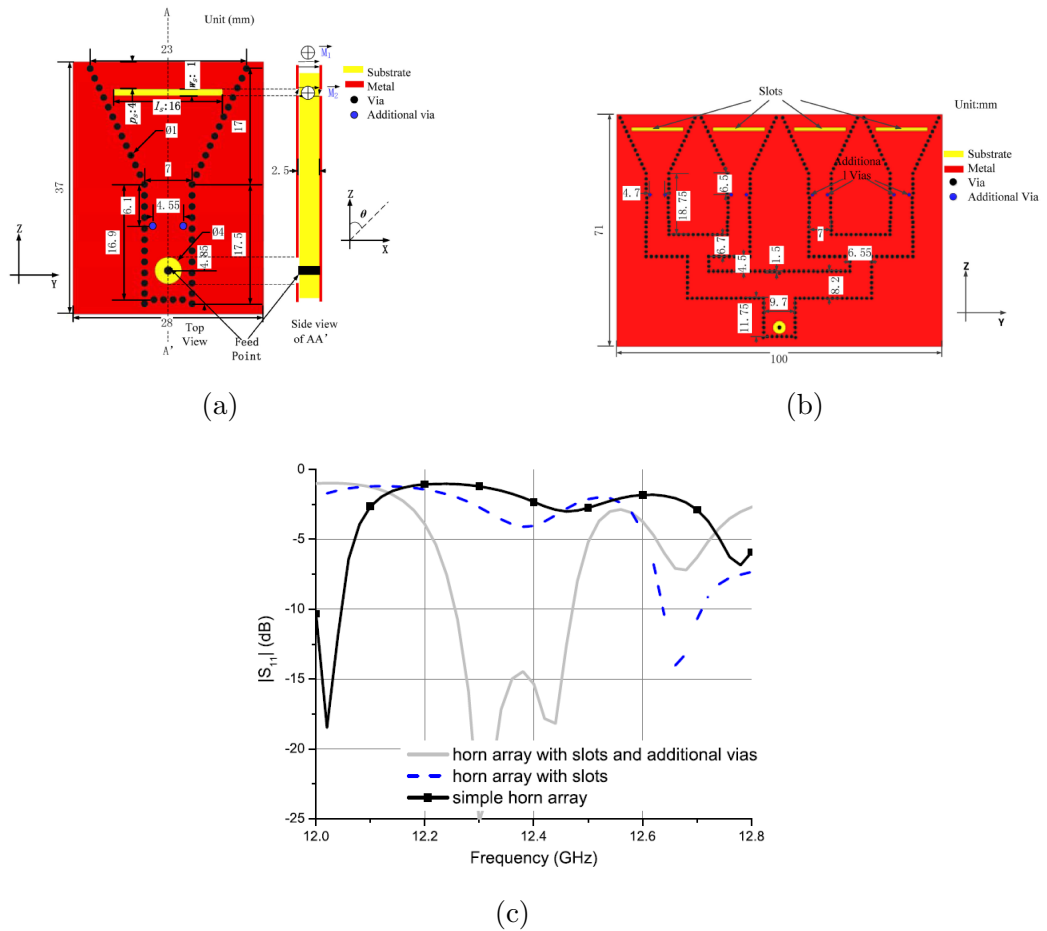
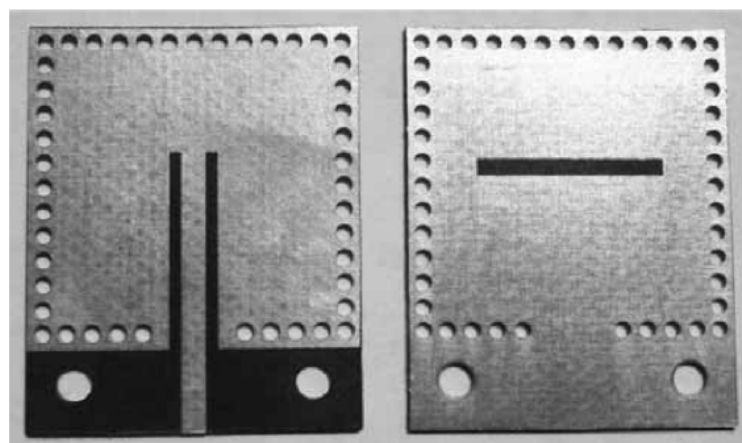
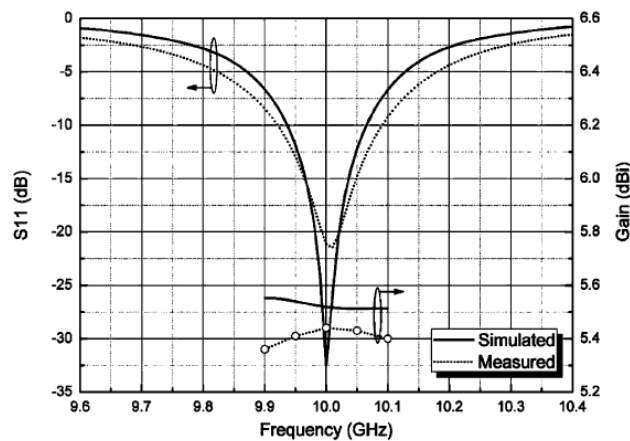


Figure 5.5: Substrate Integrated Waveguide Horn Antenna on Thin Substrate With Back-Lobe Suppression and Its Application to Arrays: (a) Top and Side view of SIW horn Antenna; (b) SIW Horn Antenna Array 1 by 4; (c) Simulated reflection coefficient with the effect on slots and vias [58]

G. Luo [59] had created a novel design method of using a slot antenna with a SIW cavity. The SIW slot antenna had a narrow bandwidth, due to the thickness of the substrate, therefore varying the thickness of the substrate could potentially increase the bandwidth. G. Luo managed to tune the slot length at a certain length, since it influenced radiation efficiency. The antenna design used a 0.5 mm Rogers Duroid 5880 with a permittivity ( $\epsilon_r$ ) of 2.2, it used SIW to act as a cavity. In [59, Fig. 5.6b], the operating frequency was at 10 GHz with a simulated and measured bandwidth of 140 MHz and 170 MHz respectively. The antenna had a gain value above 5.3 dBi at the operating frequency with a linear polarisation.



(a)



(b)

Figure 5.6: Planar Slot Antenna Backed by Substrate Integrated Waveguide Cavity: (a) Proposed SIW Cavity planar slot antenna; (b) Simulated and measured reflection coefficient and gain [59]

## 5.4 Substrate Integrated Waveguide Antennas

A flexible SIW antenna, could be useful for several applications. This SIW antenna was using a microstrip fed into an open slot antenna as shown in Fig. 5.7. This design was based on D. George [54] design. Instead of using Roger 5880, Kapton was used as a flexible substrate. The design of the antenna was simulated and optimised first on a 2-Dimensional (2-D) plane. The SIW antenna was then applied with the Miura Ori folding technique.

### 5.4.1 Single SIW Antenna - Design

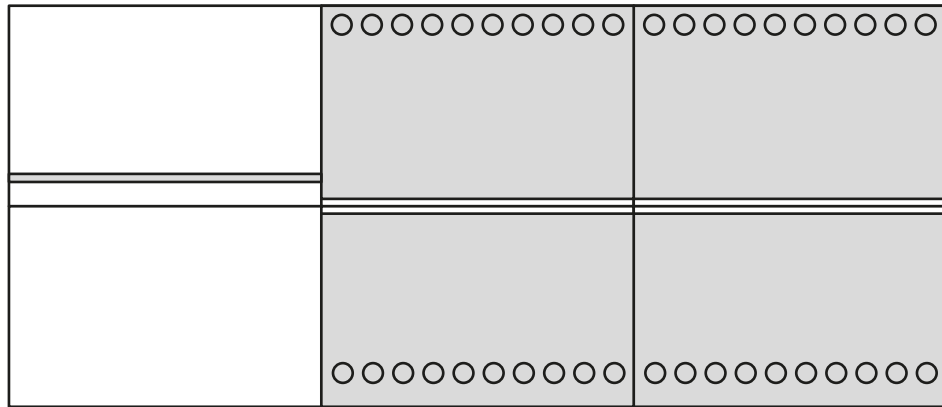


Figure 5.7: Single SIW Slot Antenna Design

This SIW antenna design used an open slot to fold, and the width, where the microstrip was fed from to determine the resonant frequency ( $Wl$ ). The parameters of the design are shown in Fig. 5.10 where: the width ( $a$ ) and length ( $b$ ) of each parallelogram, including the width of the slot, the pitch between each of the vias ( $p$ ) and the diameter of each via holes ( $d$ ) can be seen. Inner angle ( $\alpha$ ) and Folding angle ( $\beta$ ) were the main focus of this chapter, where they were analysed to determine  $S_{11}$  value, as well as, the gain of the antennas at the resonant frequency, through a set of simulations shown in Section 5.4.2.

The substrate used in that antenna was Kapton HN. It had a thickness ( $T$ ) of 0.125 mm and a permittivity ( $\epsilon_r$ ) of 3.5 with a loss tangent ( $\tan\delta$ ) of 0.0026. Given

the permittivity ( $\epsilon_r$ ) and the thickness of the substrate ( $T$ ), the width of the microstrip ( $ms$ ) was calculated to be 0.3 mm, as the input characteristic impedance was  $50 \Omega$ , using the microstrip line equation from Section 3.2.1.

Similar to Chapter 4, the SIW antenna design was investigated on a 2-D planar view by using the following parameters: the width from the centre to the via wall  $Wl$ , the slot width across the entire SIW antenna ( $sw$ ) and the microstrip offset from the edge the slot ( $MOffset$ ). A discrete port of  $50 \Omega$  was added at the beginning of the microstrip line. The width from the centre to the via wall ( $Wl$ ) was to be investigated first, see Fig. 5.8. The peak  $S_{11}$  performance was -28 dB, when  $Wl = 8.65$  mm, with a 10 dB reflection coefficient bandwidth of 100 MHz. There was a shift in the resonant frequency, as the the width from the centre to the via wall  $Wl$  shorten.

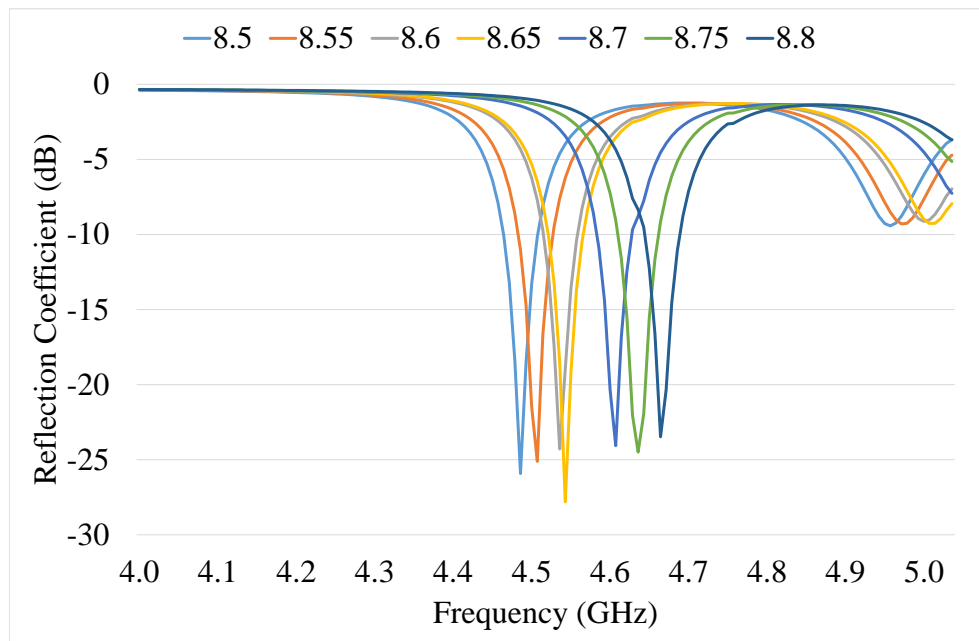
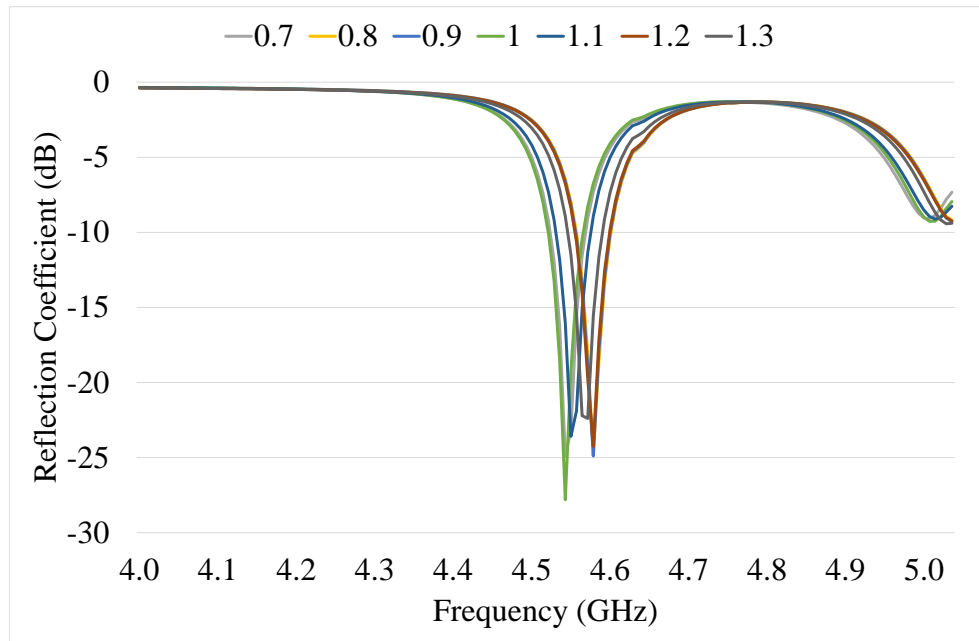


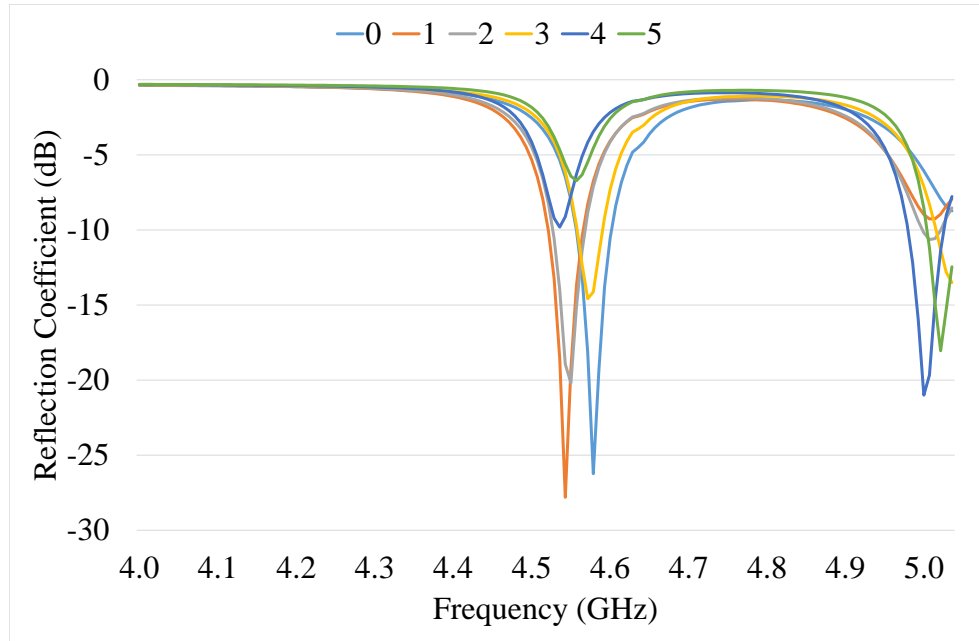
Figure 5.8: Single SIW Slot Antenna - Offset Sweep

The slot width ( $sw$ ) was varied between 0.7 mm and 1.3 mm, as seen in Fig. 5.9a. The  $S_{11}$  performances were below -20 dB with a bandwidth of 100 MHz. When  $sw = 0.7$  mm, the resonant frequency was at 4.55 GHz. The resonant frequency shifted slightly to 4.58 GHz, when  $sw = 1.3$  mm, by changing the microstrip offset

from the slot ( $MOffset$ ) between 0 mm and 5 mm, as shown in Fig. 5.9b. When  $MOffset = 0$  mm, the resonant frequency was at 4.57 GHz with a bandwidth of 50 MHz. When  $MOffset = 5$  mm,  $S_{11}$  has raised up to -7 dB, meaning that there was only 80% of the power send towards the antenna with 20% reflecting back to the input.



(a)



(b)

Figure 5.9: Single SIW Slot Antenna - (a) Slot Width Sweep; (b) MOffset Sweep

Table 5.1: Single SIW Slot Antenna - Table of Parameters

Parameters		Values ( <i>mm</i> )
Length	( <i>a</i> )	20
Width	( <i>b</i> )	20
Permittivity	( $\epsilon_r$ )	3.54
Substrate Thickness	( <i>T</i> )	0.125
Microstrip Width	( <i>ms</i> )	0.3
Microstrip offset	( <i>MOffset</i> )	1
Width from Slot to wall	( <i>Wl</i> )	8.65
Pitch distance	( <i>p</i> )	1.5
Diameter of vias	( <i>d</i> )	1
Inner Angle	( $\alpha$ )	Parameterise
Folding Angle	( $\beta$ )	Parameterise

The dimension diagram of a single SIW antenna was shown in Fig. 5.10. All the parameter values were as shown in Table 5.1. This diagram display the inner angle ( $\alpha$ ) and the folding angle ( $\beta$ ), which would be the main focus of this chapter.

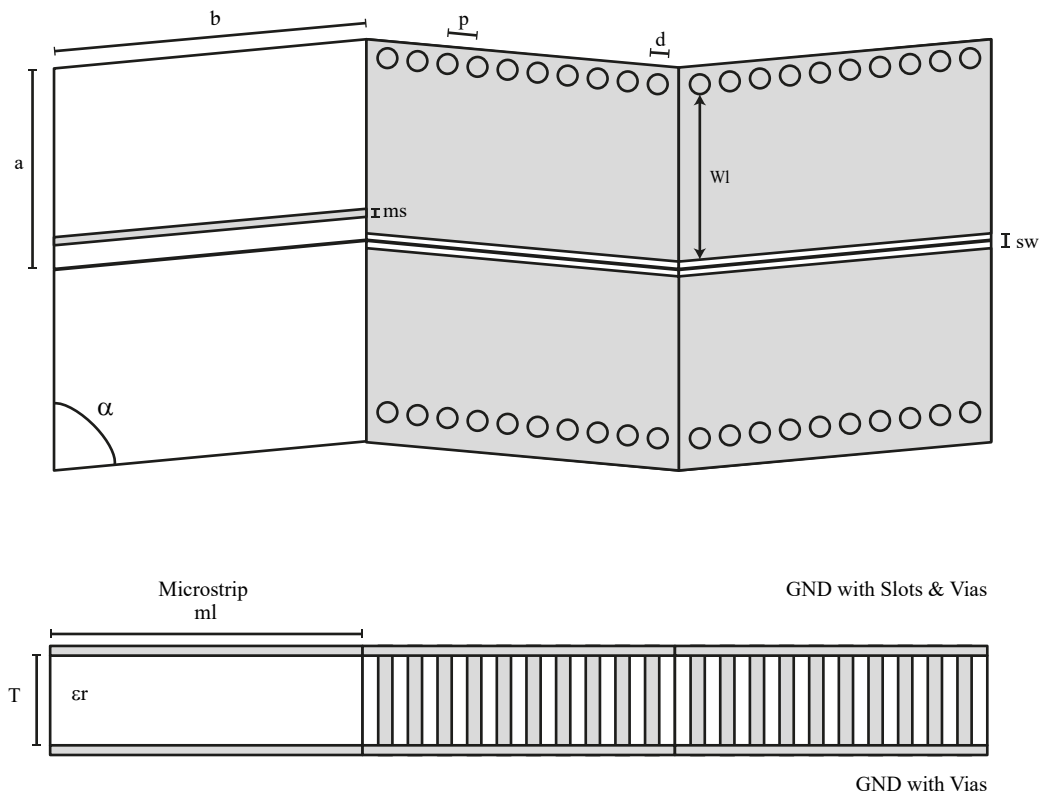
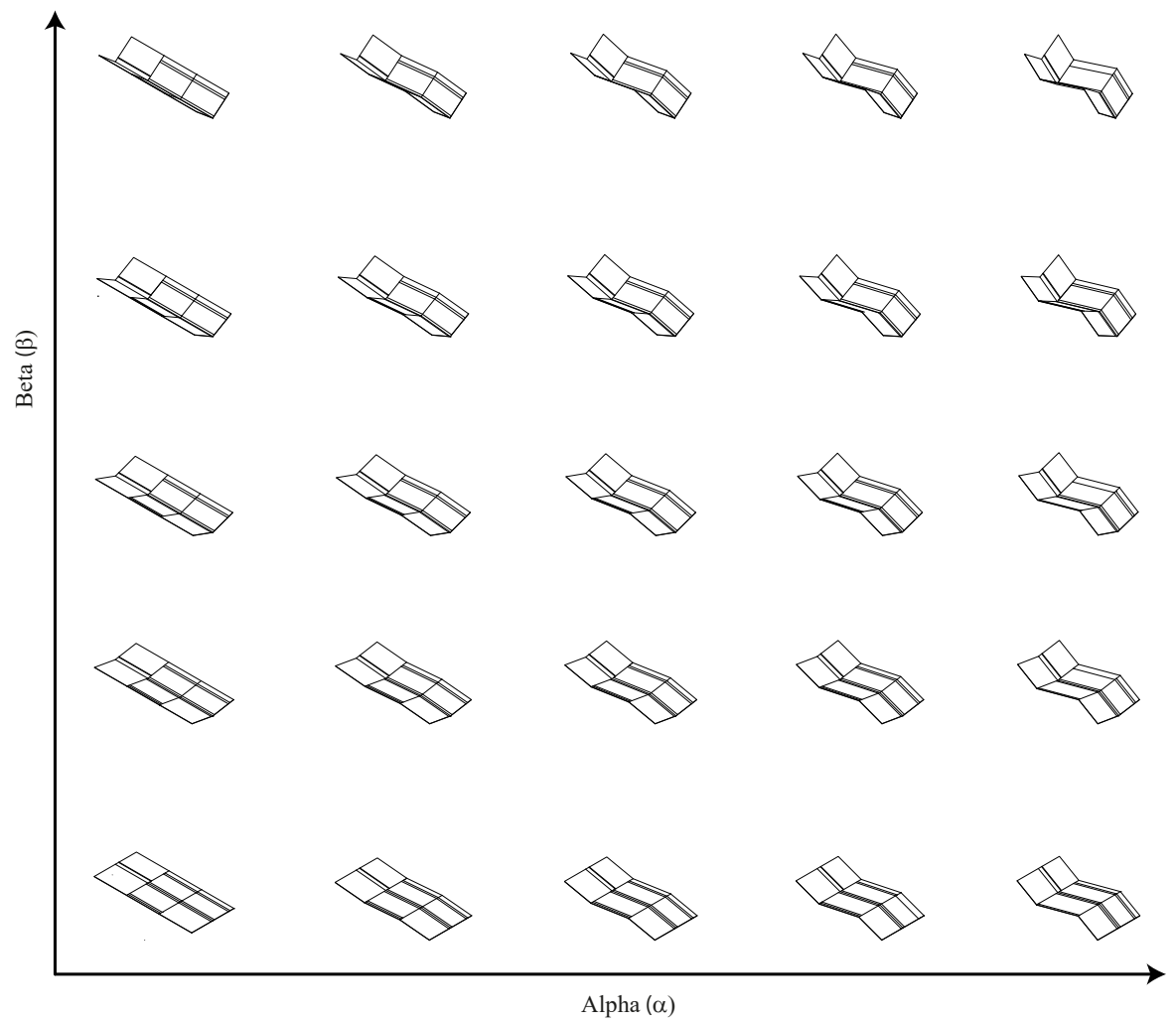


Figure 5.10: Single SIW Slot Antenna - Dimension Chart

The antenna design was created in the Computer Simulation Technology (CST) Studio. The antenna design was applied with the Miuri Ori folding technique from Section 2.2.3. The explanation of transforming 3-D polygon curves into a solid object can be found in Section 4.4.1. Fig. 5.11 represents the variation of the inner angle ( $\alpha$ ) from  $0^\circ$  to  $20^\circ$  and the folding angle ( $\beta$ ) between  $0^\circ$  and  $40^\circ$ . This created possible 25 variations between the two angles. This investigation was to determine if there would be a change in  $S_{11}$  and the gain at the resonant frequency, as the 3-D antenna design was varied.

Figure 5.11: Change in  $\alpha$  and  $\beta$



### 5.4.2 Single SIW Antenna - Simulated Results

In this section, a single SIW antenna was simulated with the parameters shown in Table 5.1. The antenna was design in an XY-plane, the far-field plots were saved on the XZ-axis, where it displayed the intended radiation pattern. The far-field plots included the co-polar and cross-polar plots. The co-polar plots plane was at  $\text{PHI} = 0^\circ$ . As for the cross-polar plot, the plane was at  $\text{PHI} = 90^\circ$ , perpendicular to the intended radiation. The resonant frequency,  $S_{11}$ , maximum gain value, as well as, the radiating angle for each configurations were simulated and exported into Microsoft Excel.

Fig. 5.12 displays all S-Parameter plots and Fig. 5.13 presents the co-polar and cross-polar plots with all possible configuration given in Fig. 5.11.

Table 5.2: Single SIW Slot Antenna - Resonant Frequency (GHz)

		Inner Angle ( $\alpha$ )				
		$0^\circ$	$5^\circ$	$10^\circ$	$15^\circ$	$20^\circ$
Folding Angle ( $\beta$ )	$0^\circ$	4.55	4.56	4.61	4.66	4.72
	$10^\circ$	4.54	4.56	4.61	4.67	4.74
	$20^\circ$	4.54	4.59	4.61	4.67	4.74
	$30^\circ$	4.57	4.59	4.62	4.67	4.74
	$40^\circ$	4.55	4.59	4.62	4.67	4.74

The Table 5.2 highlights the resonant frequency at all 25 configurations. The open slot SIW antenna was intended to operate at 4.5 GHz. When  $\alpha = 0^\circ$ , it could be seen that the resonant frequency fluctuated between each folding angle. However, when  $\alpha = 5^\circ$ , there was a gentle increase in the resonant frequency from 4.56 GHz when  $\beta = 0^\circ$ , to 4.59 GHz when  $\beta = 40^\circ$ . There was a noticeable increase in the resonant frequency as the inner angle increases. When  $\beta = 0^\circ$ , the resonant frequency increased from 4.55 GHz when  $\alpha = 0^\circ$ , to 4.72 GHz when  $\alpha = 20^\circ$ .

Overall, there was a clear upward trend when varying the inner angle ( $\alpha$ ). The resonant

frequency increased on average by 180 MHz. However, when varying the folding angle ( $\beta$ ), the resonant frequency fluctuated by a small amount.

Table 5.3: Single SIW Slot Antenna - Reflection coefficient (dB)

		Inner Angle ( $\alpha$ )				
		$0^\circ$	$5^\circ$	$10^\circ$	$15^\circ$	$20^\circ$
Folding Angle ( $\beta$ )	$0^\circ$	-20.58	-31.06	-26.23	-22.62	-20.56
	$10^\circ$	-19.12	-27.51	-32.75	-22.53	-25.05
	$20^\circ$	-16.65	-20.95	-34.67	-31.90	-25.41
	$30^\circ$	-13.45	-16.57	-22.25	-32.19	-30.35
	$40^\circ$	-10.62	-13.13	-16.87	-21.80	-37.82

Table 5.3 compared  $S_{11}$  in dB at the resonant frequency across all inner and folding angle. It could be seen that the  $S_{11}$  dropped considerably as the folding angle  $\beta$  was when  $\alpha = 0^\circ$ .  $S_{11}$  dropped from -20.58 dB when  $\beta = 0^\circ$ , to -10.62 dB when  $\beta = 40^\circ$ . However, when  $\alpha = 20^\circ$ ,  $S_{11}$  increased by a significant amount, from -20.56 dB when  $\beta = 0^\circ$ , to -37.82 dB when  $\beta = 40^\circ$ . When changing the inner angle ( $\alpha$ ),  $S_{11}$  varied around -24.21 dB on average when  $\beta = 0^\circ$ . Fig. 5.12 also showed the 10 dB reflection coefficient bandwidth, as an average, the bandwidth was 80 MHz.

In conclusion,  $S_{11}$  decreased substantially as the folding angle increased when  $\alpha = 0^\circ$ . However, the peak value shifted as the inner angle changed. Even though  $S_{11}$  decreased when  $\alpha = 0^\circ$ ,  $S_{11}$  increased dramatically as  $\alpha = 20^\circ$ .

Table 5.4 uses the maximum gain value in dBi at the resonant frequency on each configuration. The maximum gain values were gathered from the co-polar plots in Fig. 5.13. The maximum gain value across all configurations was at 2.46 dBi when  $\alpha = 20^\circ$  and  $\beta = 20^\circ$ . When  $\beta = 10^\circ$ , it was clear that it was consistently the highest gain value, comparing to other folding angles. Furthermore, as the folding angle ( $\beta$ ) increased, the maximum gain value, for  $\alpha = 0^\circ$  decreased steadily from 2.01 dBi when  $\beta = 0^\circ$ , to 1.18 dBi when  $\beta = 40^\circ$ . When  $\beta = 10^\circ$ , the maximum gain value increased

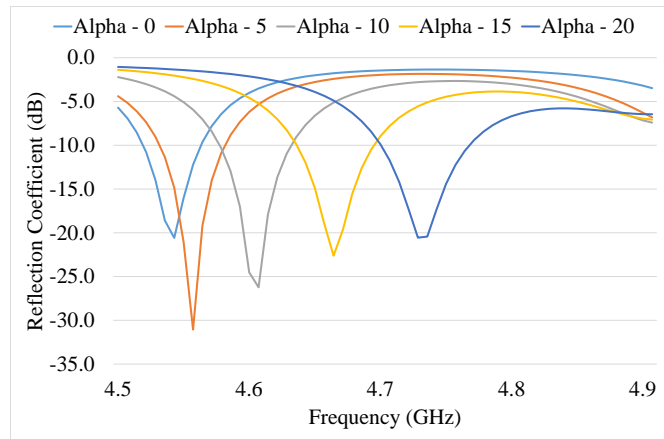
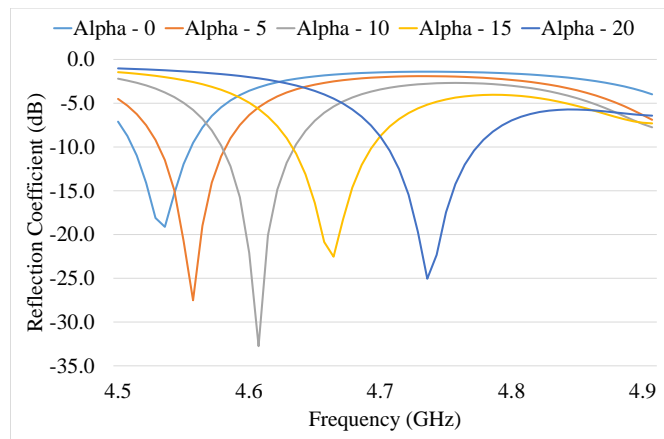
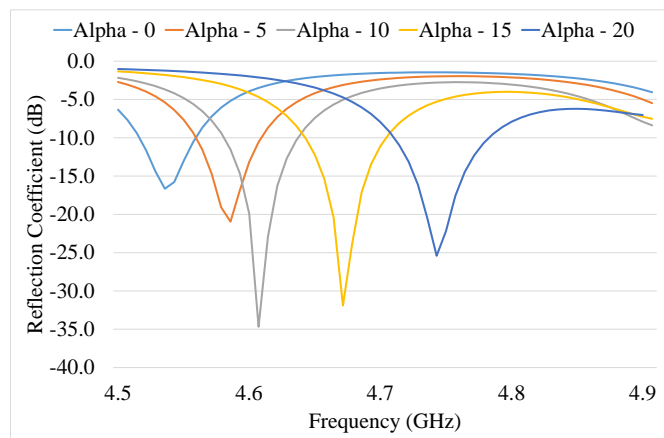
slightly from 2.18 dBi when  $\alpha = 0^\circ$ , to 2.46 dBi when  $\alpha = 20^\circ$ .

Table 5.4: Single SIW Slot Antenna - Gain (dBi)

		Inner Angle ( $\alpha$ )				
		$0^\circ$	$5^\circ$	$10^\circ$	$15^\circ$	$20^\circ$
Folding Angle ( $\beta$ )	$0^\circ$	2.01	2.08	2.09	2.24	2.29
	$10^\circ$	2.18	2.26	2.31	2.36	2.46
	$20^\circ$	2.15	2.27	2.23	2.36	2.35
	$30^\circ$	1.85	1.92	1.87	1.92	1.90
	$40^\circ$	1.18	1.22	1.08	1.15	1.08

Fig. 5.13 highlights the radiating angle and HPBW on the co-polar plots and the null region on the cross-polar plots. When varying the inner angle ( $\alpha$ ), it could be seen that there has been a shift in the radiating angle from  $0^\circ$  to  $10^\circ$ . The radiating angle was consistently half of the inner angle from  $0^\circ$ ,  $2.5^\circ$ ,  $5^\circ$ ,  $7.5^\circ$  and  $10^\circ$  respectively. The HPBW was 3 dBi below the maximum gain value, on average. The HPBW was at  $64^\circ$  across all configurations. On the cross-polar plots, as the folding angle increased, it could be seen that the null region shifted by a small amount when  $\alpha = 0^\circ$ , from  $0^\circ$  when  $\beta = 0^\circ$  to  $8^\circ$  when  $\beta = 40^\circ$ . When varying the inner angle, the null region shifted as the inner angle increased, however, when  $\alpha = 15^\circ$  and  $20^\circ$ , the null region shifted the other way into the negatives.

Overall, it could be seen that there was a downward trend as the folding angle increased. Nevertheless, it displayed an upward pattern as the inner angle increased.

(a)  $\alpha$  Sweep ;  $\beta = 0$ (b)  $\alpha$  Sweep ;  $\beta = 10$ (c)  $\alpha$  Sweep ;  $\beta = 20$

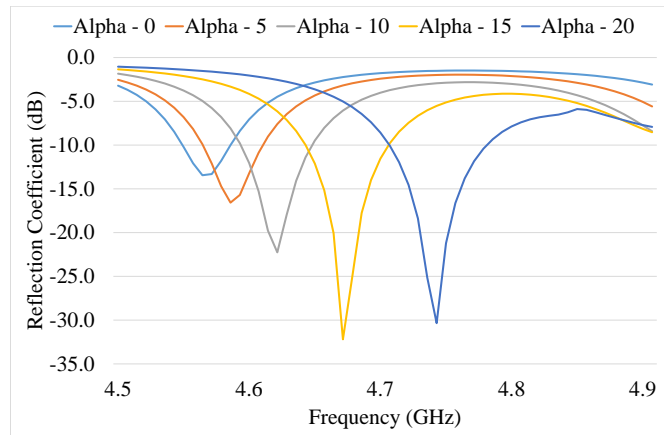
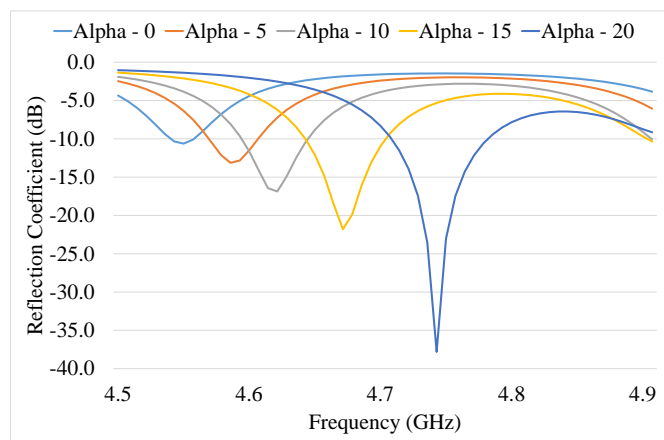
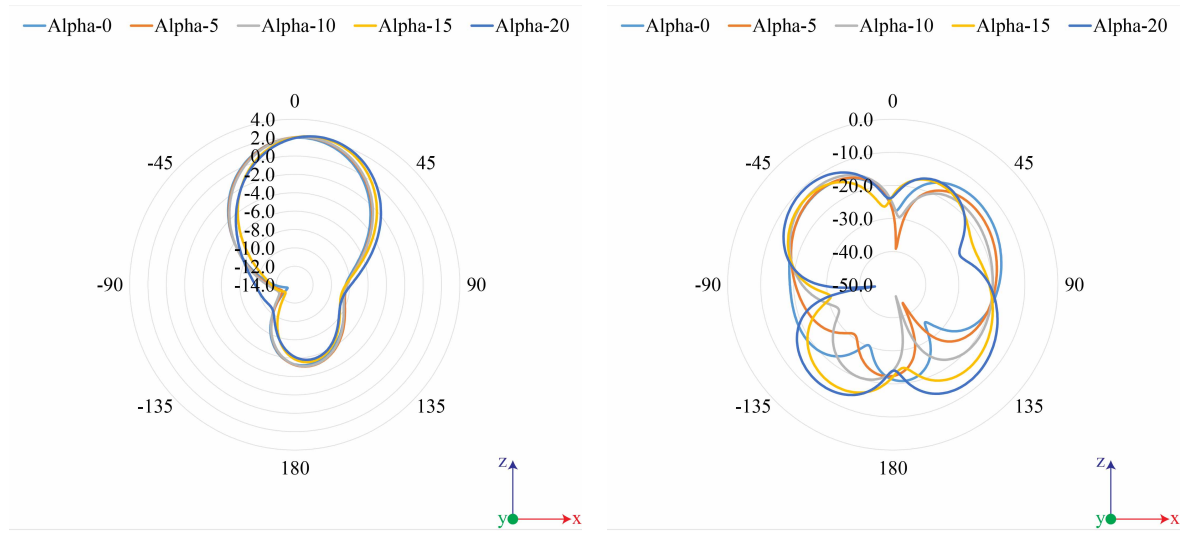
(d)  $\alpha$  Sweep ;  $\beta = 30$ (e)  $\alpha$  Sweep ;  $\beta = 40$ 

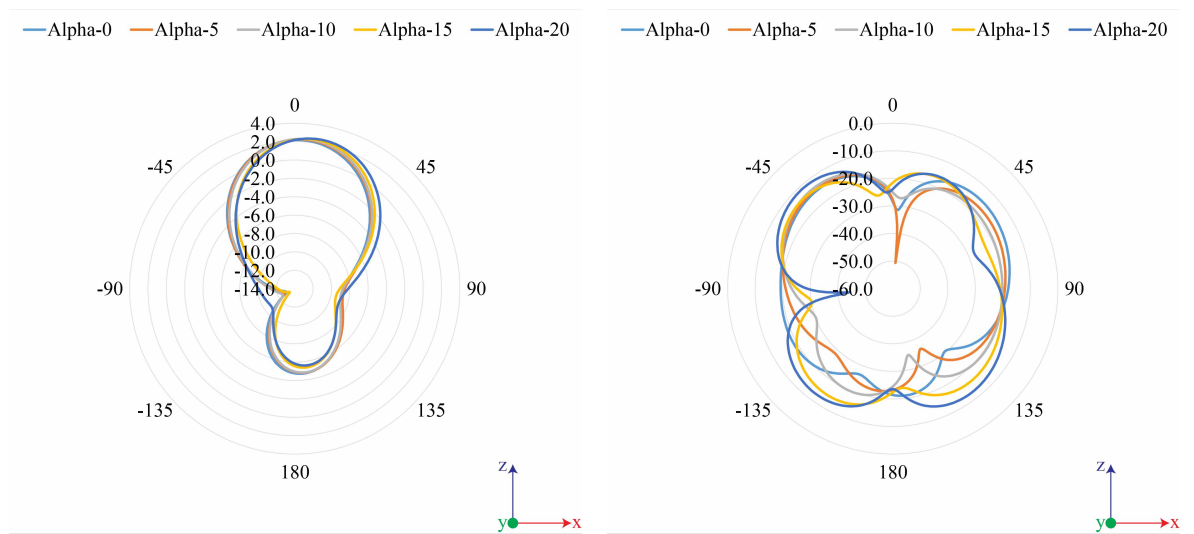
Figure 5.12: Single SIW Slot Antenna - Simulated Reflection Coefficient



(a) Co Polar

(b) Cross Polar

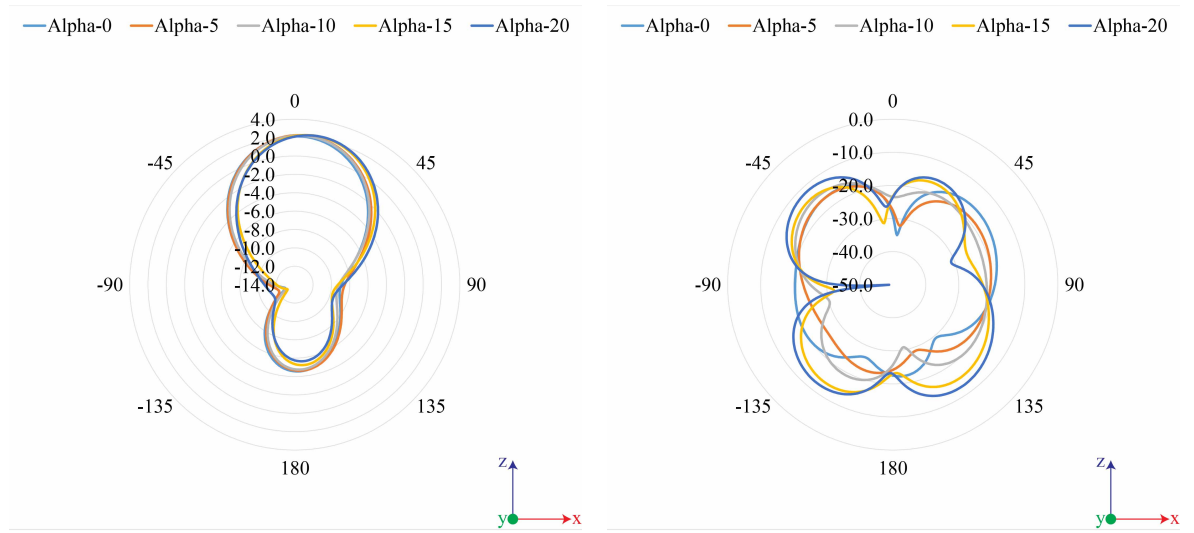
$\alpha$  Sweep ;  $\beta = 0$



(a) Co Polar

(b) Cross Polar

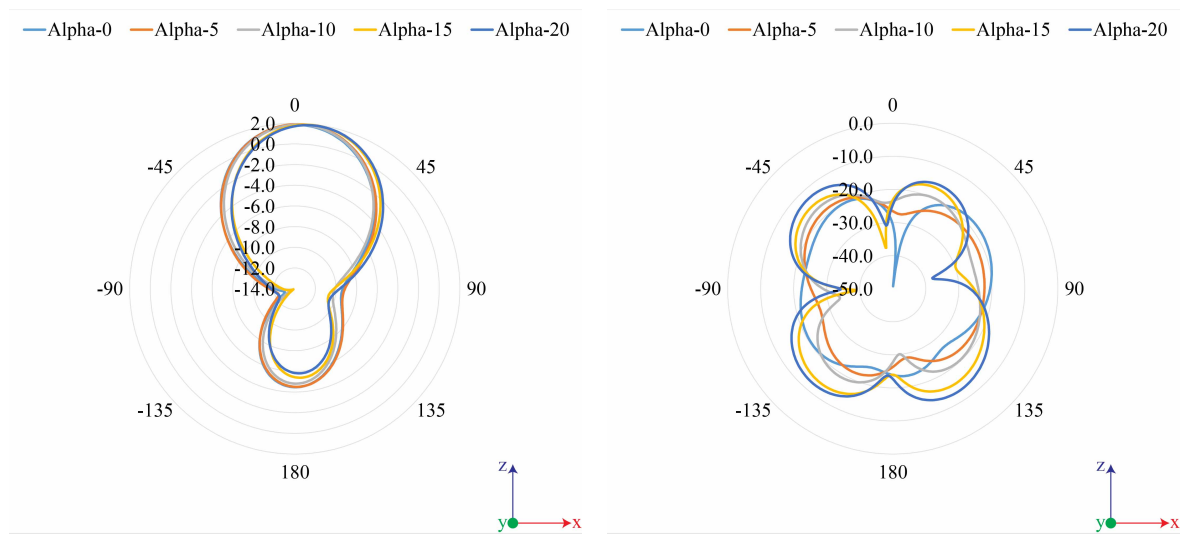
$\alpha$  Sweep ;  $\beta = 10$



(a) Co Polar

(b) Cross Polar

$\alpha$  Sweep ;  $\beta = 20$



(a) Co Polar

(b) Cross Polar

$\alpha$  Sweep ;  $\beta = 30$

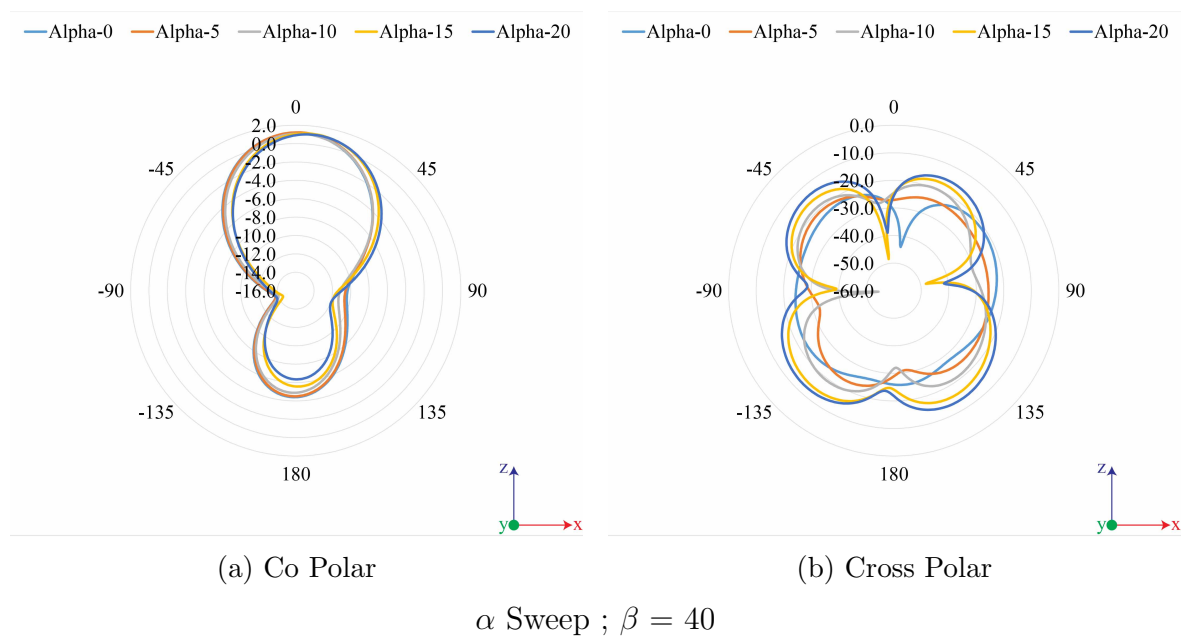


Figure 5.13: Single SIW Slot Antenna - Simulated Radiation Pattern



## 5.5 Arrays of SIW Antennas

To create an array of antennas, it was beneficial to understand the array pattern multiplication with the design. The process explained in Section 4.5, was utilised with the in-build function of the far-field array in CST Studio. As the inner and folding angle =  $0^\circ$ , the separation was moved by 2 times the length of the parallelogram. Fig. 5.14, displayed the co-polar and cross-polar plot of the total radiation pattern for a 2 by 1 array antenna, using the array pattern multiplication tool. The maximum gain raised to 4 dBi, as the null region was at -30 dBi.

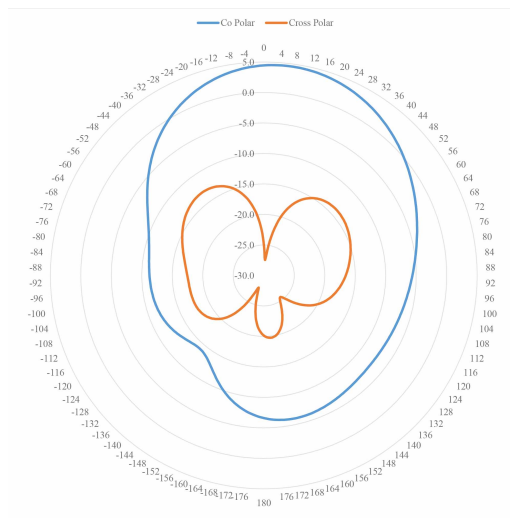


Figure 5.14: SIW Array Pattern Multiplication - Radiation Pattern

### 5.5.1 Arrays of SIW Antennas - Design

Similar to Section 5.4.2, the antenna design was mainly focused on the the impact of both inner angle ( $\alpha$ ) and the folding angle ( $\beta$ ). A matching network was required to connect the two SIW antennas together. This required using the quarter wave matching network from Section 3.2.2, to split the power across all antennas equally. The operating frequency, on average was 4.6 GHz, therefore  $\lambda/4 = 16.5$  mm. The full matching network can be seen in Fig. 5.15, and the length of each parameters are shown in Table 5.5.

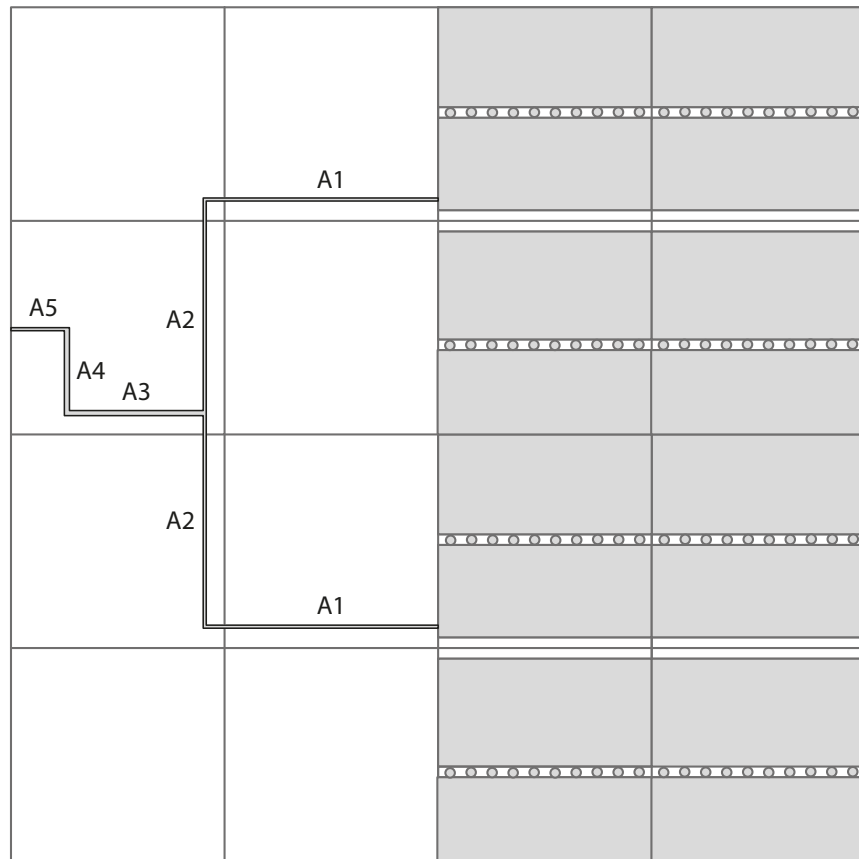
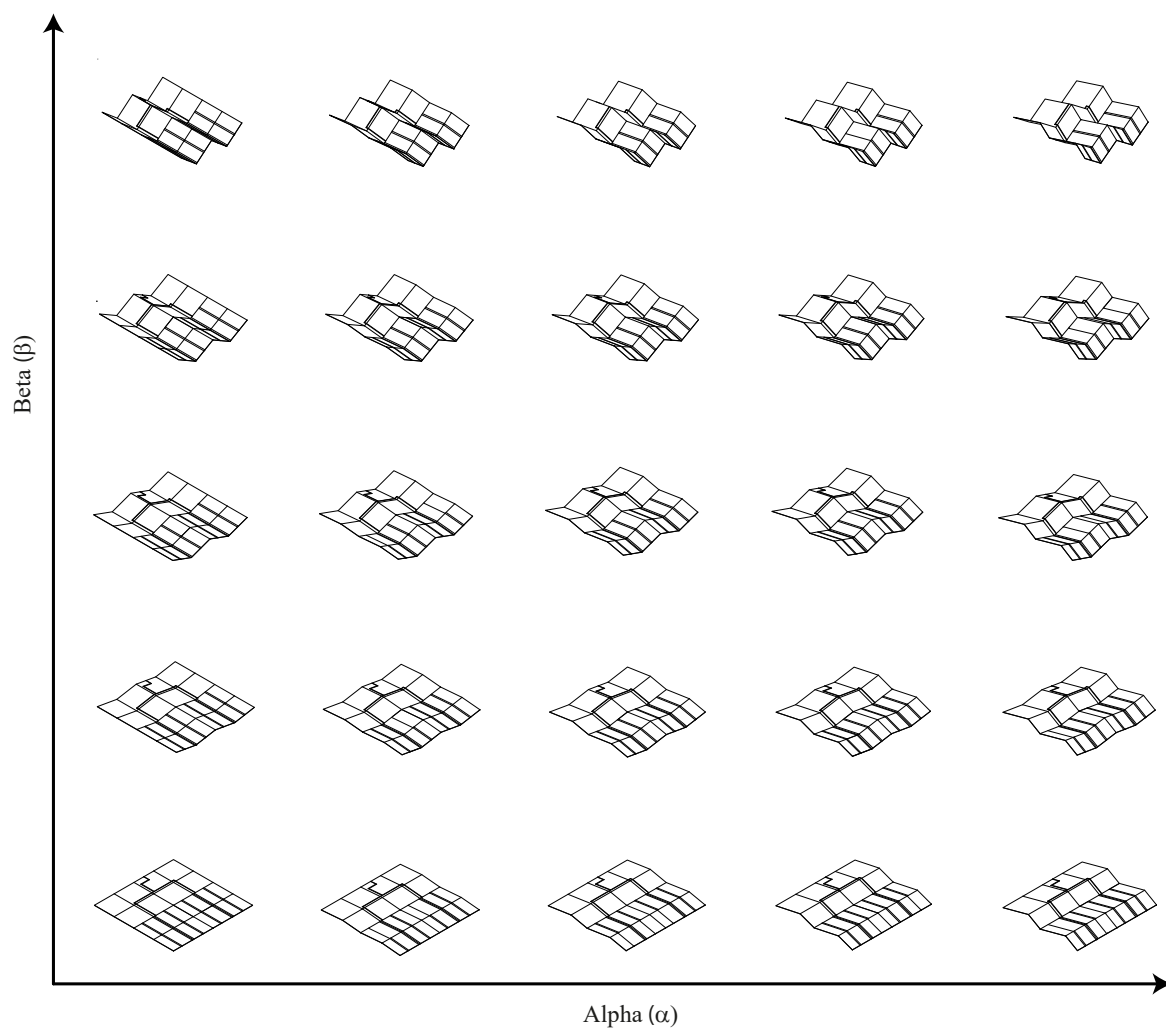


Figure 5.15: Matching Network

Table 5.5: Arrays of SIW Antennas - Matching Network Values

Parameters	Values ( <i>mm</i> )
A1	22
A2	19.905
A3	15.525
A4	7.7625
A5	5.475

The antenna design was added onto the new model with 2 SIW antennas next to each other, creating a 2 by 1 array. The method of creating the design with the Miura Ori folding technique was shown in Section 2.2.3. In Fig. 5.16, there are 25 possible configurations implementing the change in the inner ( $\alpha$ ) and folding ( $\beta$ ) angle. The inner angle ( $\alpha$ ) consisted of  $0^\circ$ ,  $5^\circ$ ,  $10^\circ$ ,  $15^\circ$ ,  $20^\circ$  and folding angle ( $\beta$ ) consisted of  $0^\circ$ ,  $10^\circ$ ,  $20^\circ$ ,  $30^\circ$ ,  $40^\circ$ .

Figure 5.16: Change in  $\alpha$  and  $\beta$

### 5.5.2 Arrays of SIW Antennas - Simulated Results

The simulation included all configurations with inner angles and folding angles, shown in Fig. 5.16. The simulated results were exported and plotted in Microsoft Excel. The simulated results included the reflection coefficient and far-field plots at the resonant frequency. To excite the antenna a  $50 \Omega$  discrete port was added to the beginning of the microstrip line.

Fig. 5.17 presents all the S-Parameter plots and Fig. 5.18 displays the co-polar and cross-polar plots with all possible configurations.

Table 5.6: Arrays of SIW Antennas - Resonant Frequency (GHz)

		Inner Angle ( $\alpha$ )				
		$0^\circ$	$5^\circ$	$10^\circ$	$15^\circ$	$20^\circ$
Folding Angle ( $\beta$ )	$0^\circ$	4.54	4.55	4.58	4.62	4.67
	$10^\circ$	4.55	4.55	4.58	4.62	4.67
	$20^\circ$	4.55	4.56	4.58	4.62	4.67
	$30^\circ$	4.55	4.57	4.59	4.62	4.67
	$40^\circ$	4.56	4.56	4.59	4.62	4.67

Table 5.6 displays the resonant frequency at all configurations with inner angle ( $\alpha$ ) and folding angle ( $\beta$ ). The array of SIW antennas had a resonant frequency on average at 4.59 GHz across all configurations. Comparing to the single SIW antenna, the resonant frequency was very similar. When varying the inner angle, there was a gradual increase in the resonant frequency. When  $\beta = 0^\circ$ , the resonant frequency was at 4.54 GHz when  $\alpha = 0^\circ$ , to 4.67 GHz when  $\alpha = 20^\circ$ . The resonant frequency remained constant as the folding angle increased. Comparing to a single SIW antenna, it displayed a very similar trend where the resonant frequency increased as the inner angle increased, but remained the same as the folding angle increased.

In general, there was an upward pattern when varying the inner angle ( $\alpha$ ), the resonant

frequency increased by 130 MHz, comparing to a single SIW antenna with 180 MHz. The resonant frequency remained constant for both single SIW antenna and an array of SIW antennas.

Table 5.7: Arrays of SIW Antennas - Reflection coefficient (dB)

		Inner Angle ( $\alpha$ )				
		$0^\circ$	$5^\circ$	$10^\circ$	$15^\circ$	$20^\circ$
Folding Angle ( $\beta$ )	$0^\circ$	-18.38	-26.78	-24.50	-16.35	-10.86
	$10^\circ$	-17.92	-27.32	-23.11	-15.43	-10.61
	$20^\circ$	-17.16	-25.50	-25.04	-14.93	-10.14
	$30^\circ$	-18.28	-24.91	-22.87	-14.44	-9.64
	$40^\circ$	-19.11	-29.73	-20.27	-13.11	-9.16

In Table 5.7 the simulated results were comparing  $S_{11}$  in dB at all resonant frequencies. Looking at the inner angle, when  $\beta = 0^\circ$ ,  $S_{11}$  fluctuated by a small amount when  $\alpha$  was between -16.35 dB and -24.50 dB. When  $\alpha = 20^\circ$ , the value dropped significantly to -10.86 dB. The decrease in  $S_{11}$  meant that only 90% of the power was transferred to the antenna. Ideally 97% or 99% would be preferred.

$S_{11}$  has decreased greatly in the array of SIW antennas for  $\alpha = 20^\circ$ , from -20.56 dB in the single SIW antenna down to -10.86 dB in the array of SIW antennas. In Fig. 5.17 the curves had a similar trend to those in Section 4.4.2, where there was another curve present at a higher frequency of 4.8 GHz. Again this could be seen as another Transverse ElectroMagnetic (TEM) mode present within the array of SIW antennas. The graphs also displayed the 10 dB reflection coefficient bandwidth. On average, the bandwidth was 80 MHz, which was similar to the single slot antenna simulated results.

Table 5.8: Arrays of SIW Antennas - Gain (dBi)

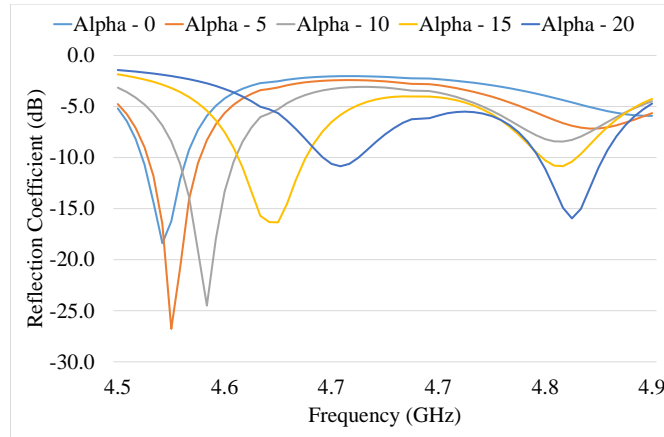
		Inner Angle ( $\alpha$ )				
		$0^\circ$	$5^\circ$	$10^\circ$	$15^\circ$	$20^\circ$
Folding Angle ( $\beta$ )	$0^\circ$	3.49	3.64	3.64	3.55	2.15
	$10^\circ$	4.04	4.12	4.17	4.14	3.90
	$20^\circ$	4.30	4.35	4.26	4.18	3.98
	$30^\circ$	4.07	4.12	3.99	3.86	3.60
	$40^\circ$	3.53	3.51	3.33	3.18	2.87

Table 5.8 uses the maximum gain value in dBi at the resonant frequency of each possible configuration. With the array of SIW antennas, the maximum gain value across all configurations was 4.35 dBi when  $\alpha = 5^\circ$  and  $\beta = 20^\circ$ . As the folding angle increased, the maximum gain value when  $\alpha = 0^\circ$  increased from 3.49 dBi when  $\beta = 0^\circ$ , to 4.30 dBi when  $\beta = 20^\circ$ , then dropped steadily back to 3.53 dBi when  $\beta = 40^\circ$ . It can be seen that when  $\beta = 20^\circ$ , it was the optimal angle to achieve the highest gain value. When the folding angle increased beyond that point, the maximum gain value dropped. When varying the inner angle, for  $\beta = 40^\circ$ , the maximum gain value dropped from 3.53 dBi when  $\alpha = 0^\circ$ , down to 2.87 dBi when  $\alpha = 20^\circ$ . Comparing the maximum gain value to the far-field array tool on CST Studio, the maximum gain value was 4 dB. It was similar with using the far-field array tool with the antenna design.

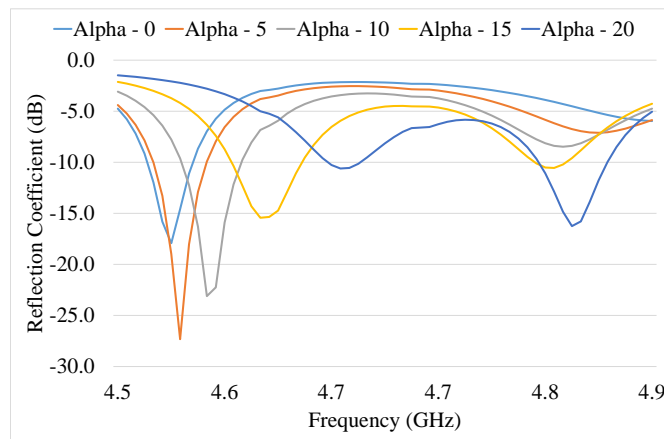
Fig. 5.18 displayed the radiating angle and HPBW on the co-polar plots, as the inner angle ( $\alpha$ ) changed, there was not a noticeable shift in the radiating angle. The only difference was the drop of the maximum gain value. On average, the HPBW with all configurations was at  $56^\circ$ . The array of SIW antennas was  $8^\circ$  smaller than a single SIW antenna. In the cross polar plots, there was a clear noticeable shift in the radiating angle at the null region. When varying the inner angle ( $\alpha$ ), the radiating angle at the null region when  $\beta = 10^\circ$  shifted from  $0^\circ$  when  $\alpha = 0^\circ$ , to  $8^\circ$  when  $\alpha = 20^\circ$ .

Overall, it could be seen that when  $\beta = 20^\circ$ , it was the optimal angle for the SIW

antenna to be radiating comparing with other folding angles. There was a drop in maximum gain value when varying the inner angle. In the cross-polar plots, there was also a noticeable shift in the radiating angle as the inner angle increased.



(a)  $\alpha$  Sweep ;  $\beta = 0$



(b)  $\alpha$  Sweep ;  $\beta = 10$

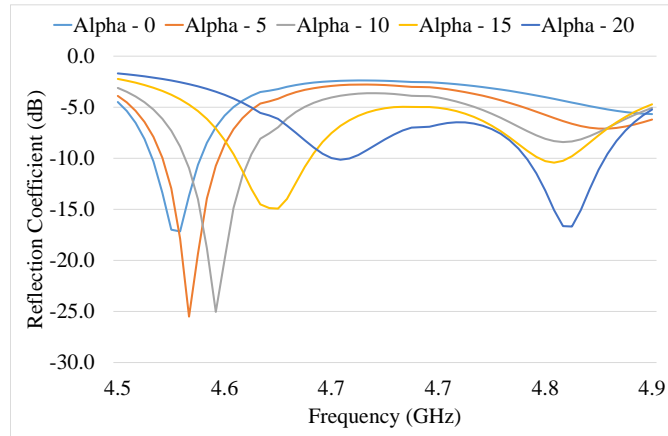
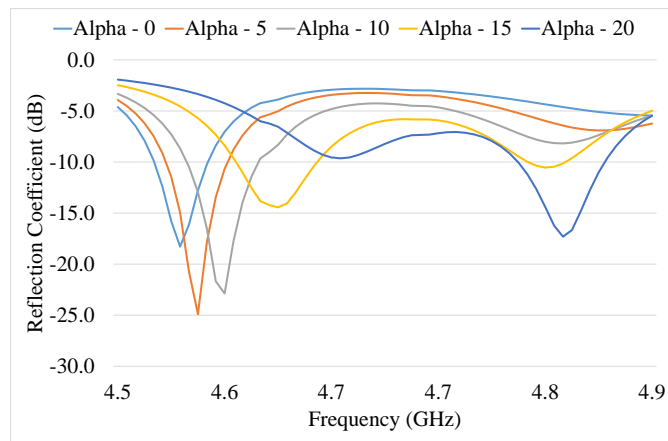
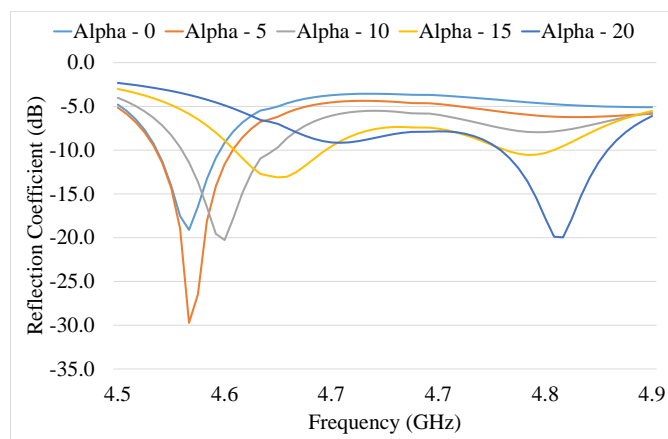
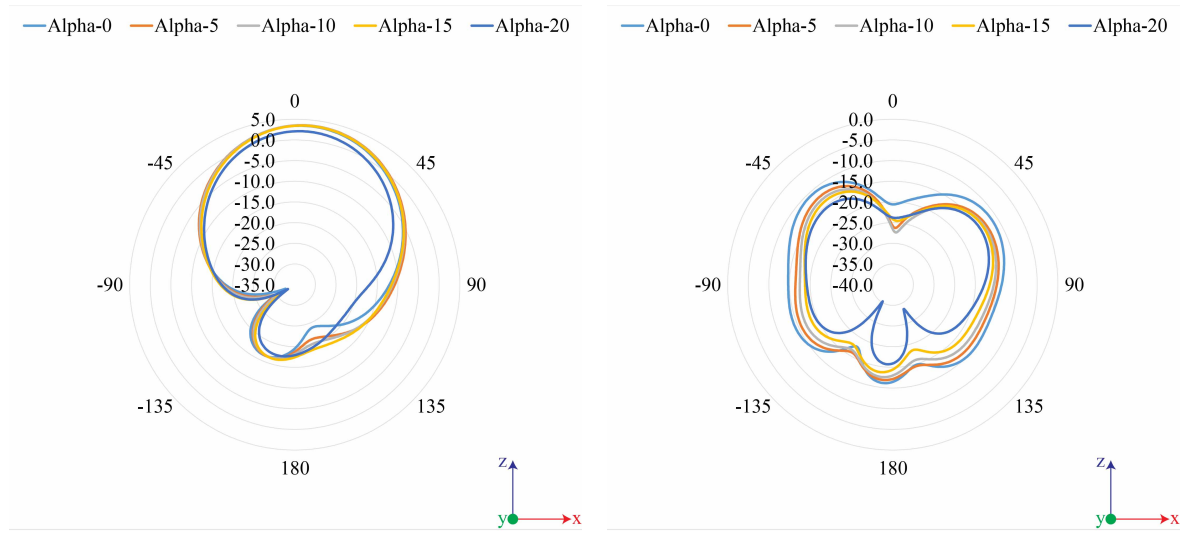
(c)  $\alpha$  Sweep ;  $\beta = 20$ (d)  $\alpha$  Sweep ;  $\beta = 30$ (e)  $\alpha$  Sweep ;  $\beta = 40$ 

Figure 5.17: Arrays of SIW Antennas - Simulated Reflection Coefficient

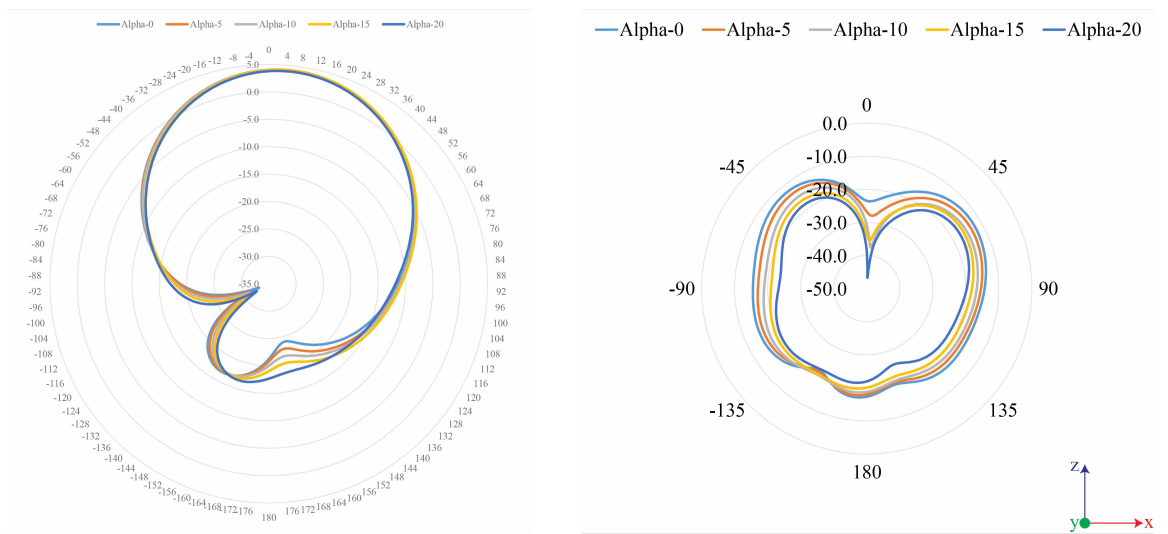




(a) Co Polar

(b) Cross Polar

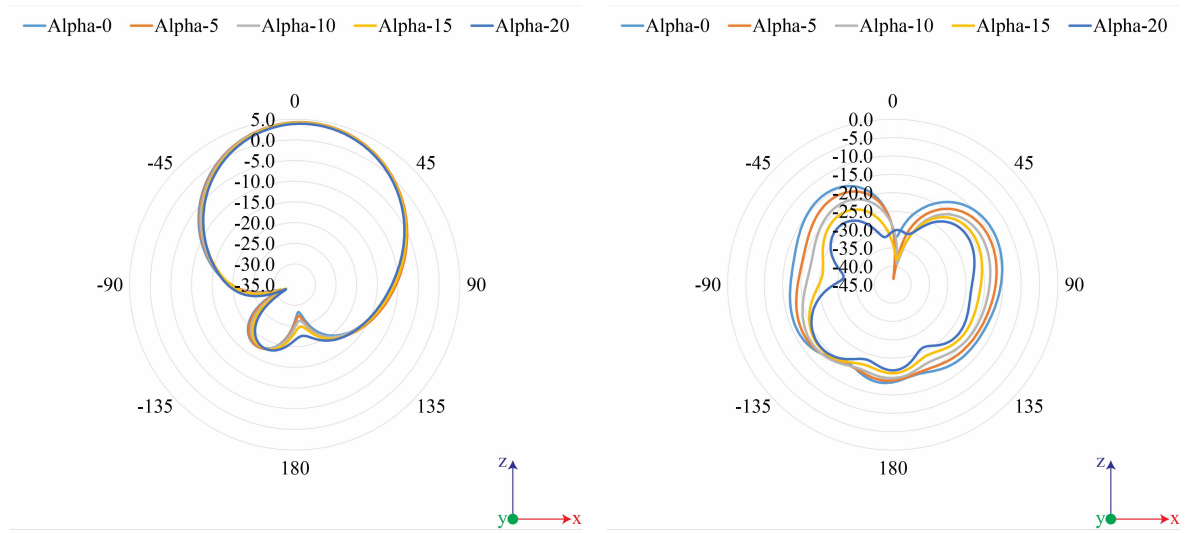
$\alpha$  Sweep ;  $\beta = 0$



(a) Co Polar

(b) Cross Polar

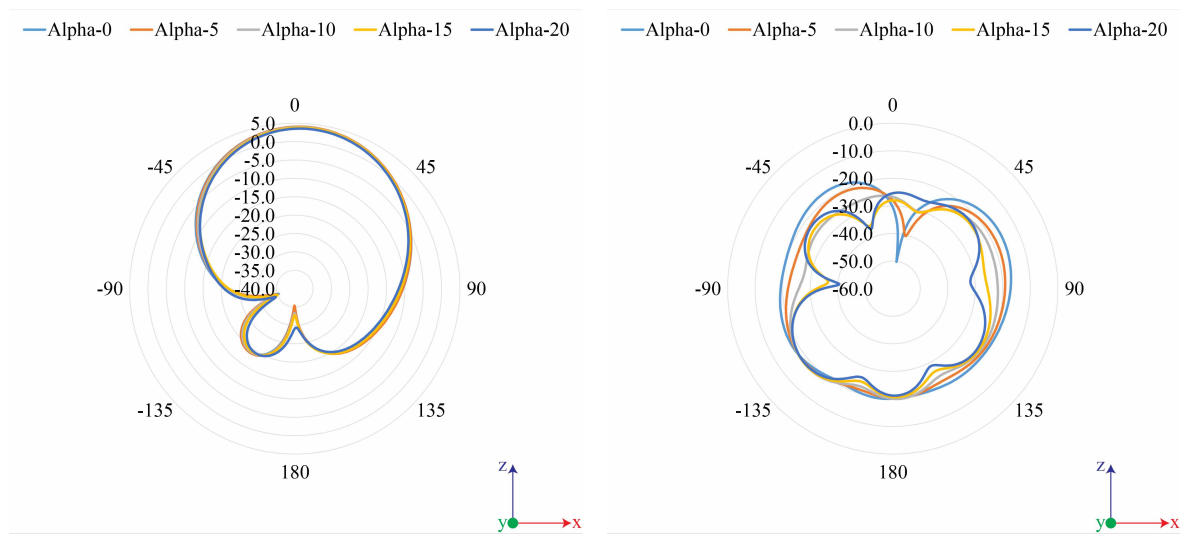
$\alpha$  Sweep ;  $\beta = 10$



(a) Co Polar

(b) Cross Polar

$\alpha$  Sweep ;  $\beta = 20$



(a) Co Polar

(b) Cross Polar

$\alpha$  Sweep ;  $\beta = 30$

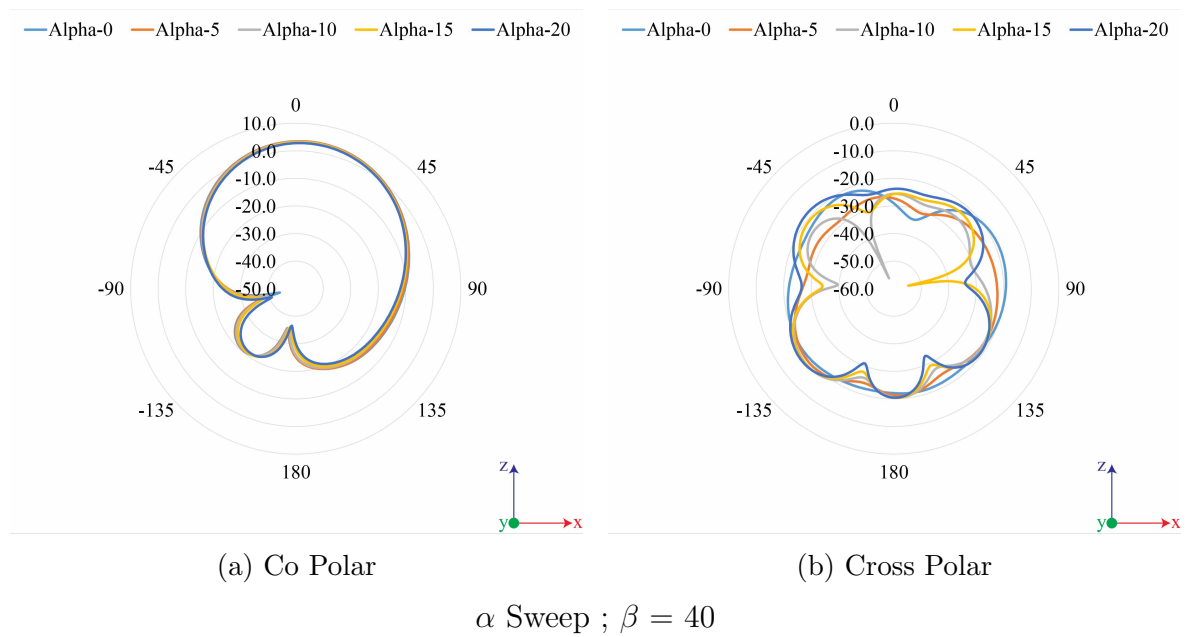


Figure 5.18: Arrays of SIW Antennas - Simulated Radiation Pattern

## 5.6 Summary and Conclusion

In this chapter an investigation was performed on a simulated SIW antenna. The antenna design had an open slot along the middle of the SIW. By utilising the open slot, the Miura Ori folding technique was applied and the structure was folded along the open slot. The SIW antenna has been optimised before applying the Miura Ori folding technique onto the design. The SIW antenna design was investigated by varying the width from the edge of the slot ( $wl$ ), slot width ( $sw$ ) and the microstrip offset ( $MOffset$ ) first. This was to find an optimised performance to apply the Miura Ori folding technique. It was decided that the operating frequency would be at 4.5 GHz.

The Miura Ori equations were applied onto the SIW antenna to achieve a foldable structure, when varying the inner angle and folding angle. From the single SIW antenna, all resonant frequency, reflection coefficient value and the maximum gain value displayed interesting results. As the inner angle  $\alpha$  increased, the resonant frequency shifted by 190 MHz. The maximum gain value also increased, as well as, the radiating angle shifted on the co-polar plots.

As the matching network was added into the design with an array of 2 by 1 SIW antennas, the simulated results were similar to a single SIW antenna results. There was a noticeable increase in the resonant frequency and the maximum gain value as the inner angle increased. However,  $S_{11}$  decreased significantly down to -9.16 dB when  $\alpha = 20^\circ$  and  $\beta = 40^\circ$ . This downward pattern could be related to that in Section 4.4.1. When modelling the structure, the curves were lofted in a Z-axis, therefore when the antenna was folded, the folded corners created an extra length that caused a mismatch between the antenna and microstrip line.

This chapter focused solely on simulations as explained at the beginning of the Chapter. However, a series of digital investigations were performed on a single SIW antenna and an array of SIW antennas. Utilising the Miura Ori folding technique in each antenna design demonstrated that antennas would still be operational given the amount of

folding occurred on the antenna. The foldable antenna structures were able to shift their resonant frequency, as well as, steering the radiating angle as the inner angle changed. Nevertheless, one problem arose from the simulated results. The modelling aspect would need to be examine and explore in more detail.

The application of this design could be beneficial in spacecraft where the SIW could be a replacement to standard waveguides, as this would lower its weight. The antenna could be used as a steerable element which could be stowed away during launch before re-deploying it again. This antenna could also be rescaled. If it is scaled down, it would be able to operate at a higher frequency. In the higher frequency, the substrates would require a smaller thickness as the wavelength will be shorter, therefore the bandwidth of this antenna would increase greatly.

# Chapter 6

## Microwave Switches using Coplanar Waveguide with Nanowires

### 6.1 Introduction

The current Wireless Fidelity (Wi-Fi) standard operates at 2.4 GHz and 5 GHz with a maximum transfer rate of 54 Mbps. Institute of Electrical and Electronics Engineers (IEEE) has proposed to create a Wi-Fi standard which will operate at 60 GHz with a maximum transfer rate of 7 Gbps.

The main challenge with operating at 60 GHz is that the wavelength is greatly reduced and can cause more reflection and absorption by objects in the room. With that in mind, there is a requirement of using switchable antennas to guide the propagation to various locations.

This chapter will focus on using nanowires as part of the switching mechanism that will allow the wave to travel through a Co-Planar Waveguide (CPW) to individual antennas. The main objectives would be to design a microwave switch on a flexible substrate, such as Kapton HN. This project is done in collaboration with the University of Surrey.

## 6.2 Coplanar Waveguide Theory

A CPW uses two ground planes with a conductor line in between [36]. It is an electrical planar transmission line with metal on the same side. A big advantage to the CPW is its ability to make fabrication simpler, as it can act as a shunt which reduces radiation loss, as well as, it can be mounted on top of the Printed Circuit Board (PCB). Another advantage is that it can provide a high frequency response, which will be beneficial in using CPW for up to 100 GHz.

The dimensions of the centre conductor strip ( $w$ ), gap between the two ground planes ( $s$ ), the thickness ( $h$ ) and the permittivity ( $\epsilon_r$ ) of the dielectric substrate will determine the effective dielectric constant ( $\epsilon_{eff}$ ) and the characteristic impedance of the line ( $Z_0$ ). In this chapter, the CPW will require the use of even mode, as it will generate an electric field from the signal to the ground plane, which will be driven by an identical signal.

Calculation of the characteristic impedance ( $Z_0$ ) and the effective dielectric constant ( $\epsilon_{eff}$ ) of a CPW can be derived by using (6.1) which applies the values of the gap between the two ground planes ( $s$ ) and the dimensions of the centre conductor strip ( $w$ ). For this chapter, the microwave switch will require a characteristic impedance of  $50 \Omega$  on the transmission lines, therefore, the following equations will be used to calculate the centre conductor strip ( $w$ ) and the gap between the two ground planes ( $s$ ).

$$Z_0 = \frac{30}{\sqrt{\epsilon_{eff}}} \frac{K(k'^0)}{K(k_0)} \quad (6.1)$$

$$\epsilon_{eff} = 1 + \frac{\epsilon_r - 1}{2} \frac{K(k_1)K(k'_0)}{K(k'_1)K(k_0)} \quad (6.2)$$

$$G = 2s + w \quad (6.3)$$

$$k_0 = w/G \quad (6.4)$$

$$k'_0 = \sqrt{1 - k_0^2} \quad (6.5)$$

$$k_1 = \frac{sh\left(\frac{\pi w}{4h}\right)}{sh\left(\frac{\pi G}{4h}\right)} \quad (6.6)$$

$$k'_1 = \sqrt{1 - k_1^2} \quad (6.7)$$

### 6.2.1 Operations with Nanowires

The use of nanowires resistive switching devices were first introduced in 2008 and made a substantial change in developing random access memory, sensors and neural systems [60].

The nanowire resistive switching device has a high carrier mobility. When the voltage is applied to the nanowire resistive switch devices, the filament of the nanowire forms between tracks. By applying appropriate voltages to the tracks, it can either break the circuit, which is caused by high resistance, or it will stay the same, which will allow signals to pass through the transmission line.

The main use of nanowires in electronic devices is in transistors. Moore's Law [61] states that the overall processing power will double every two years. This requires a tremendous amount of transistors within a computer systems. Nowadays, computers and mobile phones are much smaller. There is a requirement to design transistors in nanoscale. To allow that to succeed, it will be essential to control a gate over the channel that leads to effectively switching the transistor on and off. That will be defined by the resistance across the transistor, from a high resistance (OFF State) to



low resistance (ON state).

### 6.3 Academic Research on Microwave Switches

From the research paper contributed, on [62], the main focus was to use port switches from Skyworks to switch between each individual element. Each element led to an aperture coupled patch antenna, which was designed on a Kapton film substrate. The air separation between the aperture and the patch increased efficiency and gain.

This design had three Ultra-Wide Band port switches: Skyworks SKY13298-360LF. The port switches were implemented, when voltage was applied them. It allowed them to switch to individual elements. The first switch in the design was used at the T-Junction, this allowed to switch between each antenna pair. Further switches were for each pair routes of the signal to the individual antenna, where only one element was active at any time. The devices activated when the voltage was at 3.3 V. A switch box was built to house the physical switches. Each antenna operated between 6.0 GHz to 6.45 GHz. This is shown in Fig. 6.1.

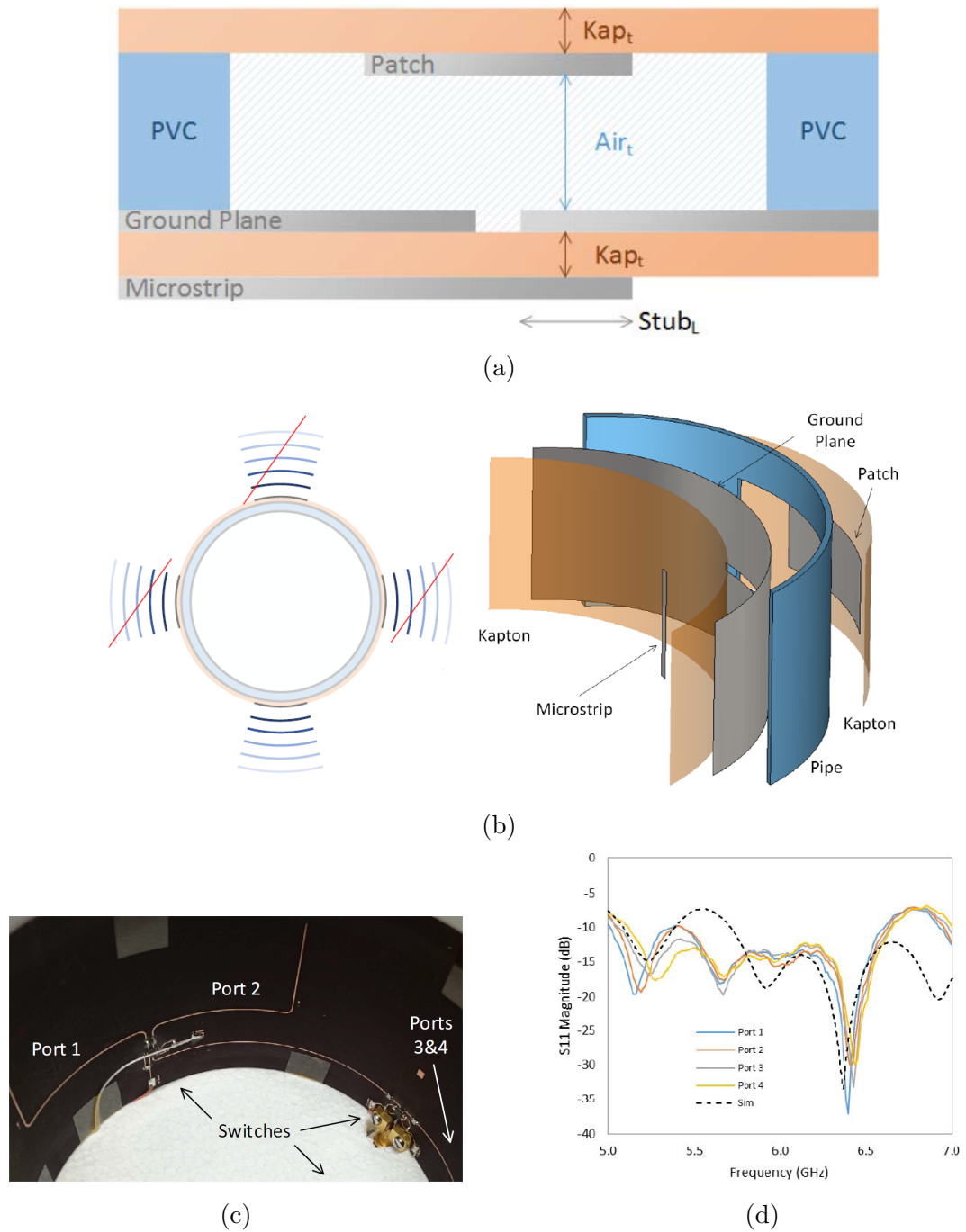


Figure 6.1: Conformal Switched Beam Antenna: (a) Side view of the aperture coupled antenna; (b) Birds eye view on a single curved antenna; (c) Fabricated antenna with a switching network using the UWB port switch; (d) Simulated and Measured Reflection Coefficient

### 6.3.1 Co-Planar Waveguides

Apart from the research contribution stated above, there were other microwave switches made for 60 GHz Wi-Fi, such as, Radio Frequency Micro-Electro-Mechanical System switches (RFMEMS). They had a complex design and a lot of adjustments and restrictions occurred during fabrication.

There were many advantages and disadvantage to using RFMEMS switches. These included using near-zero power consumption, high isolation, low insertion loss, inter-modulation products and low cost. Disadvantages included relatively low speed, power handling, high-voltage drive, packaging and cost.

G. M. Rebeiz [63] explained it in the article, “RF MEMS Switches and Switch Circuits”. The RF MEMS switch used a silicon substrate and a pull down electrode. This RF MEMS switch would attract the anchor, therefore connecting the switch contacts. The MEM switches consisted of a gold layer, with the switch being  $2.5 \mu\text{m}$  above the substrate. In [63, Fig. 6.2], a physical RF MEM switch with the measured results of the isolation and insertion loss can be seen.

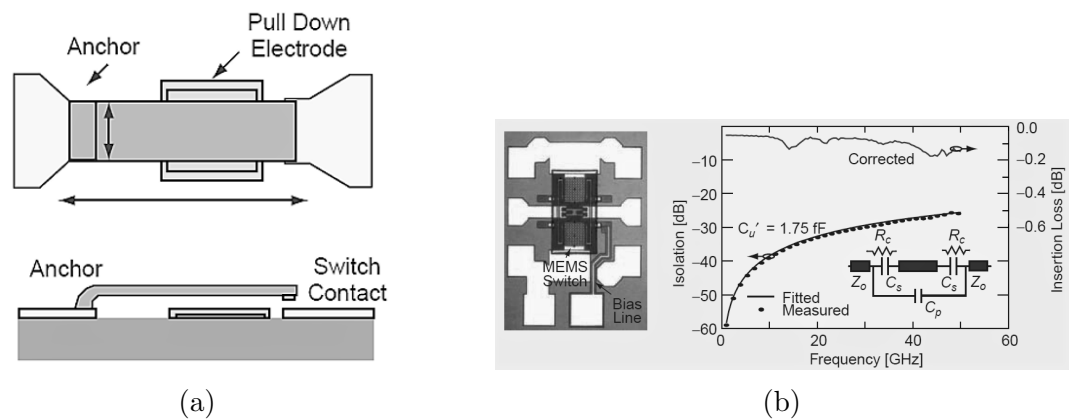


Figure 6.2: RF MEMS Switches and Switch Circuits: (a) Broadside MEMS Switches; (b) Fabricated MEMS Switch and measured isolation and insertion loss [63]

Another type of RF MEMS switch was a Field-Effect Transistor (FET) based switch, which used Gallium Arsenide [64]. The gate controlled the flow from the source to drain when the switch was functional. Voltage was applied to the gate and this allowed the transmission to go through, as shown in [64, Fig. 6.3] below. The main advantage of

this switch was the fact that the tracks are already embedded onto the PCB board and they did not require additional components. The disadvantage of this switch would be the cost of fabrication. Manufacturing process used bond wires to connect the switches together and that alone required additional labour, hence making it more expensive.

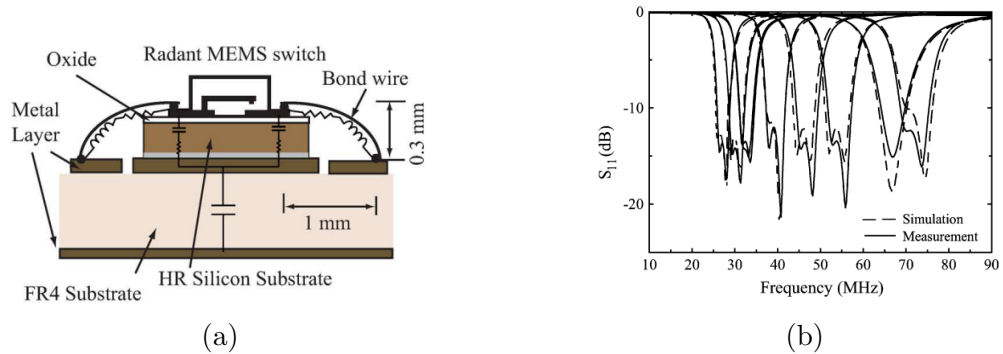


Figure 6.3: A 25 to 75-MHz RF MEMS Tunable Filter: (a) RF MEMS Switch with Bondwires; (b) Simulated Reflection Coefficient [64]

Using a flexible substrate switch would be beneficial because 60 GHz antennas can only transmit in one direction due to its high directivity [65]. Therefore, an array of antennas required a flexible substrate, which would be able to bend the antennas to the correct direction for transmission, see [65, Fig. 6.4]. The advantage of using a FET based switch on a flexible substrate would be that it could improve better signal quality and reduce size and weight. M. Chen [65] used a FET Carbon Nanotubes (CNT) on top of a flexible substrate. The advantage of using this switch would be the flexibility, which allowed the substrate to wrap around an object and enabled it to be twisted around. The main disadvantage of using a CNT solutions was the high price of the manufacturing process.

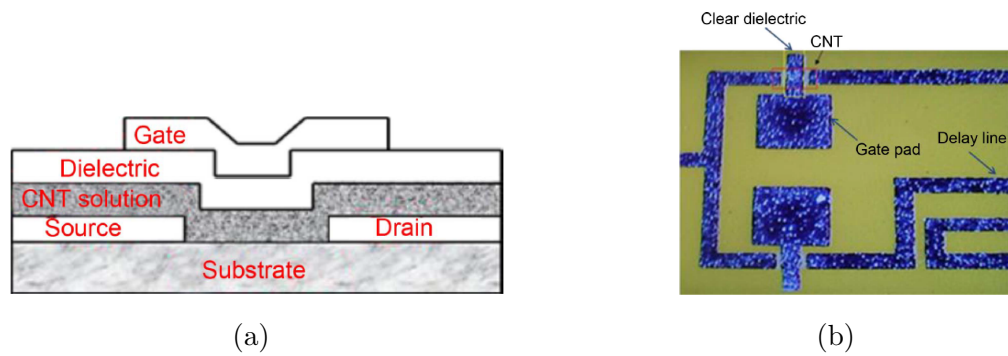


Figure 6.4: Conformal Ink-Jet Printed C Band Phased-Array Antenna Incorporating Carbon Nanotube Field-Effect Transistor Based Reconfigurable True-Time Delay Lines: (a) Layout of CNT based FET; (b) Fabricated FET with delay lines [65]

### 6.3.2 Nanowires

Nanowires have been an interest in a lot of areas including academia and industry, due to the innovative and novelty applications emerging in electronic designs. In the antenna and electronic designs, there were some scientist that introduced nanowires with their antenna design, the reviews below described some novel ideas.

In April 2013, R. Rai [66] had presented a stretchable, flexible antenna design, using silver nanowires (AgNW). The substrate he were using was polydimethylsiloxane (PDMS). When he were first testing silver nanowires, see [66, Fig. 6.5]a, he started with creating a transmission line model. The testing included the behaviour of the reflection coefficient ( $S_{11}$ ) and isolation ( $S_{12}$ ), while the material was under bending strain. Later matching the desired frequency, he designed a monopole patch antenna. In [66, Fig. 6.5]b, the patch antenna was operational with force being applied to it. There was a small change in the resonant frequency as the force increased.

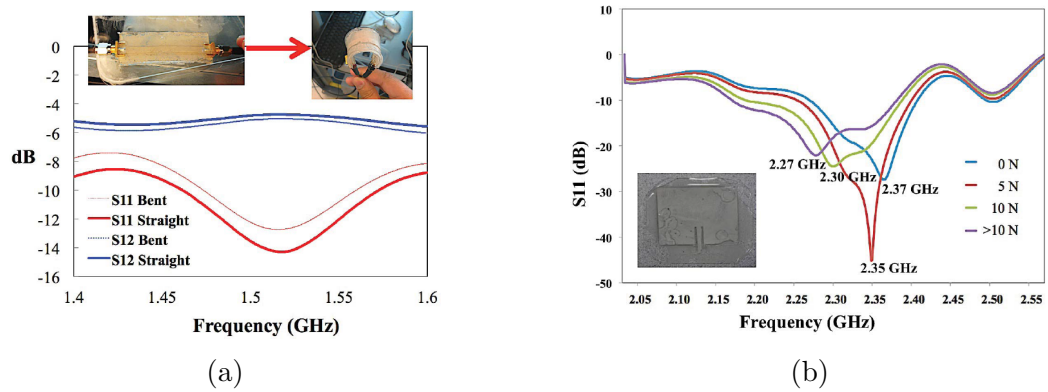


Figure 6.5: A Stretchable RF Antenna With Silver Nanowires: (a) Fabricated Transmission line model with results; (b) Fabricated RF Antenna with reflection coefficient [66]

Q. Dao studied the feasibility of silver nanowires [67]. He managed to create an optically transparent patch antenna for Millimeter (mm) wave applications. They first compared the conductivity results of the silver nanowires with a CPW transmission line, seen in [67, Fig. 6.6a]. As silver nanowires have a poor conductivity compared to copper, Q. Dao designed two patch antennas, one with silver nanowires and one with copper, to see the difference in the reflection coefficients and radiation. The simulated operating frequency was at 61 GHz for both patch antennas, but for the radiation pattern of the silver nanowires patch antenna, it was 3.7 dBi compared with 6.9 dBi for copper patch antenna, shown in [67, Fig. 6.6b] and [67, Fig. 6.6c] respectively.

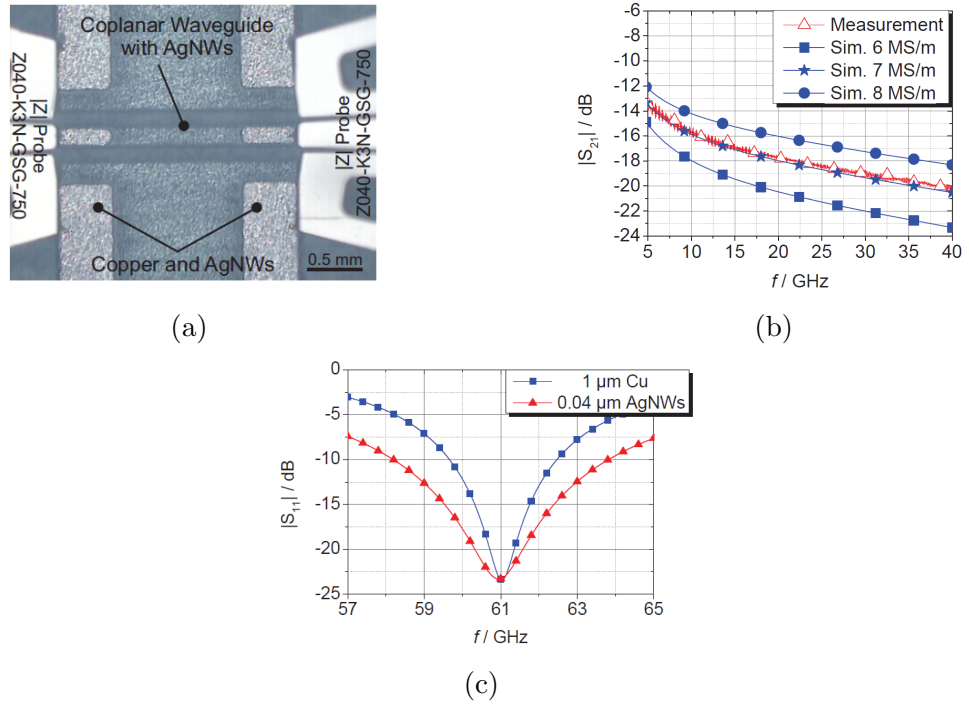


Figure 6.6: Optically Transparent Patch Antennas Based on Silver Nanowires for mm-Wave Applications: (a) Coplanar Waveguide transmission line with Silver nanowires; (b) Simulated and Measured results of the CPW transmission line; (c) Simulated results of Patch antenna operating at 61 GHz [67]

## 6.4 Microwave Switch using Coplanar Waveguide Design

A FET based microwave switch was designed on top of a CPW. The CPW had been using a flexible substrate (Kapton), which would allow it to bend enabling multiple 60 GHz antennas to radiate at different directions. The copper tracks would be printed on top of the CPW with both ground and signal tracks. In between the signal and ground tracks, there were nanowire resistive layers, which used the electric field to create various resistive states. On top of the waveguide, another layer of dielectric substrate with a gate track was placed to create a transistor.

This microwave switch had an ON state and OFF state. The OFF state had a high voltage applied across the gate track, which allowed the circuit to act in an open state enabling the signal to transmit. When there was no voltage across the gate track, the switch would go into an ON state, therefore it would act like a closed circuit and signals

would be reflected back.

### 6.4.1 Design Requirements and Constraints

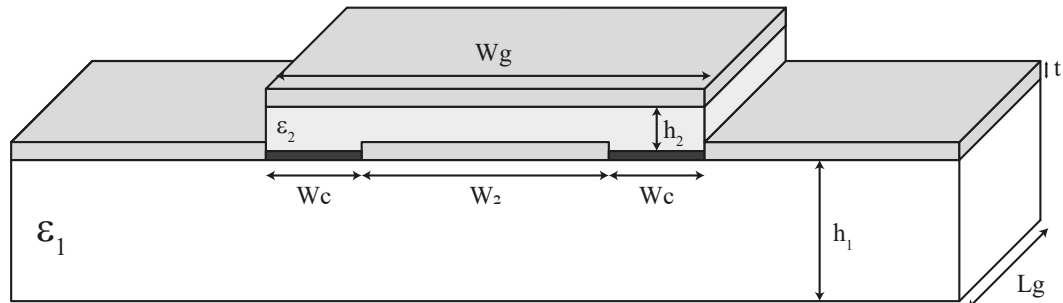


Figure 6.7: Initial Microwave Switch Design

When designing the CPW microwave switch, there were some restrictions to the dimensions. As part of a collaboration with the University of Surrey, Dr B. Mikrkhaydarov provided the minimum size that the Ink Jet Printer can fabricate. The minimum width of all metal tracks will had to be at least  $50 \mu\text{m}$ , with the minimum width gap for the Nanowire Resistive Layer to be at least  $13 \mu\text{m}$ , and the thickness of the flexible substrate between  $25 \mu\text{m}$  and  $125 \mu\text{m}$ . Another constraint would be the Ink Jet Printer incapability to print a perfect rectangle, as it dropped the ink onto a substrate creating a lump, therefore causing a problem with the dielectric and copper tracks printed on top.

A set of parameter had been used for this CPW microwave switch. There were a set of parameters that required optimisation, as shown in Fig. 6.7. Those restrictions would be taken into consideration when applied to the parameters. Table 6.1 displays the set of requirements for the microwave switch to be operational. The parameters were placed in CST Studio. As voltages cannot be applied to a specific object in CST Studio, the nanowire resisitve layer would be using an Ohmic sheet. This change in resistance allowed the signals to transmit along the CPW when  $R = 600 \text{ k}\Omega/\text{sq}$  or reflect the signals back to the input when  $R = 600 \Omega/\text{sq}$ .



Table 6.1: Design Requirement

Parameters		Values
Switch Width	$W_g$	$> 50 \mu\text{m}$
Switch Length	$L_g$	$500 \mu\text{m} - 2 \text{ cm}$
Switch Substrate thickness	$h$	$< 0.5 \mu\text{m}$
Conductor Thickness	$t$	0 (0.25 $\mu\text{m}$ when printed)
Nanowires resistance	$R_s$	On: 600 $\Omega/\text{sq}$ and Off: 600 $\text{k}\Omega/\text{sq}$
Signal Length	$W_2$	$50 \mu\text{m} - 125 \mu\text{m}$
Nanowire Width	$W_c$	13 $\mu\text{m}$

The CPW microwave switch consisted of different materials, see Table 6.2. Kapton HN was chosen to be the flexible base substrate, as it had a standard dielectric constant and a low loss tangent. For the gate dielectric, Parylene N was chosen. Copper, was chosen for metal tracks as it had high conductivity. The minimum width of the track would have had to be greater than 50  $\mu\text{m}$ , as it was the smallest size the Ink Jet Printer can fabricate.

Table 6.2: Design Material Properties

Substrate - $\epsilon_1$		Kapton HN
Permittivity	$\epsilon_r$	3.5
Loss Tangent	$\tan\delta$	0.02 @ 60 GHz
Maximum Useable Temperature		$< 360^\circ\text{C}$
Thickness of Substrate	$h_1$	25 $\mu\text{m} - 125 \mu\text{m}$
Gate Dielectric - $\epsilon_2$		Parylene N
Permittivity	$\epsilon_r$	2.7
Loss Tangent	$\tan\delta$	0.0006 @ 60 GHz
Thickness	$h_2$	$< 0.5 \mu\text{m}$
Conductor (Printable)		Copper - Cu
Conductivity	$\sigma$	$2.85 \times 10^7$
Thickness of Track	$t$	0.25 $\mu\text{m}$
Minimum Width		$> 50 \mu\text{m}$

## 6.5 Simulated Results

The set of parameters and constraints from Table 6.1 and 6.2 were considered. The design consisted of a CPW with a microwave switch in between. The microwave switch

would act as an open or closed circuit when voltage has been applied. In a closed circuit, the microwave switch would act as a shunt resistor, as shown in Fig. 6.8.

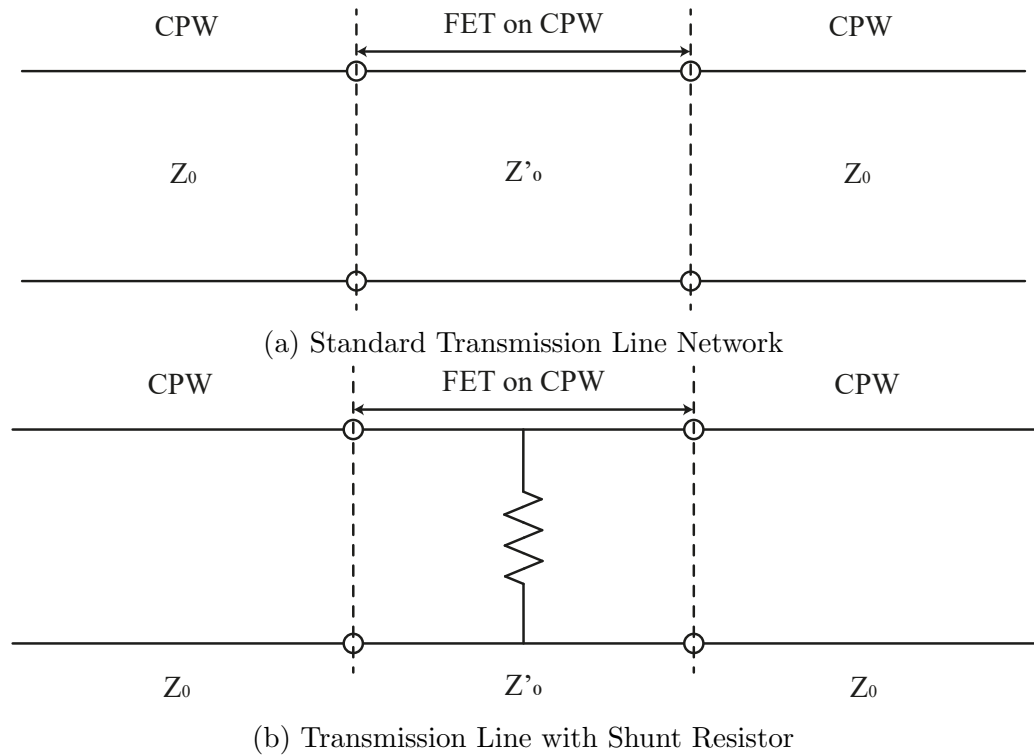


Figure 6.8: CPW Transmission Line

### 6.5.1 Initial Microwave Switch Design

Using the values from Table 6.1, the first initial design without the nanowire resistive layer was drawn on CST studio. The modelling software could do parameter sweep across any given variable with different dimensions. With the first design, it was crucial to determine if the CPW had an odd or even mode. To test that, a waveguide port was placed on the design and simulated with an E-field Monitor. By looking at the electric field of the waveguide port, it had been determined if the port was showing an even mode, see Fig. 6.9. This chapter investigated in the even mode distribution.

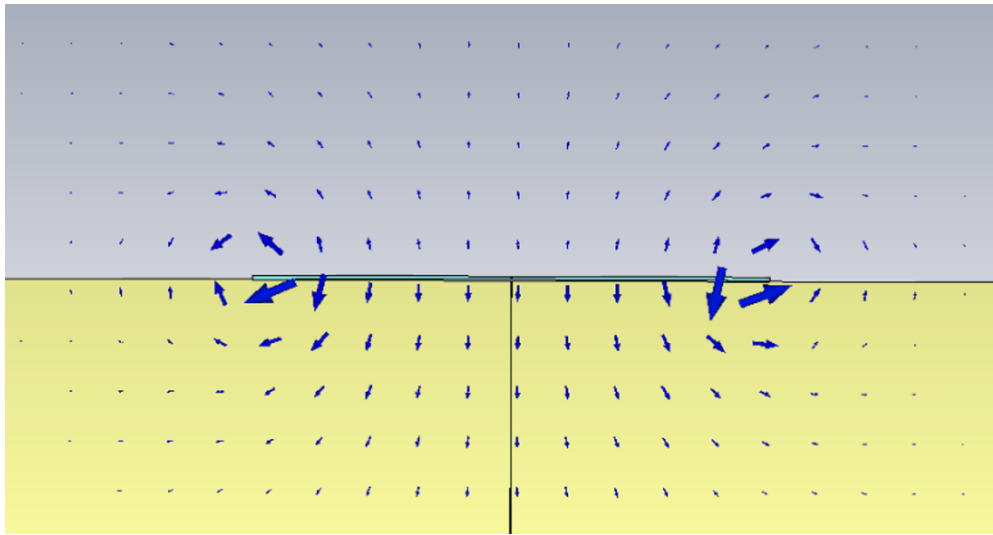


Figure 6.9: Electric Field on Waveguide Port

Apart from determining if the CPW was transmitting at an even mode distribution, it was also important to see how the wave had been transmitted within the transmission line by the characteristic of the Reflection Coefficient ( $S_{11}$ ) and the Transmission Coefficient ( $S_{21}$ ), shown in Fig. 6.10.

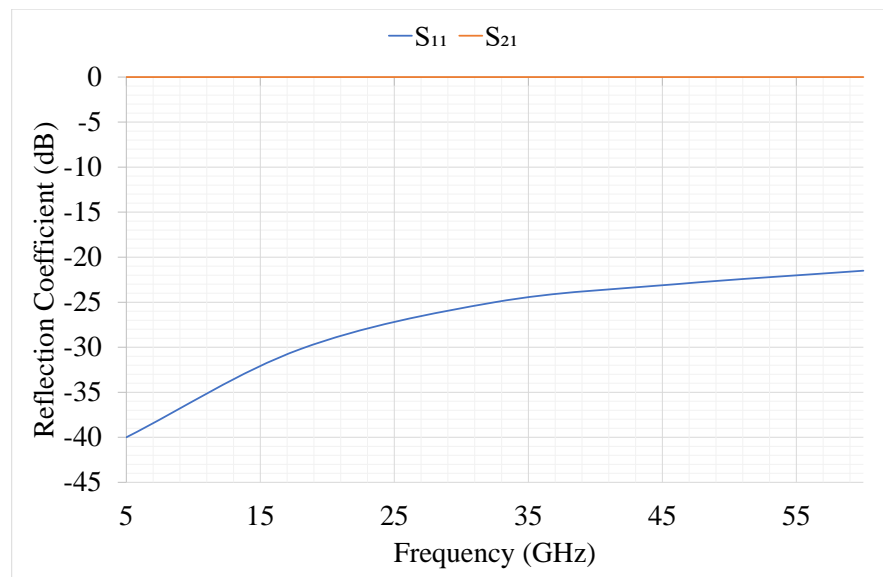


Figure 6.10: Initial Simulation Results without Microwave Switches

By varying the values of the length of the switch ( $L_g$ ) and using the parameter sweep function on CST Studio, a sweep across the frequency varying the length from 1 mm to

0.1 mm was established, which determined how well the signal had been transmitted across the band. As shown in Fig. 6.11, the best two transmissions for the microwave switch was when the length ( $Lg$ ) had been at 0.1 mm and 0.5 mm.

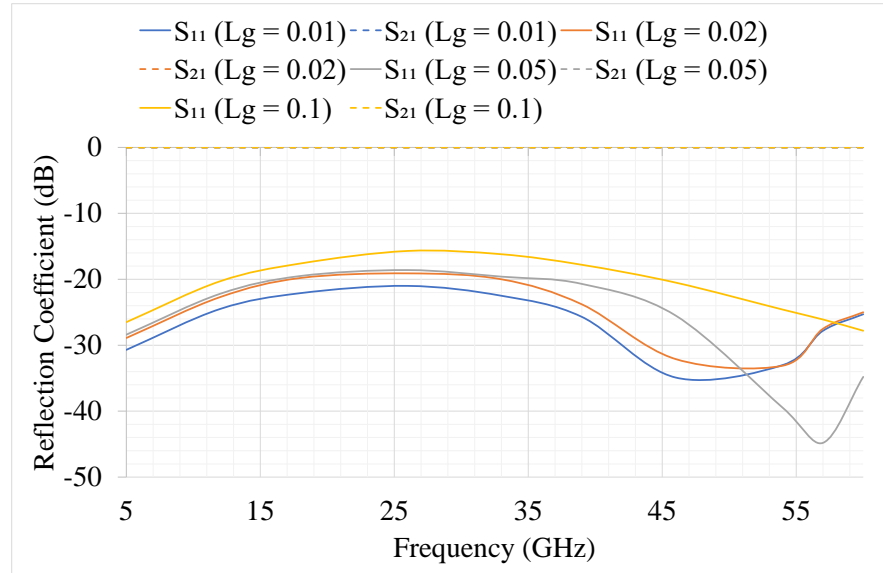


Figure 6.11: Initial Microwave Switch -  $Lg$  Sweep

When simulating, it was important to consider real world situation. Since the Ink Jet Printer from the University of Surrey had restrictions on printing, it deposited metal ink as droplets. Potentially overlapping during fabrication could occur. To overcome that, a gate offset ( $D$ ) was added to the simulations, to investigate the overlapping of the gate tracks. A parameter sweep function was used to vary the values of the gate offset. The  $0 \mu\text{m}$  occurred when the gate became a perfect rectangle, and  $5 \mu\text{m}$  was when there was  $5 \mu\text{m}$  overlapping to the gate and ground tracks. In Fig. 6.12, it had been shown, that by increasing the gate offset ( $D$ ), when the length of the switch ( $Lg$ ) was at 0.1 mm, the microwave switch would transmit less.

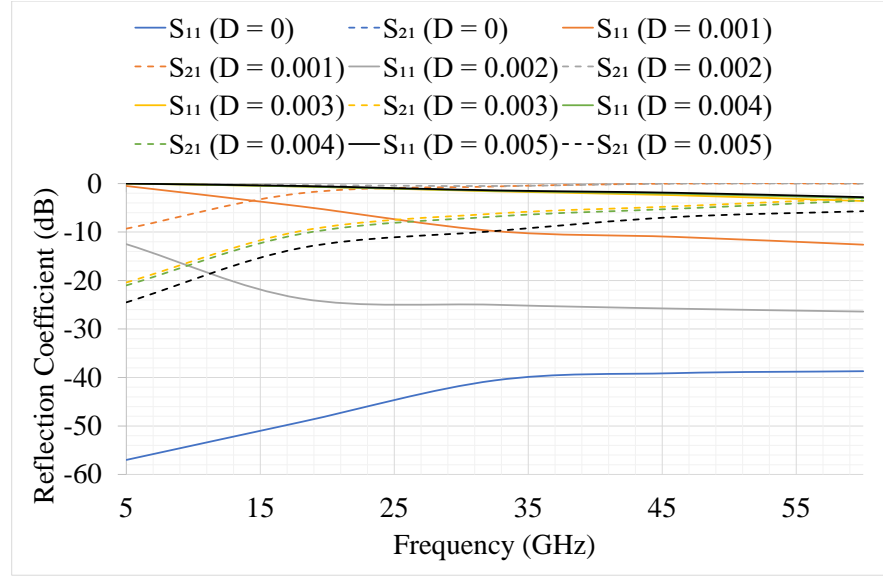
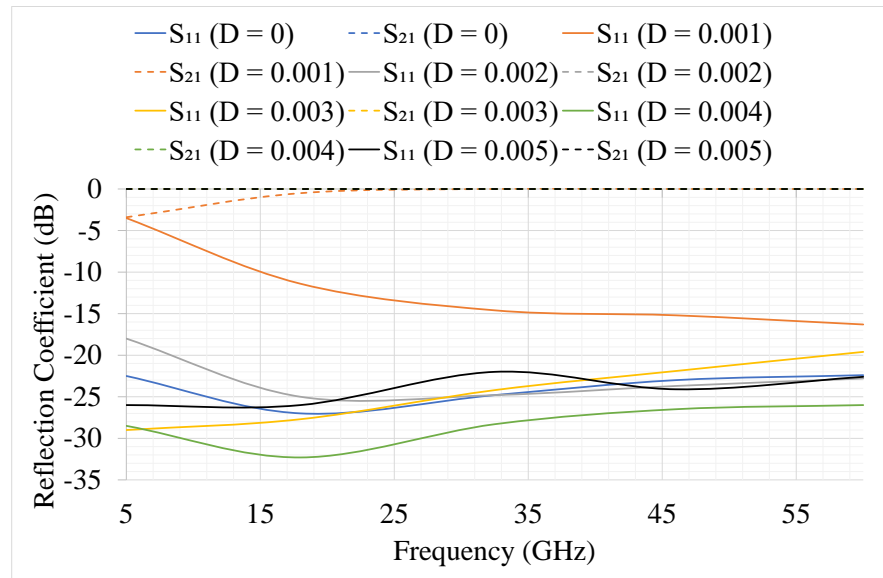
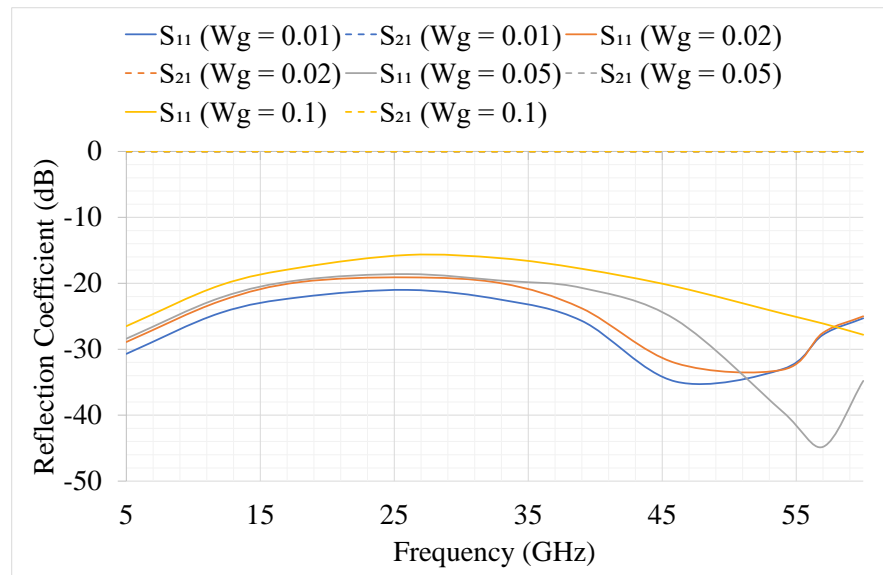


Figure 6.12: Initial Microwave Switch -  $Lg = 0.1$ ,  $D$  Sweep

When the length of the switch ( $Lg$ ) increased to 0.5 mm (Fig. 6.13), the S-Parameter displayed a different result. The simulations were propagating well along the transmission line even when the gate offset ( $D$ ) was at  $5 \mu\text{m}$  with  $S_{11}$  ranging from -20 dB to -27 dB and  $S_{21}$  staying almost 0 dB.

The aim of the microwave switch was to transmit when the resistance ( $R$ ) of the nanowire resistive layer was at  $600 \text{ k}\Omega/\text{sq}$  at an OFF state. When the resistance was at  $600 \Omega/\text{sq}$ , it would stop any signal transmitting at an ON state. To simulate the effect of the nanowire resistive layer on the microwave switch in CST Studio, the nanowires were treated as a new material, an Ohmic Sheet, with a resistance ( $R$ ) was chosen as a variable. Fig. 6.14 displays various simulations results, with values of those variables changing: Switch Length ( $Lg$ ), Gate Offset ( $D$ ), Dielectric Height ( $h_1$ ) and Resistance ( $R$ ).

Figure 6.13: Initial Microwave Switch -  $Lg = 0.5$ , D SweepFigure 6.14: Initial Microwave Switch -  $Lg$  Sweep - 0.1 mm to 0.01 mm

With added resistance in the resistive layer, the structure was able to simulate both at an ON and OFF state. Firstly, the microwave switch was simulated with the length of the switch ( $Lg$ ) between 0.1 mm to 0.01 mm to investigate if the switch would continue to operate, while the length ( $Lg$ ) varied. In Fig. 6.14 above, a parameter sweep was implemented. The results presented a trend where the shorter the switch, the better the coefficient. For example, when  $Lg = 0.01$  mm,  $S_{11}$  varied between -21 dB to -34 dB. The switch was at an OFF state meaning the signal is transmitting through the switch, however simulating on the resistance was crucial. In Fig. 6.15 below, when  $Lg = 0.01$  mm and the switch was at an OFF state, the switch transmitted similarly to Fig. 6.14, but when the switch was at an ON state, it was still transmitting with  $S_{11}$  between -15 dB and -19 dB and  $S_{21}$  at -1 dB.

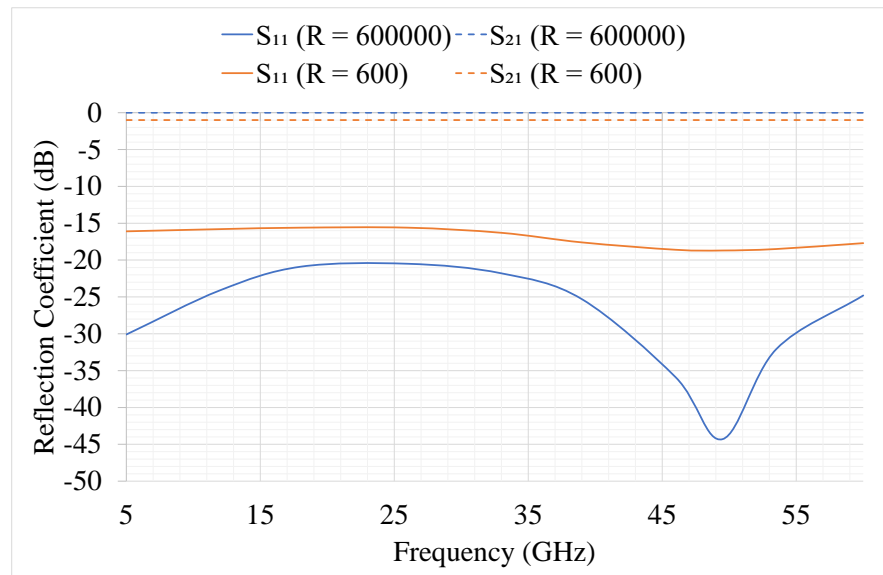


Figure 6.15: Initial Microwave Switch -  $Lg = 0.01$ , ON and OFF State

When considering a longer length of the switch ( $Lg$ ) at 0.1 mm. Different result could be observed, as seen in Fig. 6.16. When the switch was at an OFF state,  $S_{11}$  was below -16 dB and the  $S_{21}$  was at 0 dB, meaning there was a good transmission through the switch without the reflection back to the port. When the switch was at an ON state,  $S_{11}$  varied between -4 dB, while  $S_{21}$  dropped below -8 dB, meaning the switch was not

transmitting.

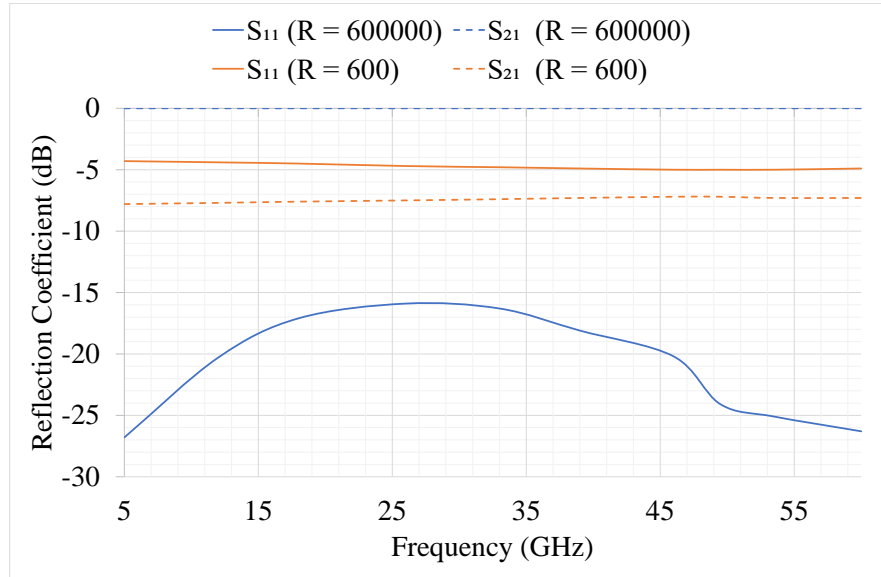


Figure 6.16: Initial Microwave Switch -  $Lg = 0.1$ , ON and OFF State

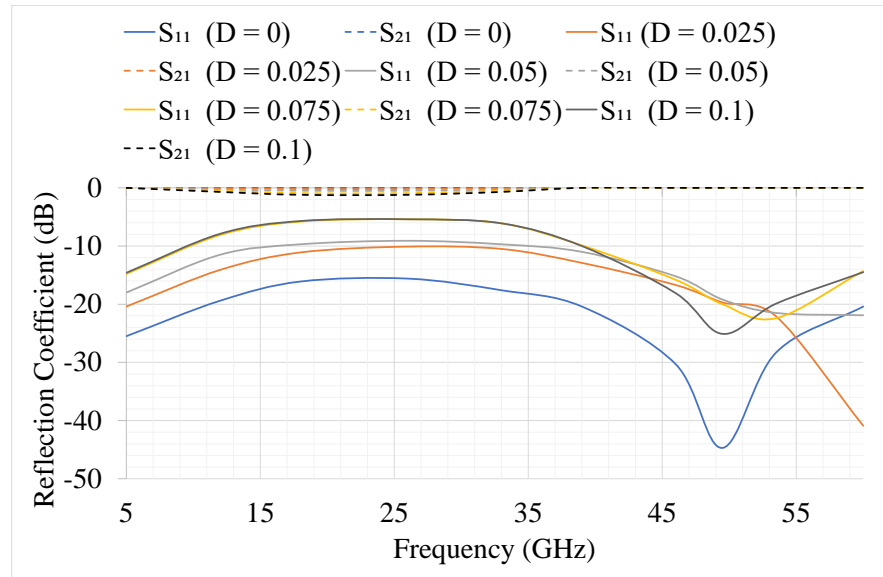
When varying the gate offset of the microwave switch, the simulation displayed a similar result to the previous when the microwave switch was in an OFF state, which allowed transmission to go through. When the gate offset ( $D$ ) was  $0 \mu\text{m}$ ,  $S_{11}$  was below  $-16$  dB. Whereas when the gate offset ( $D$ ) was higher,  $S_{11}$  rose up to  $-6$  dB and there was almost no propagation through the microwave switch. When the microwave switch was at an ON state, the switch was still transmitting meaning it will require more investigation, see Fig. 6.17.

Changing the height of the dielectric ( $h_1$ ) would reduce the capacitance between the gate track and the signal track. This would allow a better overall transmission. The values of the dielectric height ( $h_1$ ) were varied from  $1 \mu\text{m}$  to  $10 \mu\text{m}$  to determine if there was a reasonable transmission throughout the CPW to the microwave switch.

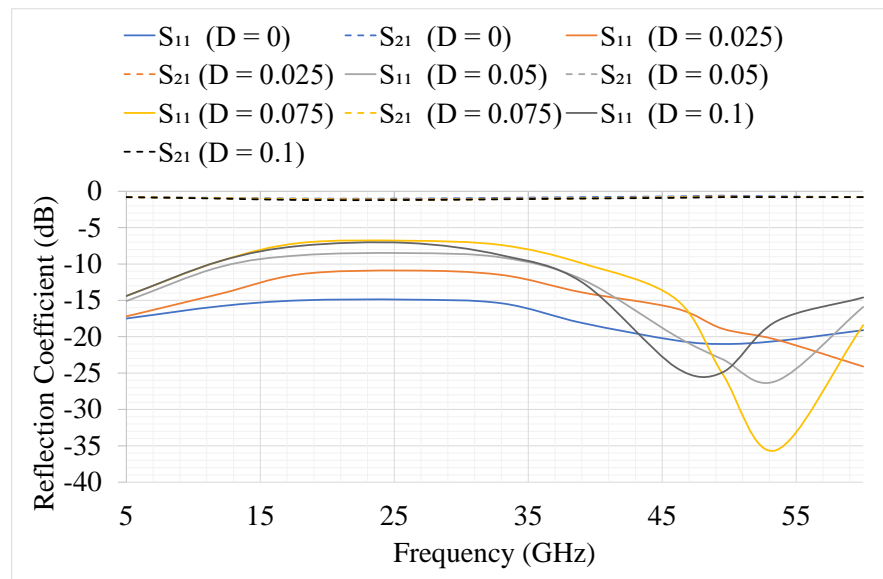
In Fig. 6.18a, the microwave switch was at an OFF state, with the height varying on  $S_{11}$ , the transmission got greater, when the distance between the gate and signal track increased. When the dielectric height ( $h_1$ ) was  $10 \mu\text{m}$ ,  $S_{11}$  stayed below  $-20$  dB but



when the dielectric height ( $h_1$ ) was  $1 \mu\text{m}$ ,  $S_{11}$  raised to  $-4 \text{ dB}$  at  $60 \text{ GHz}$ . Meaning at higher frequency there was no transmission through the microwave switch. When the microwave switch was at an ON state (Fig. 6.18b), there was still signal transmitting through the switch. When ( $h_1$ ) was at  $10 \mu\text{m}$ ,  $S_{11}$  varied around  $-11 \text{ dB}$ , but when height ( $h_1$ ) was at  $1 \mu\text{m}$ ,  $S_{11}$  varied between  $-5 \text{ dB}$  to  $-11 \text{ dB}$ .

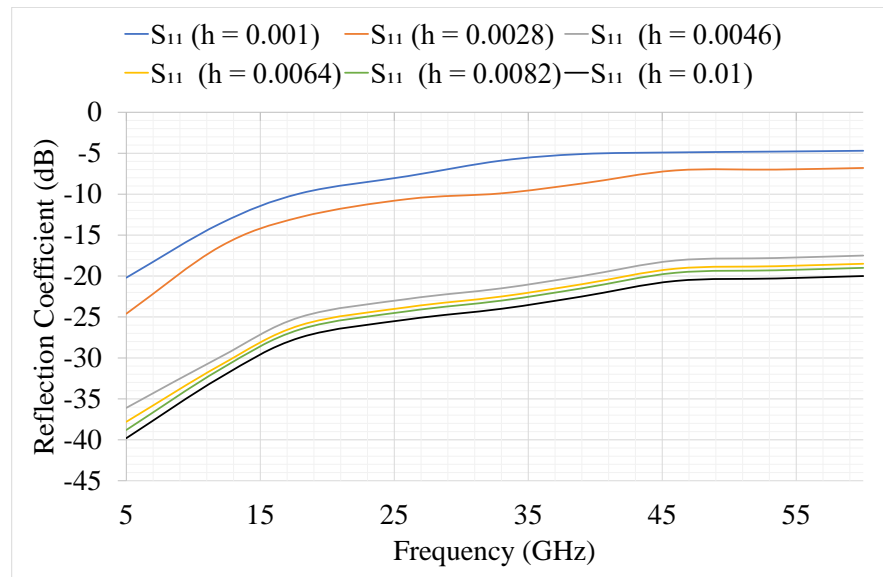


(a) OFF State

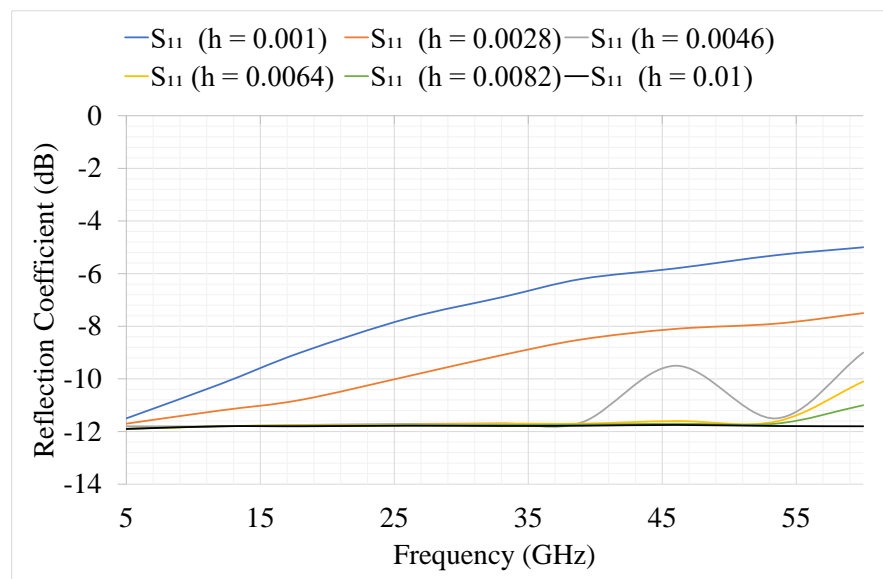


(b) ON State

Figure 6.17: Initial Microwave Switch - Gate Offset  $D$  Sweep



(a) OFF State



(b) ON State

Figure 6.18: Initial Microwave Switch - Dielectric Height  $h_1$  Sweep

Due to the restriction from the University of Surrey on the resistance of the Nanowire Resistive Switching Device, the resistance of the nanowire was above  $600 \Omega$ , as seen in Fig. 6.11 - 6.18. Fig. 6.19, investigated the resistance below  $600 \Omega$ . The set parameter such as the switch length ( $Lg$ ) was at 1 mm. Varying the resistance ( $R$ ) below  $600 \Omega$  was done to confirm, if the microwave switch was operating correctly. Looking at the results,  $S_{21}$  when the resistance ( $R$ ) was at  $6 \Omega$  and below  $-70$  dB meaning no power is received.

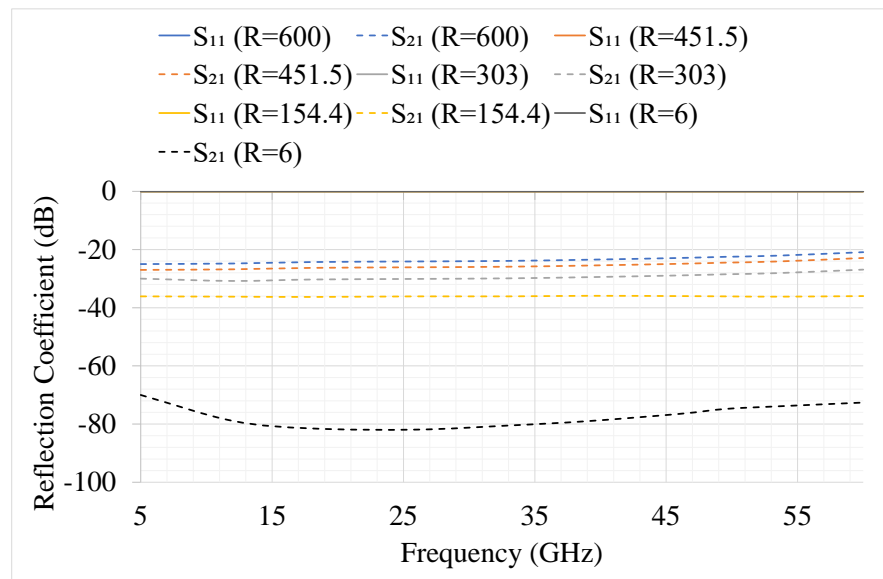


Figure 6.19: Initial Microwave Switch - Resistance Sweep -  $Lg = 1$  mm

By changing each of the parameters in this sub section, some interesting results were observed. The microwave switch was functional even if it was suppose to stop any transmission through the microwave switch. The main problem with the design was the microwave switch itself, with the gate over the signal tracks. This induced capacitance between the two metal plates, therefore the characteristic impedance dropped from  $50 \Omega$  to  $5 \Omega$ . Because there was capacitance between the gate and the signal, the power transmitted could be interfered.

### 6.5.2 Improved Microwave Switch Design

As discussed in Chapter 6.5.1, the main problem with the design was the gate track which was directly above the signal tracks and it induced capacitance, which was reducing the characteristic impedance. By using (6.8), if the inductance remained the same and the capacitance decreased, there would be an increase of the characteristic impedance. One major improvement to the microwave switch design was to split the gate track in half, since the gate was only needed over the gap between the signal and the ground tracks. When the gate track was split, the capacitance was reduced greatly, see Fig. 6.20.

$$Z_0 = \sqrt{\frac{L}{C}} \quad (6.8)$$

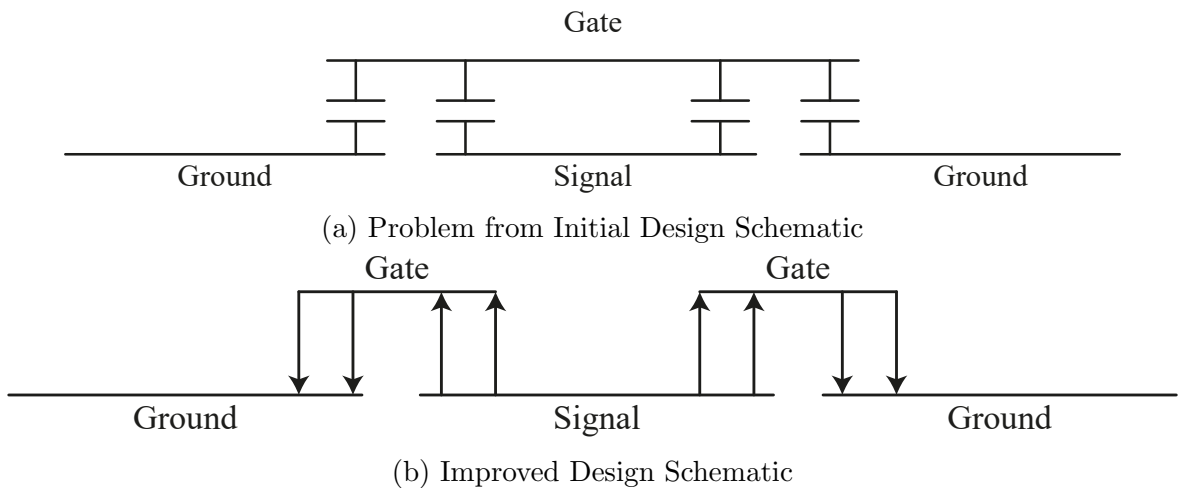


Figure 6.20: Initial and Improved Schematic Diagram

As an improved design drawn in Fig. 6.21, the gate tracks were split on each side above the gap. This would have allowed a better transmission due to less capacitance between the gate tracks and the CPW. The values of each variables such as the signal tracks width ( $W_2$ ), the gap between the signal and ground ( $W_c$ ), thickness of track ( $t$ ) and the height of the substrate would remain similar to the initial design. The switch length ( $Lg$ ), Gate offset ( $D$ ), Dielectric height ( $h_1$ ) and Resistance ( $R$ ) would be varied during this section.

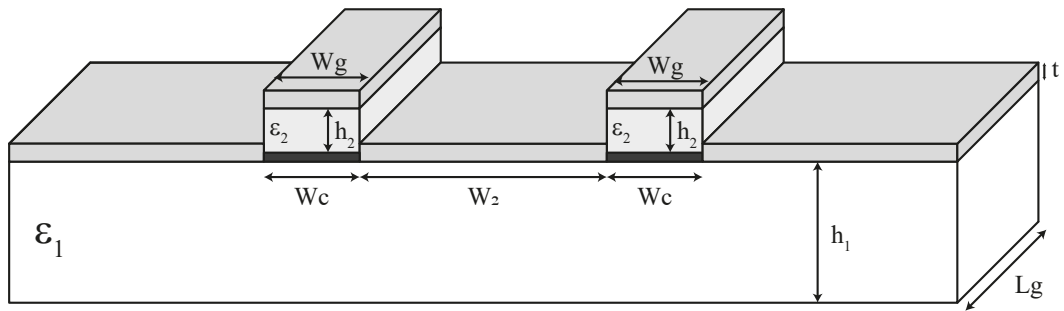


Figure 6.21: Improved Version of the CPW Microwave Switch Design

As stated above, each variable switch length, dielectric height, resistance on the nanowires and the gate offset would be simulated to determine if the microwave switch was functional. In Fig. 6.22, the microwave switch ( $Lg$ ) was parameterised ranging from 0.1 mm to 0.01 mm. The microwave switch was at an OFF state therefore there should have been a transmission throughout the whole design. When the length ( $Lg$ ) was 0.01 mm,  $S_{11}$  varied between -21 dB to -33 dB and  $S_{21}$  remained at 0 dB meaning the signal was being transferred through the microwave switch.

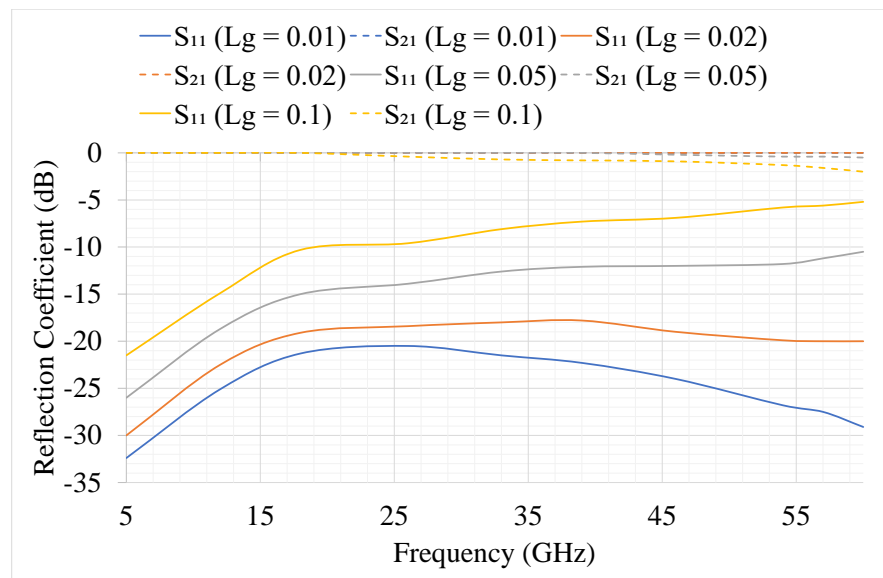


Figure 6.22: Improved Microwave Switch -  $Lg$  Sweep - 0.1 mm to 0.01 mm

When the length of the microwave switch ( $Lg$ ) was 0.1 mm, (Fig. 6.23),  $S_{11}$  was below -17 dB, while  $S_{21}$  remained at 0 dB at an OFF state. When the switch was at an ON state,  $S_{11}$  was still transmitting through the microwave switch, the values moved up

from -17 dB to -7 dB and  $S_{21}$  dropped from 0 dB to -5 dB.

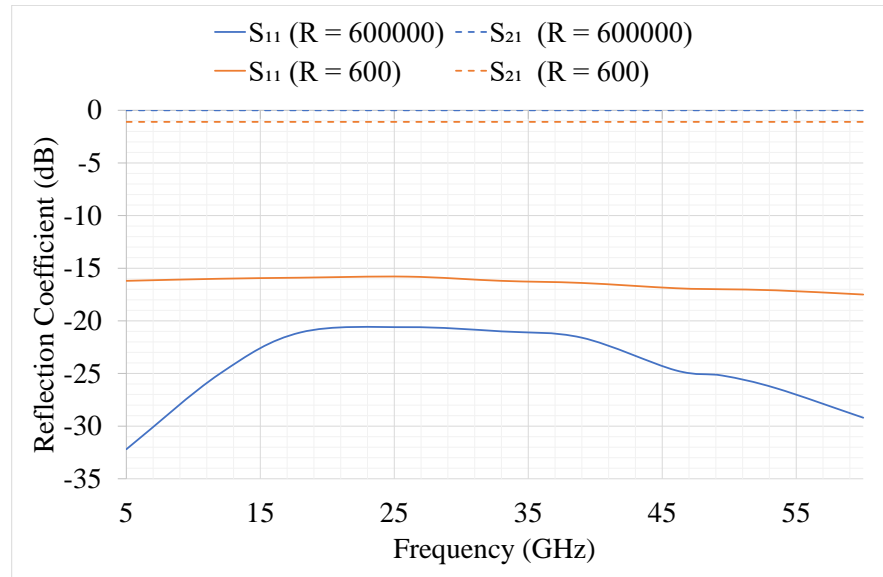


Figure 6.23: Improved Microwave Switch -  $Lg = 0.1$  mm, ON and OFF State

In Fig. 6.24, the transmission was more functional as the length of the microwave switch decreased. When it was at an OFF state,  $S_{11}$  was at -21 dB or below, with  $S_{21}$  was constant at 0 dB as expected. At an ON state, the switch was still transmitting as  $S_{11}$  was at -15 dB with  $S_{21}$  at -2 dB meaning there were still signals transmitting along the line with some reflection back to the receiver.

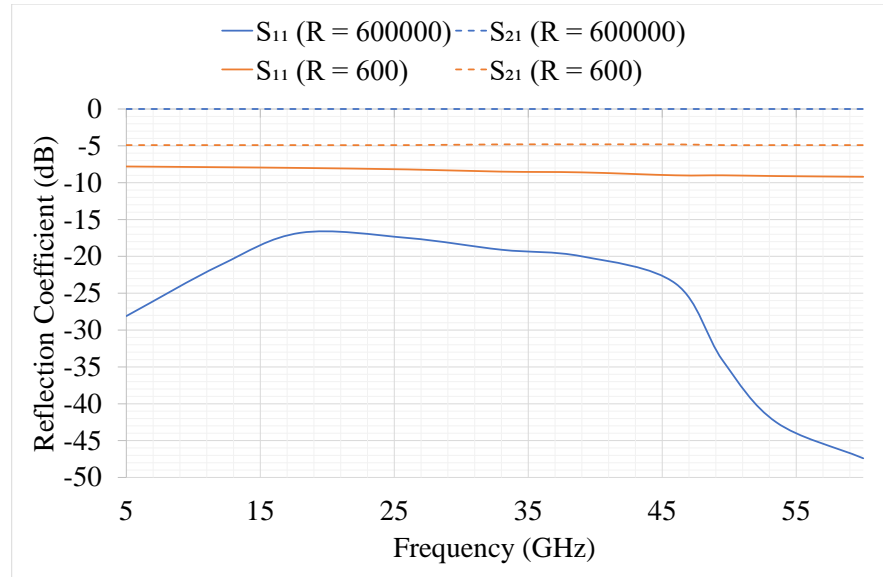
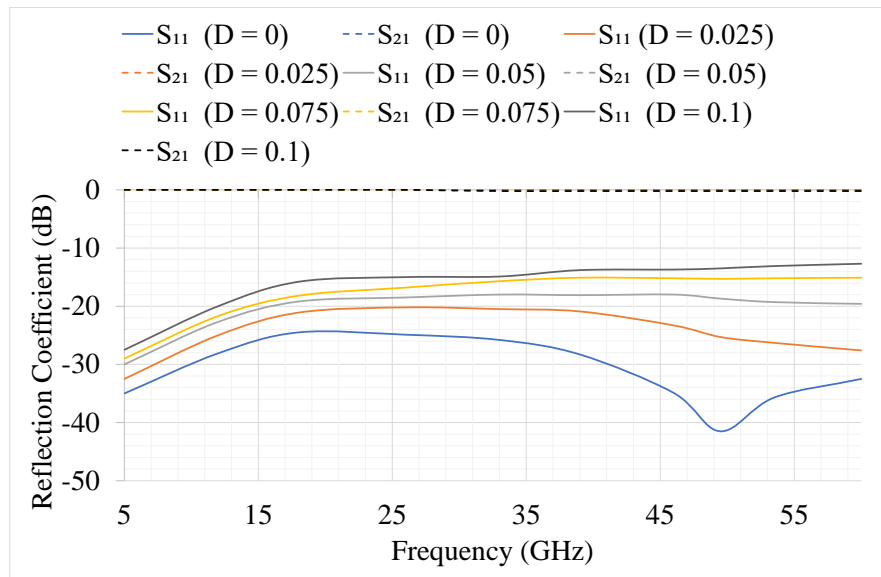


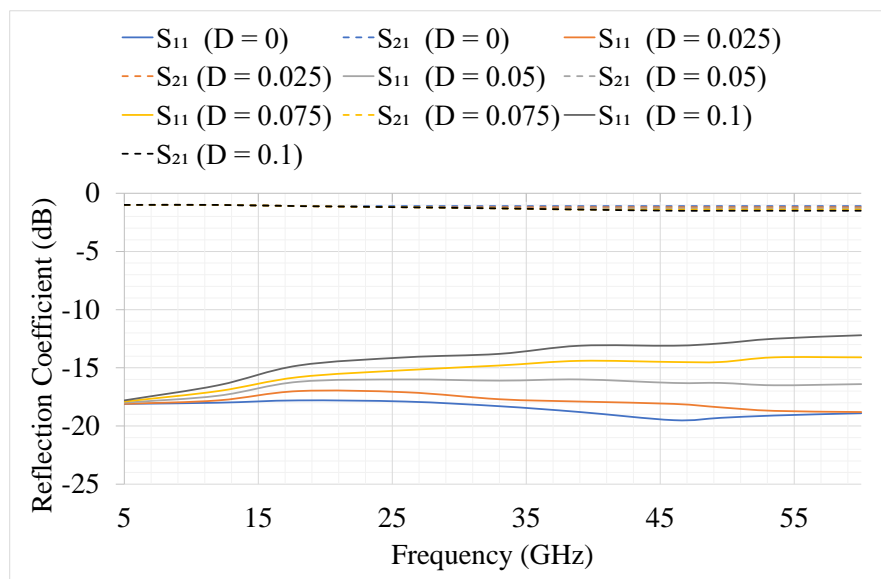
Figure 6.24: Improved Microwave Switch -  $L_g = 0.01$  mm, ON and OFF State

In Fig. 6.25a, the gate offset ( $D$ ) was varied between  $0 \mu\text{m}$  as a perfect rectangle to  $90 \mu\text{m}$  overlapping onto other tracks. When the microwave switch was at an OFF state, the larger the gate offset ( $D$ ), the worse the transmission got. When the gate offset was  $0 \mu\text{m}$ ,  $S_{11}$  was below  $-24$  dB while the gate offset ( $D$ ) was  $90 \mu\text{m}$ , the signal was still propagating through the transmission line, but with  $S_{11}$  raising up to  $-13$  dB. In Fig. 6.25b, the microwave switch was at an ON state, but with varying the gate offset ( $D$ ), there were still signals transmitting through the port with,  $S_{11}$  at  $-19$  dB and  $S_{21}$  dropping all the values to  $-1$  dB.





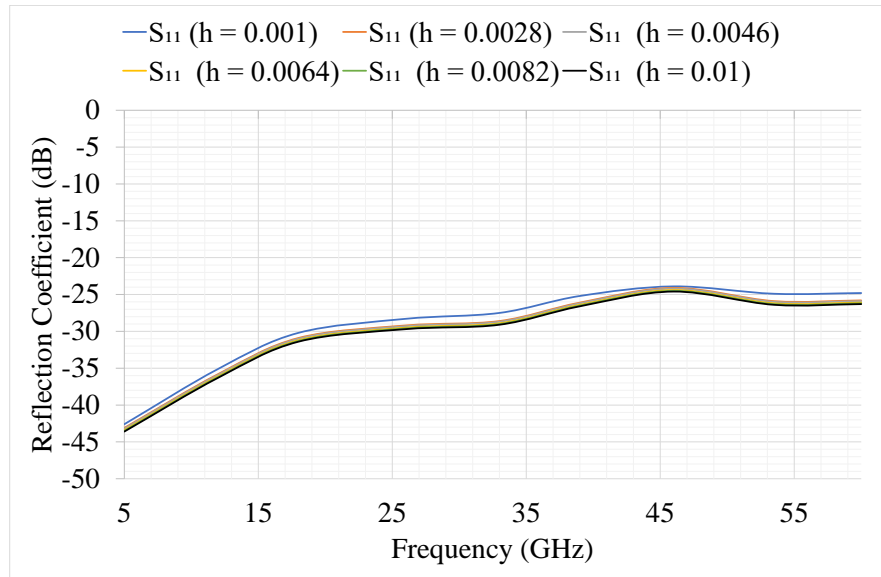
(a) OFF State



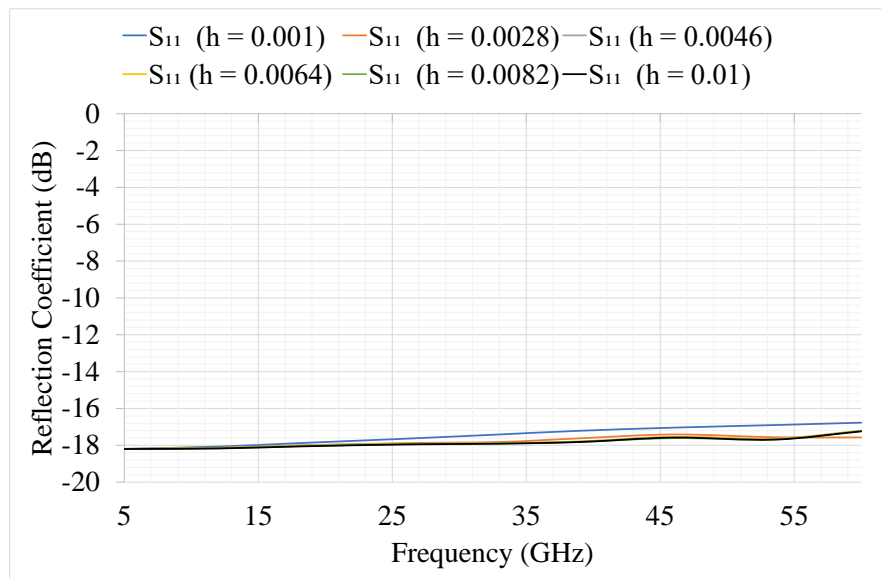
(b) ON State

Figure 6.25: Improved Microwave Switch - Gate Offset  $D$  Sweep

Similar to the sweep in the section earlier, the height of the dielectric ( $h_1$ ) would be varied because it would reduce capacitance between the gate and the CPW, allowing a better overall transmission. The dielectric height ( $h_1$ ), was varied between  $1 \mu\text{m}$  to  $10 \mu\text{m}$ . In Fig. 6.26a, the microwave switch was at an OFF state,  $S_{11}$  remained similar when varied with the dielectric height ( $h_1$ ) from -23 dB to -26 dB. Overall the microwave switch was functional throughout all frequencies. When the switch was at an ON state,  $S_{11}$  raised up to -16 dB meaning the switch was not functioning properly, as it would require the switch to stop transmission, see Fig. 6.26b.



(a) OFF State



(b) ON State

Figure 6.26: Improved Microwave Switch - Dielectric Height ( $h_1$ ) Sweep

As shown in Fig. 6.26, the microwave switch was still operational after being in an ON state. It was important to validate the resistance values lower than  $600 \Omega$ . The resistance ( $R$ ) values ranged from  $6 \Omega$  to  $600 \Omega$ , when the length of the switch was at  $0.1 \text{ mm}$ . In Fig. 6.27 below, when the resistance was at  $600 \Omega$ ,  $S_{11}$  had raised up at  $0 \text{ dB}$ , while  $S_{21}$  varied between  $-19 \text{ dB}$  and  $-25 \text{ dB}$ . When the resistance was at  $6 \Omega$ ,  $S_{21}$  dropped below  $-70 \text{ dB}$ , creating a good isolation between the two CPW ports, with no power received on either side.

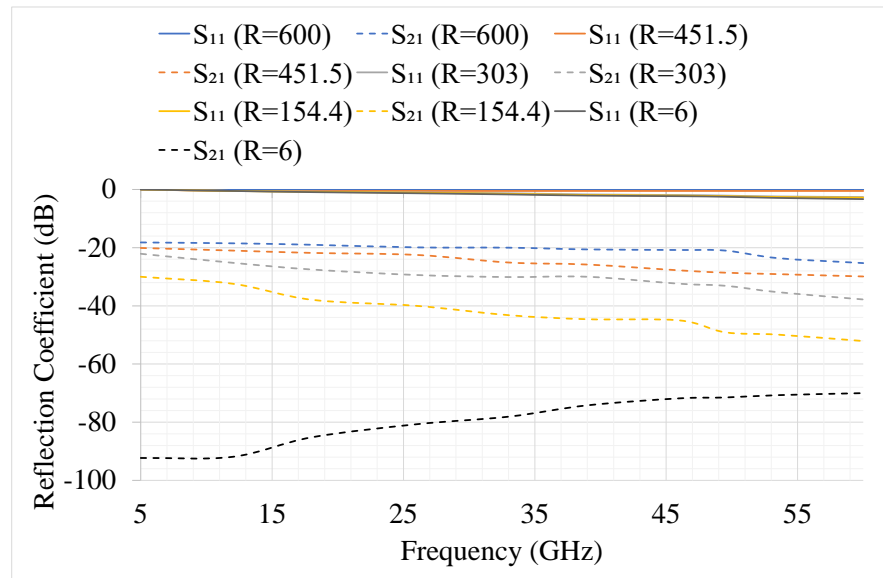


Figure 6.27: Improved Microwave Switch - Resistance Sweep -  $Wg = 0.1 \text{ mm}$

With the improved design, there were some changes to the results, compared with the initial version. The improved design with the split gate decreased the capacitance between the metal tracks, therefore allowing a better transmission through the microwave switch. From all the simulations above, it could be observed that when the resistance ( $R$ ) was at  $600 \Omega$ , there were still signals propagating through the microwave switch into other CPW port.

After discussing the results with Dr B. Mirkhayadrov from the University of Surrey, it was suggested that the material should be changed from Kapton to Quartz, as it had a stable dielectric constant with a low dielectric loss. The quartz substrate would

have a thickness of 0.5 mm, with a permittivity ( $\epsilon_r$ ) of 3.8 and a loss tangent ( $\tan\delta$ ) of 0.0001 [68]. From the sections above, it was important to observe the variables that changed  $S_{11}$  and  $S_{21}$ . This led to a collaborative article written by Dr B. Mirkhayadrov [69]. He compared his findings with the research above and investigated a new feasible way of using CPW with nanowires on a Quartz wafer substrate. One of the designs that he was investigating was a bottom-gated FET. The univeristy managed to create a resistance of  $50 \Omega$  at an ON state and  $50 \text{ K}\Omega$  at an OFF state. [69, Fig. 6.28a] illustrates the microwave switch with nanowires in between the signal and ground tracks. The frequency was operated between 5 GHz to 33 GHz, allowing this microwave switch to cover the frequency range for both microwave and millimeter wave bands. The microwave switch was tested with various of voltages across the gate, shown in Fig. 6.28b.

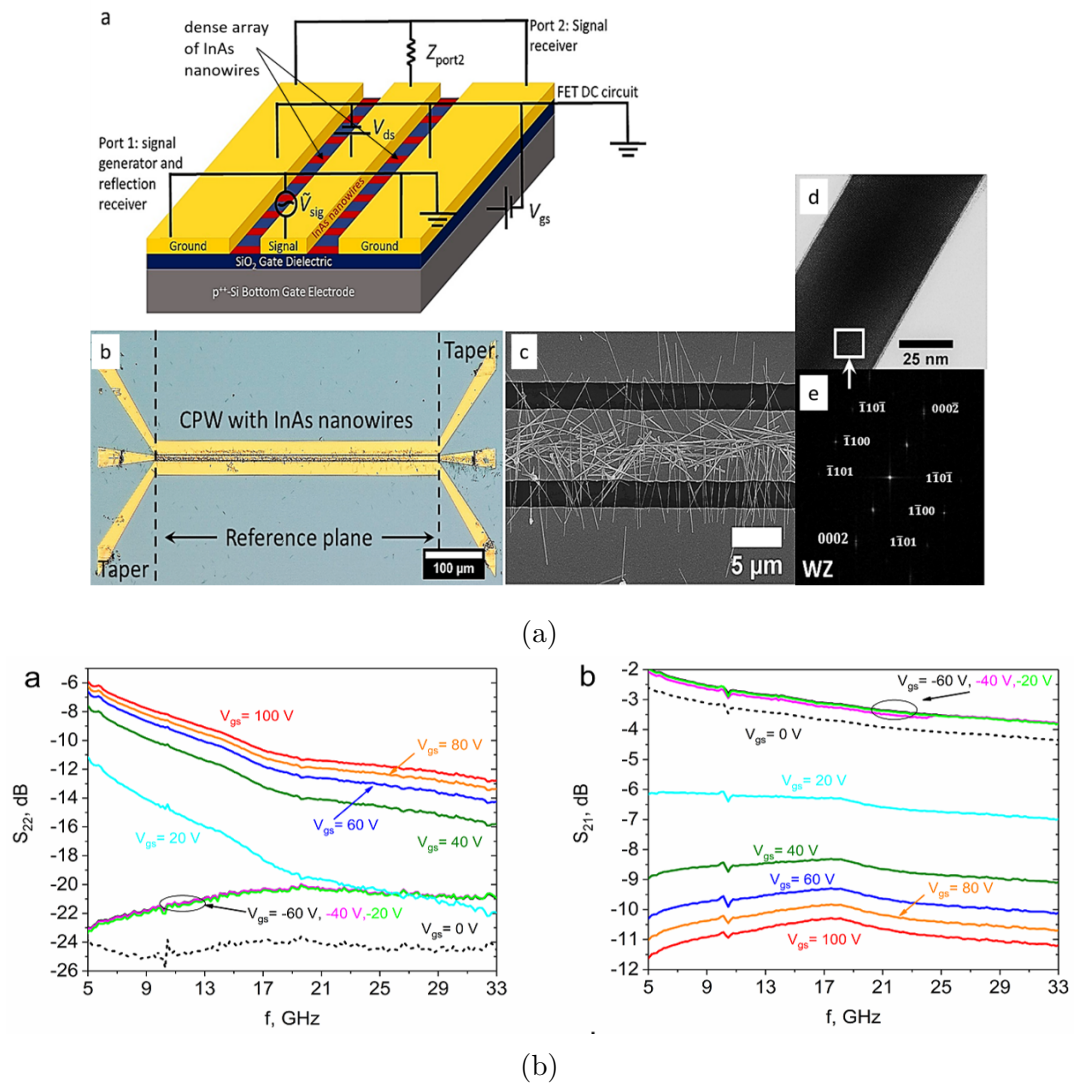


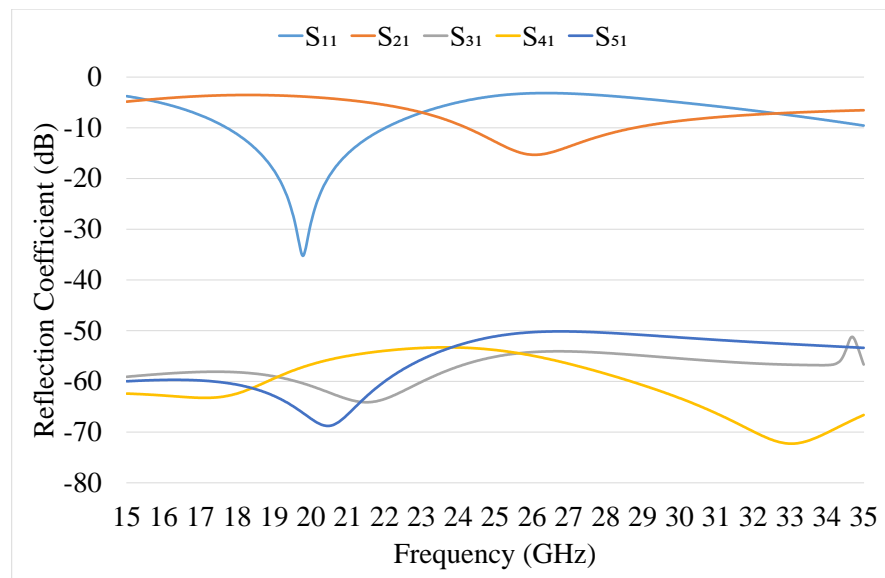
Figure 6.28: Solution processed InAs nanowire transistors as RF/microwave switches: (a) New design concept and an Optical image of the CPW switch; (b) Reflection Coefficient  $S_{22}$  AND Transmission Coefficient  $S_{21}$  at various voltage levels [69]

## 6.6 Applying Microwave Switch to Antennas

From the article [69] stated above, it was discussed that the microwave switch can be further investigated by applying an array of antennas to it. Fig. 6.29a displays the new design of the CPW microwave switch with a nanowire resistive layer at each slot towards 4 ports. A simulation was performed on the microwave switch operating at 25 GHz with port 2 being at an OFF state and port 3, 4, 5 at an ON state with  $S_{11}$  being at -20 dB, while  $S_{21}$  was at -2 dB. All other ports were at an ON state, therefore there was no power going through the other ports. see Fig. 6.29b.



(a)



(b)

Figure 6.29: Vivaldi Antennas with proposed Microwave Switch: (a) Design of the proposed Microwave Switch; (b) Simulated results when Port 2 is at an OFF state

### 6.6.1 Simulated Results

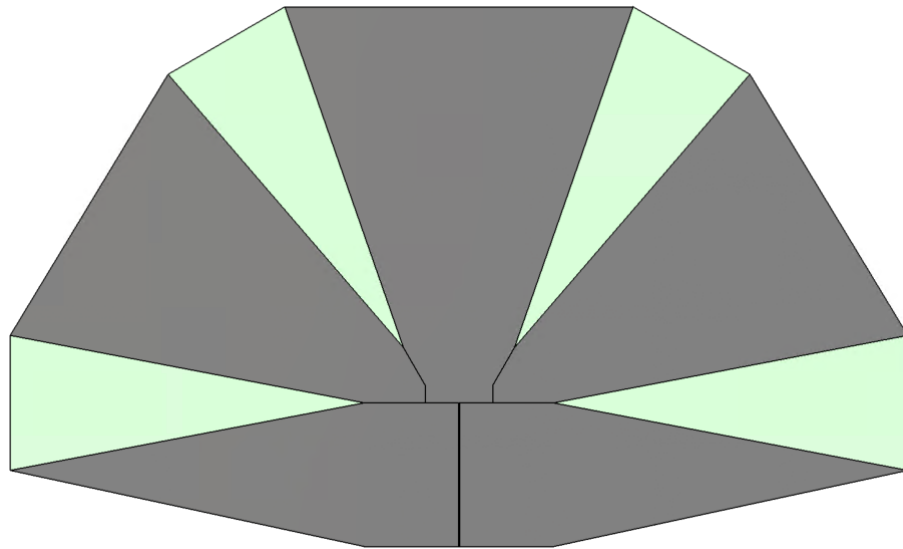


Figure 6.30: Four way Vivaldi Antenna Design with individual Microwave Switches

The functional microwave switch was redesigned for an antenna application. The design used Vivaldi antennas with a switching network using nanowire resistive layers. In Fig. 6.30, the proposed design of the Vivaldi antenna with each end radiating at different directions, ranging  $-90^\circ$ ,  $-45^\circ$ ,  $45^\circ$ ,  $90^\circ$  is presented. The purpose of the designs was to utilise the microwave switch and provide a switching mechanism that would allow power transfer to individual antenna. The operating frequency of each Vivaldi antenna was at 25 GHz. Fig. 6.31 displays the reflection coefficient ( $S_{11}$ ) of each Vivaldi antenna with individual microwave switch. Each antenna had a bandwidth under -10 dB from 22 GHz up to 26 GHz.



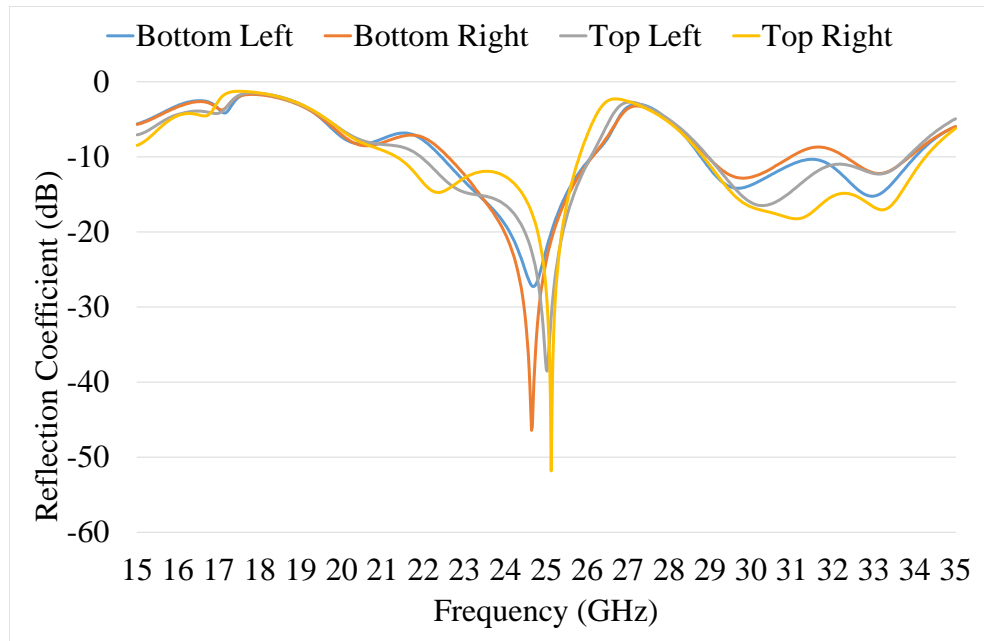


Figure 6.31: Vivaldi Antenna with Microwave Switch - Reflection Coefficient  $S_{11}$

Fig. 6.32 - 6.34, displays the far-field plots for each individual Vivaldi antenna operating. Each figure shows the radiation pattern that was simulated at 22 GHz, 24 GHz and 25 GHz respectively. For each radiation plot the maximum gain values were at 8 dBi and each antenna was radiating at the desired direction with one microwave switch at an OFF state while the rest were at an ON state.

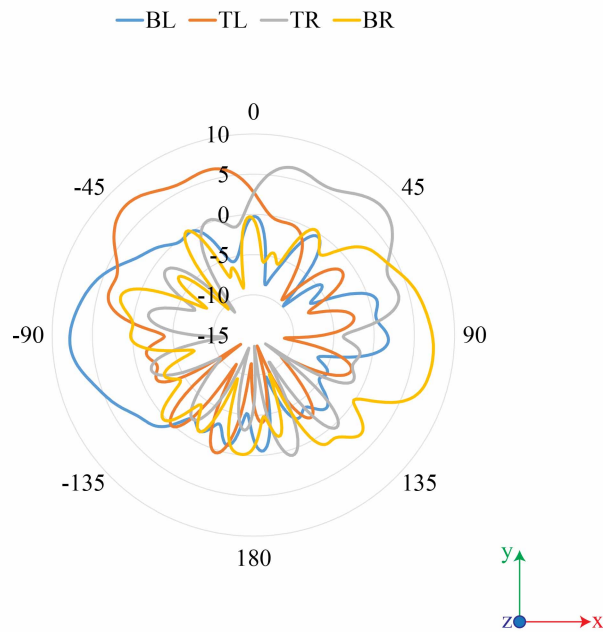


Figure 6.32: Vivaldi Antenna with Microwave Switch - Radiation pattern at 22 GHz

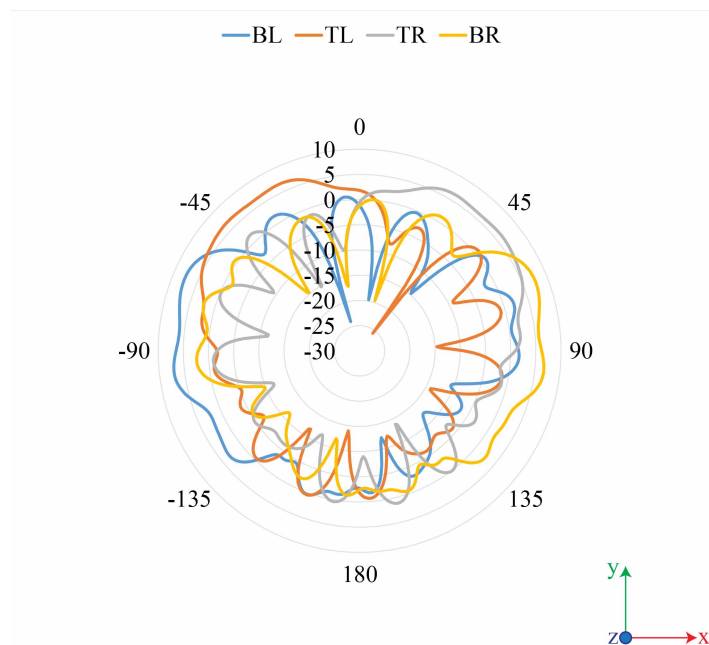


Figure 6.33: Vivaldi Antenna with Microwave Switch - Radiation pattern at 24 GHz

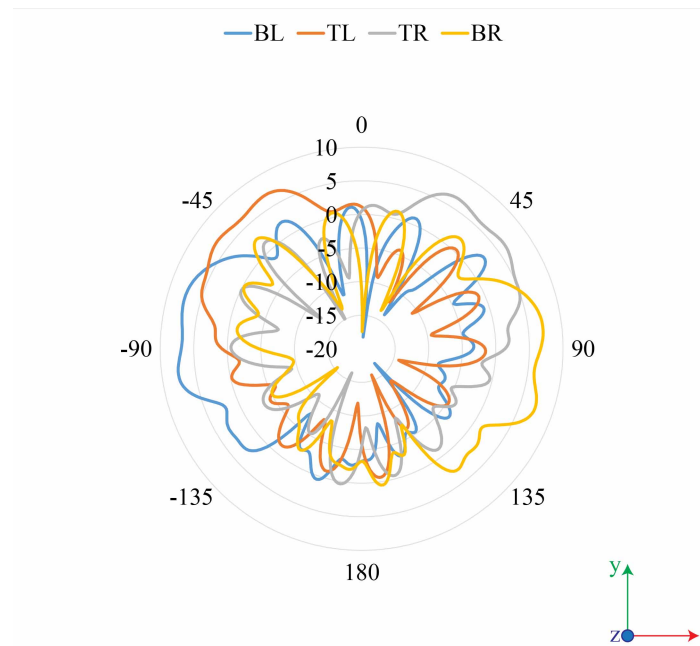


Figure 6.34: Vivaldi Antenna with Microwave Switch - Radiation pattern at 25 GHz

## 6.7 Summary and Conclusions

This chapter investigated both the initial and improved design of the microwave switch with nanowire resistive layers. Both designs presented very interesting results through a series of simulations. The microwave switch was able to be optimised and this allowed the design to utilise the ON/ OFF state from a CPW.

Fig. 6.11 - 6.19 show the initial design and its problems with the operation of the microwave switch, due to the length ( $Lg$ ), which cannot be longer than 1 mm. The change in the gate offset ( $D$ ) prove that there was a high capacitance across the gate and signal track. This caused the design to lose power through the microwave switch and reduce characteristic impedance.

As for the improved design seen in Fig. 6.22 - 6.27, all simulation results had a better performance to the initial design. The power transferred through the CPW to the microwave switch was improved. When the length of the switch ( $Lg$ ) shortens, the better the transmission since it dropped below -23 dB. Varying the gate offset ( $D$ ) still

had a minor effect on the overlay, due to the gate tracks inducing capacitance, however the loss in transmission is better than the initial design.

With the investigation of these microwave switches, the results were thoroughly discussed with Dr B. Mikrkhaydarov and Dr P. Young, hence the reason to change the substrate from Kapton to Quartz. This allowed more investigations to be done on the microwave switch with Quartz Wafer at the University of Surrey. They were able to acquire the substrate and have the design Ink Jet printed onto the material. After “Solution processed InAs nanowire transistors as RF/microwave switches” [69] was published at *Advanced Electronic Materials*, a further investigation was required to assure the operation of the microwave switch. By applying it to an array of Vivaldi antennas, the design was able to switch between each individual antenna. Unfortunately there were no physical designs or testing for this antenna, as the researchers from the University of Surrey were focusing on other projects, putting the fabrication of this antenna on hold.

# Chapter 7

## Conclusion

In this thesis two flexible substrates were investigated, Kapton and Mylar. Each having a specific permittivity and dielectric loss, as well as, having some interesting mechanical properties. The flexible substrate was chosen to create an Origami structure using various antenna types, such as Vivaldi, U Shaped Slot and Substrate Integrated Waveguide (SIW). A series of simulations and measurements were collected and interpreted, while changing a specific set of parameters, such as Inner angle ( $\alpha$ ) and Folding angle ( $\beta$ ). The flexible substrate was also used to create a microwave switch by utilising nanowires as a Field Effect Transistors (FET).

### 7.1 Summary of Thesis Achievements

Origami has been crucial to a lot of advanced science discoveries. It created a new path that allowed scientist to discover new innovative ideas and designs using various folding techniques. The ability to transform a flat sheet of paper into various intricate forms and shapes is very fascinating. For example: Miura Ori folding technique, consists of a set of four parallelograms which create a single unit cell. It is only when the units are arrayed that the positive properties, such as stiffness and rigidity arise. Another aspect to the Miura Ori folding pattern is the ability to collapse, turning a big

3-Dimensional (3-D) object into a fully folded state. The applications of using Origami folding techniques are still to be investigated to its limits. Chapter 2 only touches on its possibilities. There are still plenty other Origami techniques and new ways of applying them, that can be further investigated by researchers.

One of the aims of this research is to investigate the use of Origami folding techniques on various antenna types. Two flexible substrates such as Kapton and Mylar were initially tested. Each flexible substrate had their own unique electrical and mechanical properties. For the purpose of this investigation both flexible substrates on antenna designs consisting of a Single Linear Tapered Slot Antenna (LTSA) or Linear Tapered Vivaldi Antenna. Each flexible substrate was simulated on CST Studio with the same parameters, to determine if there is a change in permittivity or the performance of the antenna. Upon analysing the simulated and measured results, there was a small shift in the resonant frequency, due to the different permittivity on each flexible substrate. Thereafter, the antenna design was changed from a single LTSA to an array of Vivaldi antennas, where each was radiating at different phase.

Each Vivaldi antenna is  $90^\circ$  out of phases to each other. This antenna design allowed each Vivaldi antenna to radiate at all four directions. During physical measurements, each flexible substrate was assessed on the mechanical properties. As Mylar transition from a Flat to Folded state, the metallisation on the copper starts to warp and appeared to be broken upon further investigation. This caused discontinuity across the antenna, therefore disabled it from further measurements. Kapton appears to perform better physically, but still suffers as the folding angle increase over  $90^\circ$ . Chapter 3 concluded the investigation of various flexible substrates, choosing Kapton, as the flexible substrate throughout this thesis.

Chapter 4 demonstrated the antenna design using Miura Ori folding technique. The design was a U-shaped slot antenna. The slot antenna was first optimised to achieve an acceptable performance level at the desired resonant frequency. The resonant frequency was decided to be at 2.5 GHz. In order to transfer the slot antenna design into a single

Miura Ori unit cell, its equations were applied. The equations provided the width and length of the parallelogram in a 3-D format. Each rectangle on the slot antenna was parametrised with the Miura Ori equations. The output provides coordinates points in the 3-D polygon function, this created curves before lofting them into solid objects. A realistic 3-D Miura Ori model was created with a single slot antenna design, which only used two variables: Inner angle ( $\alpha$ ) and Folding angle ( $\beta$ ). This achieved one of the objectives set out at the beginning of the thesis.

The single slot antenna design was simulated on CST Studio and measured with a Vector Network Analyser (VNA) in the anechoic chamber. The outcome displayed a good trend. The measured performance of the single slot antenna remained similar, as the inner angle ( $\alpha$ ) and folding angle ( $\beta$ ) increased. On average the return loss ( $S_{11}$ ) value was below -30 dB. Although gain measurements were not performed, due to the standard horn gain being out for repair throughout the lasing of this thesis, there was a noticeable shift in the radiating angle, as the inner angle ( $\alpha$ ) increased. The single slot antenna was changed into a 2 by 2 array of slot antennas with a matching network. The Miura Ori equations were also applied to the matching network. The arrays of slot antennas were investigated both simulated and measured. The simulated gain greater than 11 dB was achieved. Comparing the measured results with simulated, it could be observed that the performance remained constant.

The second antenna design using the Miura Ori folding technique was achieved in Chapter 5. The antenna used was a SIW antenna. The SIW antenna is an open slot antenna and it was optimised to operate at 4.5 GHz. The Miura Ori equations were applied onto the SIW antenna design. The SIW antenna was simulated by varying the Inner angle ( $\alpha$ ) and Folding angle ( $\beta$ ). The simulated results displayed a good trend, as the inner angle ( $\alpha$ ) increased, the maximum gain value increased gradually and the radiating angle was steered by a small amount.

The single SIW antenna design was changed to a 2 by 1 array of SIW antennas. Simulations were performed and the simulated results displayed a similar trend as the

single SIW antenna. Physical measurements were not available due to the lack of technical staff and the lack of experience displayed by other technical staff.

One issue arose from the two antenna designs using the Miura Ori folding technique. In the simulation results, when the folding angle was at the maximum  $50^\circ$  on the slot antenna and  $40^\circ$  on the SIW antenna, the performance declined dramatically to  $-5.86$  dB and  $-9.16$  dB respectively. When modelling the antenna structures, the curves were translated in the Z-axis and lofted. As the folding angle varied, any microstrip crossing the edge of any parallelogram would have had an extended length. This was causing mismatch between the microstrip and the radiated element when observing the simulated results for the two antenna designs. Contrary to the measured results from Chapter 4, where the problem did not occur.

Chapter 6 presented a microwave switch with nanowires. Kapton was used as a flexible substrate. The switch design used a Co-Planar Waveguide (CPW) as a transmission line. In between the CPW transmission line, a Field Effect Transistor (FET) was implemented with the use of nanowires and a gate track above the CPW design. As voltage was applied to the gate track, the microwave switch was at an OFF state where there will be transmission between the two CPW ports. When there was no voltage applied to the gate track, the microwave switch was at an ON state and reflecting the power back to the input. This was simulated with Ohmic sheets with resistance value of  $600 \Omega/\text{sq}$  at an ON state and  $600 \text{ k}\Omega/\text{sq}$  at an OFF state. In the initial design, it was confirmed that the microwave switch is not operational due to high capacitance induced between the gate and signal tracks. In the improved design the gate tracks were separated between the signal tracks. This caused the performance to improve greatly. The investigation were thoroughly discussed with Dr. P. Young and Dr. B. Mikrkhaydrov. The design was adjusted to use Quartz as the base substrate. With the design, Dr. B. Mikrkhaydrov was able to publish an article, as a bottom-fed FET microwave switch. Lastly, the operating microwave switch was optimised with an arrays of Vivaldi antennas to confirm the functionality of the microwave switch.



## 7.2 Applications

The thesis gave rise to a lot of possibilities in Origami Antenna designs. Especially in space applications, where one of the main concerns in satellites is the weight of horn antennas. When operating in a low frequency such as L-band, the horn antenna becomes extremely large, therefore the weight of the horns is loaded into the satellite. Miura Ori folding technique is a possible solution where the antenna can be stowed away during launch and be able to redeploy when the satellite is in orbit. The Miura Ori folding technique can also be able to steer the radiating angle by a given amount, therefore the antenna can be adjusted to a specific location. Similarly, when the array of Vivaldi antennas is in the Flat state, it will be able to communicate between each individual satellite in a close proximity. When it is in the Folded state, it can focus all the beams into one direction allowing a higher gain towards a distant object such as a Low Earth Orbit (LEO) satellite.

Other applications like military secure communications would be beneficial as well. As the antenna structure goes into the full folded state, it could be carried around and it will be very space efficient. When it is used, it can then be unfolded, completely flat or partially folded and use the antennas in a remote location. If Origami folding techniques were applied in military grade antennas, it would have a huge impact on the way are perceived.

## 7.3 Future Work

This thesis presented the use of flexible substrates with various antenna types using Origami folding techniques. A significant amount of simulations and measurements was performed with flexible substrates. It would be intriguing to study and investigate the performances of other flexible substrates. A study could also be performed on the mechanical properties of the flexible substrates, where it is folded multiple times without the copper tracks warping or cracking, causing discontinuity.

With the two antenna designs using Miuri Ori folding technique, it would be very interesting to investigate the measured results of SIW antennas, compared to the simulated results. Also verifying the measured results with a standard horn gain to determine the maximum gain value. The design included a set of inner angles during testing. Another topic worth investigating, could include the change in the inner angle mechanically.

Apart from flexible substrates, further work on antenna designs that incorporate any Origami folding techniques would be interesting. It would also be fascinating to study the other techniques such as Kirigami, which means paper cutting. The antenna designs can be cut to a specific pattern then folded into a 3-D shape. In addition, a study on Origami Whirlpool Spiral [70] could potentially create a horn antenna with an Origami 3-D spiral.

# References

- [1] “The science of origami,” *Science*, vol. 300, no. 5620, pp. 735–735, 2003. [Online]. Available: <http://science.sciencemag.org/content/300/5620/735.1>
- [2] “Tom hull’s origami math,” 2015. [Online]. Available: <http://mars.wne.edu/thull/origamimath.html>
- [3] “Trisecting an angle with origami,” 2007. [Online]. Available: <https://www.sciencenews.org/article/trisecting-angle-origami>
- [4] “David eppsteins geometry junkyard,” 2008. [Online]. Available: <https://www.ics.uci.edu/eppstein/junkyard/origami.html>
- [5] “Dave mitchells origami heaven,” 2006. [Online]. Available: <http://www.origamiheaven.com/>
- [6] “Express your creativity,” 2019. [Online]. Available: <https://www.thesprucecrafts.com/brief-history-of-origami-2540653>
- [7] “Origami engineering,” 2019. [Online]. Available: <https://quarkmag.com/unfolding-origami-engineering-5bbee7fa0e13>
- [8] R. J. Lang, 2015. [Online]. Available: <https://langorigami.com/article/huzita-justin-axioms/>
- [9] S. Yin, *The Mathematics of Origami*, 1st ed., 2009.
- [10] “Basic origami folds,” 2019. [Online]. Available: <http://www.origami-make.org/howto-origami-fold.php>
- [11] “Origami mathematics,” 2019. [Online]. Available: <http://theconversation.com/origami-mathematics-in-creasing-33968>
- [12] “The miura ori fold,” 2019. [Online]. Available: <https://naturalorigami.wordpress.com/2016/07/18/the-miura-ori-fold>
- [13] M. Schenk and S. Guest, “Geometry of miura-folded metamaterials,” 2013. [Online]. Available: <http://www.pnas.org/content/pnas/110/9/3276.full.pdf>
- [14] “Byu engineers use origami to make more space in space,” 2012. [Online]. Available: <https://universe.byu.edu/2013/12/12/byu-engineers-use-origami-to-make-more-space-in-space/>
- [15] D. Eppstein, *Minimum Forcing Sets for Miura Folding Pattern*, 1st ed., 2014. [Online]. Available: <https://www.ics.uci.edu/eppstein/pubs/BalDamEpp-SODA-15-slides.pdf>

- [16] R. Crowell, “Cool jobs: The art of paper folding is inspiring science,” 2019. [Online]. Available: <https://www.sciencenewsforstudents.org/article/cool-jobs-paper-folding-origami-inspiring-science>
- [17] “Origami science,” 2019. [Online]. Available: <https://www.origami-resource-center.com/origami-science.html>
- [18] S. Anthony, “Folded paper lithium-ion battery increases energy density by 14 times,” 2016. [Online]. Available: <http://www.extremetech.com/extreme/168288-folded-paper-lithium-ion-battery-increases-energy-density-by-14-times>
- [19] K. Kuribayashi-Shigetomi, “Cell origami: Self-folding of three-dimensional cell-laden microstructures driven by cell traction force,” *PLOS*, 2012. [Online]. Available: <https://journals.plos.org/plosone/article?id=10.1371/journal.pone.0051085>
- [20] E. Gjerde, “Tiled hexagon tessellation,” 2013. [Online]. Available: <http://www.origamitessellations.com/docs/tiled-hexagon-tessellation-v2.pdf>
- [21] Y. Liu, “Self-folding of polymer sheets using local light absorption,” *Soft Matter*, no. 8, pp. 1764–1769, 2012. [Online]. Available: <https://pubs.rsc.org/en/content/articlelanding/2012/sm/c1sm06564e>
- [22] “Shrinky dinks inventor tells her story,” 2015. [Online]. Available: <https://www.newsobserver.com/entertainment/arts-culture/article20500794.html>
- [23] X. Liu, S. Yao, S. V. Georgakopoulos, and M. Tentzeris, “Origami quadrifilar helix antenna in uhf band,” in *2014 IEEE Antennas and Propagation Society International Symposium (APSURSI)*, July 2014, pp. 372–373.
- [24] S. Yao and S. V. Georgakopoulos, “Origami segmented helical antenna with switchable sense of polarization,” *IEEE Access*, vol. 6, pp. 4528–4536, 2018.
- [25] “Helical antennas in satellite radio channel,” 2015. [Online]. Available: <https://www.intechopen.com/books/advances-in-satellite-communications/helical-antennas-in-satellite-radio-channel>
- [26] K. Fuchi, J. Tang, B. Crowgey, A. R. Diaz, E. J. Rothwell, and R. O. Ouedraogo, “Origami tunable frequency selective surfaces,” *IEEE Antennas and Wireless Propagation Letters*, vol. 11, pp. 473–475, 2012.
- [27] S. Yao, X. Liu, and S. V. Georgakopoulos, “Morphing origami conical spiral antenna based on the nojima wrap,” *IEEE Transactions on Antennas and Propagation*, vol. 65, no. 5, pp. 2222–2232, May 2017.
- [28] S. I. H. Shah, M. M. Tentzeris, and S. Lim, “Low-cost circularly polarized origami antenna,” *IEEE Antennas and Wireless Propagation Letters*, vol. 16, pp. 2026–2029, 2017.
- [29] G. J. Hayes, Y. Liu, J. Genzer, G. Lazzi, and M. D. Dickey, “Self-folding origami microstrip antennas,” *IEEE Transactions on Antennas and Propagation*, vol. 62, no. 10, pp. 5416–5419, Oct 2014.
- [30] S. R. Seiler, G. Bazzan, K. Fuchi, E. J. Alanyak, A. S. Gillman, G. W. Reich, P. R. Buskohl, S. Pallampati, D. Sessions, D. Grayson, and G. H. Huff, “Physical reconfiguration of an origami-inspired deployable microstrip patch antenna array,” in *2017 IEEE International Symposium on Antennas and*

- Propagation USNC/URSI National Radio Science Meeting*, July 2017, pp. 2359–2360.
- [31] J. Kimionis, M. Isakov, B. S. Koh, A. Georgiadis, and M. M. Tentzeris, “3d-printed origami packaging with inkjet-printed antennas for rf harvesting sensors,” *IEEE Transactions on Microwave Theory and Techniques*, vol. 63, no. 12, pp. 4521–4532, Dec 2015.
- [32] “Origami editor 3d,” 2017. [Online]. Available: <https://sourceforge.net/projects/origamieditor3d/>
- [33] “Space communications,” 2010. [Online]. Available: <https://encyclopedia2.thefreedictionary.com/Space+Communications>
- [34] P. J. Gibson, “The vivaldi aerial,” in *1979 9th European Microwave Conference*, Sep. 1979, pp. 101–105.
- [35] Y. Erdogan, “Parameteric study and design of vivaldi antennas and arrays,” 2018.
- [36] D. M. Pozar, *Microwave engineering; 3rd ed.* Hoboken, NJ: Wiley, 2005. [Online]. Available: <https://cds.cern.ch/record/882338>
- [37] G. Kalbhor, M. Vyas, and B. P. Patil, “Antenna design for ground penetrating radar system,” *International Journal of Advanced Electrical and Electronics Engineering (IJAEED)*, vol. 2, pp. 35–39, 01 2013.
- [38] P. S. N. Rahul Singha, Dr Vakula D, “Linear tapered slot vivaldi antenna with corrugated edges for uwb application,” pp. 1–4, Jan 2014.
- [39] S. Sheel and J. C. Coetzee, “Switchable-feed reconfigurable ultra-wide band planar antenna,” in *2015 International Symposium on Antennas and Propagation (ISAP)*, Nov 2015, pp. 1–3.
- [40] D. Ziani Kerarti, F. Z. Marouf, and S. M. Meriah, “New tapered slot vivaldi antenna for uwb applications,” in *2012 24th International Conference on Microelectronics (ICM)*, Dec 2012, pp. 1–4.
- [41] A. Presse, J. M. Floc’h, and A. C. Tarrot, “Flexible uhf/vhf vivaldi antenna for broadband and gas balloon applications,” in *2017 47th European Microwave Conference (EuMC)*, Oct 2017, pp. 1218–1221.
- [42] “Military radio that transmit simultaneously on wideband and narrowband introduced by thales,” 2013. [Online]. Available: <https://www.militaryaerospace.com/articles/2013/01/Thales-military-radio.html>
- [43] “New batteries lighten load for troops in afghanistan,” 2013. [Online]. Available: <https://www.gov.uk/government/news/new-batteries-lighten-load-for-troops-in-afghanistan>
- [44] C. A. Balanis, *Antenna Theory: Analysis and Design*. New York, NY, USA: Wiley-Interscience, 2005.
- [45] S. J. Chen, C. Fumeaux, B. Chivers, and R. Shepherd, “A 5.8-ghz flexible microstrip-fed slot antenna realized in pedot:pss conductive polymer,” in *2016 IEEE International Symposium on Antennas and Propagation (APSURSI)*, June 2016, pp. 1317–1318.

- [46] S. R. Zahran, Z. Hu, and M. A. Abdalla, "A flexible circular polarized wide band slot antenna for indoor iot applications," in *2017 IEEE International Symposium on Antennas and Propagation USNC/URSI National Radio Science Meeting*, July 2017, pp. 1163–1164.
- [47] K. Fujita, D. Kanemoto, K. Yoshitomi, K. Yoshida, and H. Kanaya, "Uwb circularly polarized planar antenna on flexible substrate," in *2013 IEEE MTT-S International Microwave Workshop Series on RF and Wireless Technologies for Biomedical and Healthcare Applications (IMWS-BIO)*, Dec 2013, pp. 1–3.
- [48] S. M. Saeed, C. A. Balanis, C. R. Birtcher, A. C. Durgun, and H. N. Shaman, "Wearable flexible reconfigurable antenna integrated with artificial magnetic conductor," *IEEE Antennas and Wireless Propagation Letters*, vol. 16, pp. 2396–2399, 2017.
- [49] R. W. World, "Substrate integrated waveguide," 2012. [Online]. Available: <http://www.rfwireless-world.com/Terminology/Advantages-and-Disadvantages-of-SIW-Substrate-Integrated-Waveguide.html>
- [50] L. Wu, A. J. Farrall, and P. R. Young, "Substrate integrated waveguide switched beam antenna," *IEEE Transactions on Antennas and Propagation*, vol. 63, no. 5, pp. 2301–2305, May 2015.
- [51] A. J. Farrall and P. R. Young, "Microstrip to rotated half-mode substrate integrate waveguide planar transition," in *2014 Loughborough Antennas and Propagation Conference (LAPC)*, Nov 2014, pp. 106–109.
- [52] Z. Wang and C. Park, "Novel substrate integrated waveguide (siw) type high power amplifier using microstrip-to-siw transition," in *2013 Asia-Pacific Microwave Conference Proceedings (APMC)*, Nov 2013, pp. 101–103.
- [53] T. Yue and D. H. Werner, "A compact dual-band antenna based on siw technology," in *2018 IEEE International Symposium on Antennas and Propagation USNC/URSI National Radio Science Meeting*, July 2018, pp. 779–780.
- [54] D. M. George, A. Chandroth, C. C. H. Ng, and P. R. Young, "High-gain narrow-band slotted antenna based on ENZ SIW structure," *Journal of Physics D: Applied Physics*, vol. 51, no. 13, p. 135102, mar 2018. [Online]. Available: <https://doi.org/10.10882F1361-64632Faaad27>
- [55] J. Bai, K. Ren, Q. Chen, L. Chen, G. Zhang, and Y. Fu, "Flexible dual-frequency substrate integrated waveguide antenna based on metamaterial," in *2015 IEEE International Conference on Signal Processing, Communications and Computing (ICSPCC)*, Sep. 2015, pp. 1–4.
- [56] R. Moro, M. Bozzi, A. Collado, A. Georgiadis, and S. Via, "Plastic-based substrate integrated waveguide (siw) components and antennas," in *2012 42nd European Microwave Conference*, Oct 2012, pp. 1007–1010.
- [57] A. Ghiotto, F. Parment, T. Martin, T. P. Vuong, and K. Wu, "Air-filled substrate integrated waveguide a flexible and low loss technological platform," in *2017 13th International Conference on Advanced Technologies, Systems and Services in Telecommunications (TELSIKS)*, Oct 2017, pp. 147–149.

- [58] Y. Luo and J. Bornemann, "Substrate integrated waveguide horn antenna on thin substrate with back-lobe suppression and its application to arrays," *IEEE Antennas and Wireless Propagation Letters*, vol. 16, pp. 2622–2625, 2017.
- [59] G. Q. Luo, Z. F. Hu, L. X. Dong, and L. L. Sun, "Planar slot antenna backed by substrate integrated waveguide cavity," *IEEE Antennas and Wireless Propagation Letters*, vol. 7, pp. 236–239, 2008.
- [60] "Light Computing: Nanowire-Based System Allows For Fully Optical Binary Functions, howpublished = <https://www.evolving-science.com/information-communication/optical-binary-functions-00745>, note = Accessed: 2019-03-24."
- [61] "Moore's Law, howpublished = <http://www.moorelaw.org/>, note = Accessed: 2019-03-25."
- [62] S. Swaisaenyakorn, A. J. Cole, C. C. H. Ng, and P. R. Young, "Conformal switched beam antenna," in *2016 Loughborough Antennas Propagation Conference (LAPC)*, Nov 2016, pp. 1–4.
- [63] G. M. Rebeiz and J. B. Muldavin, "Rf mems switches and switch circuits," *IEEE Microwave Magazine*, vol. 2, no. 4, pp. 59–71, Dec 2001.
- [64] K. Entesari, K. Obeidat, A. R. Brown, and G. M. Rebeiz, "A 2575-mhz rf mems tunable filter," *IEEE Transactions on Microwave Theory and Techniques*, vol. 55, no. 11, pp. 2399–2405, Nov 2007.
- [65] M. Y. Chen, D. Pham, H. Subbaraman, X. Lu, and R. T. Chen, "Conformal ink-jet printed c band phased-array antenna incorporating carbon nanotube field-effect transistor based reconfigurable true-time delay lines," *IEEE Transactions on Microwave Theory and Techniques*, vol. 60, no. 1, pp. 179–184, Jan 2012.
- [66] T. Rai, P. Dantes, B. Bahreyni, and W. S. Kim, "A stretchable rf antenna with silver nanowires," *IEEE Electron Device Letters*, vol. 34, no. 4, pp. 544–546, April 2013.
- [67] Q. H. Dao, R. Tchuigoua, B. Geck, D. Manteuffel, P. von Witzendorff, and L. Overmeyer, "Optically transparent patch antennas based on silver nanowires for mm-wave applications," in *2017 IEEE International Symposium on Antennas and Propagation USNC/URSI National Radio Science Meeting*, July 2017, pp. 2189–2190.
- [68] "Quartz Wafer Data Sheet, howpublished = <http://www.semiwafer.com/quartz-wafer.html>, note = Accessed: 2019-03-25."
- [69] B. Mirkhaydarov, H. Votsi, A. Sahu, P. Caroff, P. R. Young, V. Stolojan, S. G. King, C. C. H. Ng, V. Devabhaktuni, H. H. Tan, C. Jagadish, P. H. Aen, and M. Shkunov, "Solution-processed inas nanowire transistors as microwave switches," *Advanced Electronic Materials*, vol. 5, no. 1, p. 1800323, 2019. [Online]. Available: <https://onlinelibrary.wiley.com/doi/abs/10.1002/aelm.201800323>
- [70] T. Fuse, P. Mulatinho, H. Bungartz, and K. Miura, *Spiral: Origami, Art, Design*. Viereck Verlag, 2012. [Online]. Available: <https://books.google.co.uk/books?id=MU9JkgEACAAJ>